Computational and Experimental Investigations of Complex Organic Reactions: From Vinylcyclopropanes to Breslow Intermediates

Dissertation

Zur Erlangung des Doktorgrades der Naturwissenschaften

Dr. rer. nat.

Der Fakultät für Chemie und Pharmazie
der Universität Regensburg

vorgelegt von

Kreutzer Dominik

aus Weiden in der Oberpfalz

Januar 2025

Die Arbeit wurde angeleitet von : Prof. Dr. Julia Rehbein

Promotionsgesuch eingereicht am : 21.01.2025

Prüfungsausschuss: Vorsitz : Prof. Dr. Oliver Tepner

1. Gutachter: Prof. Dr. Julia Rehbein

2. Gutachter: Prof. Dr. Patrick Nürnberger

3. Prüfer : Prof. Dr. Hubert Motschmann

Der experimentelle Teil der vorliegenden Arbeit wurde in der Zeit von Februar 2021 bis April 2024 unter der Leitung von Prof. Dr. Julia Rehbein am Lehrstuhl für Organische Chemie an der Universität Regensburg angefertigt.

Abbreviations

A	acceptor
Ac	acetyl
Ar	aryl
Bn	benzyl
BO	bond order
Boc	*tert*-butyloxycarbonyl
bpy	2,2′-bipyridine
calc.	calculated
CW	continuous wave
D	donor
d	day
dba	dibenzalacetone
TLC	thin-layer chromatography
DCM	dichloromethane
DEE	diethyl ether
DFT	density-functional theory
DMSO	dimethyl sulfoxide
d.r.	diastereomeric ratio
DTBMP	2,6-di-*tert*-butylpyridine
E	elektrophile
EE	ethyl acetate
EnT	energy transfer
equiv.	equivalent
e.r.	enantiomeric ratio
FG	functional group
FRET	Förster resonance energy transfer
fs	femtosecond
GS	ground state
GSB	ground state bleach
h	hour
IC	internal conversion
i-Pr	*iso*-propyl
ISC	intersystem crossing
IRC	intrinsic reaction coordinate
HOMO	highest occupied molecular orbital
L	ligand
LA	Lewis acid
LED	light emitting diode
LP	lone pair
LUMO	lowest unoccupied molecular orbital
LV	lone vacancy
M	molar
Me	methyl
Ms	mesyl
min	minute
n-BuLi	*n*-butyllithium
NBO	natural bond orbitals
nm	nanometer
NRT	natural resonance theory
ns	nanosecond
Nu	nucleophile
Ox	oxidant
P	product
p.a.	pro analysi
PBI	protected Breslow-intermediate
PC	photocatalyst
PCET	proton-coupled electron transfer
PG	protecting group
Ph	phenyl
RC	reactant complex
r.t.	room temperature
SE	stimulated emission
SET	single electron transfer
t-Buli	*tert*-butyllithium
t-BuOK	sodium-*tert*-butanolate
Tf	trifluoromethansulfonyl
TFA	trifluoroacetic acid
THF	tetrahydrofuran
TLC	thin layer chromatography
TMS	tetramethylsilane
TS	transition state
Ts	tosyl
UV-vis	ultraviolet–visible
X	halogen

Table of Contents

A. Determination of Fundamental Rules for Side-Selective Ring Openings of Fused Bicyclic Vinylcyclopropanes using DFT

1. Introduction – Part A

1.1 Ring Opening Reactions – An Alternative Way for Diastereoselective Synthesis

The synthesis of natural compounds and bioactive molecules represents one of the most pivotal and demanding domains within organic chemistry.[1] Their stereochemistry often dictates the biological activity of these substances. Many enzymes, for instance, exhibit a high degree of specificity towards a particular enantiomer that complements the corresponding receptor.[2–5] Consequently, enantiomers with mirror-image stereochemistry can exert vastly different biological effects, as exemplified by the infamous "thalidomide scandal".[6] Hence, it comes as no surprise that the development of stereoselective synthesis strategies has persisted and expanded for decades.[7–9] In addition to selectivity, contemporary efforts increasingly emphasize other factors such as atom economy, cost-effectiveness, and the avoidance of toxic byproducts, all of which are pivotal in an industrial-scale context.[10–13]

Traditionally, organic chemistry has been primarily concerned with developing strategies to introduce desired stereocenters through the formation of new carbon-carbon or carbon-heteroatom bonds.[14,15] In contrast, novel approaches aim to selectively cleave the bonds of cyclopropanes to create chiral centers.[16–18] Their bonds stand out within the realm of hydrocarbons. While hydrocarbons typically feature high bond strengths and low polarizability, making them resistant to cleavage, cyclopropane, in contrast, possesses a unique bond angle of 60°, resulting in a remarkably high ring strain of 28 kcal/mol.[19,20] Nonetheless, these groups maintain sufficient stability to endure multi-step syntheses, enabling deliberate cleavage to generate acyclic C_3-building blocks. This section presents various strategies for breaking these cyclopropane bonds.[21]

1.2 Properties of Cyclopropanes

Cyclopropane is a planar molecule with hydrogen atoms arranged in an eclipsed fashion. The distance between carbon atoms is 151 pm, falling within the range of a sp^3-hybridized carbon-carbon bond. The bond angle within the ring is 60°, which, according to the Baeyer model, would suggest a high ring strain due to a significant deviation from the ideal tetrahedral angle of 109.4°. However, the actual ring strain is 27.6 kcal/mol, which is lower than expected and approximately corresponds to that of cyclobutane with 26.5 kcal/mol, even though cyclobutane has a significantly smaller deviation from the ideal angle with its 88° bond angle.[20,22]

An early explanation for this phenomenon proposed that the sp^3 orbitals of carbon atoms do not overlap linearly but are bent away from the axis of the bond, resulting in inter-orbital angles of approximately 104°, closer to the tetrahedral angle. According to this model, the reduced orbital overlap compensates for the lower Baeyer strain. This type of bonding is visually depicted as a "banana bond" or "bent bond" and has found experimental support through electron diffraction studies of cyclopropane derivatives (Figure 1).[23]

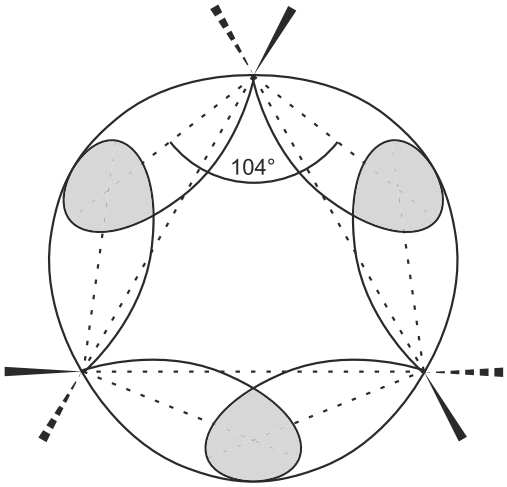

Figure 1. Depiction of the banana bond in cyclopropane. The inner angle between the carbon atoms is 60°, while the inner angle between the sp^3 orbitals is 104°.[24]

However, this model has limitations and cannot explain the similarities to olefinic systems, among other things. Cyclopropanes can, for instance, undergo electrophilic additions. Therefore, in 1947, Walsh proposed an alternative model in which the CH_2 units of cyclopropane are sp^2-hybridized, depicted in Figure 2. The CH_2 units are positioned at the corners of an equilateral triangle, with the H-C-H plane perpendicular to the C-C-C plane. The linear combination of the sp^2 hybrid orbitals oriented toward the center of the ring, a set of three molecular orbitals, is obtained, featuring strongly antibonding MOs. In contrast, combining the rather "tangentially" aligned p_z orbitals results in energetically lower-lying orbitals (Walsh orbitals).[25]

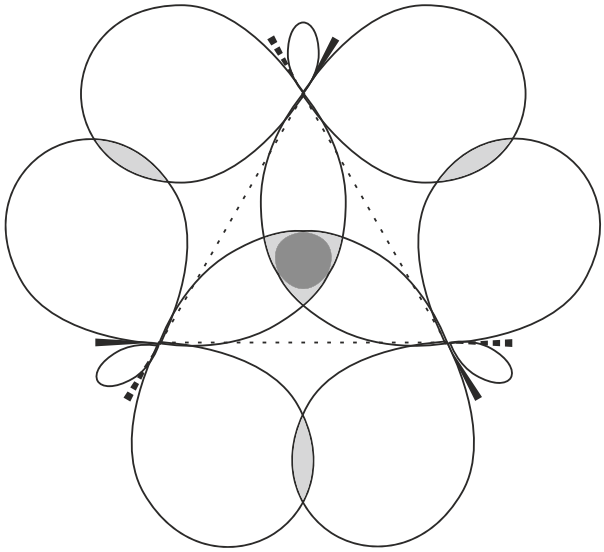

Figure 2. Orbitals of the sp^2 hybridized CH_2 units that form the frontier molecular orbitals according to the Walsh model.[25]

As a result, the LUMO orbitals in cyclopropane are formed from the sp^2 hybrid orbitals (lacking π character), while the HOMO orbitals are formed from the p orbitals (possessing π character). Therefore, cyclopropanes act as good π donors but poor π acceptors.[20] This explains, among other things, the unexpected stability of the cyclopropylcarbinyl cation through delocalization of the C-C bond with the free p orbital, resembling the interaction observed in allyl cations.[26,27] The following section will elucidate strategies for breaking this C-C bond in the three-membered ring.

1.3 Electrophilic Activation of Cyclopropanes

Despite the high ring strain of cyclopropanes, direct ring opening is only achievable under harsh conditions. The introduction of functional groups into the three-membered ring system can be harnessed to polarize it, thereby weakening the desired C-C-σ bond. Donor-substituted cyclopropanes can be attacked directly by electrophiles, facilitating ring opening under mild conditions (Scheme 1).[16,17]

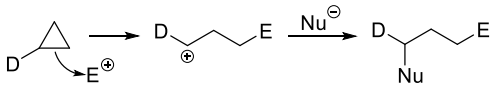

Scheme 1. Ring opening via electrophilic activation.

Moreover, employing vicinal substituted donor-acceptor cyclopropanes enables the exploitation of the inherent push-pull system, facilitating the deliberate cleavage of the central bond that already exhibits zwitterionic character in the absence of external influences. This property is commonly enhanced by the introduction of Lewis acids (LAs), which further augment the electron-withdrawing nature of the acceptor. The resulting 1,3-dipolar intermediates can subsequently be substituted by suitable electrophiles and nucleophiles (Scheme 2).[16,17]

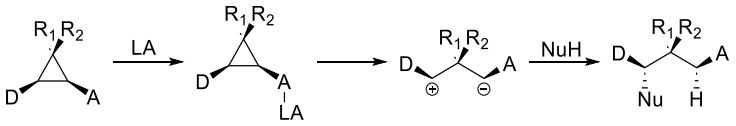

Scheme 2. Lewis acid catalyzed ring opening of a vicinal substituted donor-acceptor cyclopropane system.

Moreover, Lewis acids can be complexed with chiral molecules, enabling the obtention of enantioselective ring opening products, thus elevating the significance of cyclopropanes as building blocks in complex syntheses. In the work of Liu and Feng, for instance, this was achieved in situ through the generation of a chiral *N*,*N*'-dioxide–scandium(III) complex (Scheme 3).[28–30]

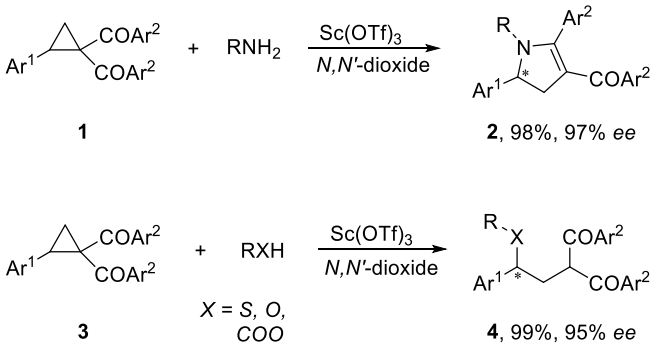

Scheme 3. Enantioselective ring opening of cyclopropanes via chiral Lewis acid complexes.

In addition to Lewis acids, Brønsted acids and bases can also be employed. However, these often trigger an elimination reaction during ring opening. To illustrate, in the cationic ring opening depicted in Scheme 4 (top), the protonation of the carbonyl group (acceptor) in the functionalized cyclopropane initiates bond cleavage, assisted by the heteroatom (donor) and its +M effect. Conversely, in the case of anionic ring opening, a carbanion (donor) is formed by the removal of the hydrogen at the α-position to the ester. This intermediate subsequently decomposes to yield the ring opening product (Scheme 4, bottom).[31]

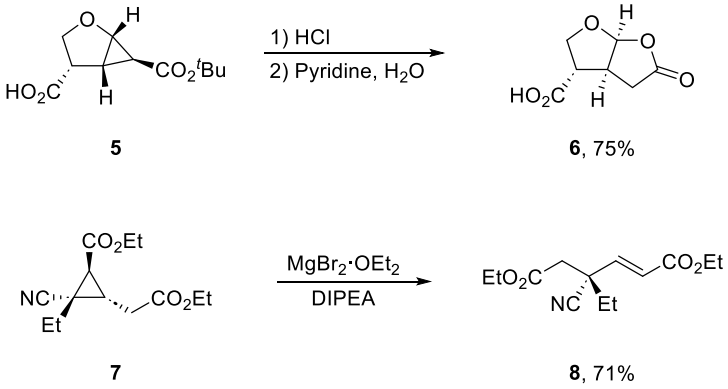

5 **6**, 75%

7 **8**, 71%

Scheme 4. Ring opening of cyclopropanes under Brønsted acids and bases activation.

1.4 Palladium Catalyzed Ring Opening of Cyclopropanes

So far, the methods for ring opening have been primarily limited to activated cyclopropane systems, relying on the partial or complete generation of an ionic species. Therefore, the use of transition metals has proven to be one of the classical approaches for fragmenting non-donor-acceptor substituted cyclopropanes. In addition to radical processes, ring opening often proceeds through the oxidative insertion of the metal into the cyclopropane system. In many cases, bond cleavage occurs via *β*-carbon elimination (Scheme 5). The ring opening, due to the critical negative charge on the *α*-carbon atom, is akin to base-mediated cleavage. Site-selectivity can be determined by electron-withdrawing groups (Scheme 5a) – also in the form of leaving groups – or chelating groups (Scheme 5b). While both types of groups lead to stereoselective ring opening, the processes differ in their activation mode, broadly categorized as electrophilic or nucleophilic.[16,32–34]

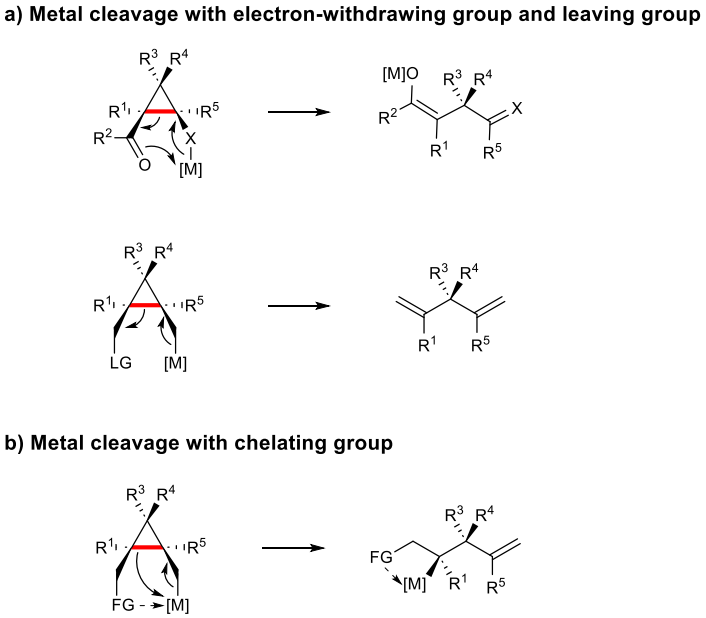

Scheme 5. Transition metal mediated ring cleavage in cyclopropane systems. The scheme was taken from *Chem. Rev.* **2021**, *121*, 140–161 and adjusted.[16]

Although various transition metals such as iridium, rhodium, zirconium, and others are suitable for this purpose, it has been focused specifically on palladium-catalyzed reactions in the following sections.[16]

Palladium-catalyzed reactions, such as the Suzuki coupling and the Heck reaction, are textbook examples for forming carbon bonds between aryl halides and nucleophiles or olefins. Both were discovered in the 1970s and, due to their outstanding importance in organic synthesis, were jointly awarded the Nobel Prize in 2010.[35] Both initiate the catalytic cycle with the oxidative addition of the aryl halide to the palladium complex PdL_2. This is followed by transmetalation (Suzuki) or *syn*-addition (Heck) of the reactants. The final product is formed through reductive

elimination (Suzuki) or *β*-hydride elimination (Heck), with the initial palladium species being regenerated (Scheme 6).[36–42]

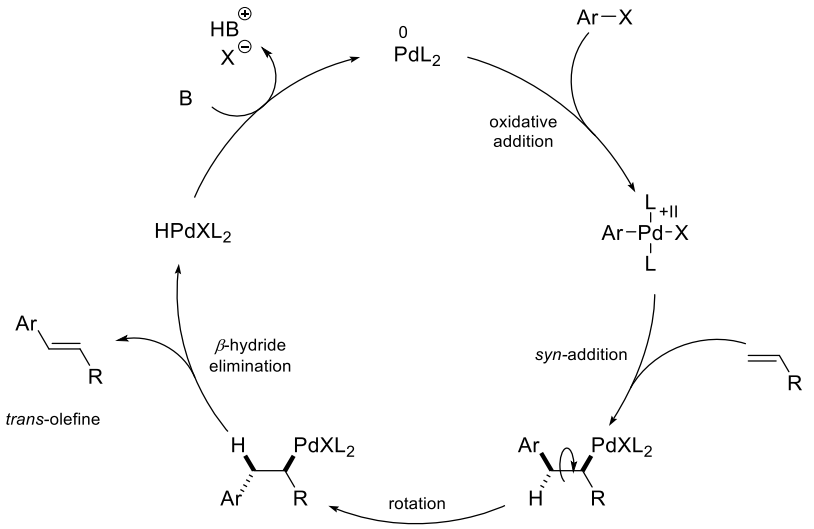

Scheme 6. Catalytic cycle of the Heck reaction.

In the Heck reaction, the sterically preferred *trans* product is typically formed. In contrast, vinyl cyclopropanes can undergo *β*-carbon eliminations, leading to ring opening (Scheme 7).[43]

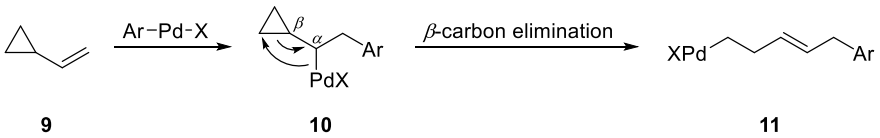

Scheme 7. Ring opening of vinyl cyclopropanes via *β*-carbon eliminations.

The prerequisite is that palladium is situated at the *α*-cyclopropyl position. However, Singh *et al*. demonstrated that terminal olefins can also initiate ring opening over a longer distance. The key is a sequence of *β*-hydride eliminations and reinsertions of the palladium complex until it reaches the corresponding *α*-position (Scheme 8).[32]

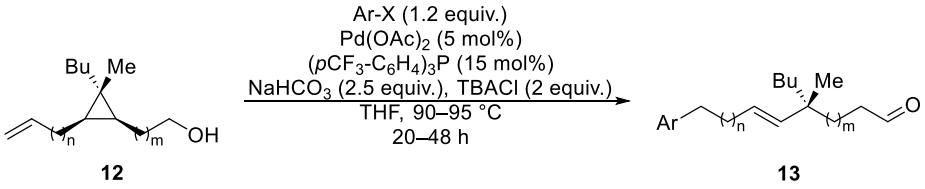

Scheme 8. Ring opening via palladium over a longer distance.

What makes this reaction particularly interesting is the influence of the hydroxyl group, which plays a crucial role as a ligand in the Pd-complex for selective ring opening. For clarity, the mechanism of the ring opening is shown for **14** where n = m = 0 (Scheme 9). The mechanism begins with the oxidative addition of the palladium species to the *α*-cyclopropyl position. The opposing hydroxyl group acts as an electron donor and coordinatively binds to the palladium

complex. Due to chelation, the subsequent β-carbon elimination proceeds regioselective, leading to the migration of the palladium species to the C^3 position. The reaction concludes with a series of β-hydride eliminations and insertions, regenerating the detached Pd species (Scheme 9).

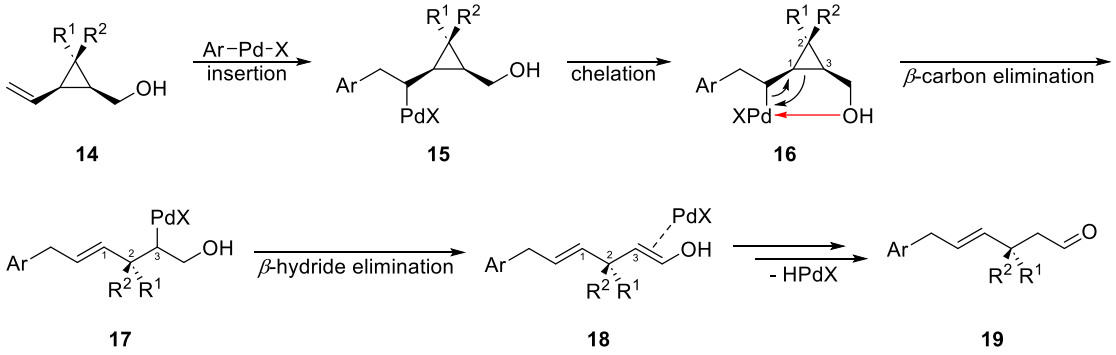

Scheme 9. Exemplary Pd-initiated ring opening aided by neighbor group effects.

A special class of these substrates includes bicyclic vinyl cyclopropanes, which are the focus of this work and crucial building blocks in synthesizing natural compounds (Figure 3). Here, too, palladium can serve as a catalyst for ring opening. The mechanistic details of this reaction will be discussed further in the main part of this work.[44]

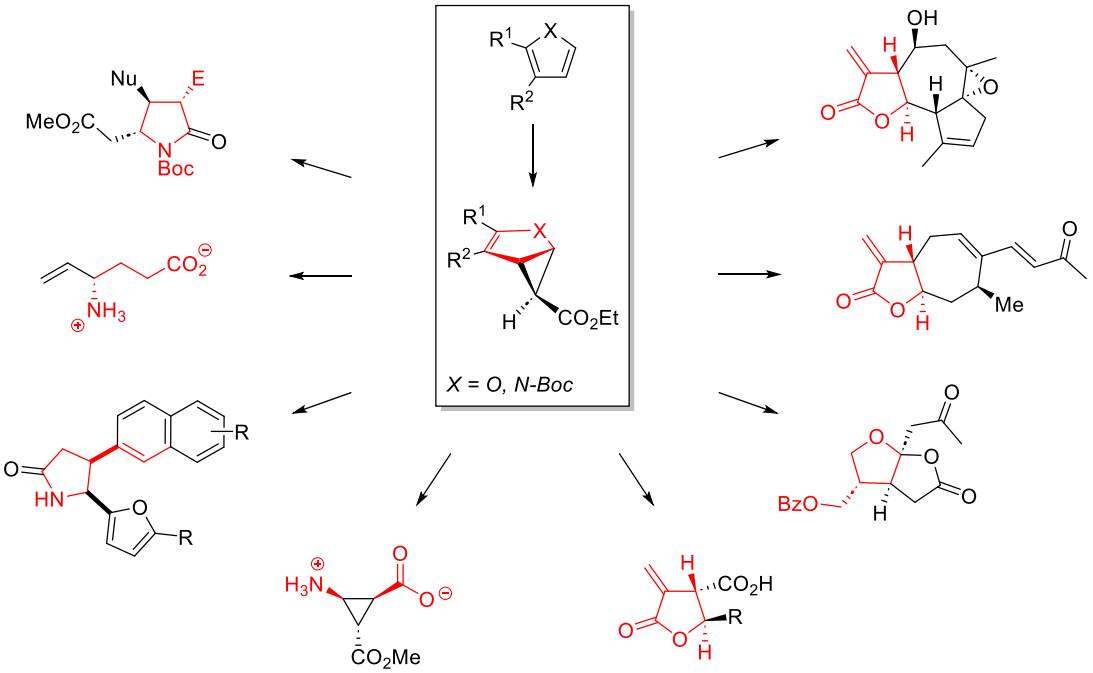

Figure 3. Scope of cyclopropanated furans and pyrroles in the synthesis of natural products. The figure was taken from *Isr. J. Chem.* **2016**, *56*, 531–539.[44]

1.5 Natural Bond Orbital Analysis

In recent decades, modern chemistry has undergone significant advancements – one of which is the increase in computational performance – offering profound insights into the structure and properties of molecules. One key aspect of these developments lies in the detailed examination of electron distribution within molecules, which directly impacts their chemical properties. A method that has garnered particular attention in this context is the analysis of natural bond orbitals (NBOs). This theoretical approach provides a powerful means to intuitively and quantitatively understand bond structures, charge distributions and electron transfers.

The concept of natural bond orbitals originates in the mathematic theory of "natural (spin-) orbitals", which were first introduced by Löwdin in 1955 and has since evolved into a fundamental tool in quantum chemistry, especially by F. Weinhold in the 1980s.[45,46]

Central for the construction of NBOs is the decomposition of delocalized electronic structure into natural atomic orbitals (NAOs) that combine to the respective natural bond orbitals. This relocalization approach of the canonical molecular orbitals recreates the Lewis structure well known by any organic chemistry. These Lewis structures are hypothetical electronic arrangements of bonds and lone electron pairs that adhere to the maximum valence electron rules.

Central for the construction of NBOs is the decomposition of delocalized electronic structure into natural atomic orbitals (NAOs) that combine to the respective natural bond orbitals. This relocalization approach of the canonical molecular orbitals recreates the Lewis structure well known by any organic chemistry. These Lewis structures are hypothetical electronic arrangements of bonds and lone electron pairs that adhere to the maximum valence electron rules.

Another key element of NBO theory is the analysis of NBO charges. These charges result from the population analysis of natural bonding orbitals, which partition electron density based on localized orbitals. This NBO charges provide insights into electron distribution and the transfer of electron density in chemical bonds. Positive NBO charges indicate that an atom has donated electron density and is electron-deficient, while negative charges suggest that an atom has accepted electron density and is electron-rich.

Furthermore, Glendening and Weinhold introduced the natural resonance theory (NRT), which builds on the NBO method, to quantitatively describe resonance.[47,48] Traditionally, resonance has been used to qualitatively represent molecules as an average of two or more idealized structures, such as those in the Kekulé benzene model[49]. The NRT method utilizes information from the first-order reduced density matrix, as employed in the NBO representation, to identify and weight the respective Lewis structures. This approach provides a robust quantitative description of electron delocalization.[47,48]

NBO theory provides an intuitive approach to interpreting bond strengths, electronic delocalization, resonance structures, and charge shifts in molecules. It facilitates the understanding of complex chemical phenomena in a clear, visual, and mathematically grounded manner (Figure 4). The application of NBOs spans from organic molecules to transition metal complexes and reactive intermediates.

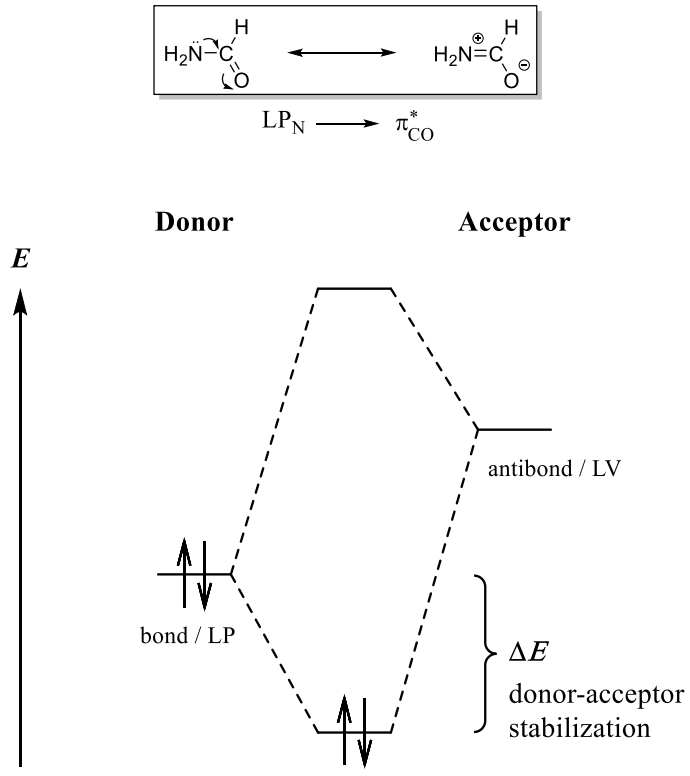

Figure 4. Visualization of the stabilizing energy of a formamide bond calculated by natural bond orbital (NBO) analysis using second-order perturbation theory.

In this thesis, the primary focus is to conduct a comprehensive investigation and application of natural bond orbitals to gain a deep understanding of the fundamental interactions required for the selective opening of cyclopropane bonds. To achieve this, the donor-acceptor interactions are evaluated by using the principles of second-order perturbation theory. This approach allows it to capture stabilizing interactions such as mesomerism or hyperconjugation through orbital occupancy.[45,46,50–55]

2. Aim of the Work – Part A

This chapter was inspired by the Pd-catalyzed transformations of [3.1.0] bicycles described by Reiser and co-workers (Scheme 10) and aims to gain a comprehensive understanding of the factors governing site-selective ring openings in annulated cyclopropyl rings.[56]

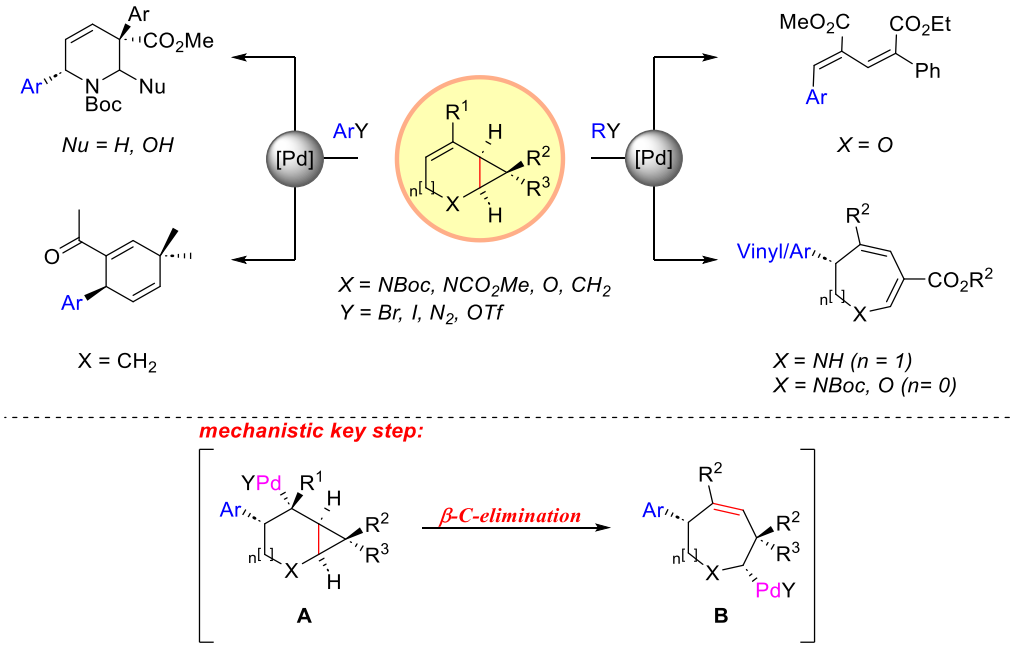

Scheme 10. Heck-Type coupling of bicyclic cyclopropanes. The scheme was taken unchanged from *ACS Catal.* **2021**, *11*, 12019−12028.[56]

The broad spectrum of reactions originating from these annulated systems provides an ideal framework to investigate the fundamental interactions leading to *endo*- and *exo*-cyclic ring openings. Here, the term "*endo bond*" refers to the fusing bond within the annulated bicyclic system, while the "*exo bonds*" pertain to the remaining two cyclopropane bonds. These bonds are represented from a perspective where they direct below the plane of the five-membered ring (Scheme 11).

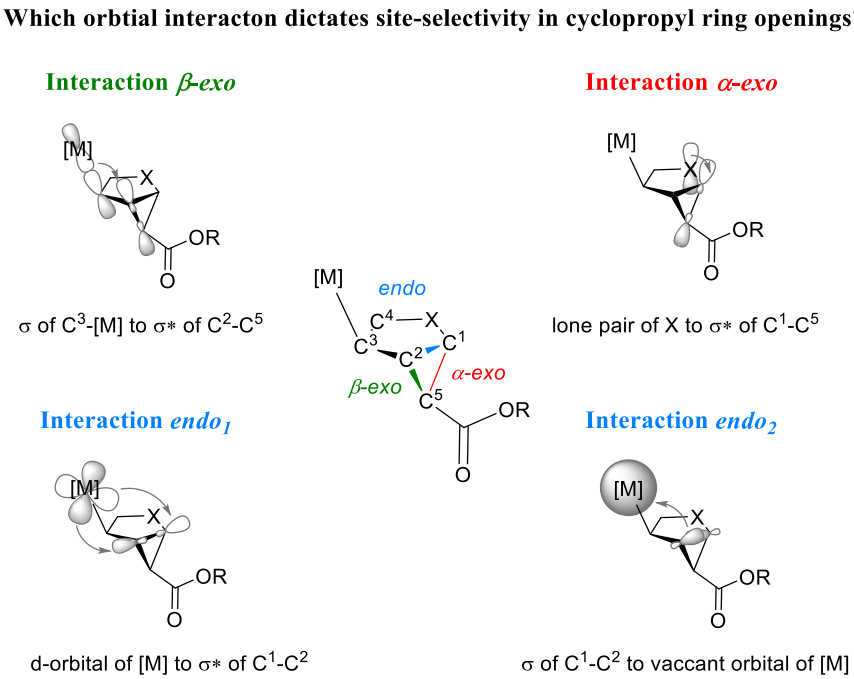

Scheme 11. Probable interactions involved in the ring openings of [3.1.0] bicycle cyclopropanes. X = O, *N*-Boc. [M] = transition metal complexes.

To achieve this, a comprehensive density-functional theory (DFT) study under three fundamental conditions: acid, base, and transition metal catalysis has been conducted. This study not only rationalizes observations in synthetically relevant Heck-type Pd-catalysis but also provides a predictive framework for future (transition) metal-catalyzed cyclopropyl ring openings.

3. Main Part – Part A

3.1 Computational Details

In this section, the computational procedures employed for the research are outlined.

Software and Packages: All density-functional theory (DFT) calculations presented in this work were conducted using the Gaussian 16 software package[57], complemented by standalone NBO 7[58] for analysis.

Geometry Optimization: Geometry optimizations were carried out using the B3LYP-D3BJ hybrid functional[59–64]. A mixed basis set, 6-31+G(d,p), was applied to hydrogen (H), carbon (C), nitrogen (N), oxygen (O), magnesium (Mg) and chloride (Cl) atoms.[65–76] The LANL2DZ basis set, along with its corresponding effective core potential (ECP), was employed for palladium (Pd) and bromine (Br) atoms.[77–80] Implicit solvation effects were considered using the SMD model.[81]

Temperature: Temperature conditions were set at either 353.15 Kelvin, aligning with specific reaction conditions reported by Reiser and co-workers, or at room temperature (298.15 K).

Stationary Points: Stationary points were rigorously characterized as either minimum energy structures or saddle points of first order (transition states) through frequency analysis within the harmonic oscillator approximation. Minimum energy structures exhibited no imaginary frequencies, while transition state structures displayed a single imaginary frequency, confirmed as the correct reaction coordinate of the elementary step of interest via visualization in GaussView 6[82]. The additional verification of a transition state by its intrinsic reaction coordinate (IRC) was omitted because it could not be calculated for flat potential energy surfaces (barrier-free transition states) or when small imaginary vibrational frequencies occurred due to heavy atoms.

Conformational Analysis: Stationary points were subjected to conformational analysis using the CREST program[83,84] with GFN-xTB methods[85] to obtain the most stable conformer. Barriers and thermodynamics along reaction paths were referenced to the minimum energy conformers.

Conformer Selection: To ensure consistency, rotamers with identical spatial orientations were utilized within a 6 kcal/mol energy range when comparing interactions among various molecules. This approach minimized discrepancies stemming from distinct structural attributes.

Orbital Analysis: Natural bond orbital (NBO) analyses were employed to determine atomic orbital populations and quantify orbital interactions. The threshold for energies acquired in a second-order perturbation theory energy analysis was set to 3 kcal/mol. Orbitals were visualized via IQmol[86], using an isovalue of 0.10 $Å^{-3}$.

Visualization: When describing a process that qualitatively applies to multiple systems discussed in the respective paragraph, it was illustrated by using the simplest systems with the fewest number of atoms. The rendered structures have been obtained by CYLview[87]. The reaction profiles have been obtained by mechaSVG[88].

Remark: Note that the computational structures have their own unique numbering system, distinct from the one used for the schemes.

3.2 Results and Discussion

The cleavage of a cyclopropane is in general driven by the release of ring strain energy.[16] However, various model systems were constructed to specifically investigate the interactions determining the outcome of a site-selective ring opening in cyclopropanated furans and pyrroles. Three major initiating events for the opening of a cyclopropane (cp) unit were examined: (I) under acidic conditions, (II) under basic conditions, and (III) through transition metal catalysis. This thesis exclusively focuses on closed-shell mechanisms, even though the radical cleavage of cyclopropanes, such as in radical clock reactions, is also well-known.[16,89–91]

3.2.1 Acid Controlled Ring Openings

In the presence of a Brønsted acid, the cyclopropane ring opens due to the protonation of the ester group at the *α*-position to C^5, which is the most basic group, resulting in a diverse array of products. To investigate *α-exo*-cyclic ring openings under acidic conditions, two fundamental examples derived from furan **1-O** and pyrrole-based **1-N** cyclopropyl bicycles for the computational study were employed.[92,93] Specifically, it was focused on bicycle **20** and **22**, derived from substrates that exhibited regioselectivity in yielding respective ring opening products (Scheme 12). To streamline computational efficiency, the *tert*-butyl groups were substituted with methyl groups. Additionally, the influence of an electron-withdrawing ester group was examined at the C^3 position in system **2-O**, as outlined in Scheme 11.

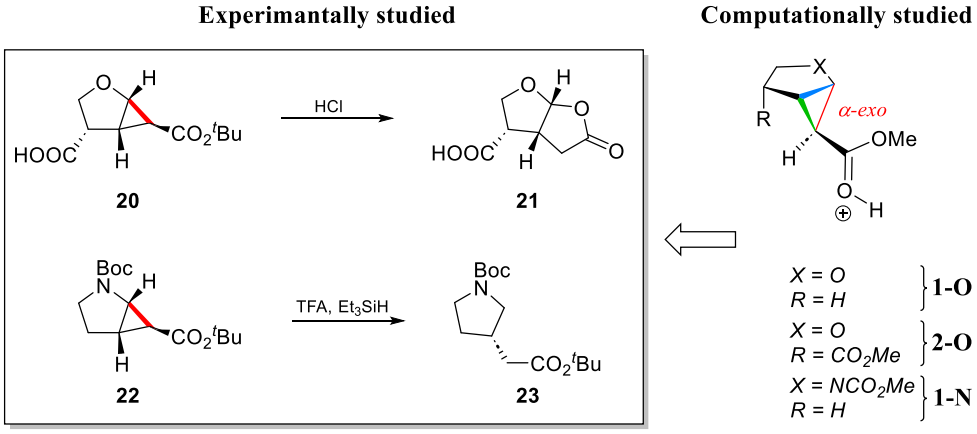

Scheme 12. Left: Experimentally studied [3.1.0] bicycle cyclopropanes undergoing acid-mediated *α-exo*-cyclic ring opening. Right: Computationally studied model compounds.

Bond Length Comparison

Our optimized structures revealed a significant increase in the *α-exo* bond length compared to the non-protonated molecules upon protonation. In all three cases, neither the *β-exo* bond nor the *endo* bond exhibited remarkable changes (Table 1). In Figure 5, a visual representation of the investigated molecules and their bond situation in different solvents is provided.

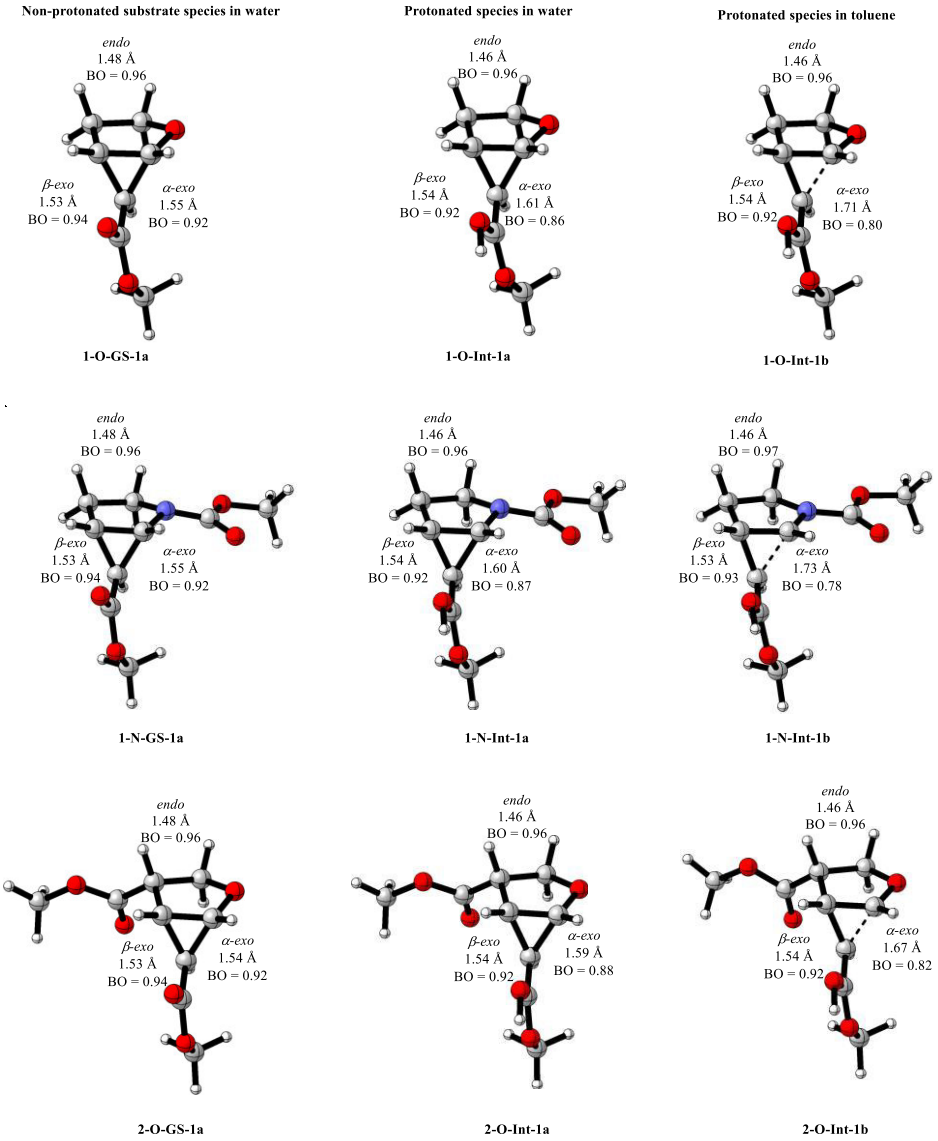

Figure 5. Rendered minimum energy structures of model species for acid-induced cyclopropane ring openings. **GS-1**: Non-protonated substrate species, **Int-1**: Protonated intermediate species. **a**: The SMD solvent model for water was used, **b**: The SMD solvent model for toluene was used. The substrate structures in water (**GS-1a**) do geometrically not differ from their respective analogs in toluene **(GS-1b**) (SI).

Table 1. Cyclopropane bond lengths in the protonated intermediate (**Int-1**) and non-protonated substrate (**GS-1**) species.

	Bond length in Å		
Structure	***α-exo* bond**	***β-exo* bond**	***endo* bond**
1-O-GS-1a	1.55	1.53	1.48
1-O-Int-1a	1.61	1.54	1.46
1-N-GS-1a	1.55	1.53	1.48
1-N-Int-1a	1.60	1.54	1.46
2-O-GS-1a	1.54	1.53	1.48
2-O-Int-1a	1.59	1.54	1.46
1-O-GS-1b	1.55	1.53	1.48
1-O-Int-1b	1.71	1.54	1.46
1-N-GS-1b	1.55	1.53	1.48
1-N-Int-1b	1.73	1.53	1.46
2-O-GS-1b	1.54	1.53	1.48
2-O-Int-1b	1.67	1.54	1.46

Impact of Solvent Polarity

It is crucial to acknowledge that the polarity of the (implicit) solvent environment profoundly influences the ring opening process. To explore a range of solvent scenarios without overextending the computational resources, two extreme cases were calculated: one using water as a protic solvent and the other employing toluene as a nonpolar solvent. It should be highlighted that implicit solvent models cover electrostatic solvent-solvent interactions, but do not account for specific solvent interactions, such as hydrogen bonds, cation–π interactions or π–π stacking.[94,95]

Solvent Comparison: Water vs. Toluene

Water, as a highly polar solvent, based on its dielectric constant (ε=78.3)[96], effectively stabilizes charged species. Consequently, it promotes a substrate-like structure, where the *α-exo* bond remains relatively intact. In contrast, nonpolar toluene yields transition state-like species, where the *α-exo* bond is nearly broken. Remarkably, both extremes of solvation lead to a significant decrease in the bond order of only the *α-exo* bond, indicating that the acid-mediated ring opening consistently favors the selective weakening of this bond, irrespective of solvent polarity. It is worth noting that, in the case of water as a solvent, there were no significant variations in bond length between the different species **1-O-Int-1a**, **1-N-Int-1a** and **2-O-Int-1a** observed.

However, when examining protonated species in toluene, variation is observed. While species **1-O-Int-1b** and **1-N-Int-1b** are comparable, species **2-O-Int-1b** exhibits a shorter bond length. This discrepancy can be attributed to steric effects, specifically diaxial interactions between the electron-withdrawing group (EWG) at C^3 and the proton on C^5. These interactions hinder the formation of a more fully opened structure in the case of species **2-O-Int-1b**.

NBO Population Analysis and Interaction Quantification

To determine and quantify the significant interactions in the cyclopropane ring, a population analysis of the natural bond orbitals (NBOs) was conducted, using second-order perturbation theory to assess the donor-acceptor interactions within the protonated species.

Table 2. Significant donor-acceptor interactions involved in the acid-mediated cyclopropane bond breaking.

	Stabilization energy in kcal/mol			
Structure	**Donor orbital**	**Acceptor orbital**		
		$\sigma^*_{\alpha-exo}$	σ^*_{endo}	$\pi^*_{C=O}$
1-O-Int-1a	**LP$_X$**	15.7	3.1	-
	$\sigma_{\alpha-exo}$	-	-	18.9
	$\sigma_{\beta-exo}$	-	-	6.1
1-N-Int-1a	**LP$_X$**	16.0	-	-
	$\sigma_{\alpha-exo}$	-	-	16.9
	$\sigma_{\beta-exo}$	-	-	6.7
2-O-Int-1a	**LP$_X$**	14.7	-	-
	$\sigma_{\alpha-exo}$	-	-	15.1
	$\sigma_{\beta-exo}$	-	-	7.5
1-O-Int-1b	**LP$_X$**	25.4	4.0	-
	$\sigma_{\alpha-exo}$	-	-	32.1
	$\sigma_{\beta-exo}$	-	-	4.3
1-N-Int-1b	**LP$_X$**	28.7	-	-
	$\sigma_{\alpha-exo}$	-	-	35.6
	$\sigma_{\beta-exo}$	-	-	3.8
2-O-Int-1b	**LP$_X$**	21.8	3.8	-
	$\sigma_{\alpha-exo}$	-	-	25.3
	$\sigma_{\beta-exo}$	-	-	5.2

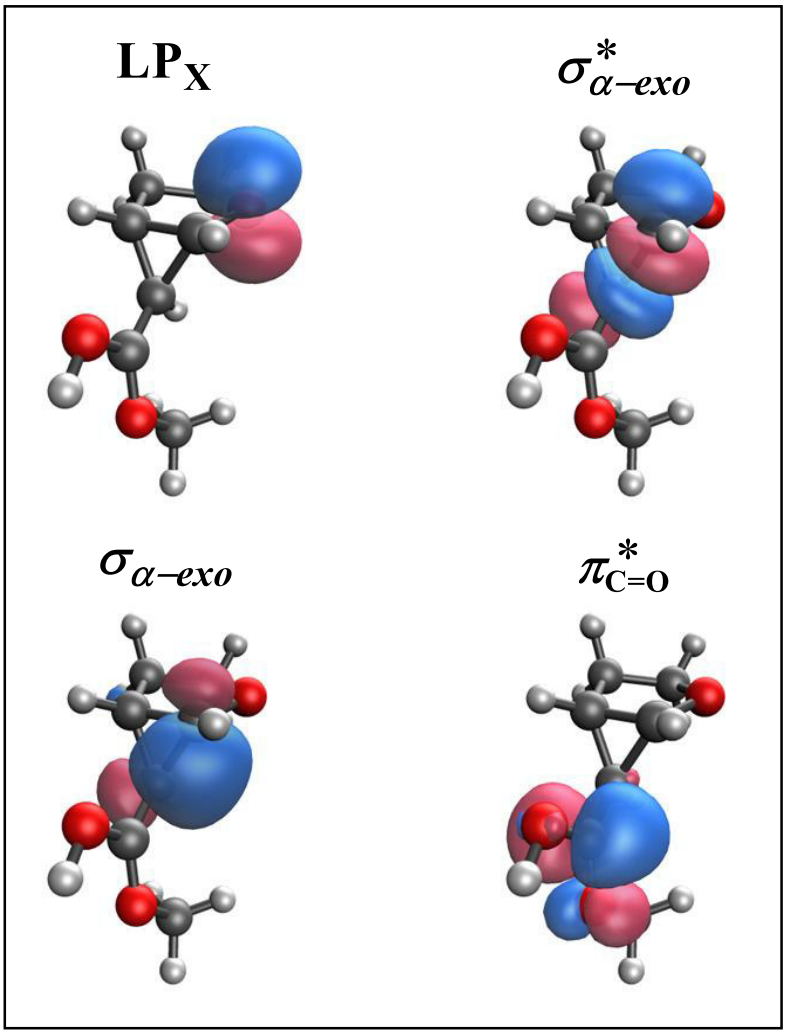

Figure 6. Visualization of selected NBOs referred to in Table 2 for **1-O-Int-1a**.

In order to break a bond during the cyclopropane ring opening, its bonding orbital must donate into an acceptor orbital, or a donor group must interact with its corresponding antibonding orbital. Table 2 lists all orbital interactions by their E2 values (stabilization energy based on second-order perturbation theory), that promote cyclopropane ring opening, excluding interactions below 3 kcal/mol, which are considered negligibly small. The primary donor interaction arises from the overlap of the lone pair originating from the heteroatom **X** in the five-membered ring with the σ*-orbital of the *α-exo* bond (Figure 6, top). Due to geometric constraints, there is no corresponding overlap with the antibonding orbital of *β-exo*. While an overlap exists between the lone pair and the σ*-orbital of the *endo* bond, it is not relevant in the ring opening due to its relatively weaker interaction.

The primary acceptor interaction, on the other hand, results from the overlap between the bonding *α*- and *β-exo* bonds with the carbonyl group of the electron-withdrawing group (EWG) attached to C^5 (Figure 6, bottom). Notably, in the case of the solvent toluene, the NBO analysis recognizes the carbonyl carbon as a carbocation due to its advanced ring opening structure. Therefore, the "choose" option of the program was utilized to treat it as a carbonyl for

comparability of interactions. This donor-acceptor interaction is the strongest and serves as the initiator of the ring opening. However, selectivity is solely based on the lone pair interaction.

The interactions in the non-protonated starting material were analyzed as a reference to further elucidate those in the cationic intermediate, as detailed in Table 3.

Table 3. Significant donor-acceptor interactions in the non-protonated substrate species. A conformer was chosen in which the carbonyl group of the cyclopropyl ring is *anti*-orientated to the *exo*-bonds.

	Stabilization energy in kcal/mol		
Structure	**Donor orbital**	**Acceptor orbital**	
		$\boldsymbol{\sigma^*_{\alpha-exo}}$	$\boldsymbol{\pi^*_{C=O}}$
1-O-GS-1a	**LPX**	11.0	-
	$\boldsymbol{\sigma_{\alpha-exo}}$	-	6.9
	$\boldsymbol{\sigma_{\beta-exo}}$	-	5.8
1-N-GS-1a	**LPX**	11.9	-
	$\boldsymbol{\sigma_{\alpha-exo}}$	-	5.6
	$\boldsymbol{\sigma_{\beta-exo}}$	-	4.7
2-O-GS-1a	**LPX**	11.0	-
	$\boldsymbol{\sigma_{\alpha-exo}}$	-	6.1
	$\boldsymbol{\sigma_{\beta-exo}}$	-	4.4
1-O-GS-1b	**LPX**	11.5	-
	$\boldsymbol{\sigma_{\alpha-exo}}$	-	6.2
	$\boldsymbol{\sigma_{\beta-exo}}$	-	5.3
1-N-GS-1b	**LPX**	12.1	-
	$\boldsymbol{\sigma_{\alpha-exo}}$	-	4.7
	$\boldsymbol{\sigma_{\beta-exo}}$	-	4.3
2-O-GS-1b	**LPX**	11.4	-
	$\boldsymbol{\sigma_{\alpha-exo}}$	-	4.7
	$\boldsymbol{\sigma_{\beta-exo}}$	-	3.9

In Table 3, it becomes evident that the primary interaction involves the overlap between the lone pair and the σ*-orbital of the *α-exo* bond. In this context, the acceptor interaction involving the carbonyl group of the cyclopropyl ring does not significantly favor one over the other. Protonation of the species enhances the acceptor strength of the carbonyl group, ultimately guiding the ring opening through the initial lone pair interaction.

Reaction Profile

From the NBOs, it can be determined that the interactions necessary for a ring opening are present in the protonated intermediates **1-O-Int-1**, **1-N-Int-1** and **2-O-Int-1**. However, to assess reactivity accurately, the reaction barrier must be calculated.

In the case of Figure 5, the bond lengths of the protonated species appear close to the respective transition states leading to the ring expansion, especially when using toluene as solvent, indicating nearly barrierless reactions. This presents a challenge in locating proper stationary structures due to a flat potential energy surface (PES). To overcome this, the convergence criteria were adjusted to "loose" while employing a higher basis set (6-311G+**). The protonation of carbonyl species is well known in literature and is therefore not calculated.[49,97,98] The results are shown in Table 4.

Table 4. Gibbs energies for stationary points in the cationic ring opening reaction using the 6-311G+** basis set.

	Energy in kcal/mol					
Structure	**GS-1a**	**TS-1a**	**GS-2a**	**GS-1b**	**TS-1b**	**GS-2b**
1-O	0.0	1.8	1.3	0.0	0.2	-0.1
1-N	0.0	1.8	1.2	0.0	-	-1.3
2-O	0.0	2.3	1.3	0.0	0.0	-0.5

The ring opening and closed species have nearly identical energy levels. In the presence of water, the reaction is thermodynamically endergonic by 1.2–1.3 kcal/mol, while in toluene, it is exergonic by 0.1–1.3 kcal/mol. The slight favoring of the reaction in the less polar solvent is expected due to the weaker *α-exo* bond. In both cases, the reaction is nearly barrierless, leading to an equilibrium between substrate and product. This equilibrium can be disrupted, for instance, by the attack of a nucleophile like water, resulting in the formation of a hemiacetal or -aminal.

To summarize, the cationic ring opening occurs rapidly, with site-selectivity primarily governed by the lone pair interaction of the heteroatom with the σ*-orbital of the *α-exo* bond.

3.2.2 Base Controlled Ring Opening

The literature documents that in a cyclopropane system substituted with an ester group, the generation of an anion at the α-position relative to the cyclopropane unit leads to the opening of the cyclopropane bond.[31] To explore this phenomenon from a theoretical perspective, a system with a similar framework was selected, making it comparable to the previous and subsequent investigations. This system, introduced by Nicolai Wurzer from the Reiser group, was initially expected to undergo a transition metal-catalyzed *endo* bond ring opening, followed by a Pd-migration and successive Suzuki cross-coupling. However, contrary to these expectations, only a *β-exo* bond opening was exclusively observed (Scheme 13).[99]

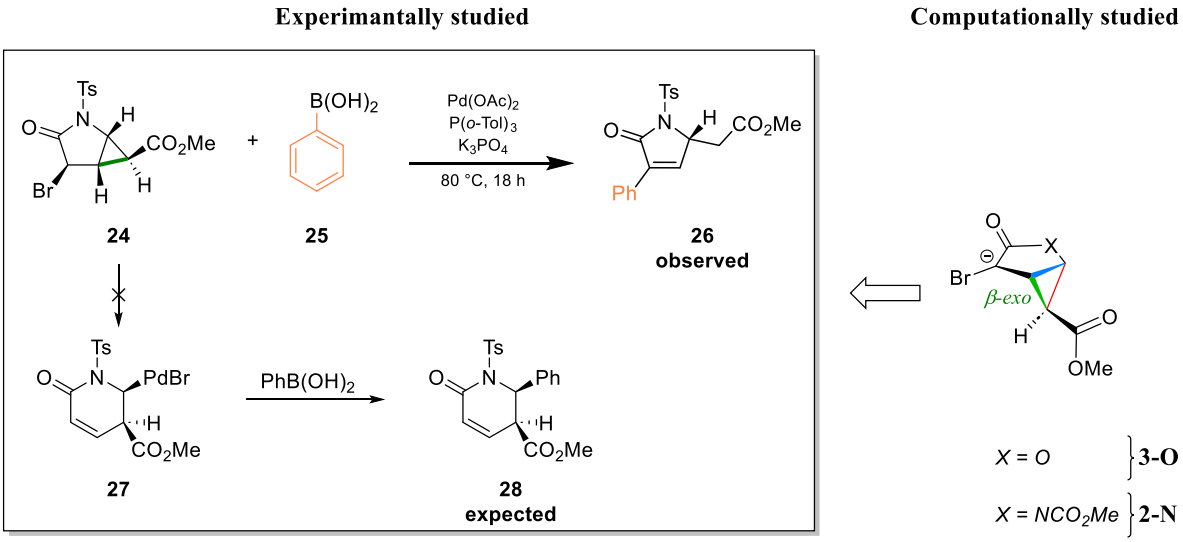

Scheme 13. Left: Experimentally studied [3.1.0] bicycle cyclopropanes undergoing base-mediated *β-exo*-cyclic ring opening. Right: Computationally studied model compound.

Based on the experimental outcome, the presence of a carbanionic species as an intermediate generated through elimination via a base was postulated. This species induces the *β-exo* ring opening, followed by a classical Suzuki cross-coupling, resulting in the observed product **26** (Scheme 14).

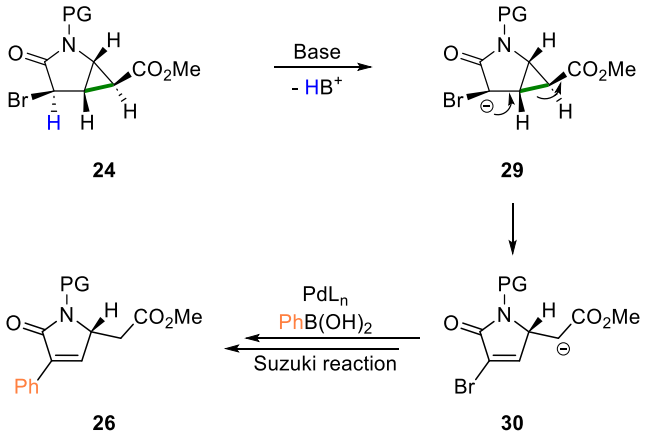

Scheme 14. Proposed mechanism for the base mediated *β-exo*-cyclic ring opening.

Computational Details

For this specific reaction, computational parameters were used, which closely match the experimental conditions. The reaction occurred in both THF and toluene, with toluene providing a higher yield (75%) compared to THF (57%). Therefore, both solvents were applied in implicit solvent models. The temperature was set at 80 °C (353.15 K) to align with the experimental conditions. In addition to the original system, a similar system with oxygen as the heteroatom was also computed for better comparison with previous and subsequent results (Scheme 13).

Bond Length Comparison

By comparing the cyclopropane bond lengths of the optimized structures in Figure 7 for the proposed carbanionic intermediates (**Int-1**) with the substrate (**GS-1**), it becomes evident that the *β-exo* bond is significantly increased, while the others exhibit minimal changes (Table 5).

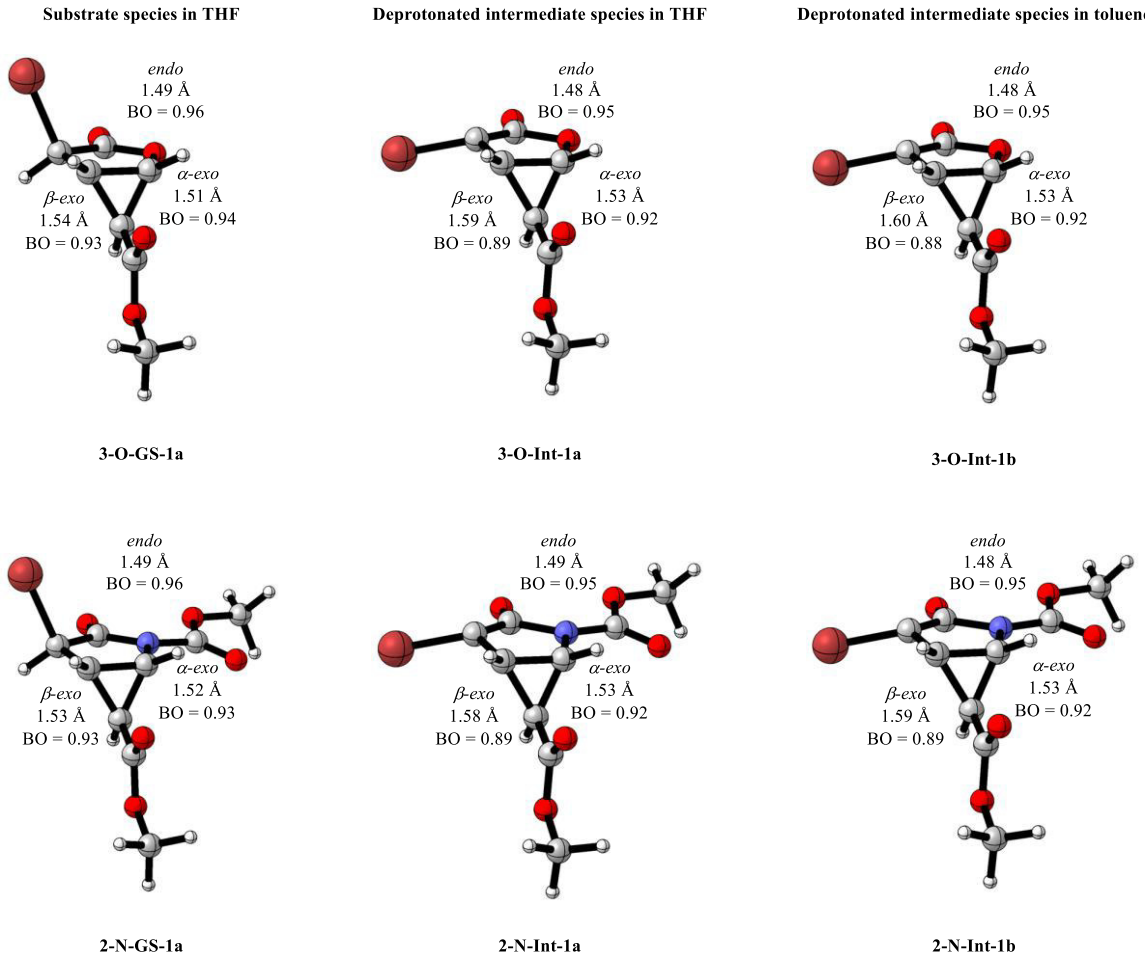

Figure 7. Rendered minimum energy structures of model species for base-induced cyclopropane ring openings. **GS-1**: Substrate species, **Int-1**: Deprotonated intermediate species. **a**: The SMD solvent model for THF was used, **b**: The SMD solvent model for toluene was used. The substrate structures in THF (**GS-1a**) do geometrically not differ from their respective analogs in toluene **(GS-1b**) (SI).

Table 5. Cyclopropane bond length in the deprotonated intermediate (**Int-1**) and non-deprotonated substrate (**GS-1**) species.

	Bond length in Å		
System	***α-exo* bond**	***β-exo* bond**	***endo* bond**
3-O-GS-1a	1.51	1.54	1.49
3-O-Int-1a	1.53	1.59	1.48
3-O-GS-1b	1.51	1.54	1.49
3-O-Int-1b	1.53	1.60	1.48
2-N-GS-1a	1.52	1.53	1.49
2-N-Int-1a	1.53	1.58	1.49
2-N-GS-1b	1.52	1.53	1.49
2-N-Int-1b	1.53	1.59	1.48

Figure 7 shows, that the oxygen (**3-O**) and nitrogen (**2-N**) systems behave similarly, with the same bond order in the cyclopropane system. Solvent effects based on to SMD model have only a minor impact on the bond situation due to the relatively small differences in the dielectric constants between THF (ε=7.6)[96] and toluene (ε=2.4)[96] compared to water (ε=78.3)[96] in the previous example.

NBO Population Analysis and Interaction Quantification

To determine the orbital interactions leading to the ring opening, it was focused on the mesomeric structure, where the deprotonated intermediate species (**Int-1**) is in its keto form. To assess the relevance of this structure, a natural resonance theory (NRT) analysis was performed to determine contributing resonance structures and their weights (Scheme 15).[47,48,51,100]

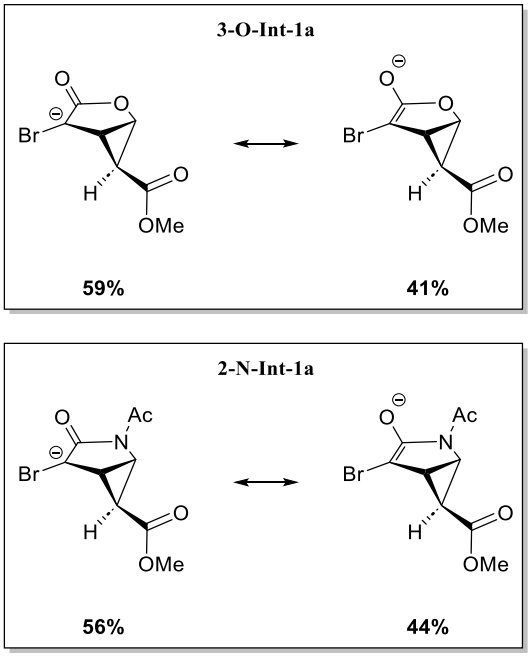

Scheme 15. Distribution of main mesomeric structures determined by an NRT analysis in THF. Populations of species in THF and toluene differ by 2% or less.

The carbanion and enolate are nearly equally present, with a slight preference for the former. This is supported by the carbon-carbon bond length of 1.40 Å for all systems, which falls between a double bond (1.33 Å)[49] and a single bond (1.54 Å)[49]. Thus, the interactions present in the carbanionic resonance structure (Table 6) are representative of the interactions within the cyclopropane unit of the molecule.

Table 6. Significant donor-acceptor interactions involved in the carbanionic [3.1.0] bicycle cyclopropanes.

	Stabilization energy in kcal/mol			
Species	**Donor**	**Acceptor**		
		$\sigma^*_{\alpha-exo}$	$\sigma^*_{\beta-exo}$	$\pi^*_{C=O}$
3-O-Int-1a	**LP$_X$**	11.3	-	-
	LP$_C$	-	21.5	-
	$\sigma_{\alpha-exo}$	-	-	5.2
	$\sigma_{\beta-exo}$	-	-	9.0
2-N-Int-1a	**LP$_X$**	11.8	-	-
	LP$_C$	-	21.3	-
	$\sigma_{\alpha-exo}$	-	-	5.1
	$\sigma_{\beta-exo}$	-	-	9.1
3-O-Int-1b	**LP$_X$**	11.7	-	-
	LP$_C$	-	23.4	-
	$\sigma_{\alpha-exo}$	-	-	5.0
	$\sigma_{\beta-exo}$	-	-	10.2
2-N-Int-1b	**LP$_X$**	11.8	-	-
	LP$_C$	-	22.2	-
	$\sigma_{\alpha-exo}$	-	-	5.0
	$\sigma_{\beta-exo}$	-	-	9.1

In contrast to the previous example, the interaction with the antibonding π* orbital is minor and appears too weak to initiate bond breaking in the non-protonated molecules (**GS-1**). This conclusion is based on the comparable values observed in the non-protonated substrates of the previous systems **1-O**, **1-N**, and **2-O** (Table 3), which do not undergo ring openings. The primary interactions involve the lone pair interactions from the heteroatom **X** with the σ orbital of the *α-exo* bond and the carbanion (C^3) with the σ* orbital of the *β-exo* bond, with the latter interaction dominating. Therefore, the initiation and selectivity of the base-mediated ring opening are solely determined by the carbanion (as visualized in Figure 8). An understanding of this interaction will be crucial when discussing interactions based on metal-carbon bonds, which exhibit carbanionic characteristics.

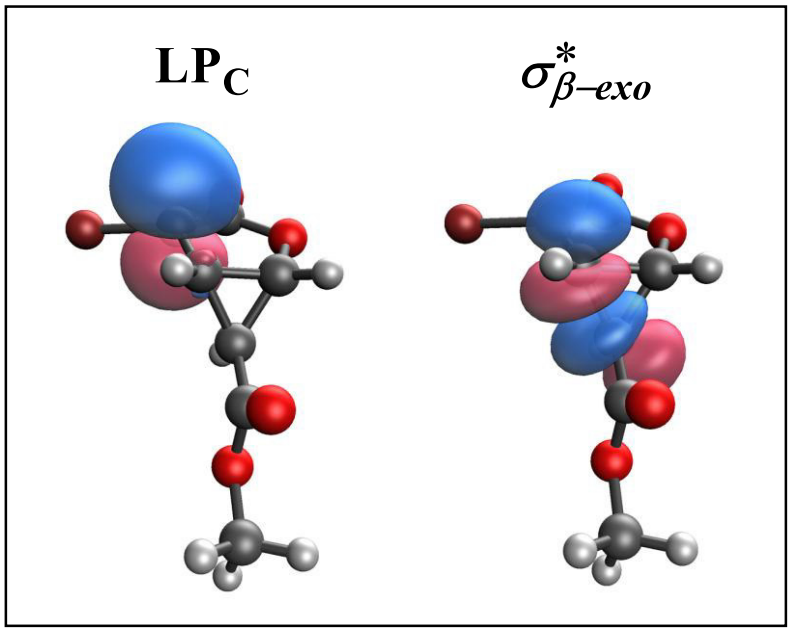

Figure 8. Visualization of selected NBOs referred in Table 6 for **3-O-Int-1b**.

Reaction Profile

In the analysis of the reaction profile, NH_3 was used as a model base, as opposed to K_3PO_4, which was utilized in the experimental setting. There are two main reasons for this choice. First, charged species are more reactive when no explicit solvent models are used because they lack stabilizing solvent interactions. This means the basicity of phosphate would be overestimated, while the basicity of ammonia (which forms an ammonium cation) would be underestimated. If the deprotonation is feasible with ammonia, it should also be feasible with the more basic phosphate. Therefore, if the computationally determined reaction barrier using the underestimated ammonia as a base is low enough to overcome, the reaction will proceed with the phosphate base as well. Second, the small size of the NH_3 molecule makes it computationally more efficient.

The Gibbs free energies of the respective stationary points are shown in Table 7.

Table 7. Gibbs energies for stationary points in the anionic ring opening reaction.

	Energy in kcal/mol									
Structure	**GS-1a**	**TS-1a**	**Int-1a**	**TS-2a**	**GS-2a**	**GS-1b**	**TS-1b**	**Int-1b**	**TS-2b**	**GS-2b**
3-O	8.7	33.8	25.0	34.0	13.9	6.5	36.1	23.8	37.7	12.2
2-N	6.9	34.8	24.5	34.8	17.9	6.5	37.0	23.0	-	16.0

As an energy reference for the reaction profile (Figure 10), the combined energy of the substrate structures **3-O-GS-1a** / **2-N-GS-1a**, along with the base NH_3 as isolated species was considered. In the initial state (**GS-1**), these species form a reactant complex (RC). The deprotonation step (**TS-1**), with a barrier ranging from 25.1 to 30.5 kcal/mol, is the rate-determining step, albeit still feasible at 80 °C. Subsequently, the resulting anionic intermediate **Int-1** undergoes cleavage of the *β-exo* bond (**TS-2**, 9.0–13.9 kcal/mol) yielding **GS-2** (Figure 9).

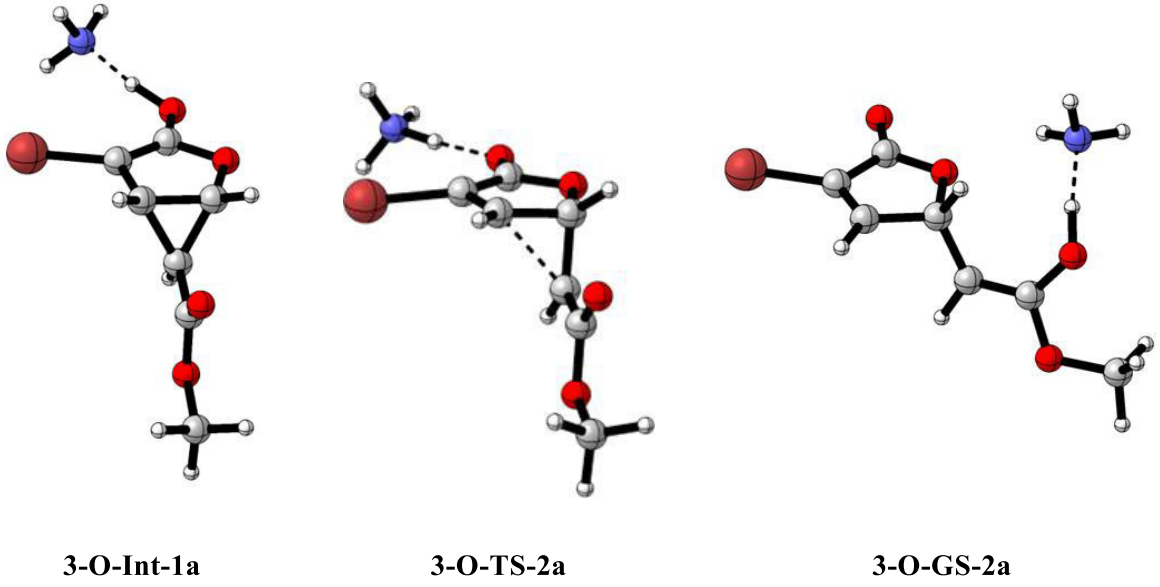

Figure 9. Anionic ring opening species. Exemplary for the **3-O** system in THF.

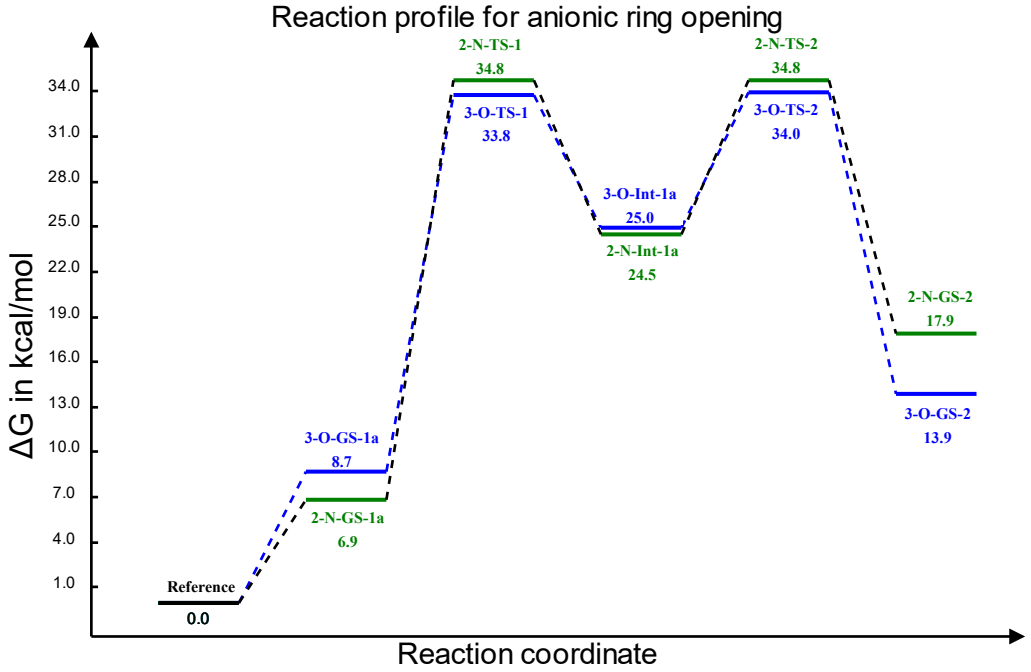

Figure 10. Reaction profile for the anionic ring opening in THF. Blue: Reaction profil of the **3-O** system. Green: Reaction Profil of the **2-N** system.

The subsequent reprotonation of **GS-2**, leading to its corresponding keto-form, serves as the starting point for the addition of a palladium species, ultimately yielding the observed product depicted in Scheme 13. This section will not explore the reaction with the transition metal species, as they are not directly involved in the current ring opening reaction. These interactions will be discussed in detail in a later chapter of this thesis.

To summarize, the deprotonation is the rate determining step, while the anionic ring opening occurs rapidly. The site-selectivity in this process is governed by the interactions facilitated by the lone pair of the carbanion.

3.2.3 Polarized Ring Openings

In light of the presented anionic ring opening, where the charge is localized at the C^3 position, it was sought to compare it with a similar system featuring a cationic charge. Recent work by Fischer *et al*. in 2022 revealed a ring expansion of a related cyclopropanated heterocycle (Scheme 16).[101]

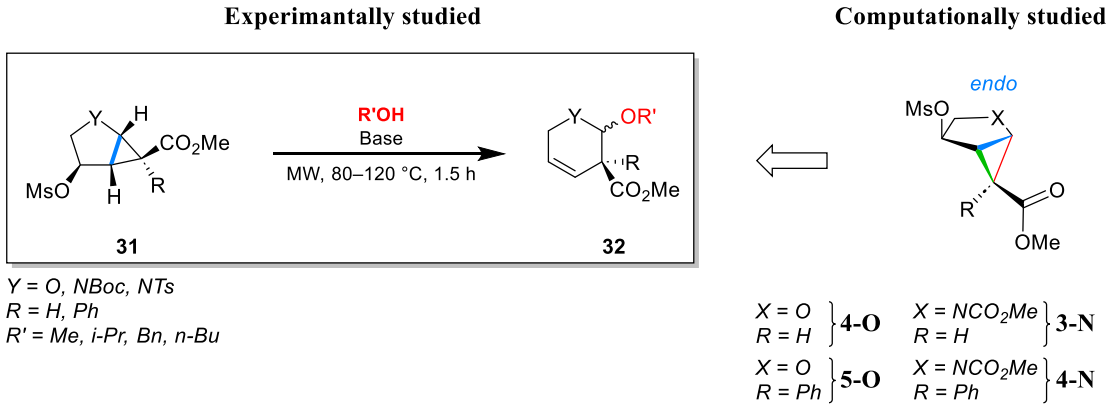

Scheme 16. Left: Experimentally studied [3.1.0] bicycle cyclopropanes undergoing endocyclic ring opening. Right: Computationally studied model compounds.

The observed product outcome was rationalized through the formation of a carbocationic species. This species undergoes an endocyclic bond cleavage, followed by a nucleophilic attack of the alcohol (Scheme 17, left). To achieve this, it was proposed that the σ orbital of the *endo* bond overlaps with the vacant orbital of the carbocation (Scheme 17, right).

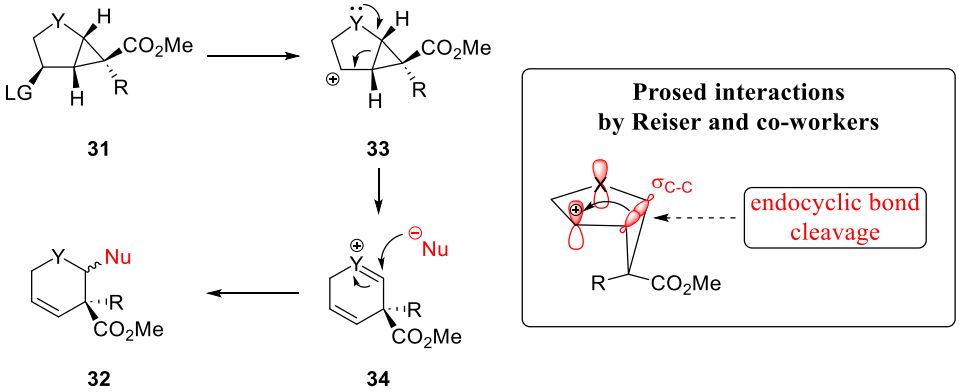

Scheme 17. Proposed mechanism and interaction from Fischer *et al*. leading to the endocyclic bond cleavage product. The orbital representation was taken from *ACS Org. Inorg. Au.* **2022**, *2*, 169–174.[101]

Based on the accumulated knowledge, the proposed mechanism may seem counterintuitive. The overlap of the bonding endocyclic orbital with the perpendicular vacant orbital of a sp^2 hybridized carbon appears geometrically unfavorable. In contrast, overlap with the σ orbital of the *β-exo* bond seems more plausible. Additionally, this interaction cannot be supported via the lone pair of the heteroatom, as demonstrated in the previous example, where there was no significant interaction between the lone pair and the antibonding *endo* bond orbital.

Computational Details

To explore the uniqueness of this system, an investigation into the NBO interactions of the respective carbocations presented in Figure 11 was initiated. To closely align with experimental parameters, methanol was employed as an implicit solvent and energies were calculated at 80 °C or 353.15 K. It emerged that the respective intermediate did not represent a stationary point on the potential energy surface (PES) within these parameters, making optimization unattainable. This suggests that the formation of a pure carbocationic species may not occur under these conditions. Nonetheless, it remains possible that such a structure could exist under different conditions, such as when considering explicit solvent models, counterions, or more precise methods and basis sets. To gain further insight into the interactions within this hypothetical intermediate, optimizations were conducted while imposing geometric constraints on the *β-exo* and *endo* bonds, utilizing the **1-O** / **1-N** cyclopropane framework. These constrained structures are incapable of opening up during the optimization. They should be noted as non-stationary points, serving solely to evaluate the feasibility of the proposed orbital interaction within such a geometry.

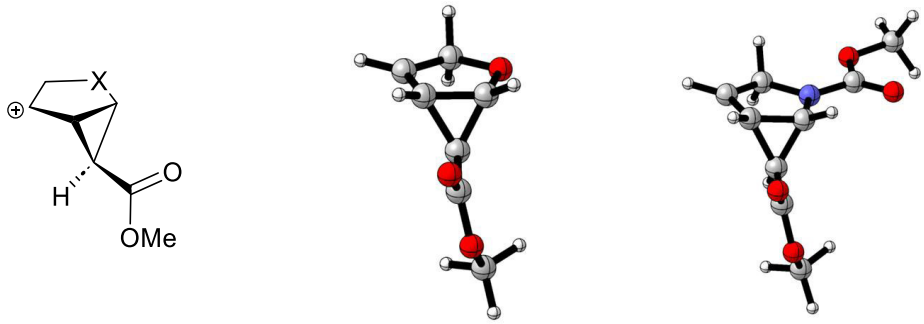

Figure 11. Hypothetical carbocationic intermediate, that is proposed to start the ring expansion. Left: Schematic structure. Right: Rendered structures of optimized species under geometric constraints.

NBO Population Analysis and Interaction Quantification

The calculations of this hypothetical system revealed that the formation of a pure carbocation at the C^3 position favors cleavage of the *β-exo* bond over the endocyclic bond (Table 8). Thus, it is anticipated that the counterion plays a crucial role in the ring expansion.

Table 8. Significant donor-acceptor interactions involved in the hypothetical carbocation. An implicit solvent model for methanol was used.

	Stabilization energy in kcal/mol			
Structure	**Donor**	**Acceptor**		
		$\sigma^*_{\beta-exo}$	σ^*_{endo}	**LV$_C$**
4-O-Int-1	**LP$_X$**	-	-	-
	$\sigma_{\beta-exo}$	-	-	20.6
	σ_{endo}	-	-	8.9
3-N-Int-1	**LP$_X$**	-	-	-
	$\sigma_{\beta-exo}$	-	-	19.6
	σ_{endo}	-	-	8.6

My colleague Aryaman Pattanaik and I propose that the ring expansion proceeds through an S_N1'-like mechanism in which the OMs group departs with the assistance of the donating endocyclic cyclopropane σ bond, resulting in a concerted process (Figure 12). While an initial overlap with the σ orbital of the *β-exo* bond may support this process, complete ring opening is disfavored due to the electron flow away from the electron-withdrawing group (-COOMe). In contrast, cleavage of the *endo* bond is thermodynamically favored, facilitated by the mesomeric lone pair interaction through the heteroatom.

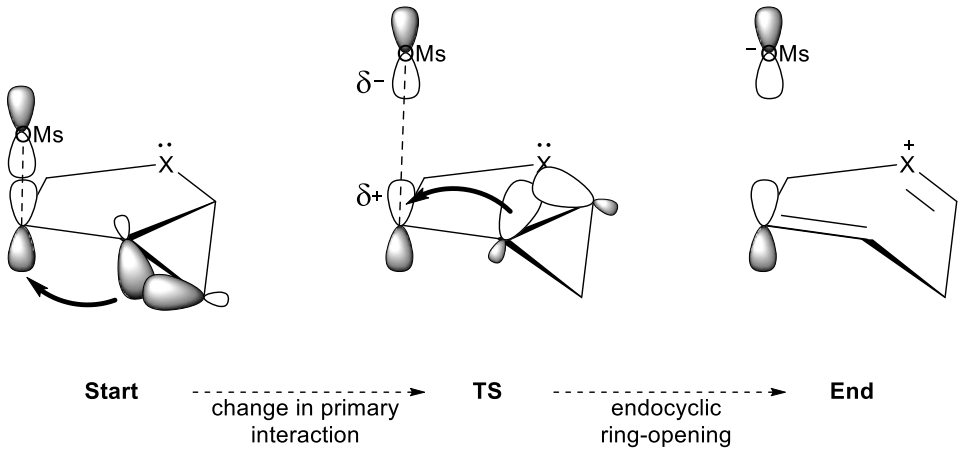

Figure 12. Schematic ring opening through an S_N1'-like mechanism.

To substantiate this hypothesis, an NBO analysis was conducted throughout the entire intrinsic reaction coordinate (IRC) based on the ring opening transition states of the systems shown in Scheme 16, with R = H (**4-O** / **3-N**) and R = Ph (**5-O** / **4-N**). Further, the C^3 carbon was treated as a carbocation to assess its interaction with the respective cyclopropane bonds (Figure 13).

Initially, a significant interaction between the vacant C^3 p-orbital and the oxygen lone pair from the OMs group was observed, stemming from the covalent bond between them, now represented as an ionic one. Additionally, a minor interaction of approximately 8 kcal/mol with the *β-exo* bond was noted, while there was no interaction with the *endo* bond at this stage of the reaction. As the reaction progressed, the *β-exo* bond's interaction increased significantly, whereas the *endo* bond interaction remained unchanged. Simultaneously, the C^2-C^3 bond length decreased, leading to a reorientation of the five-membered ring. Thus, the orientation of the empty p orbital can be roughly described by the positioning of the OMs group, which interacts with the p orbital. Computational calculations for visualizing the p orbital are provided in Figure 14. Subsequently, as the reaction proceeded further, the *β-exo* bond length continued to decrease along with its interaction, while the *endo* bond interaction became dominant near the transition state, indicating bond formation.

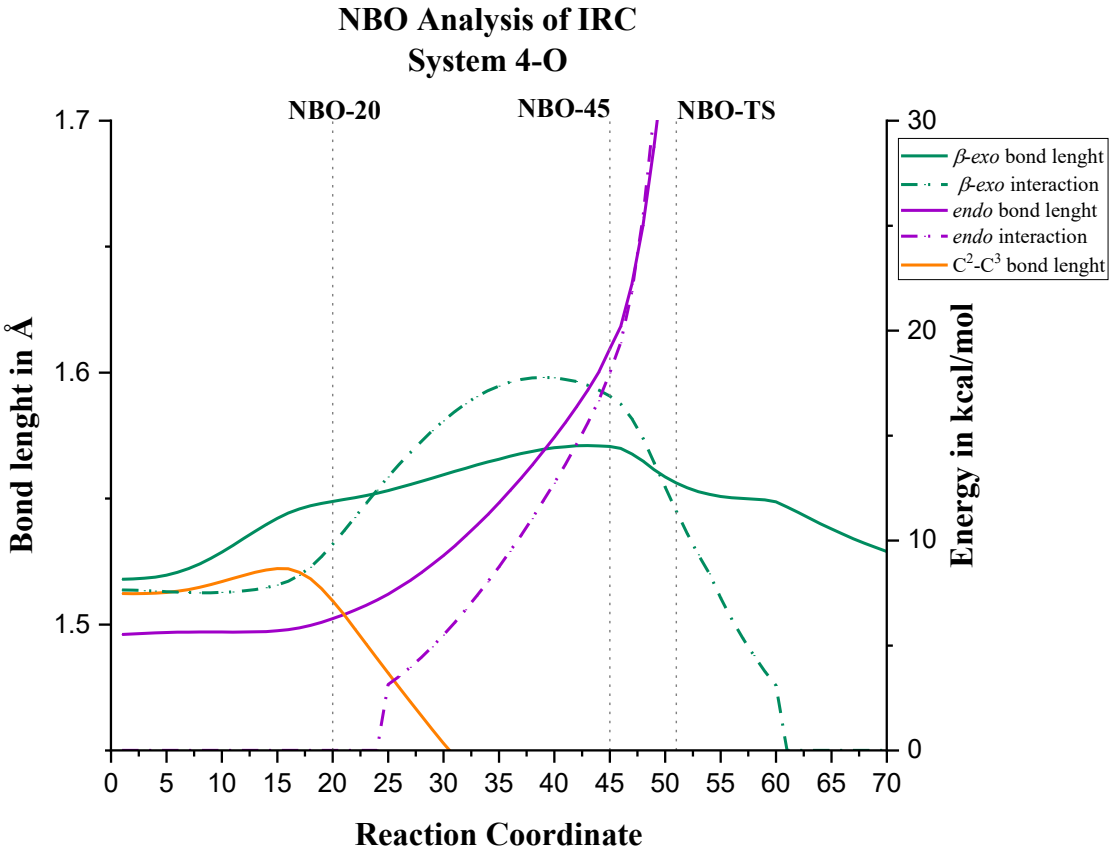

Figure 13. NBO interactions based on E2 values along the calculated IRC points from TS **4-O-TS-1** in forward and reverse direction. The interactions of significant importance were identified between the cyclopropane bonds and the vacant p orbital, compared to the absolute lengths of the bonds most affected by the ring expansion along the IRC, using the **4-O** system as example.

At first appearance, the overall good interaction between the endocyclic bond orbital and the vacant orbital is unexpected due to the nearly perpendicular orientation (84° dihedral angle between C^1-C^2-C^3-OMs at the transition state). However, this can easily be explained by the bent bond model leading to an increased overlap between the *endo* "banana" bond and the vacant orbital.

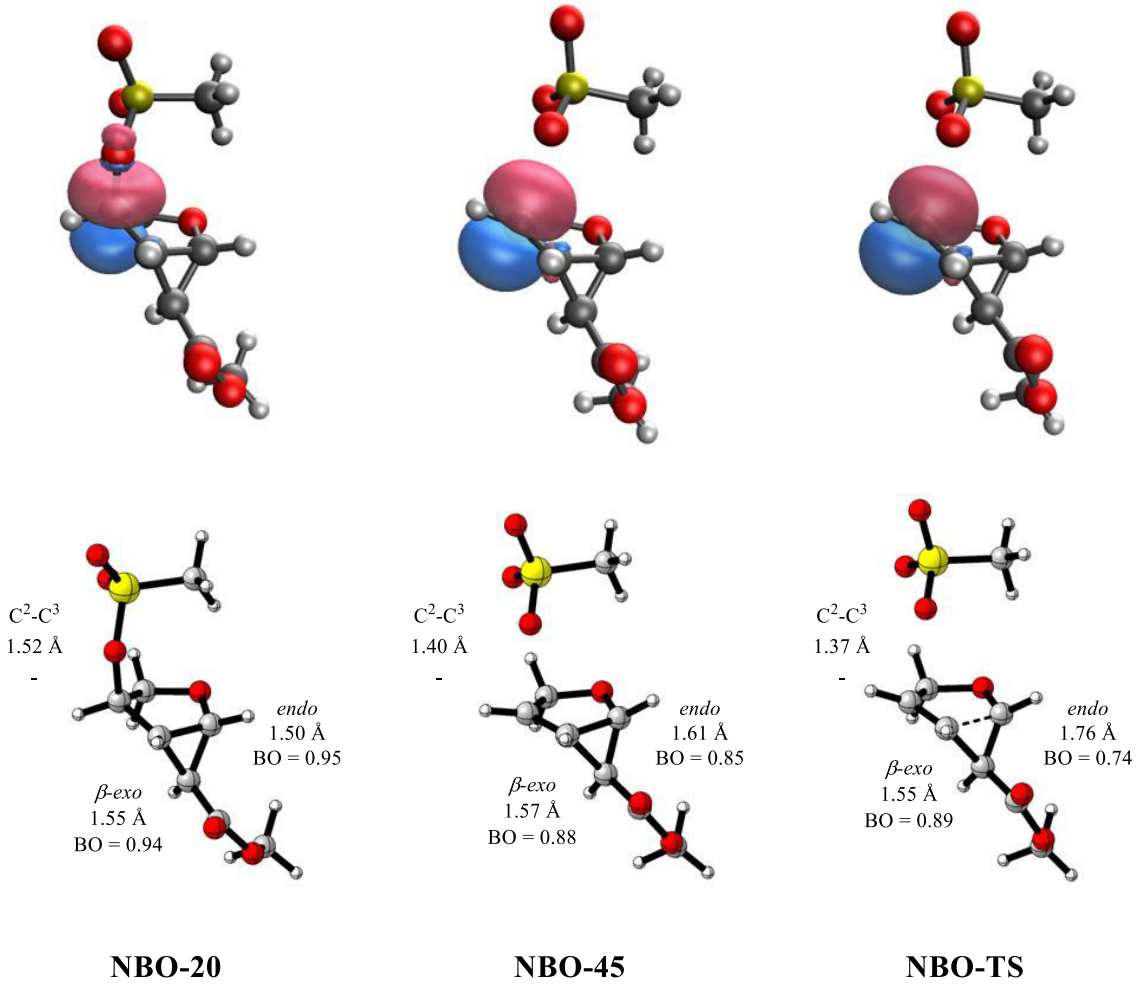

Figure 14. Visualization of the vacant p orbital according to NBO analysis along the IRC referred to in Figure 13.

Reaction Profile

The reaction profiles for the respective systems were also computed. The results are shown in Table 9. Including the phenyl group significantly increased the reaction rate, but both reactions remain feasible at 80 °C.

Table 9. Gibbs energies for stationary points in the cationic endocyclic ring opening reaction.

	Energy in kcal/mol		
System	**GS-1**	**TS-1**	**GS-2**
4-O	0.0	25.8	-6.6
3-N	0.0	16.7	-14.7
5-O	0.0	28.9	-2.1
4-N	0.0	22.2	-7.7

In summary, site-selectivity appears to be governed by the cleavage of the leaving group. During the bond-breaking process, the vacant p orbital reorients itself to establish favorable interaction with the bonding σ *endo* orbital.

3.2.4 Transition Metal catalyzed Ring Openings

Now, it is aimed to apply the accumulated knowledge to elucidate site-selectivity in palladium-catalyzed ring openings of similar frameworks. Introducing a metal into an organic molecule often involves a polarity reversal at the carbon center, altering the entire electronic structure of the molecule. Given the polarity of the C-Pd bond, one might anticipate compounds to exhibit similar reactivity to the carbanionic pathway discussed in the previous section. Such a hypothesis however neglects the fact of [Pd] being also good π-acids.[102] Indeed, the experimental transformation involved not only endocyclic ring opening but also the migration of the transition metal center to the C^1 position, resembling a 1,3-allyl migration (Scheme 18).

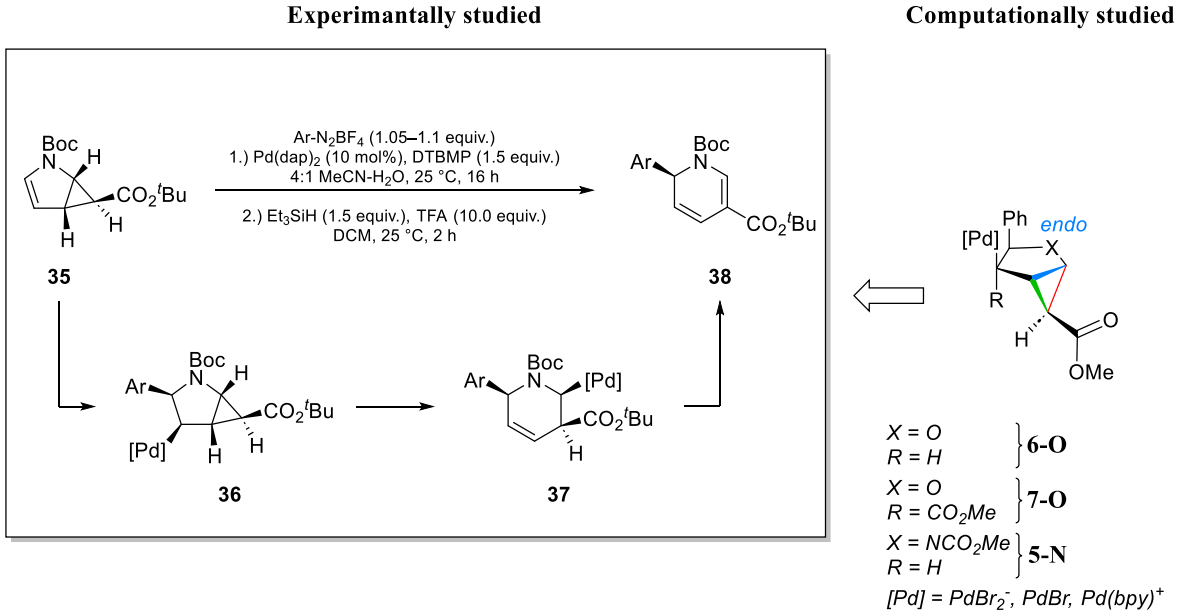

Scheme 18. Left: Experimentally studied [3.1.0] bicycle cyclopropanes undergoing transition metal mediated endocyclic ring opening. Right: Computationally studied model compounds.[56]

Computational Details

The mechanism of the ring opening has been computationally investigated by Ricardo A. Angnes from the Rehbein group, supporting the occurrence of the mentioned palladium species migration step.[56] Unlike Agnes' work, the orbital interactions involved in this reaction were also investigated. Nonetheless, these systems are close, so the same computational parameters were employed to ensure comparability. Thus, the calculations were performed with toluene being applied in an implicit solvent model at 80 °C or 353.15 K.

Reaction Profile

To gain a comprehensive understanding of the migration step, palladium centers with three different electronic natures as depicted Figure 15 were investigated. For the cationic (**c**) palladium center, the bipyridine ligand was utilized, while neutral (**b**) and anionic (**a**) palladium centers were complexed with bromides. The results are shown in Table 10.

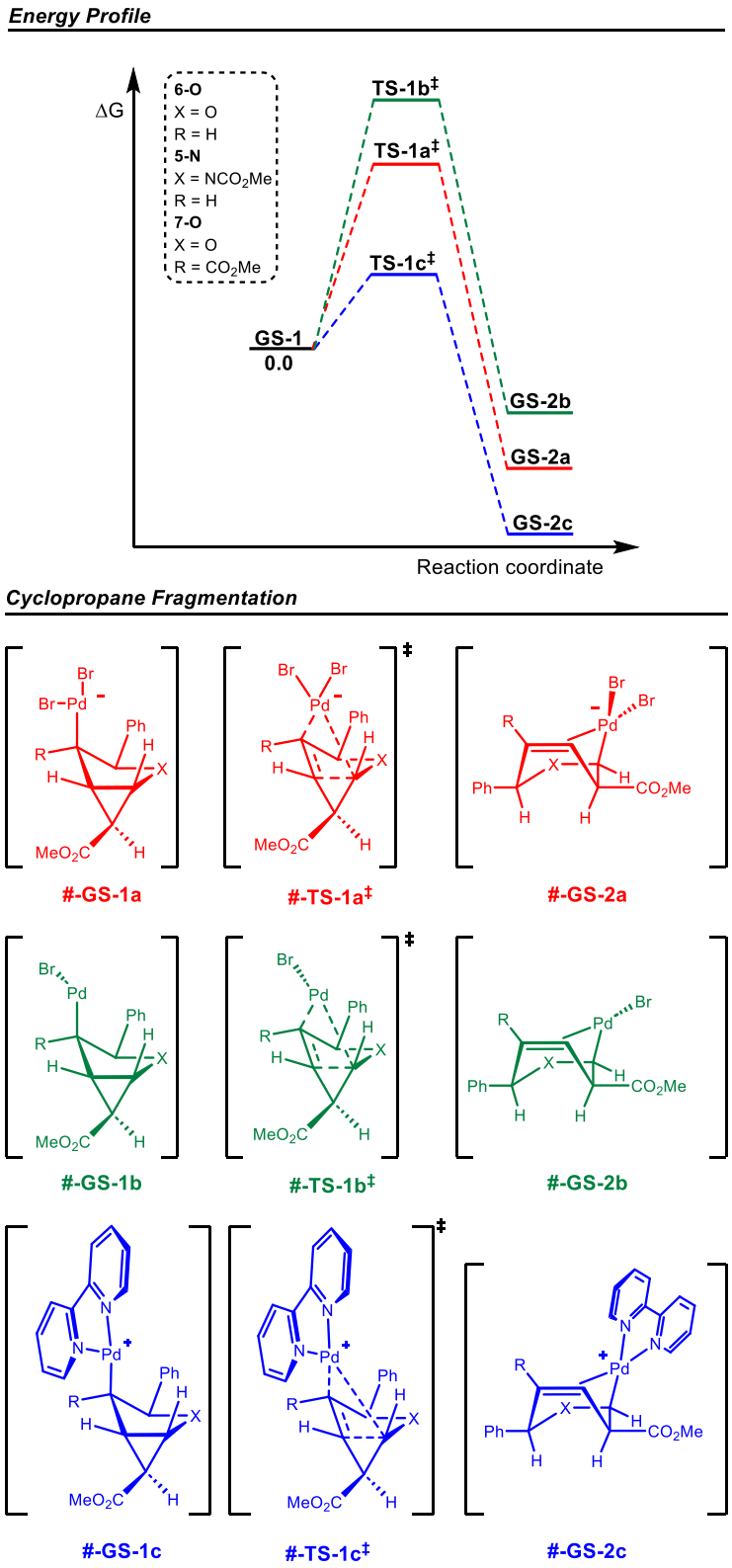

Figure 15. Top: Schematic energy profiles of the palladium migrations. Bottom: Calculated systems. The # is used as a placeholder for the respective systems (**6-O** / **5-N** / **7-O**).

Table 10. Gibbs energies for stationary points in the palladium-catalyzed ring expansion of the cyclopropane species. [a]**a**: [Pd] = $PdBr_2^-$, **b**: [Pd] = PdBr, **c**: [Pd] = $Pd(bpy)^+$. [b]**x** is used as a placeholder for **a**, **b** or **c**.

		Energy in kcal/mol		
System[a]		**GS-1x[b]**	**TS-1x[b]**	**GS-2x[b]**
6-O	**a**	0.0	18.2	-11.0
	b	0.0	18.2	-10.2
	c	0.0	4.1	-18.3
5-N	**a**	0.0	19.5	-8.0
	b	0.0	21.3	-8.0
	c	0.0	6.1	-15.4
7-O	**a**	0.0	16.1	-9.8
	b	0.0	20.2	-7.3
	c	0.0	4.0	-15.8

The calculations revealed that the activation energy barriers for the migration step in each case were reasonable and achievable under routine experimental conditions. The trends observed were consistent across all systems, with the cationic palladium center displaying the lowest activation barrier (Table 10). Considering the significant size of palladium, the migration step should involve a notable degree of activation strain as it moves into the ring. This strain must be compensated by favorable orbital interactions for the process to proceed smoothly.

As mentioned earlier, one might expect the ring opening to favor cleavage of the *β-exo* bond due to its carbanionic partial charge (Table 6). Surprisingly, a ring expansion was observed in the experiment by breaking the endocyclic bond, similar to the carbocationic pathway discussed previously. In this process, the cleavage of the leaving group played a pivotal role in orienting the molecule, enabling interactions between the vacant p orbital and the bonding *endo* bond. In this instance however, the carbon formally gains a lone pair in contrast to the previous scenario where a vacant p orbital is formed.

Therefore, the transition metal's role in the ring opening process necessitates a thorough investigation of the involved interactions. To achieve this, the second-order perturbation energies will be assessed once again through NBO analysis along the intrinsic reaction coordinate (IRC). However, the complexity of this analysis has increased.

NBO Population Analysis and Interaction Quantification

Three primary interactions come to mind, each of which could potentially account for the cleavage of the endocyclic bond. These interactions involve either a transition metal d orbital with the antibonding orbital of the endocyclic bond (**a**$_1$) or the σ orbital of the *endo* bond with the transition metal species. The respective acceptor orbitals could be the vacant s orbital of palladium (**b**$_1$) or the antibonding σ* orbital of the C^1-Pd bond (**b**$_2$). While an interaction from the bonding C^1-Pd orbital into the antibonding σ* orbital appears geometrically unfeasible, an interaction with the σ* orbital of the *β-exo* bond (**a**$_2$) seems viable, though it would not lead to a ring expansion (Figure 16).

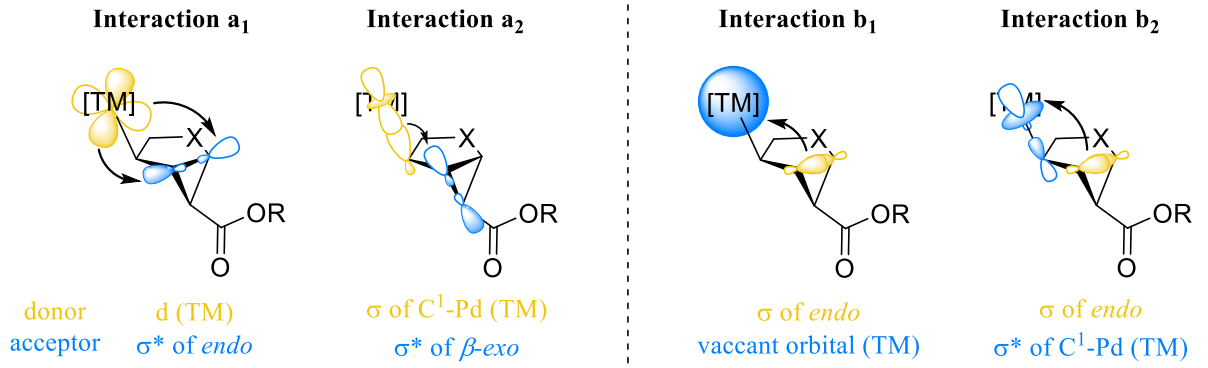

Figure 16. Schematic depiction of possible orbital interactions involved in the palladium-catalyzed endocyclic ring opening.

The orbital interactions were exclusively calculated for the anionic and neutral palladium species due to convergence issues with the positively charged species in the intrinsic reaction coordinate (IRC). These interactions, as observed along the IRC, are visually represented in Figure 17, where they are plotted against each other, provided they exceed the 3 kcal/mol threshold. Additionally, the C^1-Pd bond length, signifying the migration of the palladium species, is also plotted and extends up to the respective transition state. It is important to note that in the case of the anionic species, the "vacant orbital" refers to the empty s orbital of palladium, while for the neutral species, it is represented by an antibonding orbital between the transition metal and its ligand. For readability, these acceptor orbitals will be referred as "vacant orbitals" in both cases.

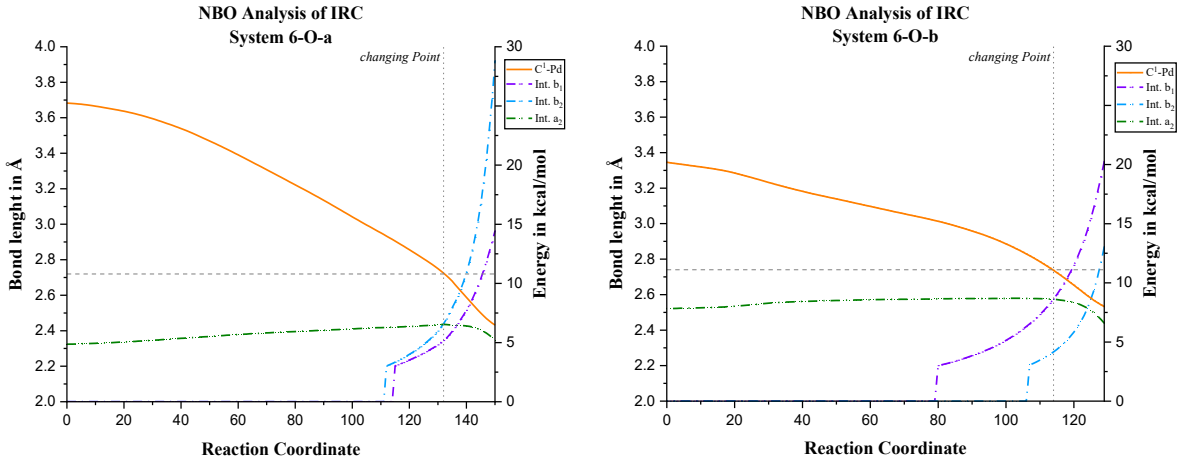

Figure 17. Main orbital interactions (Int.) involved in the palladium-catalyzed endocyclic ring opening along the IRC, up to the TS. Exemplary for the **6-O-a** and **6-O-b** systems. The full lines represent the C^1-Pd bond length. The dashed lines represent the respective orbital interaction depicted in **Figure 16**. The interaction $\mathbf{a_1}$ is below the threshold and therefore not shown.

Upon analysis, it is clear that, much like in the previous endocyclic ring opening case, there is an initial interaction with the *β-exo* bond ($\mathbf{a_2}$). However, this time, the antibonding *β-exo* orbital serves as the acceptor, akin to the base-mediated ring opening (Section 3.2.2). This interaction dominates at the start of the reaction and experiences a slight increase throughout its progress (Figure 18, Stage 1). Shortly before the transition state, the donor-acceptor interaction between the endocyclic σ-bond and the palladium species becomes dominant, effectively reversing the electron flow between the transition metal unit and the cyclopropane unit (Figure 18, Stage 2).

In the case of the anionic species, both the vacant orbital and the antibonding C^3-Pd orbital overlap significantly with the *endo* bond. This results in both of them interacting with the *endo* bond in a comparable manner. Conversely, for the neutral species, the shape of the antibonding Pd-Br orbital allows for better overlap with the σ orbital of the *endo* bond, making this interaction more significant. However, in both cases, this interaction signifies a turning point as it intensifies, while the initial $\mathbf{a_2}$ interaction declines (Figure 18, Stage 3). Additionally, the changes in the C^1-Pd bond length indicate an acceleration of the migration process.

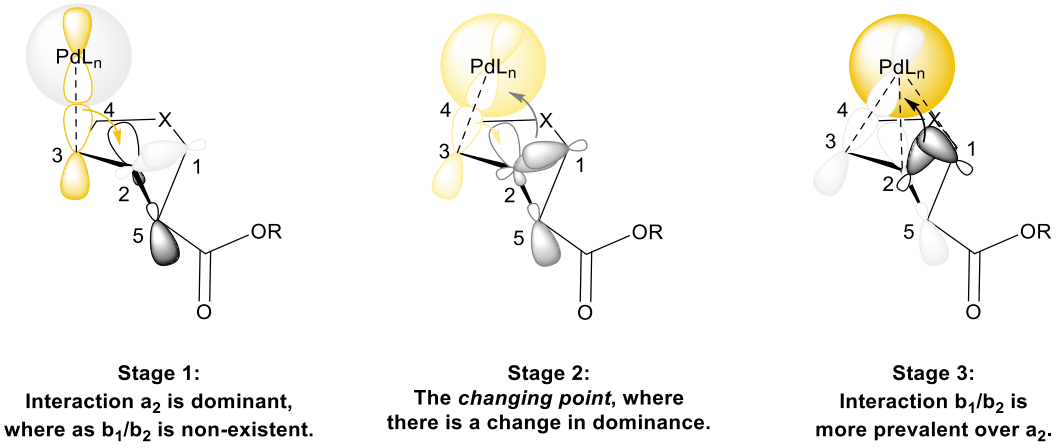

Figure 18. Schematic representation of the interactions involved along the IRC in the palladium-catalyzed endocyclic ring opening of the monocyclopropanated species.

My colleague Aryaman Pattanaik and I attempted to rationalize this critical *changing point* (Figure 18), where the dominant interactions change, by considering the geometric orientation of the respective molecule. This orientation is characterized by two key angles: The C^2-C^3-Pd angle (0–180°) and the H^4-C^4-C^3-Pd dihedral angle (-180–180°). This *changing point* was observed for all species, at an angle of approximately 77–80° and a dihedral angle of around 163–168° (Table 11). This point marks where the primary interaction, essential for completing the migration, becomes more dominant. These geometric parameters closely align with the respective transition states.

Table 11. Geometric parameters of the stationary points in the palladium-catalyzed endocyclic ring opening of the monocyclopropanated species.

		C^2-C^3-Pd Angle | H^4-C^4-C^3-Pd Dihedral angle in degree		
Structure		**GS-1**	***Changing Point***	**TS-1**
6-O	**a**	114.2 | -117.6	80.4 | 164.7	77.0 | 156.4
	b	112.1 | -125.5	78.6 | 165.8	77.2 | 158.9
	c	83.5 | 178.9	-	76.5 | 161.8
5-N	**a**	113.0 | -119.2	78.7 | 166.3	76.7 | 161.1
	b	111.6 | -125.2	78.3 | 167.5	76.6 | 161.4
	c	83.1 | -174.4	-	76.6 | 164.1
7-O	**a**	111.4 | -129.4	77.3 | 163.0	74.0 | 155.0
	b	111.6 | -126.6	77.6 | 164.4	75.9 | 157.7
	c	82.5 | -174.5	-	74.3 | 158.1

In the case of the cationic Pd system, due to steric considerations, the optimized structures are geometrically close to the transition state, and they have already formed additional interactions of the type **b_1**/**b_2**. This explains the rather low activation barrier for this species in case of the migration reaction (Table 10).

To further bolster the proposal that this reaction is *guided* by the initial **a_2** interaction, the geometric shifts along the IRC were examined. It was observed that during the migration, the palladium atom, on its way to position C^1, takes a *detour* by passing over C^2 (Figure 19).

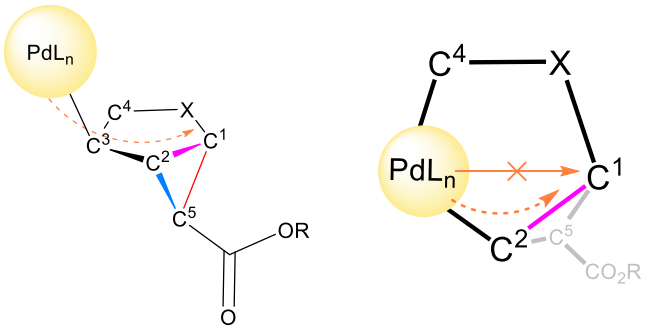

Figure 19. Migration pathway of the palladium species for 1,3 migrations. Left: Side perspective. Right: Top view.

This movement can be visualized as the metal species traversing through space during the reaction. To represent this 3-dimensional motion in a 2-dimensional format, each step of the

IRC was mapped onto a Cartesian coordinate system, where the C^1, C^2, and C^3 atoms form the XY-plane, with the C^2 atom as the center (Figure 20).

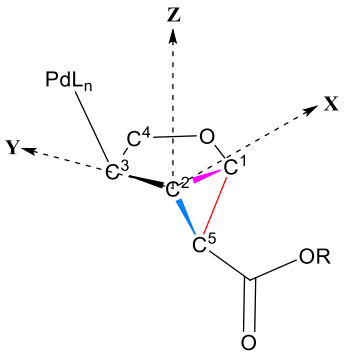

Figure 20. Schematic depiction of the applied coordinate system.

In this representation, it can be seen that the palladium atom generally follows a path toward the C^1 atom to reach the transition state. However, at the beginning of the reaction, the movement is biased towards the C^2 atom over the C^1 atom, indicating interactions between the former and the transition metal species (Figure 21).

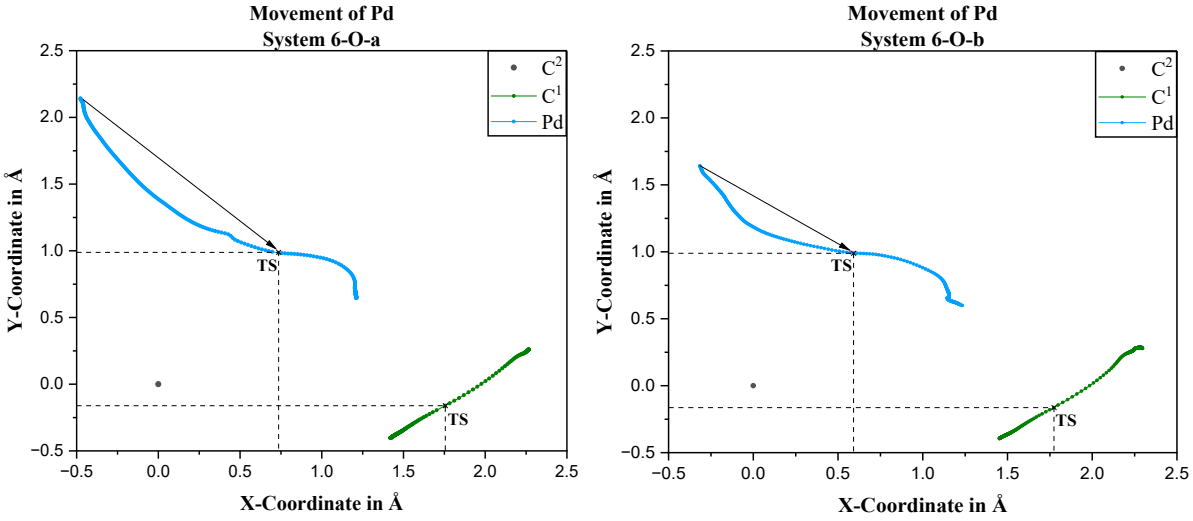

Figure 21. Movement of the Pd species through the space along the IRC, exemplary for the **6-O-a** and **6-O-b** system.

To computationally substantiate the interaction involving the vacant metal orbital that leads to migration, an in-silico study was conducted. In this study, the palladium in the neutrally charged systems (**6-O-b**, **5-N-b**, **7-O-b**) was replaced with magnesium (**6-O-Mg**, **5-N-Mg**, **7-O-Mg**). Magnesium also possesses vacant orbitals, but they are energetically inaccessible for covalent overlap. Unlike the C-Pd bond, the C-Mg bond is more akin to a carbanion with cationic magnesium in proximity. The energetic results for *endo* and *β-exo* bond cleavages in these species are consistent with the expectations. Specifically, the *exo*-cyclic ring opening is favored over the endocyclic ring opening by approximately 10–12 kcal/mol (Table 12).

Table 12. Gibbs energies for stationary points in ring opening reactions featuring MgBr as metal species.

		Energy in kcal/mol		
System	**Opening**	**GS-1**	**TS-1**	**GS-2**
6-O-Mg	***Exo***	0.0	17.1	-35.4
	Endo	0.0	29.0	-15.0
5-N-Mg	***Exo***	0.0	20.0	-37.7
	Endo	0.0	31.7	-18.2
7-O-Mg	***Exo***	0.0	13.0	-35.2
	Endo	0.0	23.1	1.0

However, when the unfavorable endocyclic ring opening was examined, it was noticed that, unlike palladium, magnesium takes a more direct path from C^1 to C^3. This suggests that the magnesium "cation" is simply following the negative charge (Figure 22).

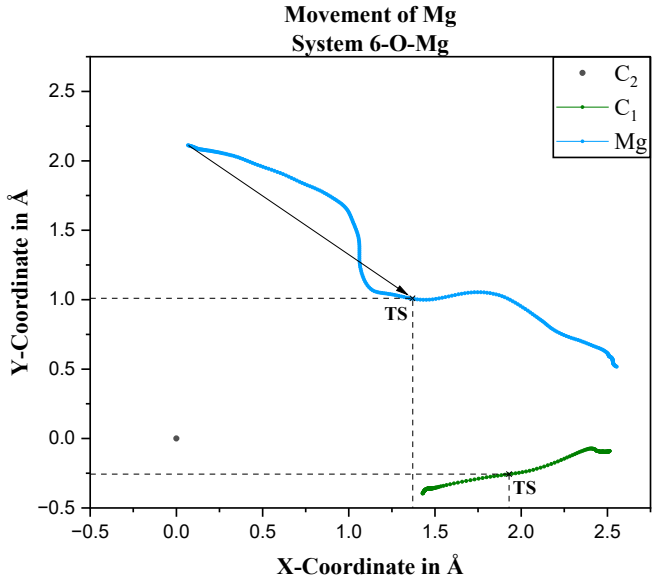

Figure 22. Movement of the Mg species through the space along the IRC, exemplary for the **6-O-Mg** system.

In summary, based on the results it is proposed that transition metals featuring accessible vacant orbitals initiate an endocyclic ring opening accompanied by the migration of the transition metal species.

4. Summary and Outlook – Part A

In this chapter, a comprehensive investigation was undertaken into the mechanisms governing the ring opening of cyclopropanated bicycles, a crucial reaction pathway in the stereoselective synthesis of highly substituted cyclic compounds.

Our analysis revealed that Brønsted acid protonation initiates a ring opening of the *α-exo* bond, with the electron-withdrawing ester at C^5 driving this reaction and selectivity guided by the neighboring heteroatom's lone pair interaction. In contrast, the reverse reaction – a deprotonation – leads to *β-exo* bond cleavage, where computational analyses highlighted deprotonation as the rate-determining step. This step relies significantly on the lone pair of the newly formed carbanion, which directs the site-selective ring opening. Following these findings, a novel mechanism was uncovered where the generation of a carbocation in an S_N1' fashion results in a ring expansion. Therefore, the reorientation of the vacant p-orbital of the forming carbocation promotes an endocyclic ring opening. Transition metal-catalyzed ring opening also led to ring expansion, though it is accompanied by migration of the transition metal species. This reaction resembles the mechanistic details discussed in Chapter 3.2.3, beginning with an interaction between the *β-exo* bond and an adjacent metal-carbon bond before shifting the dominance to the endo bond interaction. A comparative analysis of the palladium and magnesium systems further supported our findings.

These findings highlight the importance, when discussion electronic and steric effects – which can be quantified by the orbital interaction – not only at the initial stages of a reaction, as seen in the reactants or intermediates, but throughout the entire reaction process. While these early interactions can provide valuable insight into the reaction's initial trajectory, understanding how they evolve during the reaction is crucial for predicting its outcome accurately.

Implications and Future Directions

The insights into suitable interactions provide a powerful toolkit for targeting specific bond cleavages in cyclopropane ring opening. For instance, in the system discussed in Chapter 3.2.2 prior to deprotonation, the use of a base cleaves the *β-exo* bond, while a Brønsted acid opens the opposite bond. To achieve ring expansion, the cleavage of the bromonium as a leaving group could trigger that. Experimentally, it has already been shown that the use of palladium as a transition metal catalyst did not achieve the desired migration, leading to a follow-up cross-coupling compound. The reason is that the base needed in this kind of catalytic cross-coupling reaction triggers the ring opening at the *β-exo* bond first (Scheme 19).

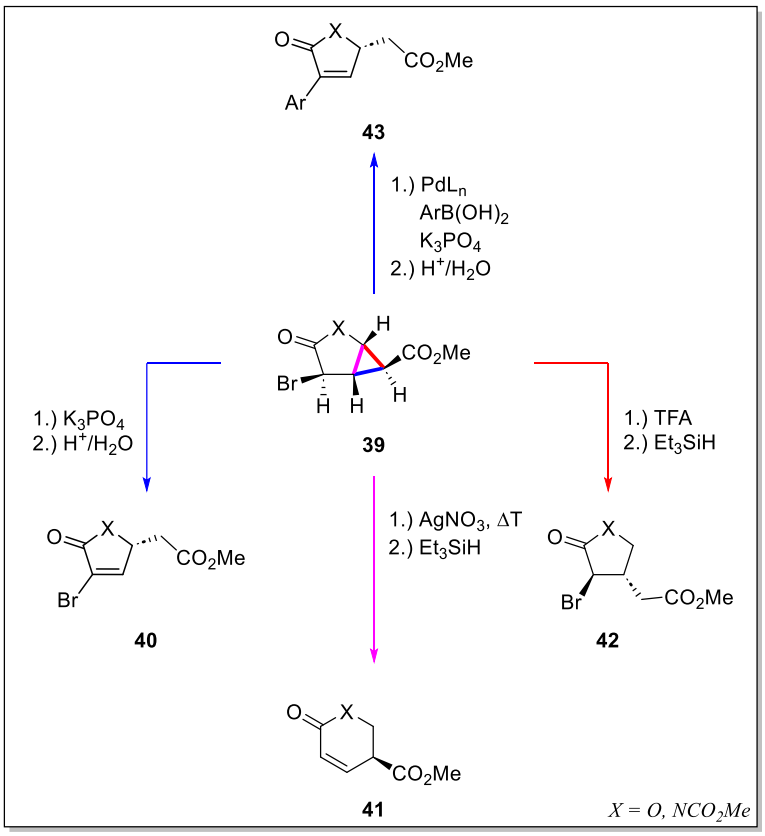

Scheme 19. Conceivable site-selective ring openings at a chosen substrate.

By recognizing the fundamental problem, achieving transition metal migration could, for example, involve protecting the carbonyl at the C^4 position, which deters deprotonation and potentially favors the migration of the palladium species.

Furthermore, the recognition that the vacant orbital of the transition metal species is the key to the migration process opens doors to exploring alternative, less expensive transition metals such as nickel. This endeavor could lead to more cost-efficient reactions with proper optimization.

In summary, this research has unveiled a variety of interactions and mechanisms, shedding light on the intricacies of cyclopropane ring opening. These discoveries not only advance the understanding of these processes but also hold promise for the development of new and more efficient reactions in organic synthesis.

B. Role of Intramolecular Hydrogen Bonding in the Competition of Retro-Aldol vs. Retro-Diels-Alder Reactions Mechanism

1. Introduction – Part B

1.1 Hydrogen Bonds in Synthesis

Hydrogen bonds are widely recognized as attractive interactions, renowned for their essential roles in biological systems. They are responsible for structuring proteins and DNA, and they underpin the unique properties of polar protic solvents, which can effectively dissolve highly polar molecules.[103–112] In chemical reactions, hydrogen bonds can energetically stabilize partially charged species, directly impacting the activation barriers of reactions. This feature makes hydrogen bonds an appealing tool for catalysis.[113] For instance, intermolecular hydrogen bonding plays a pivotal role in the enzyme-catalyzed hydrolysis of peptide bonds through mechanisms like the catalytic triad.[114,115] Moreover, hydrogen bonds are central in the realms of organocatalytic and organometallic synthesis. In many of these cases, the directionality and feasibility of forming hydrogen-bonded complexes govern stereoselectivity.[116–125]

Thioureas are common examples of hydrogen bond catalysis in Michael additions and aldol reactions. In these reactions, the amino groups (−NHR) of the thiourea catalysts form intermolecular hydrogen bonds with the carbonyl oxygen of the substrate, activating it towards nucleophilic attack. Furthermore, the use of chiral thiourea catalysts can render these reactions enantioselective.[113,126–128] Another example of enantioselective hydrogen bond catalysis is seen in proline-catalyzed aldol reactions. Here, a secondary amine in the proline forms an intramolecular hydrogen bond with the carbonyl group of the aldehyde substrate. This interaction not only orients the substrate but also stabilizes the enamine intermediate, thereby facilitating the formation of the C-C bond stereoselective (Scheme 20).[116,123,124,129–131]

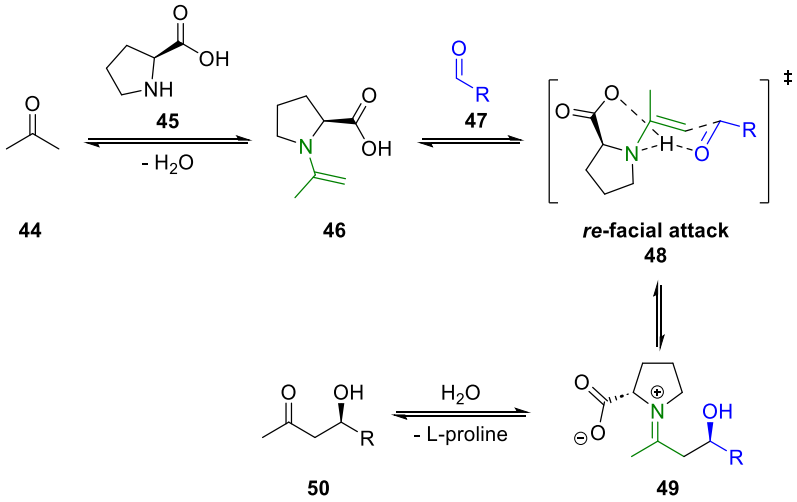

Scheme 20. L-proline catalyzed asymmetric aldol reaction.[131]

1.2 Diels-Alder and Aldol Reactions

The Diels-Alder reaction is a venerable and potent synthetic transformation that has profoundly impacted the field of organic chemistry. First introduced by Otto Diels and Kurt Alder in the early 20th century, it has become a cornerstone of synthetic organic chemistry. This iconic reaction involves the cycloaddition of a conjugated diene and a dienophile to construct a six-membered ring, yielding two new σ-bonds and one π-bond.[132–137]

One of its distinguishing features is its stereospecificity. In a [4+2] cycloaddition, a *cis* configured dienophile yields the respective *cis* product, while a *trans* configured dienophile yields the corresponding *trans* product. This remarkable stereochemical outcome is a result of the concerted nature of the reaction (Scheme 21).

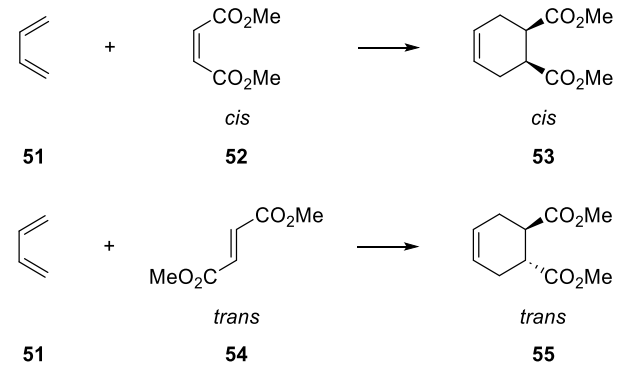

Scheme 21. Stereospecific products from Diels-Alder reaction.

The reaction's regioselectivity, on the other hand, is governed by the HOMO-LUMO pair with the most favorable energy match. This results in products where the donor and acceptor substituents are positioned to maximize orbital overlap, leading to the *para* or *ortho* configuration of the products (Scheme 22).

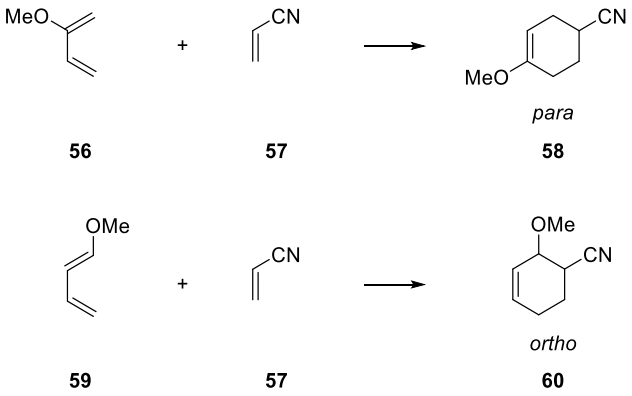

Scheme 22. Regioselectivity in Diels-Alder reactions.

Aldol reactions on the other hand, are another fundamental class of reactions in organic chemistry. It involves the reaction of two carbonyl compounds (e.g., aldehydes or ketones) under acid or basic catalysis, resulting in the formation of a *β*-hydroxy carbonyl compound,

commonly known as an aldol (Scheme 23). The stereoselectivity of aldol reactions is highly dependent on the steric and electronic factors of the participating reactants, which is described by the Zimmermann-Traxler model.[138–141]

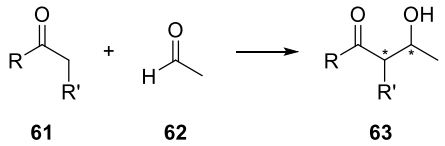

61 **62** **63**

Scheme 23. Schematic aldol addition.

Both the Diels-Alder and aldol reactions represent powerful synthetic transformations that have significantly impacted the field of organic chemistry. Their ability to construct complex molecular frameworks with high efficiency and selectivity has made them indispensable tools for synthetic chemists worldwide.

2. Aim of the Work – Part B

Building upon the insights gained in the previous Part A, the primary focus is on elucidating an intriguing follow-up reaction observed in the context of geminal disubstituted furans **64**, as documented by Reiser and co-workers.[56] In this particular scenario, the absence of a proton for subsequent *β*-H-dehydropalladation challenges the anticipated course of events following the cyclopropane ring opening.

Conventionally, one would expect a secondary arylation through Heck coupling of the post-cyclopropane ring opening intermediate **66**, culminating in the formation of product **67**. However, experiments have unveiled an unexpected and unprecedented occurrence – a retro-Diels-Alder reaction. This unique reaction pathway results in the exclusive formation of a single *diastereomer* **69**, contrary to the anticipated production of the commonly known two stereoisomers (Scheme 24).

Therefore, the research endeavors extend to a comprehensive computational study aimed at closely examining and understanding the intricacies of this distinctive follow-up reaction. By unraveling the mechanisms and factors governing this retro-Diels-Alder reaction, it is aimed to contribute valuable insights to the broader understanding of complex reaction pathways and expand the scope of our knowledge in the field.

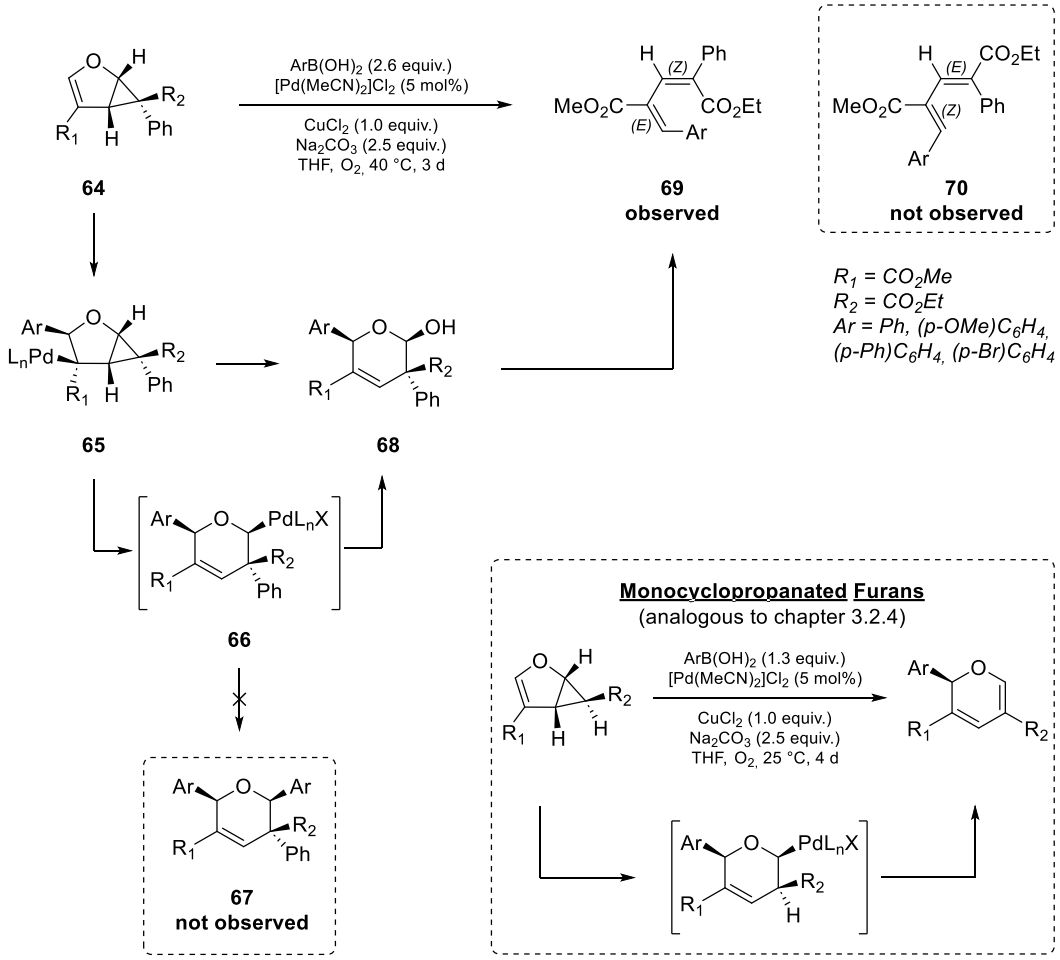

Scheme 24. Experimental conditions and proposed intermediates for the formation of single retro-Diels-Alder reaction product **69** via a transition metal mediated *endo* opening of a cyclopropyl group.

3. Main Part – Part B

3.1 Computational Details

The same computational parameters and programs were employed to maintain continuity with the computational details in Chapter 3.1 of Part A. However, the temperature was set to 40 °C (313 K), aligning with the experimental conditions and implicit solvation effects of THF were considered using the SMD model. To improve computational efficiency, ethyl groups were replaced with methyl groups.

3.2 Results and Discussion

To comprehensively investigate the assumed retro-Diels-Alder reaction, it is necessary to examine each preceding mechanistic step, starting with the substrate. This task is divided into three parts: The ring expansion of the cyclopropane unit, the removal of the palladium species, and the ring opening leading to the product.

3.2.1 Ring Expansion

Given the detailed discussion on transition metal-catalyzed ring openings in Chapter 3.2.4 of Part A, an in-depth investigation will be omitted and an analogous palladium-mediated ring expansion will be assumed. To align with the experimental conditions, an anionic palladium species was assumed for the investigated system **8-O** (Figure 23, top) – due to the lower activation barrier compared to the neutral species (see Part A for details).

The activation barrier for palladium migration is 13.5 kcal/mol (Figure 23, bottom), comparable to the previously calculated **7-O-a** system (16.1 kcal/mol), that is based on a similar framework. Consequently, under the specified reaction parameters, the ring expansion proceeds freely.

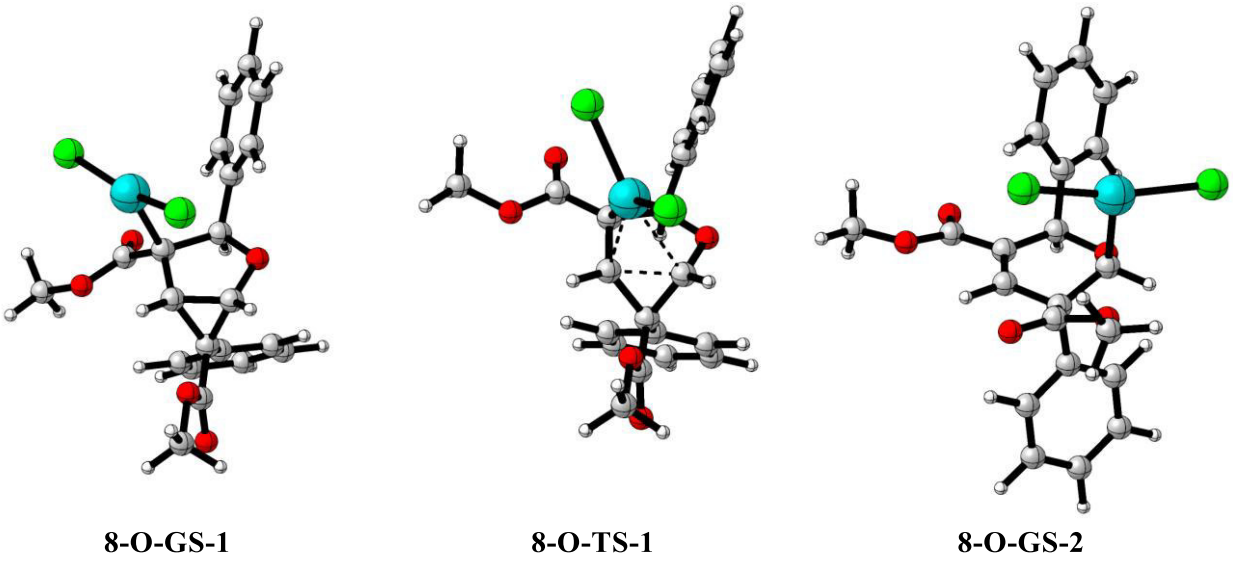

8-O-GS-1 **8-O-TS-1** **8-O-GS-2**

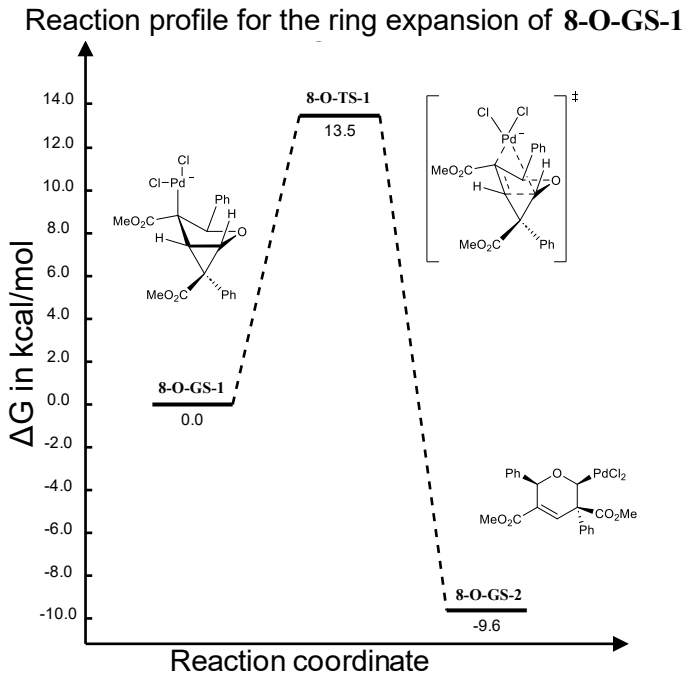

Figure 23. Top: Rendered structures for the palladium-mediated ring expansion of **8-O-GS-1**. Bottom: Reaction profile for palladium mediated ring expansion of **8-O-GS-1**.

3.2.2 Depalladation

In the monocyclopropanated systems discussed earlier, following the ring expansion, the species typically undergoes a formal, albeit disallowed, *trans*-*β*-hydride elimination of the palladium species. This process involves base-assisted elimination of the respective proton. However, since the geminal cyclopropanated species lacks a "*β*-hydride", an alternative mechanism is involved in the recovery of catalytic palladium.

In the publication of Wurzer *et al*., it was outlined that water was employed as a nucleophile to displace palladium from the species.[56] Notably, water was stoichiometrically generated via the Wacker cycle to facilitate this displacement. This is supported by the isolation of lactamol **73** from a reaction involving a geminal cyclopropanated pyrrole in aqueous MeCN (Scheme 25).

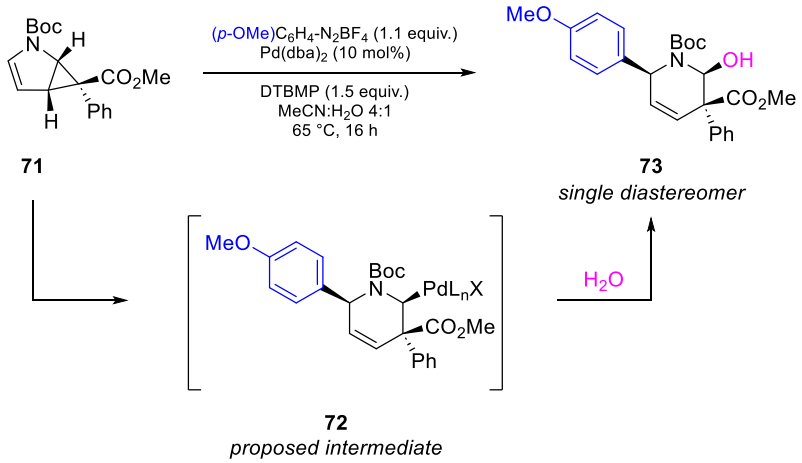

Scheme 25. Mechanistic studies by Wurzer *et al*., where a depalladated species was isolated.[56]

Although a corresponding lactol from a furan species was not specifically isolated, the occurrence of its formation is plausible, analogous to the observed lactamol **73**. However, this work diverges from the interpretation that water or hydroxide can displace the palladium species through a nucleophilic mechanism due to the carbanionic nature of the respective carbon. Instead, a reductive elimination process leading to a halocarbon intermediate prior to a nucleophilic attack is proposed. Moreover, the palladium species may act as a Lewis acid, further supporting the cleavage of the leaving group (Scheme 26).

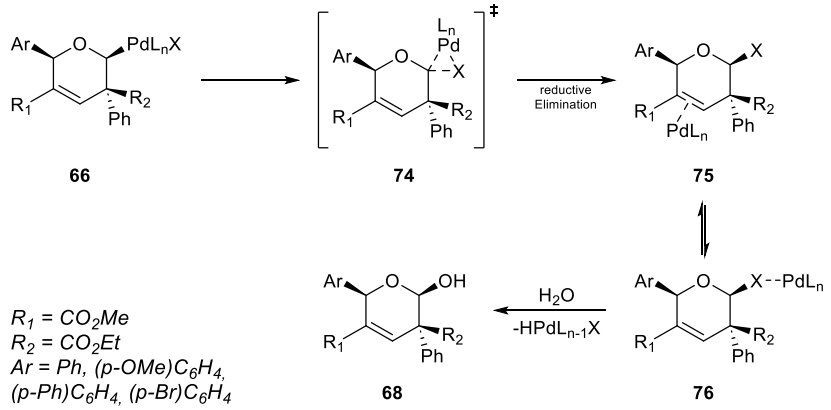

Scheme 26. Proposed mechanism for the depalladation of **8-O-GS-2**, modeled on the framework of **66**.

The activation barrier of the reductive elimination of **8-O-GS-2** is 24.5 kcal/mol, which is feasible at a reaction temperature of 40 °C (Figure 24, bottom). The formed halocarbon **8-O-GS-3** is more likely to undergo a substitution reaction compared to the palladated species **8-O-GS-2**, which lacks a proper leaving group. Considering the stereochemistry of the isolated lactamol **73** (Scheme 25), the corresponding substitution with water cannot follow an S_N2 reaction mechanism. Therefore, an S_N1 reaction in this analogous system **8-O** is suspected. Consequently, product **8-O-GS-3** can facilitate the respective cleavage by rearranging to form **8-O-GS-4** (Figure 24, top).

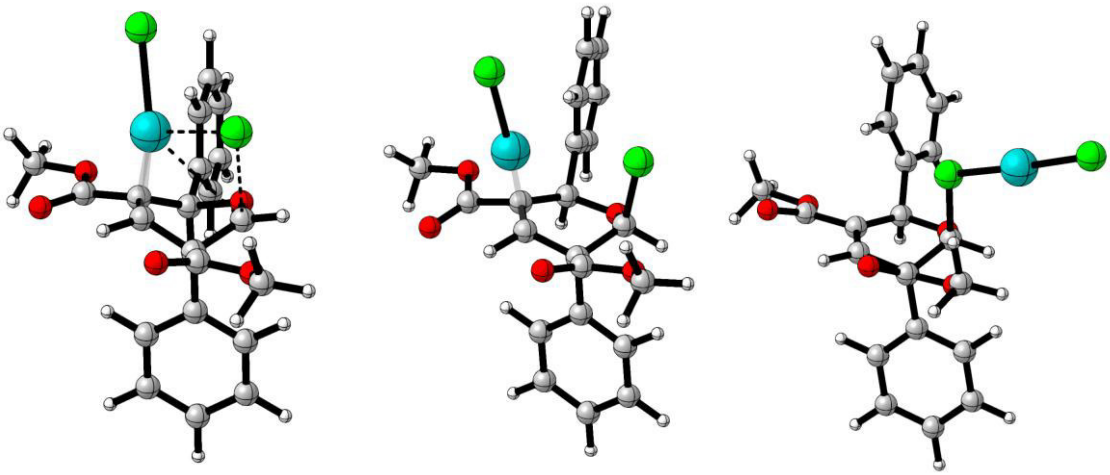

8-O-TS-2 **8-O-GS-3** **8-O-GS-4**

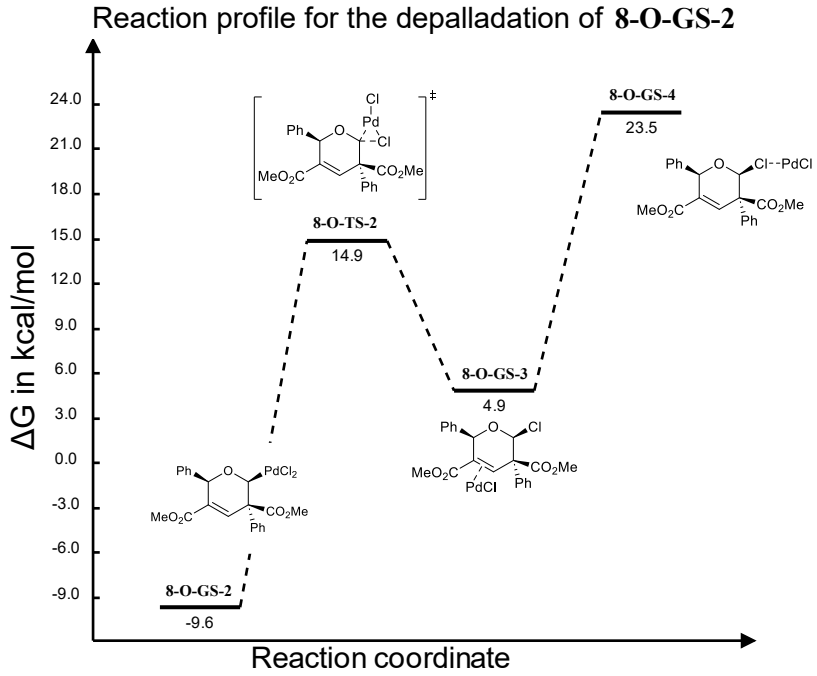

Figure 24. Top: Rendered structures involved in the depalladation of **8-O-GS-2**. Bottom: Reaction profile for the depalladation of **8-O-GS-2**.

However, this work refrains from addressing why the subsequent substitution reaction exhibits stereoselectivity. This is due to the considerable computational costs in terms of time and resources without providing a direct answer to the central question (see Chapter 2 of Part B). Consequently, in the following section, both diastereomers of the hemiacetal were considered for the ring opening.

3.2.3 Retro-Diels-Alder

Commencing from the formed hemiacetals where the hydroxy group is either in the *R* (**8-O-GS-5a**) or *S* (**8-O-GS-5b**) configuration, it was computationally determined that **8-O-GS-5a**, mirroring the configuration of the isolated lactamol **73**, is marginally more stable than **8-O-GS-5b**, by 1.8 kcal/mol due to the H-Bond interaction (Figure 25).

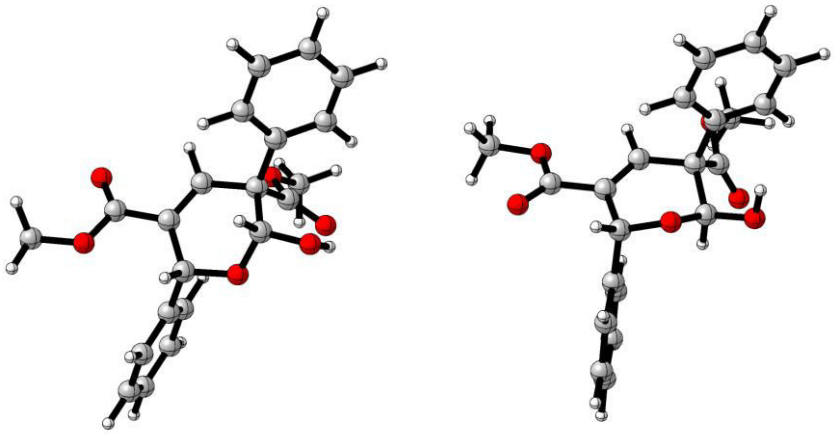

8-O-GS-5a **8-O-GS-5b**

Figure 25. Rendered structures of the two hemiacetal diastereomers.

To assess the potential interconversion of these diastereomers, the kinetic barrier for a base-assisted water exchange (Scheme 27) was calculated. The activation barrier is, within a 0.1 kcal/mol error margin, identical for both species at 39.7 kcal/mol, starting from the respective reactant complexes. Thus, the substantial kinetic barrier, combined with the lack of a driving force as indicated by the thermodynamics, suggests that an isomerization between the two species is unlikely.

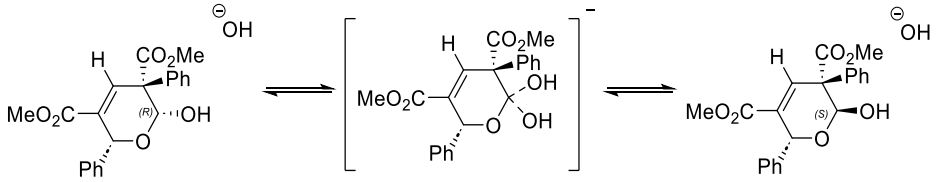

8-O-GS-6a **8-O-TS-3** **8-O-GS-6b**

Scheme 27. Isomerization between *R*- and *S*-conformer.

A retro-Diels-Alder reaction of the hemiacetals would result in the cleavage of formic acid and the formation of two potential 1,3-butadienes, namely, **8-O-GS-7a** and **8-O-GS-7b**, with the former being the exclusive observed product (Scheme 28). To maintain clarity, the following discussion is focused on the ring opening pathway initiated from the more stable substrate **8-O-GS-5a**, given that the data qualitatively aligns with that of **8-O-GS-5b**. However, the raw data for the latter is accessible in the supporting information for future reference.

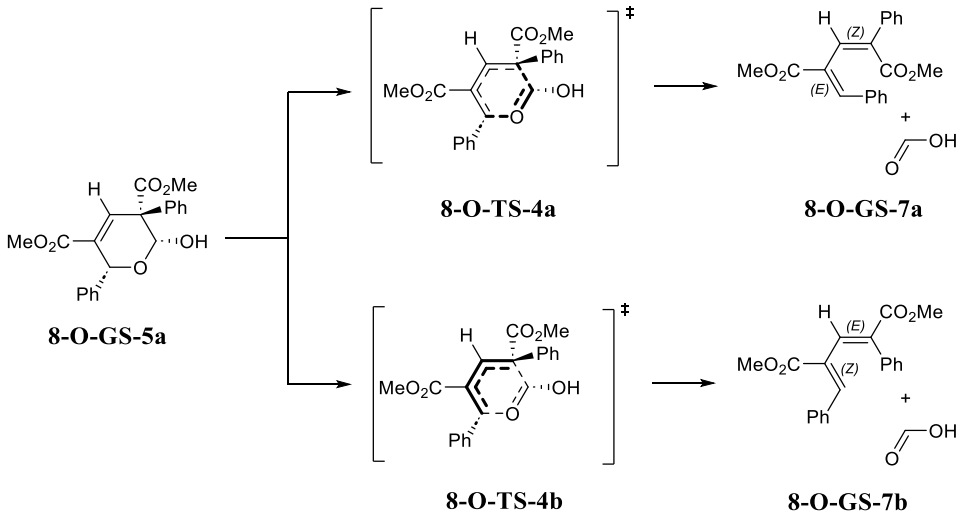

Scheme 28. Reaction pathways of the retro-Diels-Alder reaction. The ring opening can either occure with the dienophile positioned over the diene (**8-O-TS-4a**) or vice versa (**8-O-TS-4b**), leading to the respective products **8-O-GS-7a** and **8-O-GS-7b**. Bonds drawn in bold indicate that the corresponding part is spatially on top (see Figure 26, top).

Contrary to the experimental results, the formation of the unobserved product **8-O-GS-7b** is both kinetically ($\Delta\Delta G^{\ddagger}$ = 5.9 kcal/mol) and thermodynamically ($\Delta\Delta G^{\ddagger}$ = 1.3 kcal/mol) favored (Figure 26). However, this implies that if the expulsion of formic acid indeed corresponds to a retro-Diels-Alder reaction, the process must follow a considerably more energetically demanding pathway, involving a change in stereochemistry around an alkene center. This deviation from the typical and straightforward minimum energy pathway of a rather common reaction raises questions about the likelihood of the cyclo-reversion being a retro-Diels-Alder reaction.

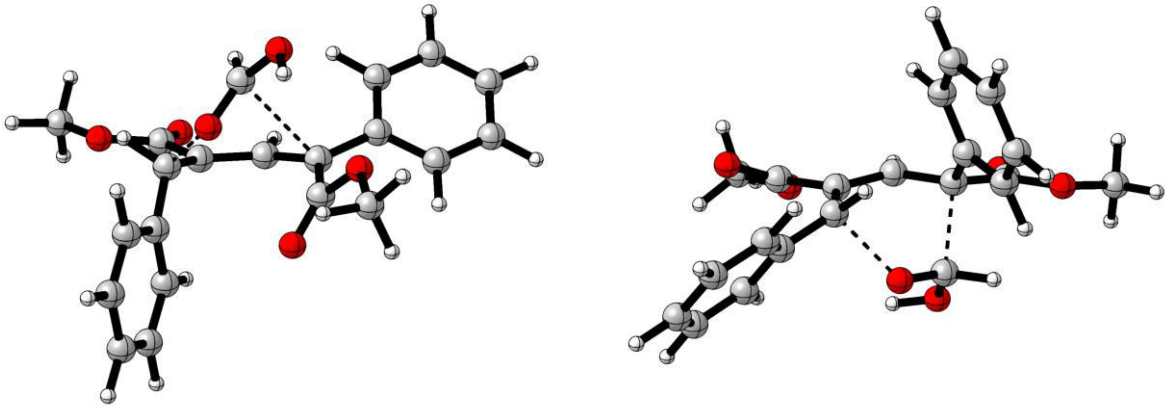

8-O-TS-4a **8-O-TS-4b**

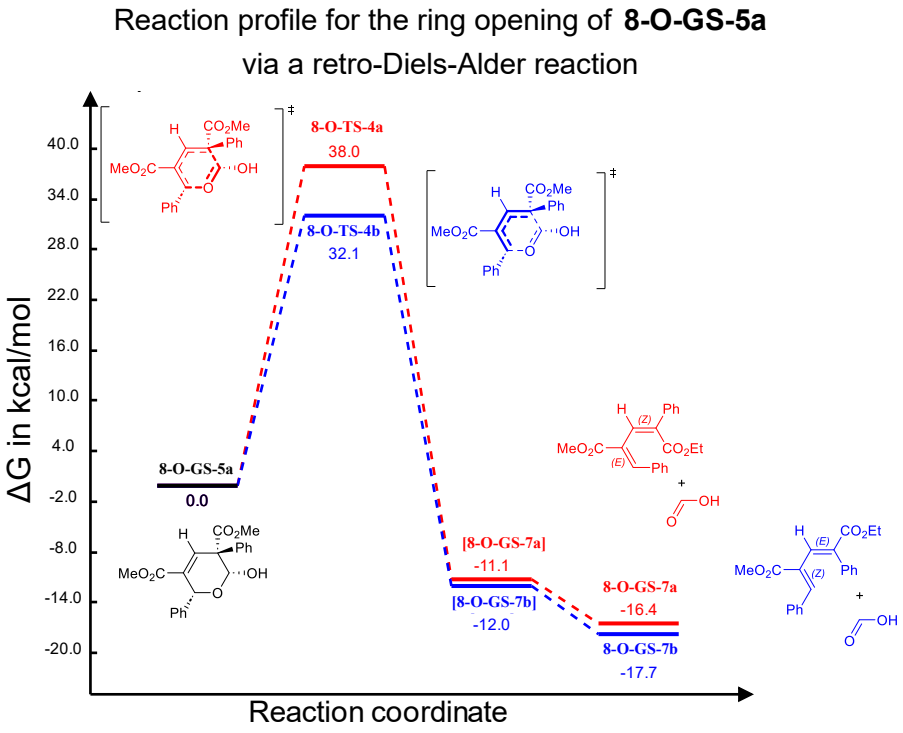

Figure 26. Top: Rendered structure of the retro-Diels-Alder transition states. Bottom: Reaction profile for the retro-Diels-Alder reaction of **8-O-GS-5a**. Squared brackets are used to indicate a reactant complex, where the separated molecules are still in spatial proximity.

In compounds featuring an intramolecular hydrogen bonding involving a "*β*-hydroxy carbonyl", there exists the potential for initiating a C-C-σ bond cleavage, leading to a stepwise retro-aldol type fragmentation. Moreover, decarboxylation of *β*-hydroxy carboxylic acids and enantio-enrichment of *β*-hydroxy ketones under catalytic conditions are quite well known in the literature.[142,143] The latter observation is particularly relatable, given that the products remain in the same phase, unlike the former case, where the release of carbon dioxide renders the reaction irreversible. The calculation of this stepwise mechanism (Scheme 29) aligns with the

observed data, showing that the free energy of the respective transition state **8-O-TS-5a** (Figure 27) is lower than that of the retro-Diels-Alder by 6.0 kcal/mol for **8-O-GS-5a** and 2.2 kcal/mol for **8-O-GS-5b** (Figure 28).

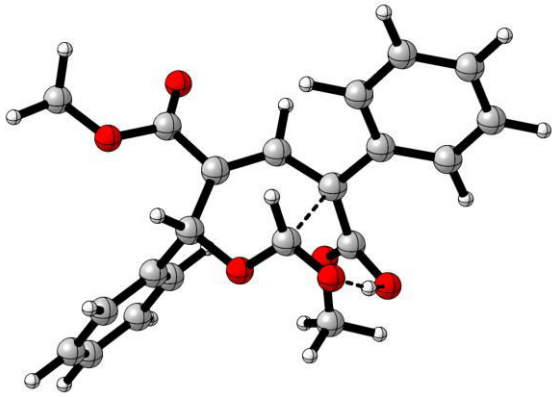

8-O-TS-5a

Figure 27. Rendered structure of retro-aldol transition state **8-O-TS-5a**.

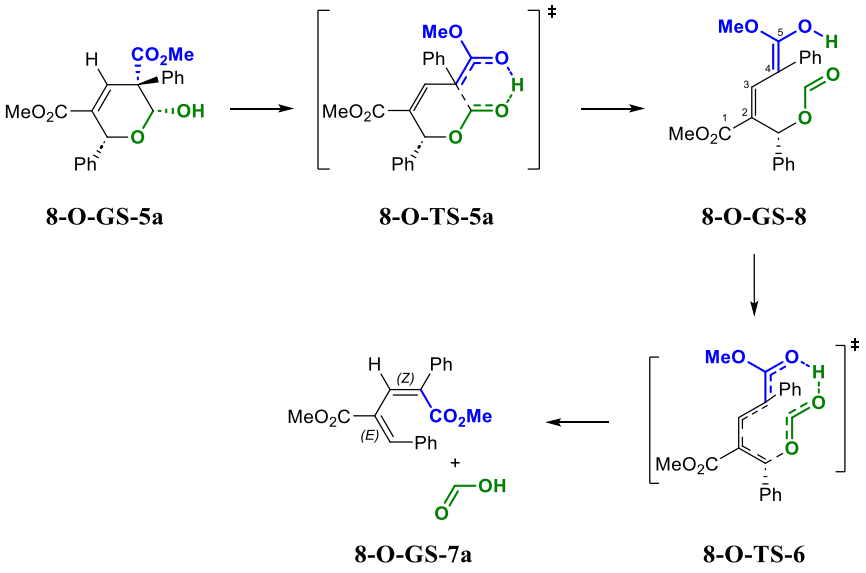

Scheme 29. Reaction pathways of the retro aldol reaction followed by a conjugate base elimination of formic acid. The parent chain of **8-O-GS-8** is numbered according to IUPAC.

So, assuming that the first step of this cyclo-reversion is indeed a retro-aldol step, a greater driving force for the next should be present, while the reformation of the starting compound should be slowed down. The former is given by the expulsion of formic acid in an alkaline milieu, while the latter effect is provided by the ester group present in the C^1 position of **8-O-GS-8**. The electron-withdrawing nature of the ester group engages the enolate in extended conjugation and drains away the electron density from the C^4 carbon, making it less nucleophilic for attacking and reforming the starting compound. The absence of the ester group

could impede the subsequent expulsion step **8-O-TS-6**, as seen with the **71** as a substrate, where the hydroxy form could be isolated as lactamol **73**.

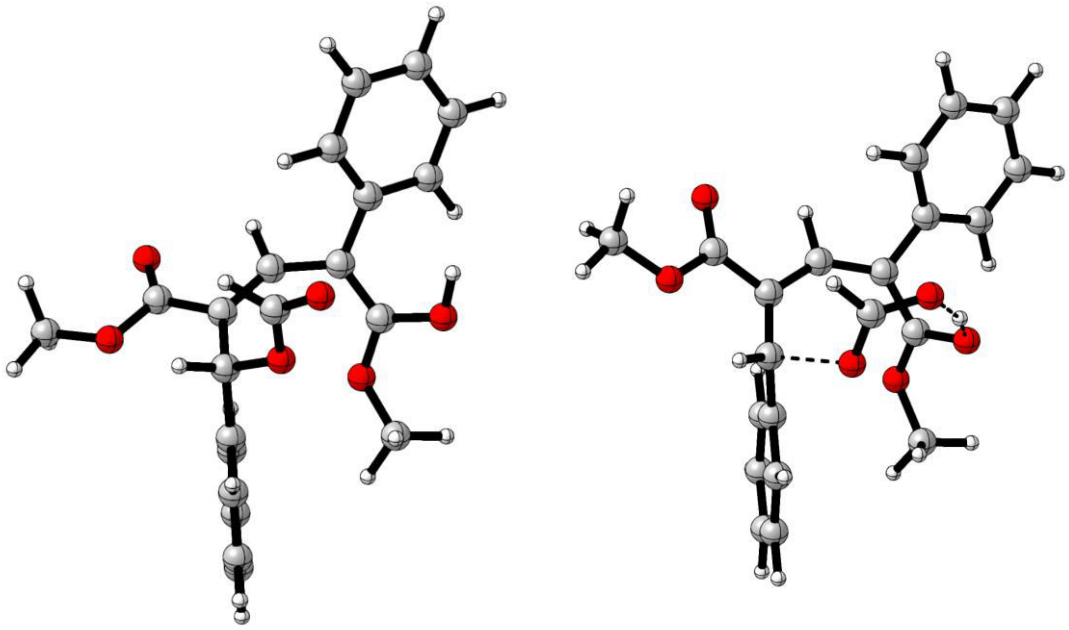

8-O-GS-8 **8-O-TS-6**

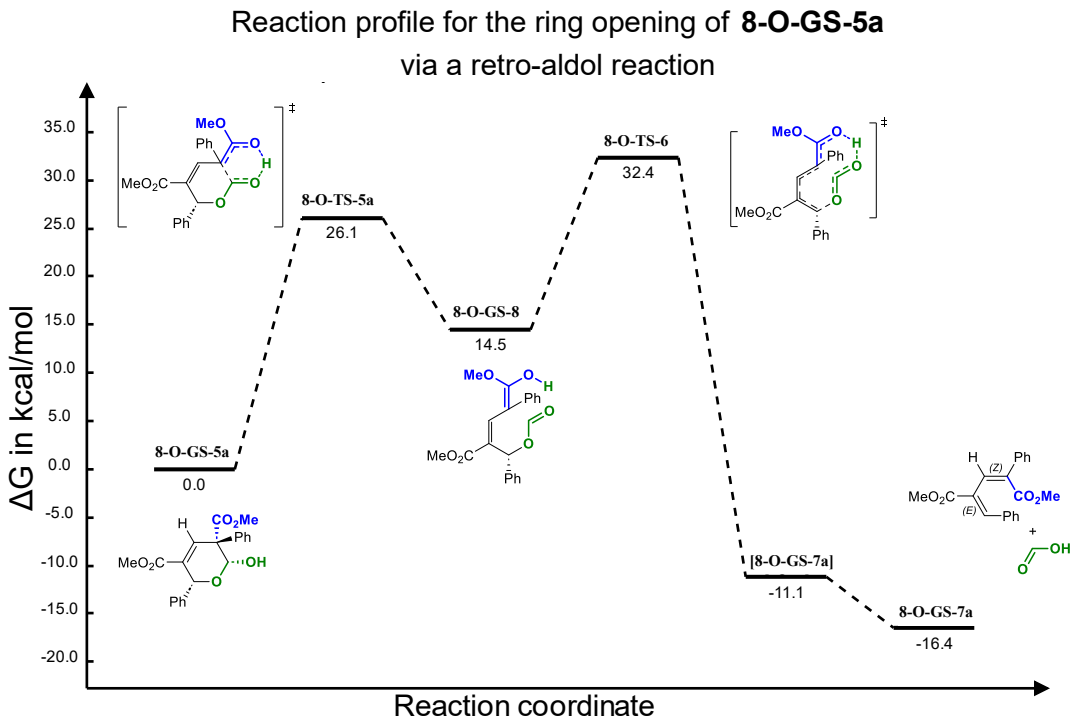

Figure 28. Top: Rendered structure of the intermediate **8-O-GS-8** and transition states **8-O-TS-6**. Bottom: Reaction profile for the retro-aldol reaction of **8-O-GS-5a**. Squared brackets are used to indicate a reactant complex, where the separated molecules are still in spatial proximity.

4. Summary and Outlook – Part B

Chapter 3 of this part undertakes a detailed computational exploration of the retro-Diels-Alder reaction, centering on geminal disubstituted furans (**64**). The study is prompted by the unusual occurrence of a stereoselective retro-Diels-Alder reaction, leading to a single diastereomer (**69**) instead of the anticipated secondary arylation.

The investigation unfolds through three pivotal stages:

Ring Expansion

Leveraging insights from earlier discussions on transition metal-catalyzed ring openings, an anionic palladium species (**8-O**) was assumed and determined a feasible activation barrier (13.5 kcal/mol) for the ring expansion process.

Depalladation

Addressing the challenge of palladium expulsion in the absence of a "β-hydride", the suggested water-mediated nucleophilic displacement was rejected in favor of a proposed reductive elimination mechanism. It reveals an activation barrier of 24.5 kcal/mol, resulting in the formation of the halocarbon **8-O-GS-3**.

Retro-Diels-Alder vs. Retro-Aldol

Evaluating the stability of hemiacetals (**8-O-GS-5a** and **8-O-GS-5b**), a kinetic barrier analysis was conducted, suggesting improbable interconversion. Intriguingly, despite experimental disparities, the retro-Diels-Alder favored product (**8-O-GS-7b**) demonstrates a notable alignment with both kinetic and thermodynamic preferences. This discrepancy prompts a critical reevaluation of its conventional classification as a typical retro-Diels-Alder reaction. Upon deeper investigation, we propose that the engagement of hydrogen bond interactions introduces an alternative and more favorable retro-aldol pathway, exclusively yielding the observed product **8-O-GS-5a**.

Further discussions

We acknowledge computational limitations in addressing the stereoselectivity of the subsequent substitution reaction. Therefore, we emphasized the significance of considering both diastereomers in the ring opening process. Nonetheless, a more detailed investigation of this mechanistic step could be valuable. This pursuit promises not only to unravel hidden complexities but also to unveil new avenues for advancing the understanding and application of unexpected stereoselective reactions.

Conclusion

The computational insights have offered a nuanced understanding of the unexpected stereoselective ring opening reaction. Intramolecular hydrogen bonds emerge as crucial elements, potentially unlocking diverse reaction pathways. This part of the thesis serves as a guiding beacon for future method development in stereoselective synthesis, underscoring the indispensable role of computational studies in advancing chemical understanding.

C. Photophysical Characterization and Reactivity Mechanisms of Protected Breslow-Intermediates

1. Introduction – Part C

1.1 *N*-Heterocyclic Carbenes in Organocatalysis

The field of organocatalysis has gained growing relevance in the pursuit of environmentally friendly and economically viable methodologies for chemical synthesis and peaked with the Nobel Prize in the year 2021.[144] Unlike classical catalysis, where valuable transition metals like palladium, platinum, or ruthenium are often employed, organocatalysts are small organic molecules capable of catalyzing chemical reactions. For instance, proline, a nontoxic, inexpensive, and chiral compound, finds use in aldol condensations and Michael reactions.[116,145]

NHCs are well known as ligands for metal complexes, but also in the field of organocatalysis. These species are often referred as persistent carbenes, that origins from an electronic "push-pull", within the molecules, where lone pairs of a neighboring heteroatom donate into the "empty" p orbital of the carbene carbon, reducing its electrophilicity. Simultaneously, the neighboring electron-withdrawing atoms reduce its nucleophilicity. The combination of mesomeric and inductive effects favors singlet-state carbenes over the more reactive triplet-state carbenes (Figure 29).[146,147]

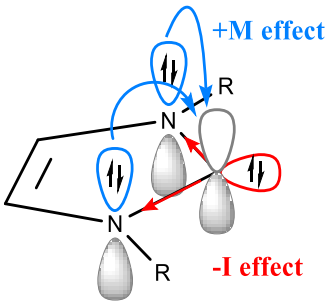

Figure 29. Electronic effects stabilizing NHCs.

In the organacatalysis NHCs are known to utilize umpolungs reactions.[148] In his mechanistic investigations, regarding the NHC catalyzed formation of benzoin from benzaldehyde, Breslow proposed 1958 the formation of an "activated aldehyde" – later known as "*Breslow-intermediate*" – as a key step in the catalysis (Scheme 30).[149]

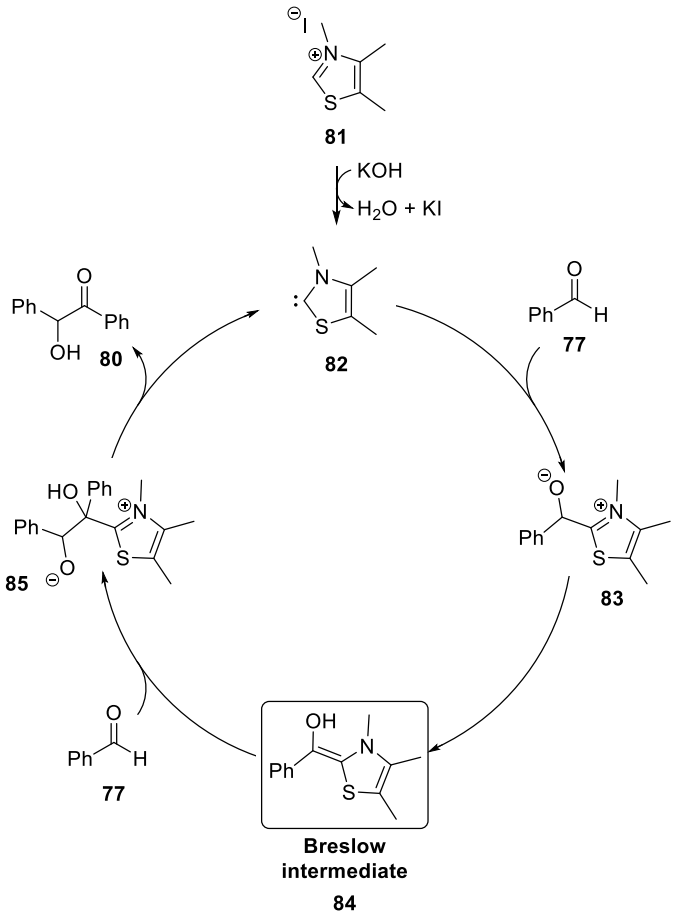

Scheme 30. Example of a NHC catalyzed benzoin reaction.

1.2 NHC-Stabilized Radicals

The formation of the Breslow intermediate, an enaminol species generated during aldehyde activation, is widely accepted. Notably, Berkessel's mechanistic investigations revealed the *in-situ* characterization of diaminoenols – products of aldehyde and carbene reactions – via NMR in 2012, followed by X-ray diffraction analysis of Breslow intermediates in 2013.[150,151]

In 2015, however, the Rehbein group challenged the solely ionic mechanism. While acknowledging the formation of the Breslow intermediate, they proposed an additional key intermediate derived from the Breslow intermediate via a single-electron transfer (SET) process, supported by computational calculations and EPR spectroscopy (Scheme 31).[152]

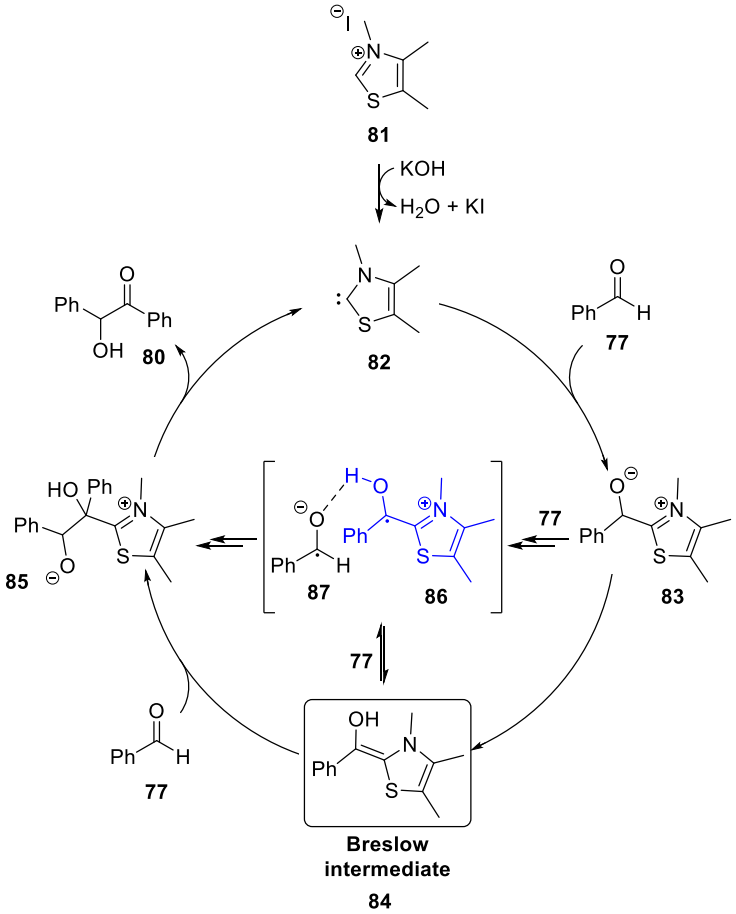

Scheme 31. Example of a NHC catalyzed benzoin reaction, including an alternative reaction path via the formation of a Breslow-intermediate-like radical **86** (blue). The Breslow-intermediate connects to the radical pair **86** and **87** via an SET.

The formation of radicals was observed at the start of the reaction, and its generation was shown to depend on the presence of both the Breslow-intermediate and the aldehyde.[152] This is further supported by isotopic labeling experiments, which not only confirmed this requirement but also revealed kinetic isotope effects similar to those previously reported by White *et al*. for the overall reaction. This similarity suggests that the rate-limiting step for radical generation and the overall reaction may be the same.[153,154]

Subsequent investigations by Rehbein highlighted that radicals resembling the Breslow intermediate can form in reactions beyond benzoin condensation, suggesting this is a broader phenomenon in aldehyde activation catalyzed by NHCs. Moreover, computational results aligned well with experimentally determined reaction kinetics, further supporting this alternative mechanistic pathway.[154]

Prompted by these statements, Regnier *et al*. explored the oxidation behavior of Breslow intermediates and identified the formation of radical species when exposed to air. However, these investigations indicated that one-electron oxidation of the Breslow intermediate forming the NHC-stabilized radical, as shown in Scheme 31 is followed by a deprotonation, leading to the generation of acylium cations (Scheme 32). These radicals were proposed to be more prevalent in the reaction environment than Breslow-intermediate-like radicals.[155]

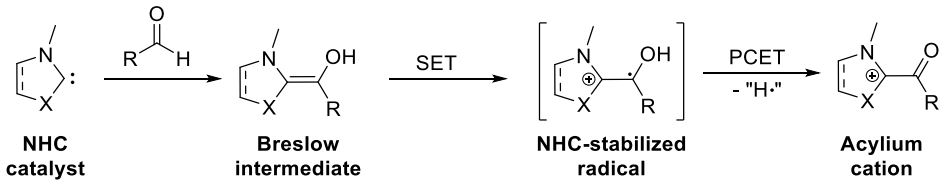

Scheme 32. Proposed formation of an acylium cation via a proton-coupled electron transfer (PCET), after the oxidation of the Breslow-intermediate by Regnier *et al*.[155]

Despite observations of radical formation in benzoin-type reactions, the role of these radicals as genuine intermediates in the reaction mechanism remains unverified. Nonetheless, these studies are fundamental for the future development of dual-catalysis (Section 1.4) involving radical reactions, in which the Breslow-intermediate is directly involved.

1.3 Photochemistry

Photochemical reactions have been recognized since the late 19th century, with Giacomo Ciamician pioneering the use of sunlight to reveal new synthetic strategies.[156,157] Throughout the subsequent century, photochemical reactions gained substantial significance in organic synthesis. They complement thermal reactions by offering novel synthetic pathways, allowing, for example, the control over the regioselectivity of pericyclic reactions through the choice of thermal or photochemical reaction pathways (Scheme 33).[137,158,159]

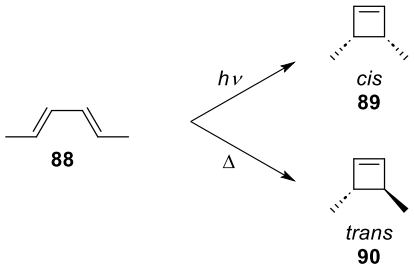

Scheme 33. Pericyclic reaction under regioselective control.

Unfortunately, numerous organic molecules only absorb in the high-energy UV range rather than the visible region of the spectrum, potentially leading to unwanted side reactions. However, using photocatalysts enables the conversion of light into chemical potential, facilitating photochemical reactions within the visible spectrum. Moreover, photocatalysis enables the simultaneous presence of only a catalytic amount of excited molecules, reducing the likelihood of side reactions.[160]

The realm of visible-light-mediated photocatalysis can be distinguished into electron and energy transfer processes. Scheme 34 illustrates the fundamental principle of photoredox catalysis using a Ru(II) species as an example. Under visible light irradiation, the photocatalyst transitions to its excited state, exhibiting improved reduction and oxidation potentials compared to the ground state. The excited catalyst can initiate a single electron transfer (SET) in a suitable substrate, catalyzing a redox reaction. For instance, blue light transitions $Ru(bpy)_3^{2+}$ to its electronically excited state $Ru^*(bpy)_3^{2+}$, enabling the oxidation of Donor **D** to $\mathbf{D}^+$. The original catalyst $Ru(bpy)_3^{2+}$ is then regenerated by reducing Substrate **S** to $\mathbf{S}^-$. Conversely, $Ru^*(bpy)_3^{2+}$ can also reduce the electron acceptor **A** to $\mathbf{A}^-$. The resulting species $Ru(bpy)_3^+$ can oxidize Substrate **S** to $\mathbf{S}^+$, completing the cycle and reforming the catalyst $Ru(bpy)_3^{2+}$.[160]

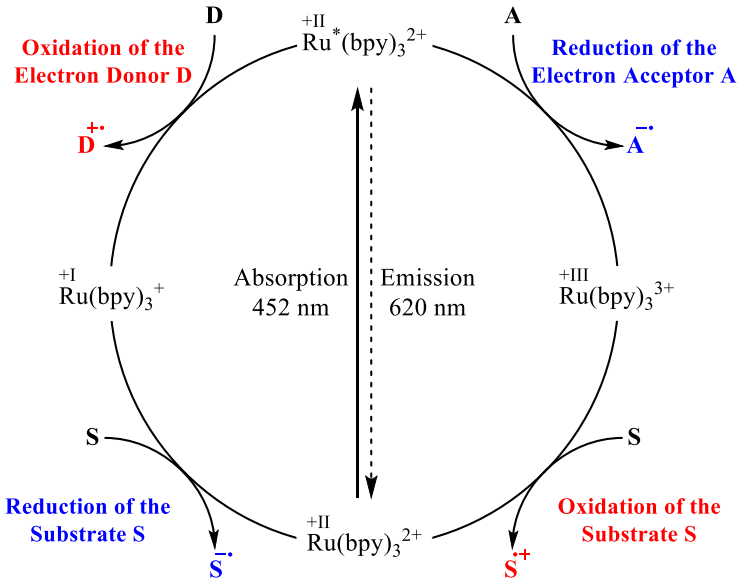

Scheme 34. Visible light photoredox catalysis illustrated in the case of $Ru(bpy)_3^{2+}$.[160]

Energy transfer (EnT) catalysis represents another type of photocatalysis. In contrast to transferring electrons between the excited catalyst and the substrate (SET), EnT catalysis involves the direct transfer of the excited state energy from the photocatalyst to the corresponding substrate (Scheme 35). This process results in the substrate becoming "indirectly excited" or "sensitized".[161–163]

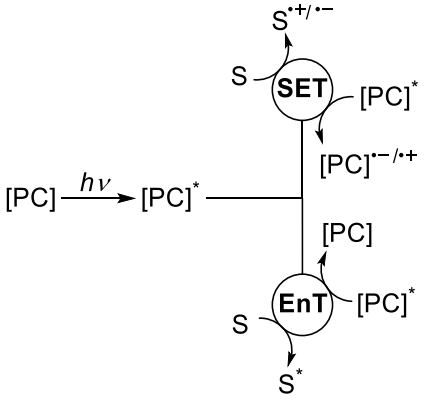

Scheme 35. Simplified schema of photocatalytic processes. SET = photoredox process, EnT = photosensitization process.[163]

In essence, all visible-light-mediated energy transfer (EnT) processes are initiated by the electronic excitation of the photocatalyst. This occurs through the absorption of a photon (10^{-15} s), leading to excitation from the S_0 state to some higher vibrational level of either the S_1 or a higher electronically excited singlet state. While there are rare exceptions, molecules in condensed phases rapidly relax to the lowest vibrational level of S_1 via internal conversion (10^{-12} s) according to Kasha's rule. However, the lifetime of the excited singlet state, undergoing emission via fluorescence (10^{-10}–10^{-7} s), is too short to facilitate an EnT process. Alternatively,

molecules in the S_1 state can undergo a spin conversion to the first triplet state T_1. This conversion of S_1 to T_1 is known as intersystem crossing (10^{-10}–10^{-8} s). These processes are visualized in a Jablonski diagram (Figure 30).[164]

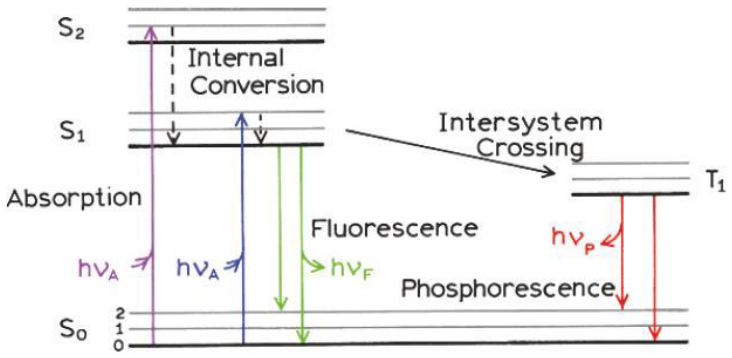

Figure 30. Jablonski diagram. The figure was taken from Lakowicz, *Principles of fluorescence spectroscopy*.[164]

The transition from T_1 to the singlet ground state S_0 is spin-forbidden, resulting in a much longer lifetime of the excited species (10^{-7}–1 s). This extended lifetime enables the possibility of bimolecular quenching processes, such as an energy transfer (EnT) from the photocatalyst to a suitable substrate.[163,164] Heavy atoms are frequently employed in photocatalysis as they facilitate intersystem crossing due to spin-orbit interactions.[164]

Mechanistically, non-radiative energy transfer (EnT) can occur through Förster (resonance) energy transfer (FRET) or Dexter Energy Transfer (Figure 31). The FRET relies on dipole-dipole interactions between donor **D** and acceptor **A**. The excited state donor $\mathbf{D}^*$ induces a dipole in the ground state acceptor **A**, leading to oscillation. FRET is typically observed in singlet-singlet EnT processes, but it is prohibited between an excited triplet state and a singlet ground state according to Wigner's spin conservation rule. Therefore, in photosensitized organic reactions in solution, Dexter EnT prevails, involving the simultaneous intermolecular exchange of excited-state and ground-state electrons.[163]

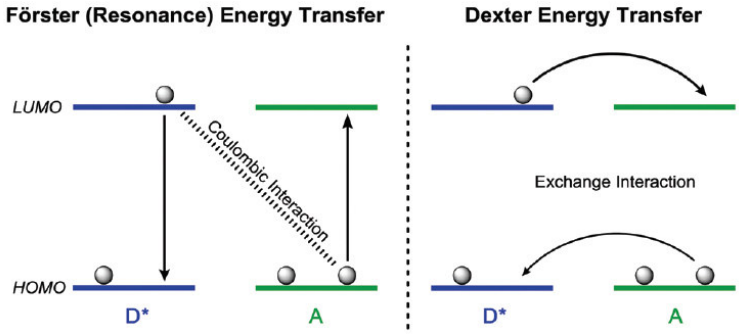

Figure 31. Schematic depiction of Förster and Dexter EnT processes. The figure was taken from *Chem. Soc. Rev.* **2018**, *47*, 7190–7202.[163]

To facilitate this double electron transfer, the distance between the molecules must be less than 2 nm (compared to 10 nm in FRET).[164–166] This proximity is achieved by forming a collision complex facilitated by the diffusion of substrates in the solution. In addition to the spatial requirement, it is essential that the energy functions of the donor and acceptor overlap (Figure 32). In summary, Dexter EnT predominantly governs triplet-triplet EnT processes.[163]

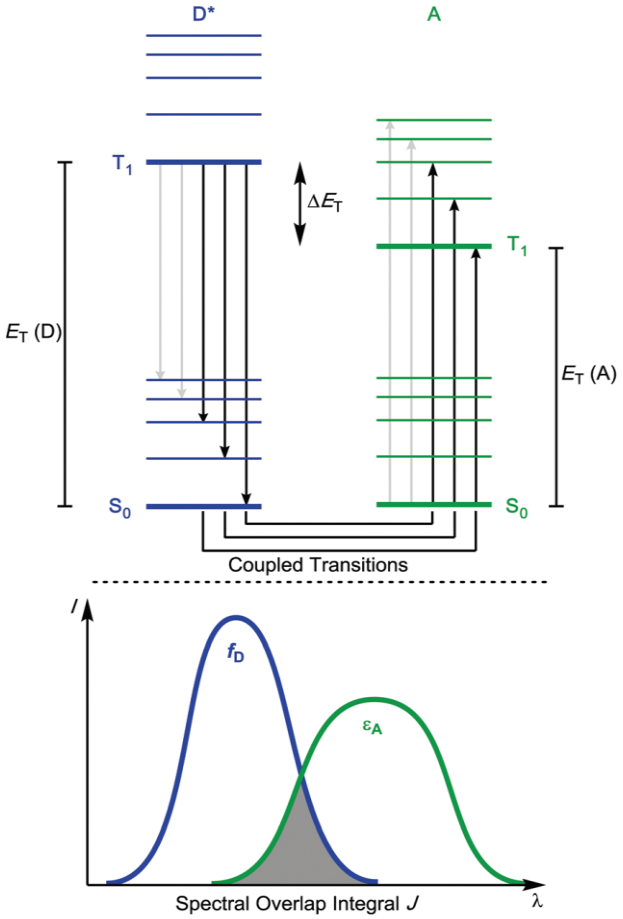

Figure 32. Jablonski schema and spectral overlap integral for a Dexter EnT. f_D = normalized donor emission spectrum, ε_A = normalized acceptor absorption spectrum. The figure was taken from *Chem. Soc. Rev.* **2018**, *47*, 7190–7202.[163]

1.4 Dual Catalysis

Over the years, researchers have explored various catalytic strategies to overcome limitations and enhance the efficiency of transformations. Dual catalysis, an innovative paradigm that integrates the cooperative action of two distinct catalysts, has emerged as a powerful tool for synthesizing complex molecules. Traditionally, single catalyst systems have played a pivotal role in promoting specific reactions by providing a suitable environment for the transformation of substrates. However, challenges arise when a desired reaction involves multiple steps or when diverse functional groups are present. Dual catalysis addresses these challenges by orchestrating the complementary roles of two catalysts, often of different types, to simultaneously activate multiple substrates, leading to *cascade reactions*, where all reactants are in the same vessel ("*one-pot*").[167–171]

The synergy between catalysts in a dual catalysis system enables the exploitation of diverse reactivity patterns and accelerates the formation of complex molecular architectures. This approach has found applications across various branches of chemistry, from organic synthesis to materials science and biochemistry.[172,173] Therefore, it is not surprising that *N*-heterocyclic carbene (NHC) catalysis is also used in such connected catalytic cycles.[174] The next section is focused on a few selected examples, that combine the NHC catalysis with photoredox catalysis.

In 2012, DiRocco and Rovis achieved stereoselective α-acylation of tertiary amines by combining chiral NHC catalysis and photoredox catalysis. The NHC, formally generating an acyl anion, worked in tandem with the photocatalyst, which oxidized the tertiary amine to an iminium cation in the presence of *m*-dinitrobenzene (*m*-DNB) under irradiation with blue light. This synergistic collaboration between the two independently working catalytic cycles facilitated the formation of a new C-C bond (Figure 33).[175]

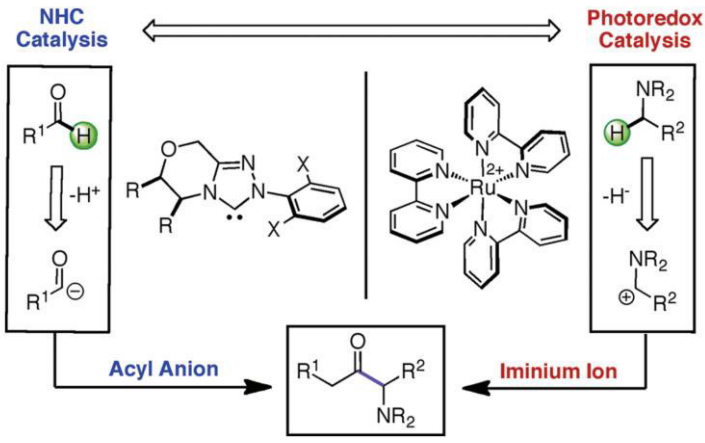

Figure 33. Proposed dual catalysis mode by DiRocco and Rovis. The scheme was taken from *J. Am. Chem. Soc.* **2012**, *134*, 8094−8097.[175]

In 2019, it was demonstrated by Ohmiya and Chi, that a radical derived from the Breslow-intermediate can engage in a coupling process with transient alkyl radicals during C-C bond formation.[176,177] This unique radical/radical coupling is based on the persistent radical effect (PRE), a kinetic phenomenon.[178] This discovery significantly broadens the potential applications of NHC-based radical catalysis. For example, thiazolium-derived NHCs were shown to facilitate the decarboxylative coupling of aryl aldehydes with tertiary or secondary alkyl radicals, derived from redox-active esters of carboxylic acids, to produce aryl alkyl ketones. In this approach, the redox ester serves as a source of alkyl radicals, while the Breslow-intermediate requires deprotonation – assisted by Cs_2CO_3 – to achieve a reduction potential sufficient for single-electron transfer (SET) with the redox ester. Following this SET process, the resulting radical form of the Breslow-intermediate couples with the alkyl radical. This method offers broad substrate compatibility and has been successfully applied to the functionalization of pharmaceutical compounds and natural products.[179]

In 2020, the Studer group published a cooperative NHC and photoredox catalysis in order to synthesize β-trifluoromethylketones via radical alkene acyltrifluoromethylation. The process involved irradiating a photocatalyst based on iridium with blue light. The excited Ir^{3+} species then undergoes reductive quenching to an Ir^{2+} species facilitated by the trifluoromethanesulfinate anion. The resulting radical species, formed through oxidation, engaged in a radical/radical cross-coupling with a persistent ketyl radical. This ketyl radical was produced by a reductive single electron transfer (SET) of an acylazolium intermediate – generated in situ from benzoyl fluoride and an NHC – allowing for the recovery of the catalytic Ir^{3+} species (Scheme 36).[180]

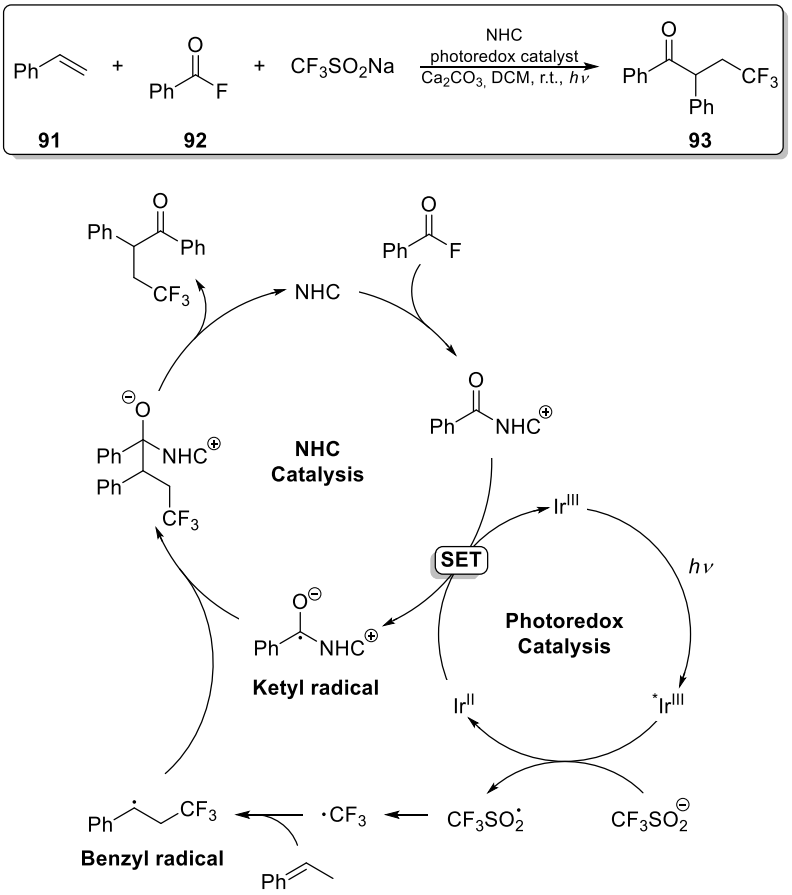

Scheme 36. Proposed dual catalysis mechanism by Qing-Yuan *et al*., in which the ketyl radical is formed via a reductive SET.

As mentioned in Section 1.2, Rehbein and co-workers challenged the classical accepted catalytic cycle of the benzoin condensation proposed by Breslow in the 1950s. Through a combination of electron paramagnetic resonance (EPR) spectroscopy and computational analysis, they proposed the involvement of a radical species derived from the Breslow-intermediate. This proposition was further supported by experimental evidence demonstrating the generation of a stable *O*-methylated Breslow-intermediate, which exhibited an EPR signal upon adding an aldehyde, suggesting the formation of a radical species (Scheme 37).[152]

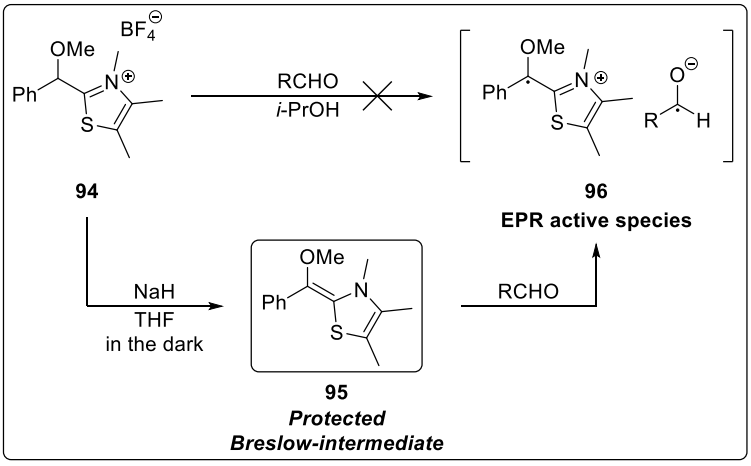

Scheme 37. Generation of Breslow-like radicals from a protected Breslow-intermediate by the addition of an aldehyde.

Based on these results, Studer *et al*. once again reported a radical/radical cross-coupling induced via a cooperative NHC and photoredox catalysis in 2022. However, in this instance, the ketyl radical was formed via an oxidative SET of the Breslow-intermediate (Scheme 38).[181]

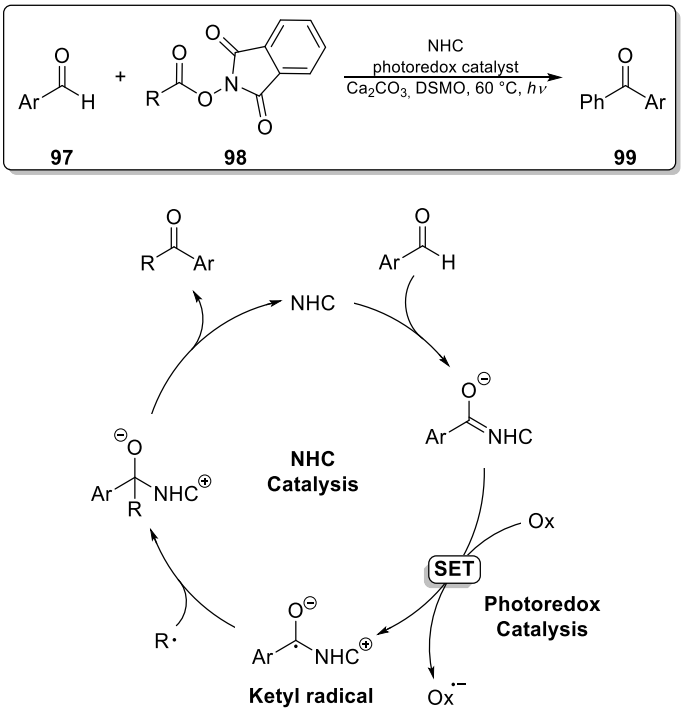

Scheme 38. Proposed dual catalysis mechanism by Studer *et al*., in which the ketyl radical is formed via an oxidative SET.

These examples highlight the promising potential of cooperative catalysis involving NHC and photocatalysis, opening novel pathways for product formation and indicating a growing prevalence in the field of organocatalysis.

1.5 Transient Absorption Spectroscopy

In the realm of mechanistic studies, transient absorption spectroscopy stands out as a crucial tool that is precious in addressing the challenges associated with characterizing short-lived species. This technique facilitates the close observation of excited states and intermediates throughout a reaction, offering valuable insights into the intricacies of mechanistic processes, especially in the field of photochemistry.

In this method, a short light pulse ("pump") is directed at the sample, inducing the transition of the molecule from the ground state (S_0) to a metastable excited state. The change in the electronic state leads to alterations in the molecular system. The evolution of this process is then monitored by a pulsed light source characterized by high bandwidth, known as the probe pulse, which interacts with the excited species. Possible interactions are the excitation to an even higher electronic state, called excited state absorption (ESA) or stimulated emission (SE), in which the emission of two photons and, thus, the relaxation of the excited species into the ground state is induced by the absorption of one photon. Additionally, in the region of the pump wavelength, the absorbance signal is lowered, which is called ground state bleach (GSB). This occurs because the respective species have already been excited by the pump pulse. The described processes and their respective signals are simplified depicted in Figure 34. It is also possible that GSB, ESA and SE are overlapping, complicating the evaluation of such difference spectra.[182–185]

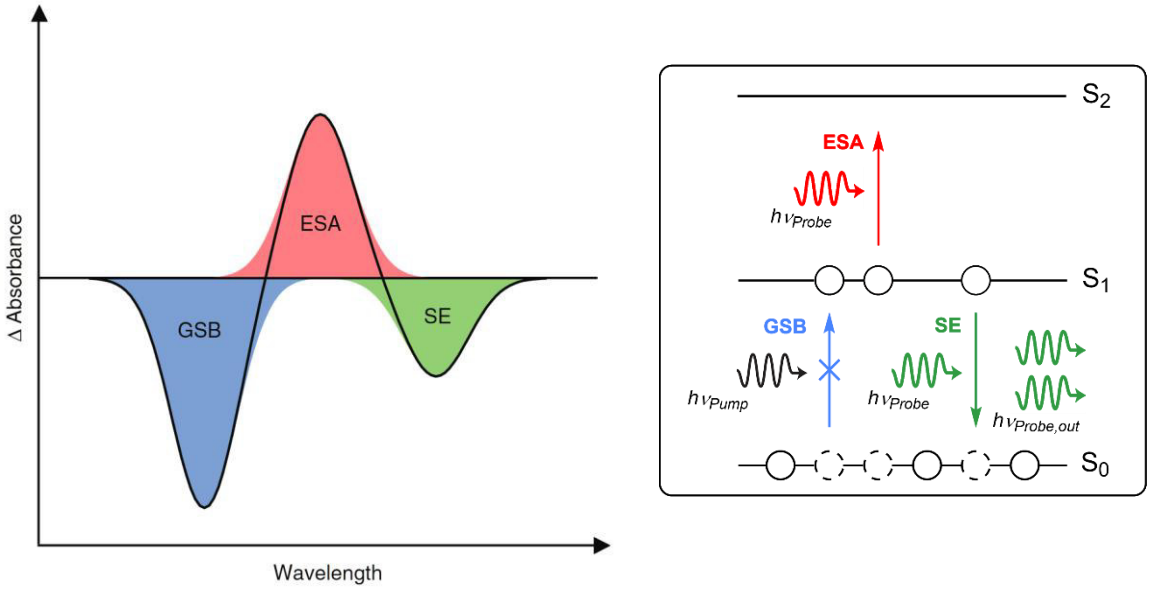

Figure 34. Left: Simplified depiction of possible signals obtained in pump-probe transient absorption experiments. Right: Schematic illustration of the origin of the respective signals due to the absorption or (stimulated) emission of molecules. The figure on the left was taken from Chergui, *Ultrafast structural dynamics of biological systems*.[182]

Throughout the measurement, the absorption spectrum of the probe pulse is recorded against its time delay to the pump pulse, where $\Delta t = 0$ corresponds to both pulses arriving at the sample simultaneously (Figure 35). The absorption behavior of a molecule is measured against a reference, where no pump pulse has interacted with the sample. Therefore, the change in absorbance ΔA or optical density ΔOD is represented as:[183,185]

$$\Delta OD(\lambda, \Delta t) = OD_{pump-probe}(\lambda, \Delta t) - OD_{probe}(\lambda) = \log_{10}\left(\frac{I_{probe}(\lambda)}{I_{pump-probe}(\lambda, \Delta t)}\right)$$

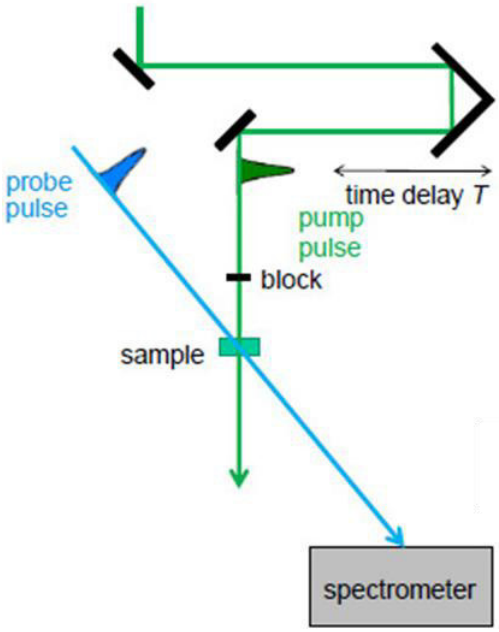

Figure 35. Principle of the pump-probe transient absorption experiment. The figure was taken from Patrick Nürnberger's lecture script.[186]

Each resulting spectrum is referred to as a transient and can be mapped (Figure 36). The timescale depends on the distance of the delay stage. In contrast, the time resolution depends on the duration of the two pulses, ranging from femtosecond resolution with ultrashort laser pulses to microsecond resolution with pulsed flashlamps.[185]

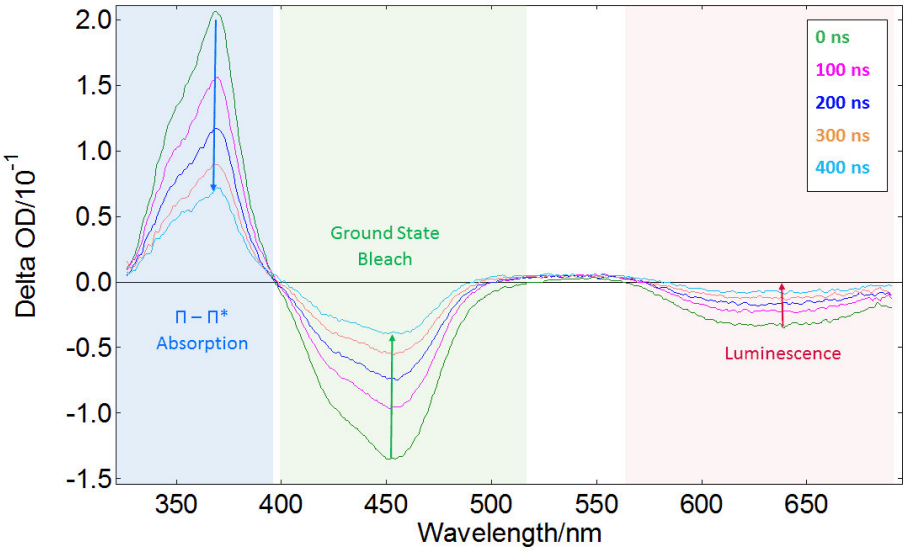

Figure 36. Experimental spectral transient absorption map of $[Ru(bpy)_3]Cl_2$ using a Nd:YAG laser providing a pump pulse of 355 nm. The figure was taken from www.edinst.com.[183]

When the sample does not undergo further reactions, it subsequently exponentially decays to the ground state. This results in a decrease in both GSB and ESA. If, however, the ground state bleach does not fully recover, it indicates that an irreversible photochemical reaction has occurred on the observed timescale, leading to the formation of a new photoproduct.

2. Aim of the Work – Part C

This section of the thesis aims to characterize the photophysical properties of the excited Breslow-intermediate, providing foundational data for future dual catalysis projects involving both a NHC and a photoredox cycle. A key challenge is the short lifetime of the Breslow-intermediate, which limits its possibilities to interact with photocatalysts and complicates its characterization. To address this, *O*-methylated Breslow-intermediates as introduced in Section 1.4, were used. These modified species exhibit a longer lifetime, allowing direct experiments. Their electronic structure is nearly identical to that of the original Breslow-intermediate, ensuring that the data generated is transferable (Figure 37).

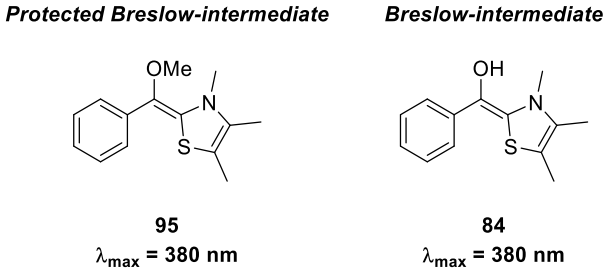

Figure 37. Left: An example of a protected Breslow-intermediate and its maximum absorbance. Right: The corresponding Breslow-intermediate and its maximum absorbance.[187,188]

Additionally, the investigation aims to explore potential photochemical pathways that may lead to undesired reactions under specific conditions, known as *loss channels*. The focus will be on three primary areas of investigation. Firstly, examining the role of solvents, which have the potential to alter the stereochemistry of the Breslow-intermediate. Secondly, exploring the sensitivity of the intermediate to air, which can result in its decomposition. Lastly, investigating intramolecular hydrogen atom transfer (HAT) reactions, which may lead to unwanted side reactions but could also present opportunities for new reaction pathways.

The data obtained via UV-vis spectroscopy were generated and evaluated in cooperation with our collaboration partner, Gabriel Mayer, from the Nürnberger group.

3. Main Part – Part C

3.1 Computational Details

In this section, the computational procedures employed for the research are outlined. The excited state calculations and respective orbital analysis were provided by Gabriel Mayer, our collaboration partner from the Nürnberger group.

Software and Packages: All density-functional theory (DFT) and post-Hartree-Fock calculations presented in this work were conducted using the Turbomol version 7.5.1[189,190].

Geometry Optimization: Geometry optimizations were carried out using the B3LYP-D3BJ hybrid functional and the triple zeta basis set def2-TZVP[191–194] for the electronic ground state S_0 and def2-TZVPD[195] for the electronic excited state S_1. Implicit solvation effects were considered using the COSMO solvent model[196] with the parameters for MeCN.

UV-vis Spectra: The UV-vis spectra were simulated using time-dependent DFT[197] (B3LYP, def2-TZVPD) and post-Hartree-Fock (ADC(2)[198]/CC2[199], aug-cc-PVTZ[200–203]) methods. For each simulation, 35 states were requested.

Temperature: Temperature conditions were set at 298.15 K.

Stationary Points: Stationary points were rigorously characterized as either minimum energy structures or saddle points of first order (transition states) through frequency analysis within the harmonic oscillator approximation. Minimum energy structures exhibited no imaginary frequencies, while transition states displayed a single imaginary frequency, confirmed as the correct reaction coordinate of the elementary step of interest via visualization in GaussView 6.

Conformational Analysis: Stationary points were subjected to conformational analysis using the CREST program with GFN-xTB methods to obtain the most stable conformer. Barriers and thermodynamics along reaction paths were referenced to the minimum energy conformers.

Orbital Analysis: Natural transition orbital (NTO) analyses[204] were employed to determine orbital interactions of excited species. Visualization of orbitals was performed via Chimera 1.16[205], using an isovalue of 0.0356 $Å^{-3}$ for occupied orbitals and 0.0456 $Å^{-3}$ for virtual orbitals.

Visualization: When describing a process that qualitatively applies to multiple systems discussed in the respective paragraph, it is illustrated by using the simplest systems with the fewest number of atoms.

Remarks: Any deviations from the specified computational procedures outlined in this section will be explicitly addressed in the respective paragraph of the following chapters. Note that the computational structures have their own unique numbering system, distinct from the one used for the schemes.

3.2 Experimental Parameters

The protected Breslow-intermediates (PBI) were prepared and stored in a glovebox to maintain their integrity. UV-vis measurements samples were prepared ~~within~~ in the glovebox under a nitrogen atmosphere, with water concentrations below 1 ppm and oxygen concentrations ranging from 1–30 ppm. Dry and degassed (freeze-pump-thaw) solvents were used for dilution, with stock solutions stored in the glovebox. Dilution concentrations ranged from 0.1–0.2 mM to achieve maximum absorbance between 0.3 and 1.0. Absorption measurements under irradiation and for comparative samples were conducted using 2x10 mm quartz glass cuvettes, while fluorescence measurements utilized 10x10 mm cuvettes of the same material. Due to quality issues with the sealing, screw cap cuvettes featuring a septum were replaced by Starna cuvettes, which feature glass joints. The protected Breslow-intermediates (Figure 38) were irradiated with a laser pulse at 355 nm in transient absorption spectroscopy or a blue LED at 385 nm (550 mW radiant flux).

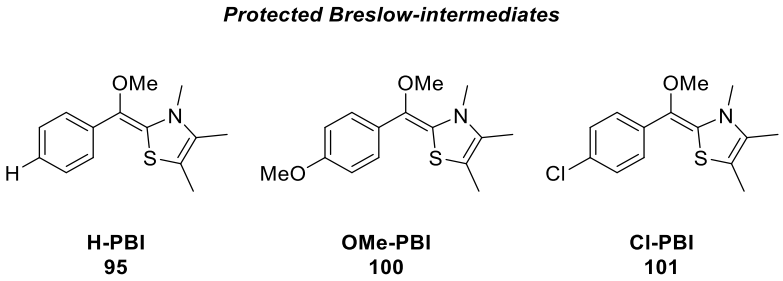

Figure 38. Measured protected Breslow-intermediates. For clarity, only the respective *E*-isomers are shown.

3.3 Results and Discussion

3.3.1 Synthesis of the Protected Breslow-Intermediates

The synthesis of the *O*-methylated Breslow-intermediates is based on the work of the former group members, Kirsten Zeitler, Stephanie Ruser and Jenny Phan under the supervision of Julia Rehbein.[154,206] However, significant adjustments made to enhance efficiency, purity and yield (see experimental part for details). Therefore, the yield of the bottleneck of the reaction, step **I** (Scheme 39) – exemplified for R = H – was increased from 72% to 92%. Additionally, the product was obtained as a colorless powder rather than a brown slurry, which is anticipated due to the absence of a larger conjugated system.[206]

The synthesis began with the deprotonation of 4,5-dimethylthiazole, using *t*-BuLi as a bulky base, followed by a reaction with an aldehyde to form the carbinol **104**. The choice of *n*-BuLi over *t*-BuLi resulted in the formation of fenipentol derivatives as undesired side products. Subsequently, the carbinol **104** was quantitatively methylated to ether **105** using NaH as the base and MeI as the electrophile. The stable precursor of the protected Breslow-intermediate **106** was obtained as a salt, utilizing the Meerwein reagent $Me_3O(BF_4)$ as the methylation agent. Finally, the protected Breslow-intermediate **107** was formed by a deprotonation with NaH (Scheme 39). The **H-PBI**, featuring a phenyl group, serves as the reference system. At the same time, the *p*-OMe substituted product (**OMe-PBI**) represents an electron-rich system, and the *p*-Cl substituted product (**Cl-PBI**) serves as an electron-deficient system.

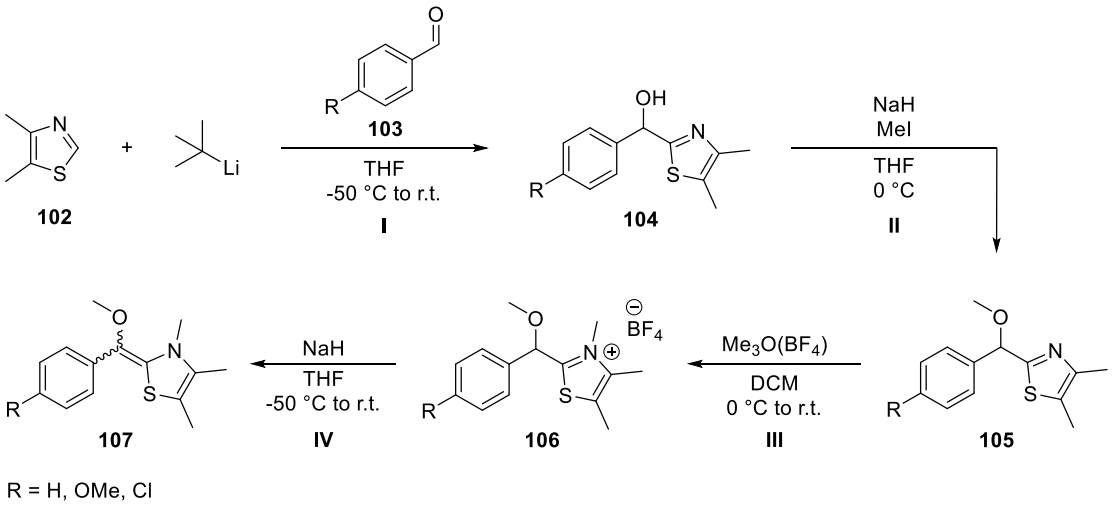

Scheme 39. Synthesis of the protected Breslow-intermediates. **I**: Up to 92% yield. **II**: Up to quantitative yield. **III**: Up to quantitative yield. **IV**: Up to 75% yield. The *Z*-isomer is the major component of **107**, comprising 63–66%. The detailed procedures and respective yields are provided in the Experimental Part D.

Computational calculations suggest that the *Z*-isomer is the thermodynamically more stable product of the protected Breslow-intermediates by approximately 1 kcal/mol. This finding is consistent with experimental NMR measurements, which identify the *Z*-isomer as the main diastereomer (Table 13). Although the elimination of compound **106** proceeds under kinetic

control, the thermodynamic data remains relevant. According to Hammond's postulate, in a kinetically controlled single-step reaction, the transition state leading to the more stable *Z*-isomer is likely lower in energy, which aligns with our computational findings. The preference for the *Z*-isomer is attributed to the increased steric hindrance in the *E*-isomer.[138,159]

Table 13. The difference in electronic energies for stationary points including zero-point vibrational energy. [a]$\Delta E = E_{Z\text{-isomer}} - E_{E\text{-isomer}}$. [b]Species were calculated in the gas phase (left values) and with an implicit solvent model (right values). [c]Ratio of the *E*- to the *Z*-isomer (*E*:*Z*). [d]C_6D_6 was used as a solvent for the NMR. The same samples were measured again one week later, showing no change in their spectra.

Species	**Δ*E* in kcal/mol**[a,b]	**Boltzmann distribution**[b,c]	**NMR distribution**[c,d]
H-PBI	1.0 / 1.0	18:82 / 18:82	35:65
OMe-PBI	1.0 / 1.0	18:82 / 18:82	35:65
Cl-PBI	0.9 / 1.1	22:78 / 16:84	37:63

3.3.2 Photophysical Properties of Breslow-Intermediates

The experimental UV spectra in MeCN of the species showed a maximum in absorbance at 380 nm (ε=19965 L·mol^{-1}·cm^{-1}), 365 nm (ε=17542 L·mol^{-1}·cm^{-1}) and 390 nm (ε=14216 L·mol^{-1}·cm^{-1}) for **H-PBI**, **OMe-PBI**, and **Cl-PBI**, respectively. To gain further insight into the electronic excitation, the spectra were simulated using TDDFT and post-HF theories (for details, see Chapter 3.1). However, differences between the two methods were insignificant. Therefore, only the spectra and data obtained by post-HF theory using ADC(2) were depicted in the following sections unless stated otherwise. It was determined that the *Z*-isomers are slightly blue-shifted compared to the *E*-isomer (Table 14).

Table 14. Calculated maximum in absorbance λ_{max} and oscillation strength f for the protected Breslow-intermediates in the blue light region for the *E*- (left) and *Z*-isomer (right).

Species	λ_{max} / nm	f
H-PBI	370.9 / 369.3	0.331 / 0.322
OMe-PBI	358.4 / 346.4	0.362 / 0.371
Cl-PBI	383.9 / 382.9	0.374 / 0.409

To better align with the experimental data, the calculated UV-vis spectra were generated by superposing the simulated spectra of the *E*- and *Z*-isomers in a ratio of 35:65 (Figure 39, left).

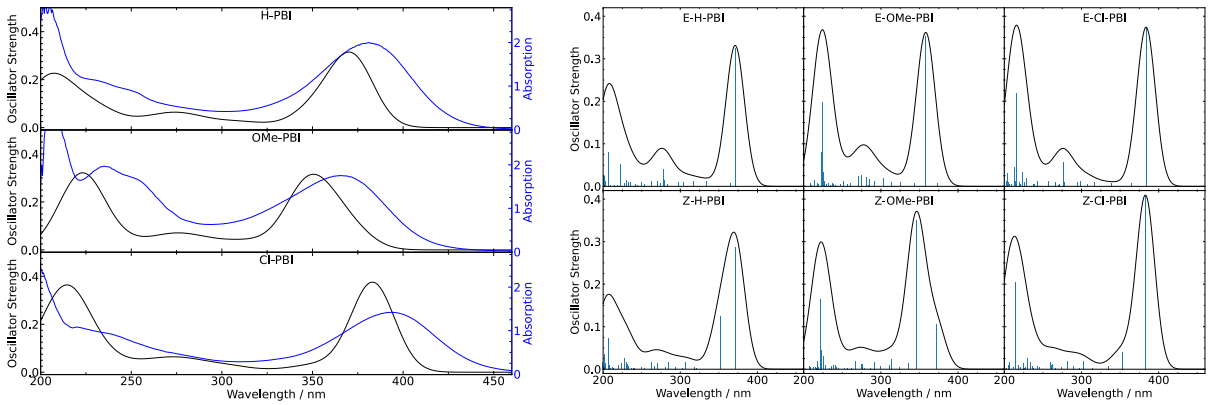

Figure 39. Left: Experimental spectra (blue) and simulated spectra (black). Right: Simulated spectra of the single diastereomers. Spectra were simulated at the ADC(2)/aug-cc-pVDZ level of theory.

The high similarity between the simulated spectra and the experimental one suggests that the chosen computational options describe the electronic excitation of the system well. Analysis of the natural transition orbitals (NTOs) indicates that the electronic transition yielding the absorption maxima involves a charge transfer from the thiazole to the phenyl group, accompanied by the breaking of the π-bond between the two units. That π→π* transition of the double bond is consistent with expectations and was observed in both isomers of all protected

Breslow-intermediates. This phenomenon is illustrated by depicting the NTOs of the **H-PBI** as an example in Figure 40.

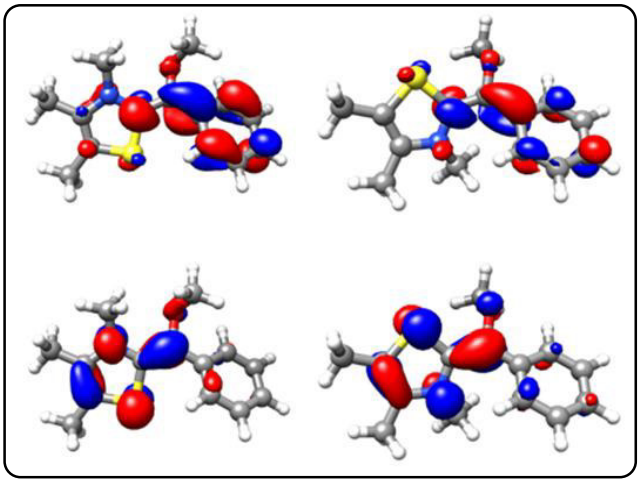

Figure 40. NTOs of the **H-PBI**, that are involved in the electronic transition, yielding the absorption maxima at 380 nm. Bottom: Highest occupied transition orbital (HOTO). Top: Lowest unoccupied transition orbital (LUTO).

The resulting charge separation from this transition may lead to the formation of a biradical species. Additionally, intersystem crossing ($S_1 \rightarrow T_1$) appears feasible, with a calculated energy gap of about 15–20 kcal/mol between the states (Table 15).[96,207]

Table 15. Calculated singlet-triplet energy gap ΔE between the S_1 and T_1 state of the **H-PBI** for the *E*- (left) and *Z*-isomer (right), whereas the S_1 state is lower in energy. [a]The implicit COSMO solvent model with the parameters for MeCN was used.

	ΔE (S_1-T_1) in kcal/mol	
Method / basis set	***E*-isomer**	***Z*-isomer**
B3LYP / def2-TZVPD[a]	21.2	20.7
ADC(2) / aug-cc-PVTZ	15.9	15.0
CC2 / aug-cc-PVTZ	16.8	15.2

Additionally, the lifetimes of the excited (singlet) species were measured via the decay of its fluorescence signal. All protected Breslow-intermediates displayed a weak fluorescence emission signal, which overlapped with Raman signals (Figure 41). The results of the fluorescence measurements are summarized in Table 16.

Table 16. Results of the fluorescence measurements. The Raman scattering signals are calculated as the difference between the wavenumber of the excitation and the wavenumber of the Raman signal.

Species	Excitation wavelength / nm	Fluorescence emission maxima / nm	Raman scattering signal / cm^{-1}	Lifetime / ns
H-PBI	380	457	3006	10.3
OMe-PBI	364	432	2962	11.1
Cl-PBI	390	455	2965	7.4

Based on these results, it is assumed that the decay of the excited species proceeds radiatively via fluorescence and non-radiatively via intersystem crossing, which is common for species with this moderate singlet-triplet gap.[96,207]

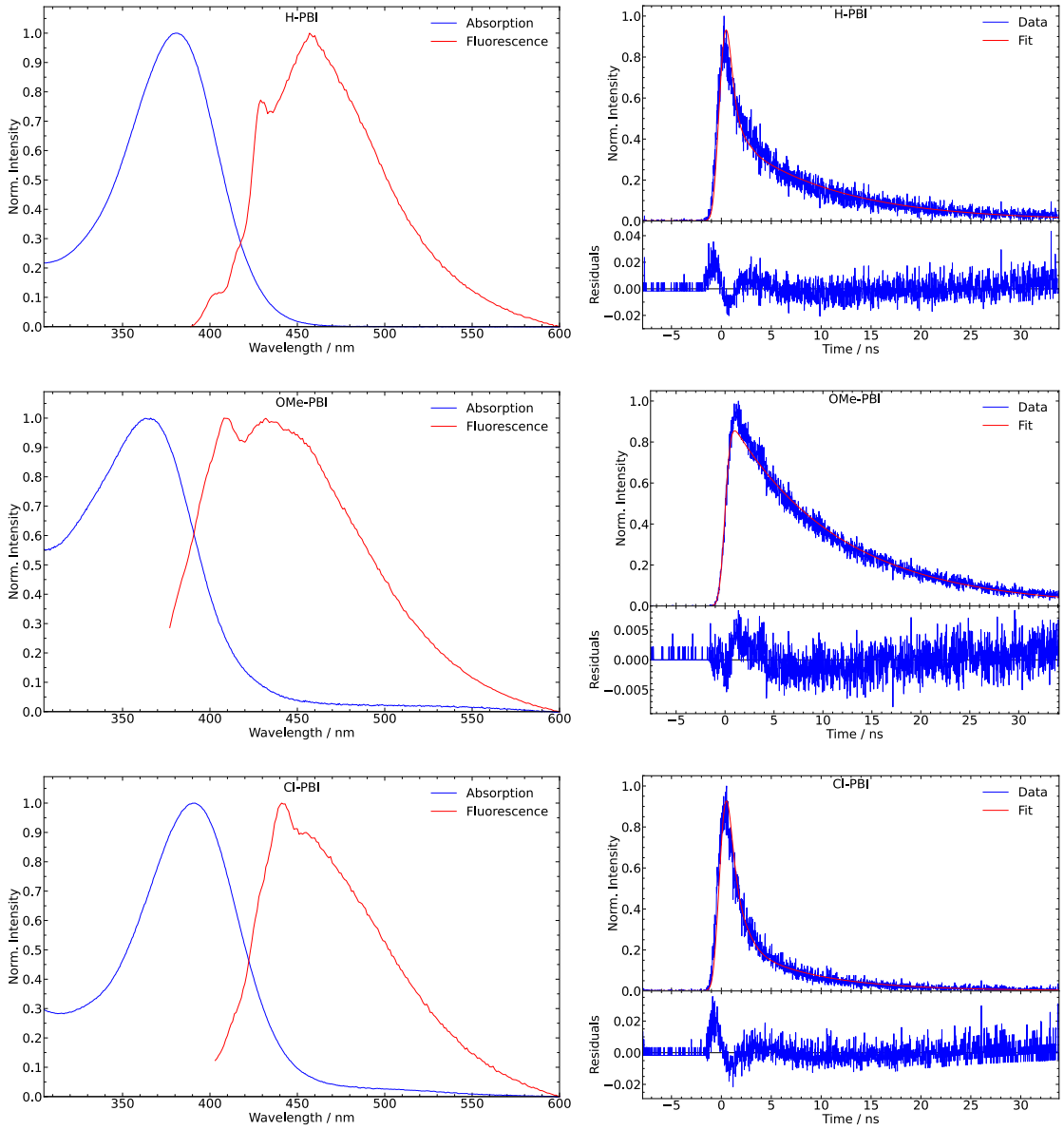

Figure 41. Left: Normalized absorption (blue) and emission (red) spectra of the protected Breslow-intermediate species. Right: Corresponding fluorescence decay, measured via TCSPC (blue) and exponential fit (red) in order to determine the lifetime.

To evaluate the photophysical behavior of the excited species, transient absorption spectra were recorded using a 355 nm pump pulse and a streak camera. A pulsed xenon flashlamp serving as the probe pulse. The delay timescale ranged from 0.5 to 100 µs.

The transient absorption map of **H-PBI** on a 10 µs timescale exhibits a nearly constant negative signal around 380 nm, representing the maximum absorption of the species caused by excitation via the pump pulse (photobleaching). Additionally, a negative signal at $\Delta t = 0$, ranging from around 350 to 500 nm, originated from the fluorescence signal overlapping with the GSB. Surprisingly, besides this initial negative signal, there was a nearly constant positive signal with a peak at 420 nm. Measurements on a longer timescale of 100 µs showed no change in the mapped spectra. Similar results were observed for **OMe-PBI** and **Cl-PBI** (Figure 42).

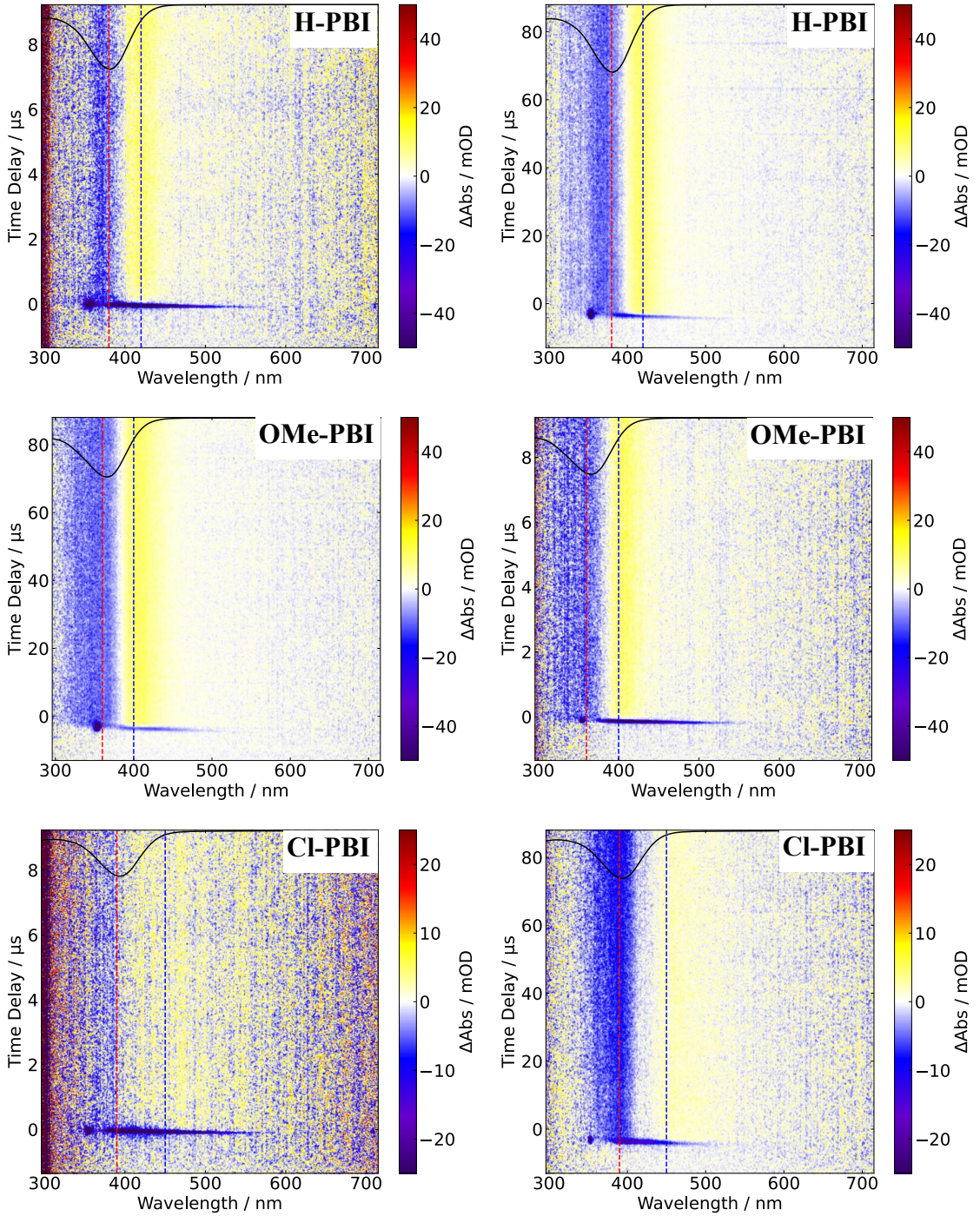

Figure 42. Transient absorption map of **H-PBI** (top), **OMe-PBI** (middle) and **Cl-PBI** (bottom) on a 10 µs (left) and 100 µs (right) timescale. The red line (380 nm for **H-PBI**, 360 nm for **OMe-PBI**, 380 nm for **Cl-PBI**) marks the peak of the constant negative signal and the blue line (420 nm for **H-PBI**, 400 nm for **OMe-PBI**, 450 nm for **Cl-PBI**) is marking the peak of the newly formed positive signal. The black line at the top of each spectrum depicts its absorption spectra.

These observations suggest that a new stable product has formed on a timescale faster than 0.5 µs. Considering the previous data regarding the UV-vis spectra of the diastereomers, the redshift in the absorption signal may indicate an isomerization process favoring the *E*-isomer. A difference spectrum created by subtracting the simulated spectrum of the *E*-isomer from that of the *Z*-isomer in a 1:1 ratio predicts a decrease in absorption below 390 nm and an increase above 400 nm, supporting this hypothesis (Figure 43).

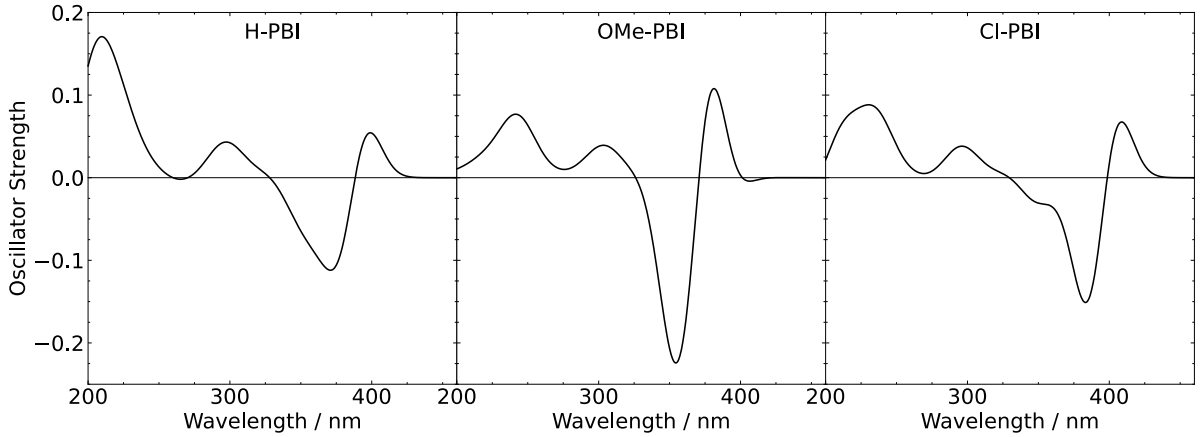

Figure 43. Calculated difference spectra for the diastereomers of the protected Breslow-intermediates in a 1:1 ratio, based on the TDDFT simulations at B3LYP/def2-TZVPD level of theory.

To experimentally support this hypothesis, an NMR experiment was conducted using a freshly synthesized charge of **H-PBI**. Three NMR samples were prepared in dry and degassed THF-d_8. One sample was irradiated with a blue LED light for 30 minutes, while another was irradiated for 60 minutes. The last sample served as a non-irradiated reference. The irradiation significantly changed the ratio of diastereomers, favoring the predicted *E*-isomer (Table 17).

Table 17. THF-d_8 was used as a solvent for the NMR. Irradiation at 385 nm (550 mW radiant flux). The NMR was obtained 1 h after the irradiation, which was performed in accordance with the general parameters in Chapter 3.2. [a]Ratio of the *E*- to the *Z*-isomer (*E*:*Z*). [b]The THF-d_8 contained 550 ppm H_2O.

Species	Irradiation time / min	[a]NMR distribution
H-PBI	0	45:55
	30	61:39
	60	64:36
	[b]60	41:59

The isomerization process appears to be nearly completed after 30 minutes of irradiation, as no significant change was observed upon further irradiation. However, when non-dried THF-d_8 (550 ppm water) was used, the isomerization process was reversible, resulting in even more *Z*-isomer compared to the reference sample. Therefore, traces of water in the solvent seem to be sufficient to protonate the respective double bond, enabling rotation and leading to the formation of the thermodynamically favored product (Scheme 40).

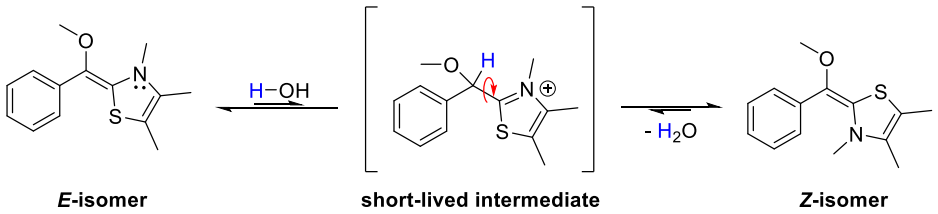

Scheme 40. Proposed isomerization process in the protected Breslow-intermediates **H-PBI** catalyzed by water.

Based on these results, the choice of solvent can significantly influence the isomerization process of Breslow-intermediates under irradiation. Solvents containing acidic protons such as *i*-PrOH, commonly used in benzoin condensation reactions, are likely to suppress photo-induced changes in the configuration of Breslow-intermediates. In contrast, in solvents like THF, which lack acidic protons, the Breslow-intermediate may undergo isomerization under irradiation. Nonetheless, the addition of small amounts of water may suppress this effect assuming protonation occurs more rapidly than subsequent reactions.

However, in addition to solvents containing acidic protons such as water or alcohols, other electrophilic solvents like MeCN, commonly employed in photoreactions due to its absorption in the far UV region, could yield similar outcomes. Hence, the preceding NMR experiment was replicated using MeCN-d_3 as the solvent. The results indicated that irradiation did not alter the ratio of the diastereomers (Table 18). This observation contrasts with the results obtained in THF-d_8, suggesting a solvent-dependent influence on the isomerization process.

Table 18. MeCN-d_3 was used as a solvent for the NMR, which was obtained 1 h after the irradiation. The irradiation was performed in accordance with the general parameters in Chapter 3.2. [a]Ratio of the *E*- to the *Z*-isomer (*E*:*Z*). .

Species	Irradiation time / min	NMR distribution[a]
H-PBI	0	45:55
	30	45:55
	60	45:55

To exclude the possibility of thermic isomerization, the barrier of the reaction was calculated using the Gaussian 16 program package with the B3LYP/6-31(d) method and basis set. The calculated activation energy of 30.6–32.2 kcal/mol at 298.15 K indicates that thermic isomerization is unlikely to occur. Therefore, chemical isomerization appears to be the only plausible mechanism (Scheme 41).

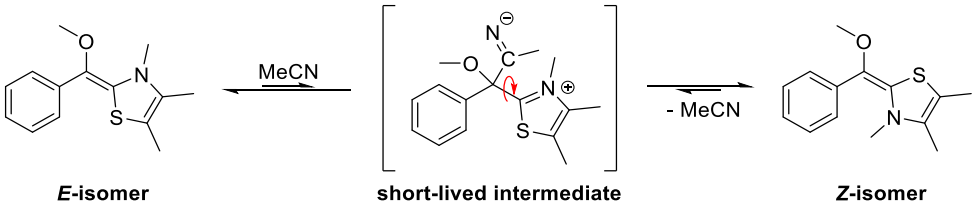

Scheme 41. Proposed isomerization process in the protected Breslow-intermediates **H-PBI** catalyzed by MeCN.

Consequently, in NHC catalysis, the choice of solvent may play a crucial role in the enantioselectivity of the reaction, especially if the Breslow-intermediate is key to the stereoselectivity. The more electrophilic the solvent, the more likely it is to promote a non-photochemical isomerization, resulting in a thermodynamic equilibrium of the isomers.

3.3.3 Air Sensibility of the Protected Breslow-Intermediate

NHC catalysis typically requires air-free conditions due to the sensitivity of NHCs to oxygen and moisture. However, oxidative NHC-catalyzed reactions have been reported, where air or other oxidants are used to generate various NHC-bound azolium intermediates.[208] In this context, the goal was to investigate the impact of air/oxygen on the (protected) Breslow-intermediate and to explore how it behaves under light-induced excitation.

To begin, a **H-PBI** sample was prepared under inert conditions as outlined in Chapter 3.2. The cuvettes were then connected to a 100 mL flask filled with air and separated from the sample by a Teflon plug valve. Initially, the sample was irradiated for 5 minutes, showing no change in signal, thereby excluding reactions purely reliant on light that could influence the absorption spectrum. Subsequently, measurements continued while gradually exposing the system to air by opening the plug valve without stirring. After approximately 2 minutes, the signal of the sample began to decrease rapidly, indicating oxygen diffusion into the solution. The substrate appeared fully decomposed within 3–5 minutes (Figure 44). **OMe-PBI** and **Cl-PBI** samples exhibited similar behavior.

In a reference measurement conducted in the dark, no decomposition occurred within 20 minutes. To further investigate, the experiment was repeated, but after 5 minutes, the sample was irradiated for 5 seconds. Subsequently, the initial decrease in absorbance continued at a constant rate, albeit much slower compared to continuous irradiation. After 12 minutes, a second light pulse was administered to assess whether the process would accelerate, but the decreasing rate of the signal remained nearly constant. The experiment concluded after 20 minutes.

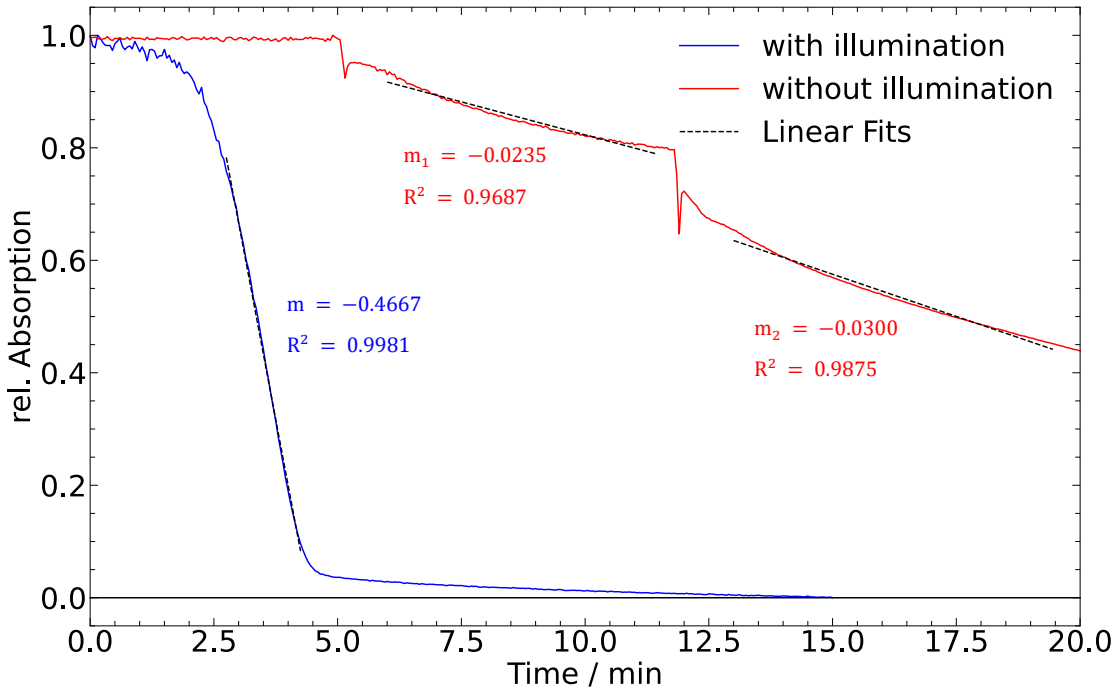

Figure 44. Time-resolved oxygen-induced decomposition of **H-PBI** measured at 380 nm in MeCN. The experiment was conducted under continuous irradiation at 385 nm (blue) and with only two light pulses (red). The slope m represents the reaction rate in min^{-1} based on the relative absorption of the species.

To rule out specific solvent effects attributed to the electrophilic nature of MeCN, as discussed in Chapter 3.3.2, the experiment was repeated in THF, yielding consistent results (Figure 45).

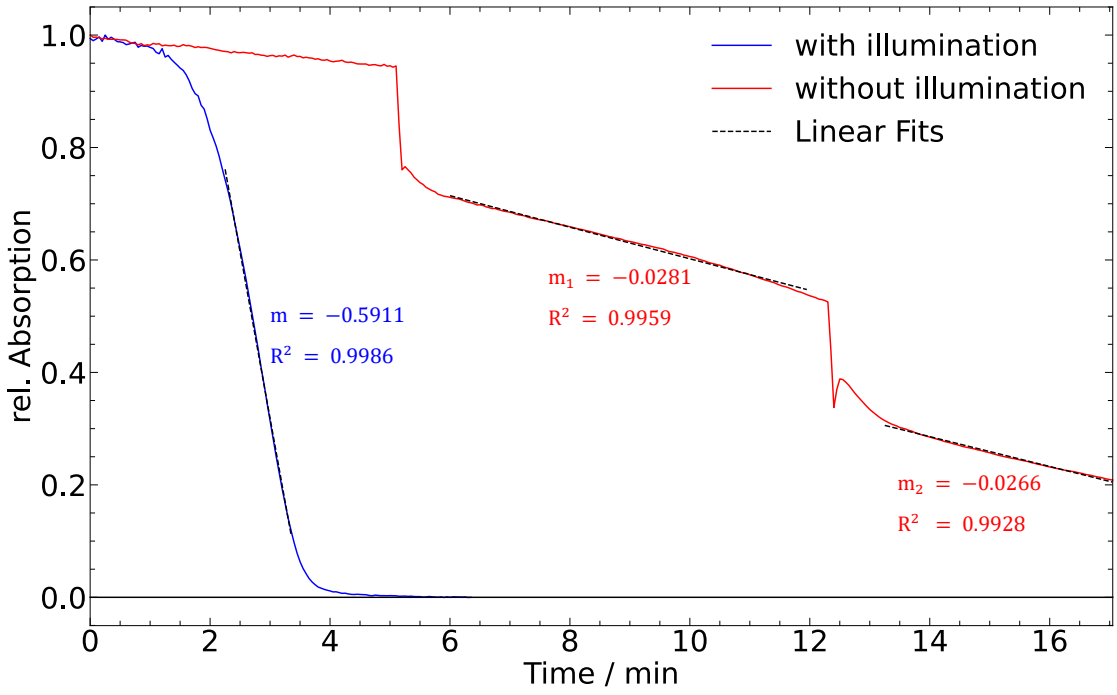

Figure 45. Time-resolved oxygen induced decomposition of **H-PBI** measured at 380 nm in THF. The experiment was conducted under continuous irradiation at 385 nm (blue) and with only two light pulses (red). The slope m represents the reaction rate in min^{-1} based on the relative absorption of the species.

To further assess the impact of irradiation, additional experiments were conducted varying the radiation power (Figure 46). The radiant flux was measured before each experiment using a power meter, with the sample positioned at a distance corresponding to a maximum power of 550 mW, denoted as 100% in subsequent analyses. The signal decreased with a similar rate between 100% and 25% power indicating, that the reaction is diffusion-controlled (Table 19). Lowering the power further showed a significant decrease in the rate, indicating a change in the rate-determining step. However, even at 1% power, the assumingly oxidation reaction completes within 10–12 minutes.

Table 19. Reaction rates for the oxidation of **H-PBI** in MeCN, by varying the radiation power. The reaction rates are based on the relative absorption of the species (Figure 46).

Species	Radiation power / %	reaction rate / min^{-1}	Coefficient of determination
H-PBI	100	$1.261 \pm 6x10^{-3}$	0.9991
	50	$1.629 \pm 1x10^{-3}$	0.9975
	25	$1.379 \pm 1x10^{-3}$	0.9963
	10	$0.541 \pm 5x10^{-3}$	0.9990
	5	$0.486 \pm 4x10^{-3}$	0.9995
	1	$0.299 \pm 8x10^{-3}$	0.9824

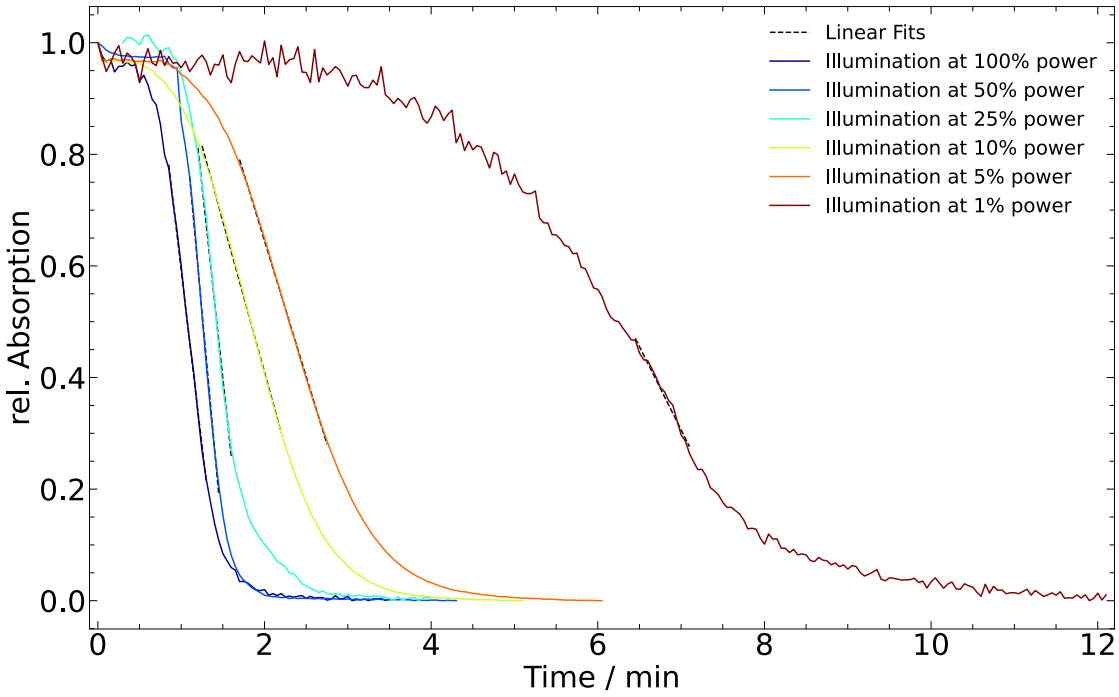

Figure 46. Time-resolved oxygen induced decomposition of **H-PBI** measured at 380 nm in MeCN. The experiment was conducted at different irradiation powers referring 550 mW as 100%.

To gain further insights into the decomposition of the substrate, the **H-PBI** sample was diluted in THF and exposed to air for 1 hour under stirring. Subsequently, methylbenzoate **108** and thiazolone **109** were identified as the decomposition products by NMR and high-resolution mass spectrometry (HRMS) measurements.

Additionally, the calculated absorption spectra of the species indicate a maximum absorption in the 200–250 nm region, which is consistent with the experimental UV-vis absorption spectra (Figure 47).

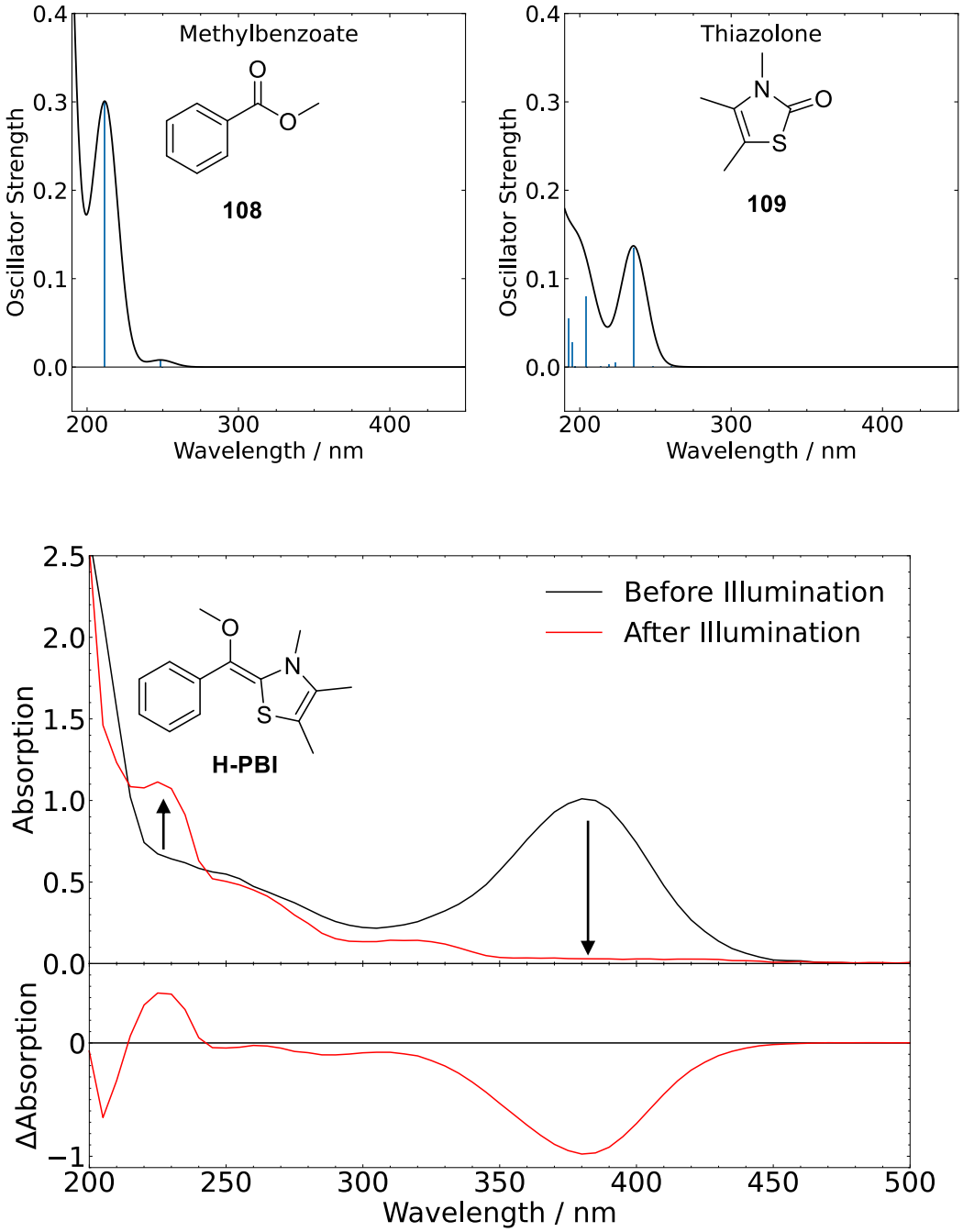

Figure 47. Top: Calculated absorption spectra of the decomposition products **108** and **109** formed by the exposure of the **H-PBI** with air. Bottom: Experimental UV-vis spectrum of the time-dependent decomposition of the **H-PBI** exposed to air.

The necessity of initiating the decomposition reaction with a short light pulse, particularly when not further irradiating it, suggests a radical chain mechanism. The proposal suggests that the reaction initiation involves the formation of a superoxide and a radical cation, akin to the ketyl radical proposed by our group in 2015 (see Chapter 1.4).[152]

The excitation of the protected Breslow-intermediate **95** enhances its oxidation potential, facilitating the formation of the superoxide. Oxygen is reduced to superoxide at a potential of -0.75 V (vs. S.C.E.), while cyclovoltammetric studies by Phan *et al*. show that the peak potential of **H-PBI** is at -1.07 V.[206,209] Hence, while a redox reaction is feasible in the ground state, excitation of the species further enhances this process (see Chapter 1.3).

Subsequently, the ketyl radical **110** reacts with triplet oxygen in a radical/radical cross-coupling reaction. The peroxide radical **111** propagates the reaction by forming a superoxide **112** and inducing a ketyl radical **110** through interaction with another protected Breslow-intermediate **95**. The superoxide **112** then forms an endoperoxide **113**, which upon opening yields the determined decomposition products **108** and **109**. The radical chain terminates when the superoxide reacts with a ketyl radical cation **110** forming the biradical **114** (Scheme 42).

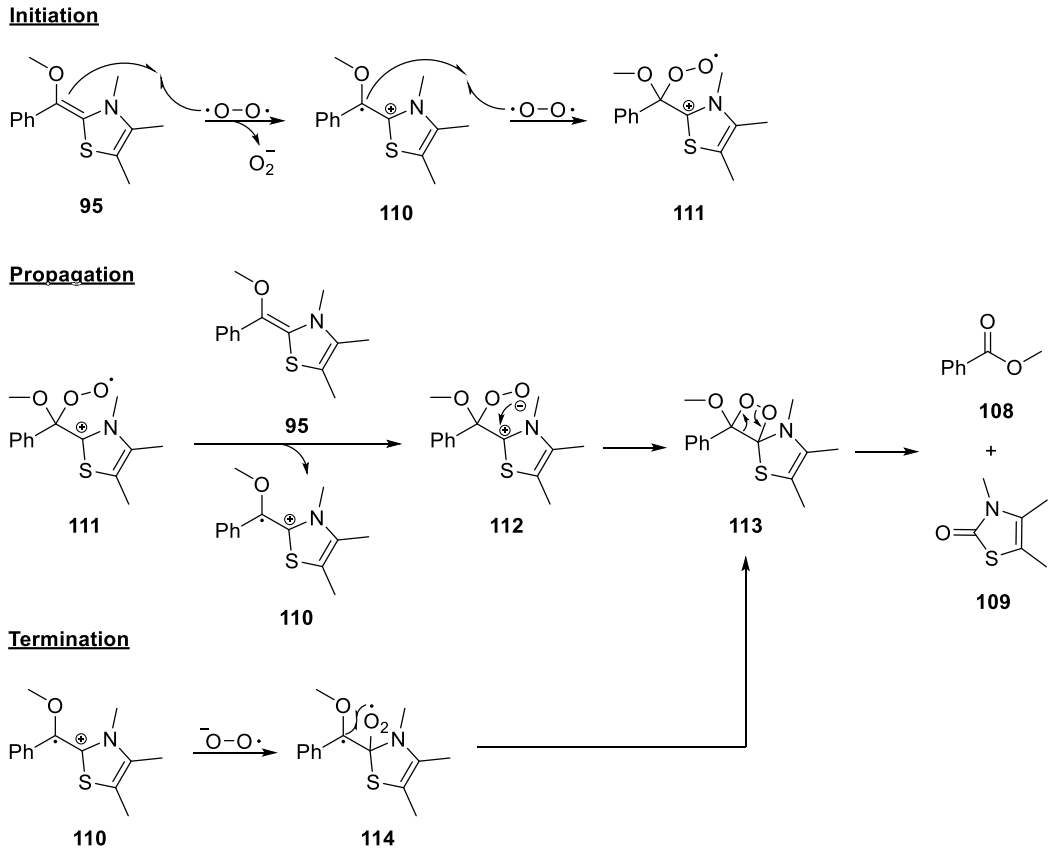

Scheme 42. Proposed radical chain reaction of the oxygen-induced decomposition of **H-PBI**.

In the case of continuous irradiation, the reaction proceeds significantly faster, which can be explained in different ways. Either the reaction occurs analogously to the described radical chain mechanism, with the change in reaction speed attributed to a higher radical concentration,

or irradiation generates oxygen in the singlet state. Singlet oxygen is considerably more reactive than its triplet analog and can directly form an endoperoxide with the protected Breslow-intermediate. It is also plausible that both mechanisms occur simultaneously (Scheme 43).[210]

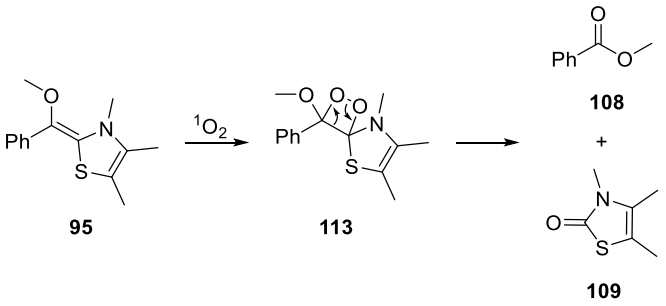

Scheme 43. Proposed oxygen-induced decomposition of **H-PBI** with oxygen in the singlet state.

To investigate the potential involvement of singlet oxygen, additional oxidation experiments were conducted analogous to previous ones, but this time using deuterated acetonitrile during the irradiation. This choice was motivated by the significantly longer lifetime of singlet oxygen in MeCN-d_3 (1631 µs at 25 °C) compared to MeCN-H_3 (90 µs at 25 °C).[211] As the reaction rate of the singlet oxygen with its acceptor competes with its unimolecular decay rate, a significantly faster oxidation of the respective species was anticipated.[207,210] Experiments at radiation powers of 100% (550 mW), 10% (55 mW), and 5% (27 mW) were conducted, comparing the results with those presented in Table 19. Surprisingly, the reaction rates were similar, showing no significant deviation from those measured in MeCN-H_3 (Table 20). Thus, it follows that singlet oxygen is not involved in the oxidation, and the observed increase in rate during irradiation likely stems from an enhanced formation of radicals, as proposed in Scheme 42.

Table 20. Reaction rates for the oxidation of **H-PBI** in MeCN-H_3 and MeCN-d_3 at different radiation power. The reaction rates are based on the relative absorption of the species.

Species	**Radiation power / %**	**reaction rate / min^{-1}**	
		MeCN-H_3	**MeCN-d_3**
H-PBI	100	$1.261 \pm 6x10^{-3}$	$1.37 \pm 1x10^{-2}$
	10	$0.541 \pm 5x10^{-3}$	$0.58 \pm 1x10^{-2}$
	5	$0.486 \pm 4x10^{-3}$	$0.518 \pm 7x10^{-3}$

However, in a photocatalytic reaction, where the Breslow-intermediate is sensitized into a triplet state species, the possibility of a direct radical/radical chain reaction with oxygen in the triplet state also becomes highly probable. Consequently, it is strongly advised to conduct all reactions involving cooperative catalysis, incorporating NHC and photocatalysis, under inert conditions to prevent unwanted decomposition reactions induced by oxygen.

3.3.4 Intramolecular H-Atom-Transfer in Protected Breslow-Intermediates

In 2019, the Hopkinson group reported a photoenolization Diels-Alder reaction of acid fluorides and trifluoroacetophenones. The mechanism involved a nucleophilic attack of an NHC on the acid fluoride, resulting in an addition-elimination reaction that released fluoride and formed an *ortho*-toluoyl azolium intermediate. Upon direct excitation of the species with blue light, it is proposed to undergo an ISC into the T_1 state, followed by an intramolecular 1,5-hydrogen atom transfer (HAT) from the *ortho*-benzylic position to the radical-like oxygen. A subsequent relaxation leads to the diene formation, which can be trapped via a cyclization reaction. The catalytic cycle concludes with the release of the NHC species (Scheme 44).[212]

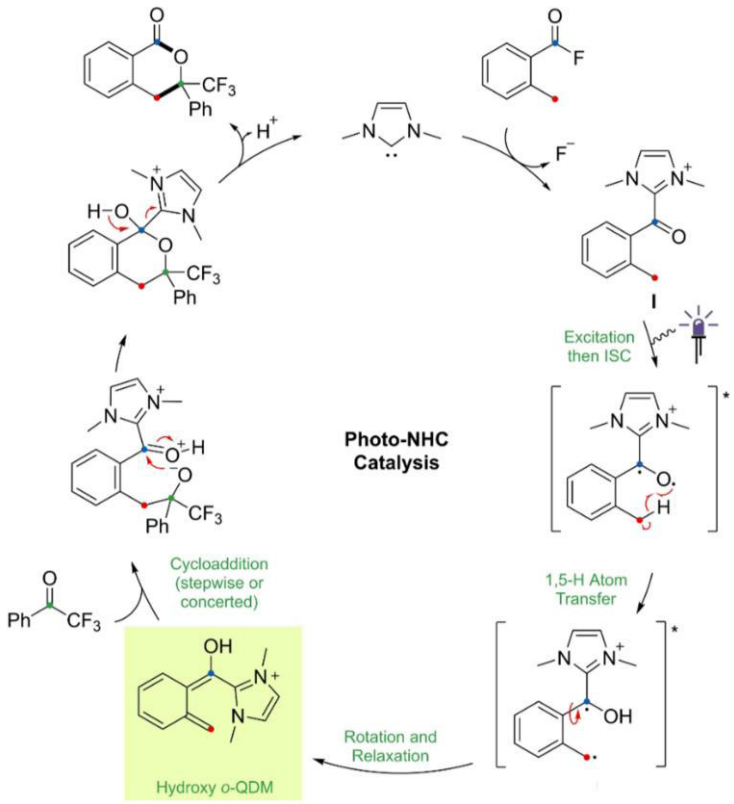

Scheme 44. NHC-catalyzed photoenolization/Diels-Alder reaction of acid fluorides with trifluoroacetophenones. The scheme was taken from *ChemPhotoChem.* **2020**, *4*, 5147–5153 and adjusted.[212]

Inspired by these findings, the aim was to develop a similar system based on an oxidative photocatalytic NHC cycle involving the Breslow-intermediate (see Chapter 1.4). To achieve this, a protected Breslow-intermediate **DiMe-PBI** was introduced, utilizing a 2,6-dimethylphenyl group as the aryl system (Figure 48).

Protected Breslow-intermediate

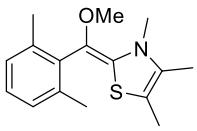

DiMe-PBI
115

Figure 48. Protected Breslow-intermediate used in HAT reaction experiments.

Assuming that the excitation of **DiMe-PBI** via light undergoes an ISC to a triplet state, similar to Hopkinson's system, either a radical 1,4-HAT or a 1,5-HAT can be anticipated, as depicted in Scheme 45.

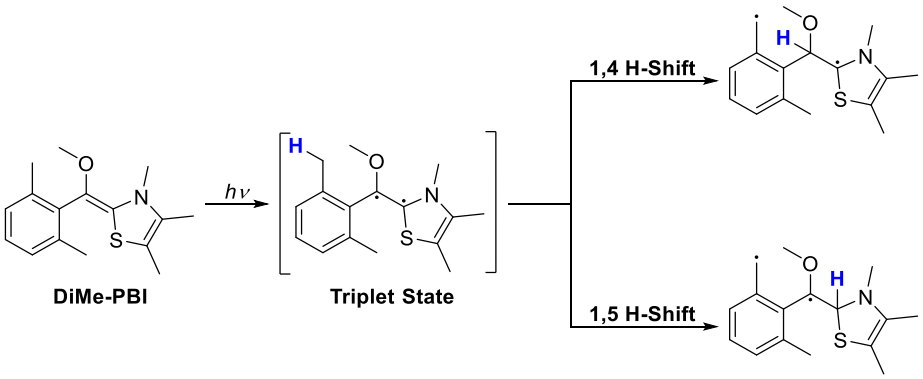

Scheme 45. Possible HAT reactions of the **DiMe-PBI**.

Computational calculations favor a 1,5-HAT with a barrier of 24.7 kcal/mol over a 1,4-HAT with a higher barrier of 32.8 kcal/mol. The transition state of the 1,5-HAT adopts a six-membered half-chair conformation (Figure 49). Although the barrier is too high to occur at room temperature, it becomes feasible at higher temperatures, such as 40 °C, in line with the reaction parameters used by Hopkinson and co-workers.

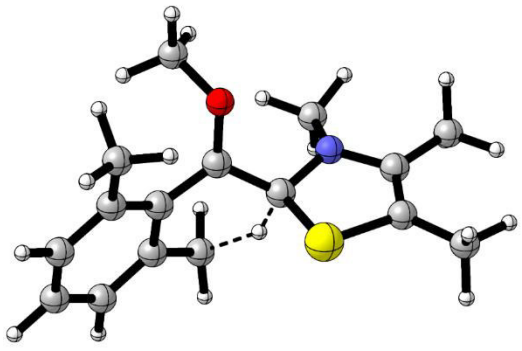

Figure 49. Transition state of the 1,5-HAT of the **DiMe-PBI** in the triplet state. Calculated in the Gaussian 16 program package using uB3LYP/6-31g(d) as method and basis set.

However, during transient absorption spectroscopy conducted on a 100 µs timescale, a strong GSB signal was observed but only a weak absorption signal (Figure 50). The ratio of the integral of the negative signal to the integral of the positive signal (moving average DADS) is only 6%. This suggests the occurrence of a photochemical reaction, likely the discussed 1,5-HAT. Therefore, it is possible that the intramolecular hydrogen shift occurred via the more reactive excited singlet state of **DiMe-PBI**. The barrier for such a reaction was not calculated due to the demanding computational effort necessitating TDDFT methods.

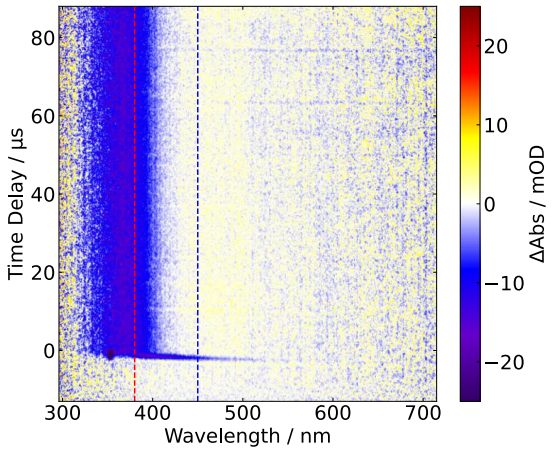

Figure 50. Transient absorption map of **DiMe-PBI** on a 100 µs timescale. The red line at 380 nm marks the peak of the constant negative signal and the blue line at 450 nm marks the peak of the newly formed positive signal. The absorption maximum of **DiMe-PBI** is at 370 nm.

Hence, it can be concluded that *o*-substituted aldehydes employed in NHC catalysis can undergo intramolecular hydrogen atom transfer (HAT) reactions when engaging in cooperative photocatalysis reactions.

4. Summary and Outlook – Part C

In summary, the investigation into the photophysical properties and reactivity mechanisms of protected Breslow-intermediates has revealed several key findings.

Photophysical Properties

Through computational calculations and experimental measurements, we have gained quantitative data regarding the UV-vis absorption and emission, the lifetime of the excited species, and the photophysical and solvent-induced influences on the diastereomer ratios of the respective protected Breslow-intermediates. Our theoretical and experimental findings indicate that the *Z*-isomer is thermodynamically favored product due to its reduced steric hindrance. However, irradiation with blue light can shift the ratio toward the *E*-isomer. This shift occurs because, in its electronically excited state, the respective double bond is weakened, allowing the molecule to freely rotate. Additionally, UV-vis absorption experiments and corresponding calculations showed that the probability of exciting the *Z*-isomer with the LED used is higher, leading to an enrichment of the *E*-isomer.

Air Sensitivity

Furthermore, the mechanistical investigations, regarding oxygen during the irradiation of the protected Breslow-intermediates, revealed a possible radical chain mechanism leading to the decomposition of the respective species. Therefore, we advise performing photochemical reactions involving Breslow-intermediates exclusively under inert conditions.

Intramolecular H-Atom-Transfer

Moreover, the investigation into the reactivity mechanisms under photochemical conditions has revealed insights into intramolecular hydrogen atom transfer (HAT) processes. By combining transient absorption spectroscopy with computational modeling, we have proposed potential pathways for HAT reactions on suitable substrates. These findings suggest opportunities for the application of protected Breslow-intermediates in catalytic processes.

Conclusion

Overall, the research contributes to understanding the fundamental properties and reactivity pathways of Breslow-intermediates. By elucidating their photophysical behavior and reactivity towards basic conditions, a groundwork for their rational design and application in various catalytic transformations was laid. Moving forward, further studies exploring their applications in synthetic chemistry hold promise for advancing the field of catalysis and enabling the development of more efficient and sustainable chemical processes.

D. Experimental Part

1. General Information

Chemicals and Solvents

Commercially available chemicals were purchased in high quality and were used without further purification unless otherwise stated. All reactions were carried out in flame dried glassware under an atmosphere of predried nitrogen unless otherwise stated. Solvents were either distilled before use or were available in p.a. quality. Anhydrous solvents were prepared by a solvent purification system or, if not available, by established laboratory procedures.[213] The water content was controlled by Karl Fischer titration. The THF used in synthesis and spectroscopic experiments contained no radical stabilizer. All bases were titrated before use, to determine the respective concentration. The reported yields are referred to the isolated compounds unless otherwise stated.

Chromatography

Thin layer chromatography was performed with TLC precoated aluminum sheets (Merck) Silica gel 60 F254, 0.2 mm layer thickness. Visualization was done with UV light ($\lambda = 254$ nm). Column chromatography was performed with flash silica gel 60 (Merck, 0.040–0.063 mm particle size).

NMR-Spectroscopy

^{1}H NMR spectra were recorded on FT-NMR-spectrometer of the type Bruker Avance 300 (300 MHz for ^{1}H, 75 MHz for ^{13}C, 282 MHz) or BRUKER Avance III 400 "Nanobay" (400 MHz for ^{1}H, 100 MHz for ^{13}C). Chemical shifts for ^{1}H NMR were reported as δ, parts per million (ppm), relative to the center line signal of $CHCl_3$ at 7.26 ppm, benzene at 7.16 ppm, MeCN at 1.94 ppm, THF at 1.72 ppm and DMSO at 2.50 ppm. Spectra were evaluated in 1st order and coupling constants *J* were reported in Hertz (Hz). The following notations indicate the multiplicity of the signals: s = singlet, bs = broad singlet, d = doublet, t = triplet, q = quartet, p = quintet, sex = sextet, sept = septet, and m = multiplet, and combinations thereof. Chemical shifts for ^{13}C NMR were reported as δ, parts per million (ppm), relative to the center line signal of $CDCl_3$ at 77.16 ppm, benzene-d_6 at 128.06 ppm and DMSO-d_6 at 39.70 ppm. The MestReNova software was used to analyze and visualize the NMR data.

Mass Spectrometry

High-resolution mass spectra were recorded at the Central Analytical Laboratory of the University of Regensburg using a Jeol AccuTOF GCX system with electron ionization (EI) as the ion source.

2. Experimental Procedures

(4,5-dimethylthiazol-2-yl)(phenyl)methanol 116

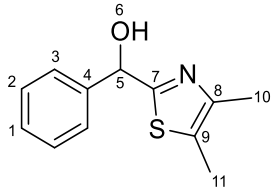

116

4,5-dimethylthiazole (0.42 mL, ρ = 1.07 g/cm^3, 4.0 mmol, 1.10 equiv.) was diluted in 3.5 mL anhydrous THF. After the solution was cooled to -50 °C, *t*-BuLi (1.7 mL, 2.4 mol/L, 4.1 mmol, 1.10 equiv.) was added dropwise over 10 min. The reaction mixture was stirred for 45 minutes at -50 °C. Freshly distilled benzaldehyde (ρ = 1.07 g/cm^3, 0.37 mL, 3.6 mmol, 1 equiv.) was diluted in 2.0 mL anhydrous THF and added to the reaction mixture. The reaction mixture was stirred for 30 minutes at -50 °C and 90 minutes at room temperature. The reaction was quenched by adding 6 mL ammonium chloride solution. The organic phase was extracted with diethyl ether (3x 6 mL) After removal of the solvent under reduced pressure, the solid crude product was washed with hexanes (3x 1.5 mL). The title compound was obtained as yellow solid (728 mg, 3.3 mmol, 92%).

^{1}H-NMR (400 MHz, $CDCl_3$) δ / ppm = 7.46 (m, 2H, H-3), 7.34 (m, 3H, H-1, H-2), 5.93 (s, 1H, H-5), 4.59 (bs, 1H, H-6), 2.27 (s, 3H, H-10), 2.25 (s, 3H, H-11).

^{13}C-NMR (101 MHz, $CDCl_3$) δ / ppm = 169.56 (C-7), 147.45 (C-8), 141.83 (C-4), 128.57 (C-2), 128.22 (C-1), 127.14 (C-9), 126.54 (C-3), 73.41 (C-5), 14.51 (C-10), 11.31 (C-11).

(4,5-dimethylthiazol-2-yl)(4-methoxypheny)methanol 117

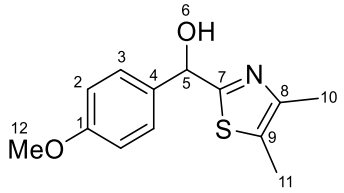

117

4,5-dimethylthiazole (3.6 mL, ρ = 1.07 g/cm^3, 34.0 mmol, 1.2 equiv.) was diluted in 27 mL anhydrous THF. After the solution was cooled to -78 °C, *n*-BuLi (20.4 mL, 1.6 mol/L, 32.6 mmol, 1.05 equiv.) was added dropwise over 10 min. The reaction mixture was stirred for 10 minutes at -78 °C. Freshly distilled *p*-Anisaldehyde, (2.8 mL, ρ = 1.12 g/cm^3, 27.4 mmol, 1 equiv.) was diluted in 14 mL anhydrous THF and added to the reaction mixture. The reaction mixture was stirred for 10 minutes at -78 °C and 60 minutes at room temperature. The reaction was quenched by adding 50 mL ammonium chloride solution. The organic phase was extracted with diethyl ether (3x 50 mL). After removal of the solvent under reduced pressure, the solid crude product was washed with a boiling mixture of hexanes and diethyl ether in a ratio of 1:1 (50 mL). The title compound was obtained as white solid (3.19 g, 12.8 mmol, 38%).

^{1}H-NMR (400 MHz, $CDCl_3$) δ / ppm = 7.38 (m, 2H, H-3), 6.89 (m, 2H, H-2), 5.88 (d, *J* = 2.9 Hz, 1H, H-5), 3.80 (s, 3H, H-12), 3.45 (d, *J* = 3.2 Hz, 1H, H-6), 2.29 (m, 6H, H-10, H-11).

^{13}C-NMR (101 MHz, $CDCl_3$) δ / ppm = 169.11 (C-7), 159.67 (C-1) ,147.51 (C-8), 134.00 (C-9), 127.97 (C-3), 127.13 (C-4) 114.03 (C-2), 73.43 (C-5), 55.29 (C-12), 14.64 (C-10), 11.33 (C-11).

The synthesis was performed by Alberto Núñez as research assistant.

(4-chlorophenyl)(4,5-dimethylthiazol-2-yl)methanol 118

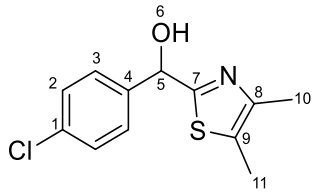

118

4,5-dimethylthiazole (1.87 mL, ρ = 1.07 g/cm^3, 17.67 mmol, 1.05 equiv.) was diluted in 12 mL anhydrous THF. After the solution was cooled to -50 °C, *t*-BuLi (7.60 mL, 2.3 mol/L, 17.7 mmol, 1.05 equiv.) was added dropwise over 10 min. The reaction mixture was stirred for 30 minutes at -50 °C. Freshly distilled *p*-chlorobenzaldehyde (2.37 g, 16.8 mmol, 1 equiv.) was diluted in 5 mL anhydrous THF and added to the reaction mixture. The reaction mixture was stirred for 30 minutes at -50 °C and 90 minutes at room temperature. The reaction was quenched

by adding 25 mL ammonium chloride solution. The organic phase was extracted with diethyl ether (3x 25 mL). After removal of the solvent under reduced pressure, the solid crude product was filtered through silica gel (5 cm) with hexanes (300 mL) and hexanes / ethyl acetate = 10:1 (300 mL). After elution with ethyl acetate, the solvent was removed under reduced pressure. The title compound was obtained as yellow solid (2.80 g, 11.0 mmol, 65%).

^{1}H-NMR (400 MHz, $CDCl_3$) δ / ppm = 7.40 (m, 2H, H-3), 7.33 (m, 2H, H-2), 5.91 (s, 1H, H-5), 4.16 (bs, 1H, H-6), 2.28 (m, 3H, H-10), 2.27 (m, 3H, H-11).

^{13}C-NMR (101 MHz, $CDCl_3$) δ / ppm = 169.59 (C-7), 147.60 (C-8), 140.21 (C-4), 134.09 (C-1), 128.78 (C-2), 127.93 (C-3), 127.45 (C-9), 72.86 (C-5), 14.55 (C-10), 11.33 (C-11).

(2,6-dimethylphenyl)(4,5-dimethylthiazol-2-yl)methanol 119

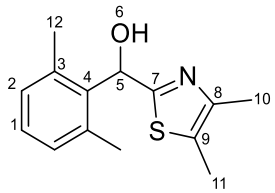

119

4,5-dimethylthiazole (4.0 mL, ρ = 1.07 g/cm^3, 37.8 mmol, 1.05 equiv.) was diluted in 23 mL anhydrous THF. After the solution was cooled to -50 °C, *t*-BuLi (21.0 mL, 1.8 mol/L, 37.8 mmol, 1.05 equiv.) was added dropwise over 10 min. The reaction mixture was stirred for 90 minutes at -50 °C. Freshly distilled 2,6-dimethylbenzaldehyde (4.82 g, 36.0 mmol, 1 equiv.) was diluted in 25 mL anhydrous THF and added to the reaction mixture. The reaction mixture was stirred for 30 minutes at -50 °C and 60 minutes at room temperature. The reaction was quenched by adding 50 mL ammonium chloride solution. The organic phase was extracted with diethyl ether (3x 50 mL). After removal of the solvent under reduced pressure, the solid crude product was with hexanes (300 mL). The title compound was obtained as white solid (4.68 g, 18.9 mmol, 53%).

^{1}H-NMR (400 MHz, $CDCl_3$) δ / ppm = 7.13 (d, $^{3}J_{H,H}$ = 7.6 Hz, 1H, H-1), 7.02 (d, $^{3}J_{H,H}$ = 7.6 Hz, 2H, H-2), 6.32 (s, 1H, H-5), 4.46 (bs, 1H, H-6), 2.34 (s, 6H, H-12), 2.31 (s, 3H, H-10), 2.27 (s, 3H, H-11).

^{13}C-NMR (101 MHz, $CDCl_3$) δ / ppm = 169.05 (C-7), 147.27 (C-8), 137.44 (C-3), 137.15 (C-4), 129.30 (C-2), 128.35 (C-1), 126.96, (C-9) 69.89 (C-5), 20.60 (C-12), 14.62 (C-10), 11.31 (C-11).

HRMS (EI+, 70 eV): calcd. for $C_{14}H_{17}NOS^{\cdot+}$ = 247.1031 found 247.1029.

(2-(methoxy(phenyl)methyl)-4,5-dimethylthiazole 120

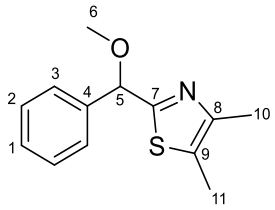

120

A suspension of NaH (123 mg, 60% (w/w), 3.1 mmol, 1.1 equiv.) in 2.5 mL anhydrous THF was prepared. After the suspension was cooled to 0 °C, the carbinol **116** (507 mg, 2.79 mmol, 1 equiv.) was diluted in 2.3 mL anhydrous THF and added dropwise to the reaction mixture. The reaction mixture was stirred for 10 minutes at 0 °C. MeI (0.15 mL, ρ = 2.28 g/cm^3, 2.39 mmol, 1.05 equiv.) was added dropwise at 0 °C. The solution was allowed to warm up to room temperature and stirred for 18 h. The reaction was quenched by adding 6.5 mL ammonium chloride solution. The organic phase was extracted with dichloromethane (3x 12 mL). After removal of the solvent under reduced pressure, the title compound was obtained as white solid (512 mg, 239 mmol, 95%).

^{1}H-NMR (400 MHz, $CDCl_3$) δ / ppm = 7.45 (m, 2H, H-3), 7.35 (m, 2H, H-2), 7.30 (m, 1H, H-1), 5.46 (s, 1H, H-5), 3.45 (s, 3H, H-6), 2.29 (m, 6H, H-10, H-11).

^{13}C-NMR (101 MHz, $CDCl_3$) δ / ppm = 167.44 (C-7), 147.74 (C-8), 139.91 (C-4), 128.58 (C-2), 128.19 (C-1), 127.13 (C-9), 126.79 (C-3), 83.13 (C-5), 57.38 (C-6), 14.72 (C-10), 11.35 (C-11).

(2-(methoxy(phenyl)methyl)-4,5-dimethylthiazole 121

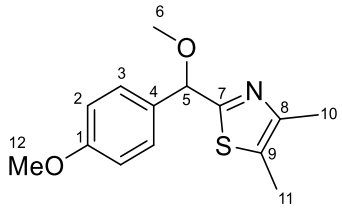

121

A suspension of NaH (690 mg, 60% (w/w), 17.3 mmol, 1.1 equiv.) in 14 mL anhydrous THF was prepared. After the suspension was cooled to 0 °C, the carbinol **117** (3.44 g, 15.7 mmol, 1 equiv.) was diluted in 13 mL anhydrous THF and added dropwise to the reaction mixture. The reaction mixture was stirred for 10 minutes at 0 °C. MeI (1.03 mL, ρ = 2.28 g/cm^3, 16.5 mmol, 1.05 equiv.) was added dropwise at 0 °C. The solution was allowed to warm up to room temperature and stirred for 18 h. The reaction was quenched by adding 35 mL ammonium chloride solution. The organic phase was extracted with dichloromethane (3x 50 mL). After removal of the solvent under reduced pressure, the title compound was obtained as white solid (2.48 g, 9.4 mmol, 65%).

^{1}H-NMR (400 MHz, $CDCl_3$) δ / ppm = 7.36 (m, 2H, H-3), 6.88 (m, 2H, H-2), 5.41 (s, 1H, H-5), 3.79 (s, 3H, H-12), 3.42 (s, 1H, H-6), 2.29 (s, 3H, H-10), 2.28 (s, 3H, H-11).

^{13}C-NMR (101 MHz, $CDCl_3$) δ / ppm = 167.80 (C-7), 159.53 (C-1), 147.73 (C-8), 132.04 (C-9), 128.16 (C-3), 126.91 (C-4) 113.97 (C-2), 82.72 (C-5), 57.20 (C-6), 55.26 (C-12), 14.72 (C-10), 11.34 (C-11).

The synthesis was performed by Alberto Núñez as research assistant.

2-((4-chlorophenyl)(methoxy)methyl)-4,5-dimethylthiazole 122

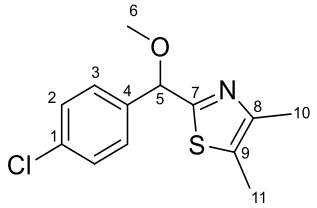

122

A suspension of NaH (488 mg, 60% (w/w), 12.1 mmol, 1.1 equiv.) in 12 mL anhydrous THF was prepared. After the suspension was cooled to 0 °C, the carbinol **118** (2.80 g, 11.0 mmol, 1 equiv.) was diluted in 10 mL anhydrous THF and added dropwise to the reaction mixture. The reaction mixture was stirred for 10 minutes at 0 °C. MeI (0.72 mL, ρ = 2.28 g/cm^3, 11.6 mmol, 1.05 equiv.) was added dropwise at 0 °C. The solution was allowed to warm up to room temperature and stirred for 20 h. The reaction was quenched by adding 30 mL ammonium chloride solution. The organic phase was extracted with dichloromethane (3x 50 mL). After removal of the solvent under reduced pressure, the title compound was obtained as white solid (2.77 g, 10.3 mol, 97%).

^{1}H-NMR (400 MHz, $CDCl_3$) δ / ppm = 7.38 (m, 2H, H-3), 7.32 (m, 2H, H-2), 5.43 (s, 1H, H-5), 3.44 (s, 3H, H-6), 2.30 (s, 3H, H-10), 2.28 (s, 3H, H-11).

^{13}C-NMR (101 MHz, $CDCl_3$) δ / ppm = 166.92 (C-7), 147.89 (C-8), 138.47 (C-4), 133.97 (C-1), 128.75 (C-2), 128.13 (C-3), 127.29 (C-9), 82.41 (C-5), 57.41 (C-6), 14.70 (C-10), 11.35 (C-11).

2-((2,6-dimethylphenyl)(methoxy)methyl)-4,5-dimethylthiazole 123

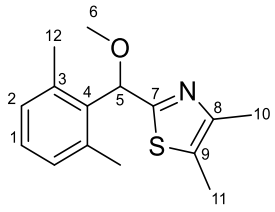

123

A suspension of NaH (800 mg, 60% (w/w), 20.1 mmol, 1.1 equiv.) in 15 mL anhydrous THF was prepared. After the suspension was cooled to 0 °C, the carbinol **119** (4.50 g, 18.2 mmol, 1 equiv.) was diluted in 20 mL anhydrous THF and added dropwise to the reaction mixture. The reaction mixture was stirred for 10 minutes at 0 °C. MeI (1.19 mL, ρ = 2.28 g/cm^3, 19.1 mmol, 1.05 equiv.) was added dropwise at 0 °C. The solution was allowed to warm up to room temperature and stirred for 18 h. The reaction was quenched by adding 35 mL ammonium chloride solution. The organic phase was extracted with dichloromethane (3x 75 mL). After removal of the solvent under reduced pressure, the title compound was obtained in quantitative yield as colorless oil (4.69 g, 17.9 mmol).

^{1}H-NMR (400 MHz, $CDCl_3$) δ / ppm = 7.13 (d, $^3J_{H,H}$ = 7.6 Hz, 1H, H-1), 7.02 (d, $^3J_{H,H}$ = 7.6 Hz, 2H, H-2), 6.32 (s, 1H, H-5), 4.46 (bs, 1H, H-6), 2.34 (s, 6H, H-12), 2.31 (s, 3H, H-10), 2.27 (s, 3H, H-11).

^{13}C-NMR (101 MHz, $CDCl_3$) δ / ppm = 169.05 (C-7), 147.27 (C-8), 137.44 (C-3), 137.15 (C-4), 129.30 (C-2), 128.35 (C-1), 126.96, (C-9) 69.89 (C-5), 20.60 (C-12), 14.62 (C-10), 11.31 (C-11).

HRMS (EI+, 70 eV): calcd. for $C_{15}H_{19}NOS^{\cdot+}$ = 261.1187 found 261.1173.

2-(methoxy(phenyl)methyl)-3,4,5-trimethylthiazol-3-ium tetrafluoroborate 124

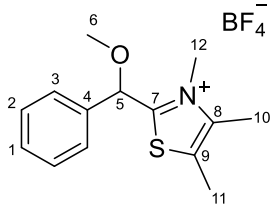

124

The ether **120** (476.1 mg, 2.0 mmol, 1 equiv.) was diluted in 4 mL anhydrous DCM. After the solution was cooled to 0 °C, trimethyloxonium tetrafluoroborate (302 mg, 2.0 mmol, 1 equiv.) was added to the reaction mixture. The solution was allowed to warm up to room temperature and stirred for 18 h. After removal of the solvent under reduced pressure, the crude product was dissolved in ethyl acetate (5 mL) and extracted with water (2x 10 mL). The aqueous phase was extracted with dichloromethane (3x 20 mL). After removal of the solvent under reduced

pressure, the title compound was obtained in quantitative yield as white solid (684 mg, 2.0 mmol).

^{1}H-NMR (400 MHz, $CDCl_3$) δ / ppm = 7.43 (s, 5H, H-1, H-2, H-3), 5.90 (s, 1H, H-5), 3.81 (s, 3H, H-12), 3.43 (s, 3H, H-6), 2.43 (s, 3H, H-10), 2.38 (s, 3H, H-11).

^{13}C-NMR (101 MHz, $CDCl_3$) δ / ppm = 172.15 (C-7), 143.96 (C-8), 134.04 (C-1), 130.83 (C-4), 130.41 (C-9), 129.58 (C-2), 128.34 (C-3), 78.72 (C-5), 57.60 (C-6), 38.21 (C-12), 12.22 (C-10), 11.99 (C-11).

2-(methoxy(4-methoxyphenyl)methyl)-3,4,5-trimethylthiazol-3-ium tetrafluoroborate 125

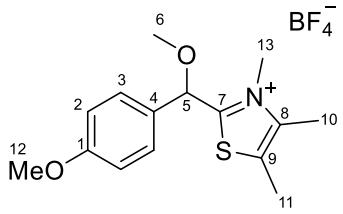

125

The ether **121** (4.94 g, 18.7 mmol, 1 equiv.) was diluted in 4 mL anhydrous DCM. After the solution was cooled to 0 °C, trimethyloxonium tetrafluoroborate (2.77 g, 18.7 mmol, 1 equiv.) was added to the reaction mixture. The solution was allowed to warm up to room temperature and stirred for 18 h. After removal of the solvent under reduced pressure, the crude product was washed with boiling hexanes (3x 15 mL). After removal of the solvent residues under reduced pressure, the title compound was obtained in quantitative yield as brown solid (5.65 g, 15.5 mmol, 83%).

^{1}H-NMR (400 MHz, $CDCl_3$) δ / ppm = 7.32 (m, 2H, H-3), 6.91 (m, 2H, H-2), 5.79 (s, 1H, H-5), 3.77 (s, 3H, H-12), 3.75 (s, 3H, H-13), 3.37 (s, 3H, H-6), 2.41 (s, 3H, H-10), 2.34 (s, 3H, H-11).

^{13}C-NMR (101 MHz, $CDCl_3$) δ / ppm = 172.46 (C-7), 161.00 (C-1), 143.88 (C-8), 130.73 (C-9), 129.81 (C-3), 125.80 (C-4), 114.91 (C-2), 78.30 (C-5), 57.21 (C-6), 55.44 (C-12), 38.03 (C-13), 12.13 (C-11), 11.88 (C-10).

The synthesis was performed by Alberto Núñez as research assistant.

2-((4-chlorophenyl)(methoxy)methyl)-3,4,5-trimethylthiazol-3-ium tetrafluoroborate 126

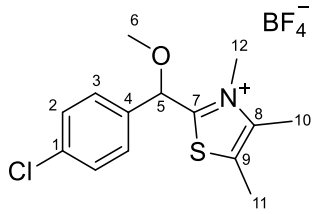

126

The ether **122** (2.77 g, 10.3 mmol, 1 equiv.) was diluted in 55 mL anhydrous DCM. After the solution was cooled to 0 °C, trimethyloxonium tetrafluoroborate (1.53 g, 10.3 mmol, 1 equiv.) was added to the reaction mixture. The solution was allowed to warm up to room temperature and stirred for 18 h. After removal of the solvent under reduced pressure, the crude product was washed with diethyl ether (5x 10 mL). After removal of the solvent under reduced pressure, the title compound was obtained as white solid (3.74 g, 10.1 mmol, 98%).

^{1}H-NMR (400 MHz, $CDCl_3$) δ / ppm = 7.45 (m, 4H, H-2, H-3), 5.97 (s, 1H, H-5), 3.89 (s, 3H, H-12), 3.48 (s, 3H, H-6), 2.45 (s, 3H, H-10), 2.41 (s, 3H, H-11).

^{13}C-NMR (101 MHz, $CDCl_3$) δ / ppm = 171.77 (C-7), 144.15 (C-8), 136.55 (C-4), 132.69 (C-1), 130.79 (C-9), 129.84 (C-2), 129.74 (C-3), 77.74 (C-5), 57.81 (C-6), 38.42 (C-12), 12.29 (C-10), 12.12 (C-11).

2-((2,6-dimethylphenyl)(methoxy)methyl)-3,4,5-trimethylthiazol-3-ium tetrafluoroborate 127

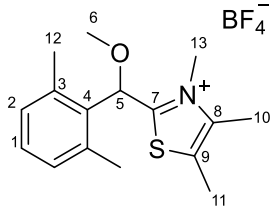

127

The ether **123** (4.69 g, 17.9 mmol, 1 equiv.) was diluted in 35 mL anhydrous DCM. After the solution was cooled to 0 °C, trimethyloxonium tetrafluoroborate (2.65 g, 17,9 mmol, 1 equiv.) was added to the reaction mixture. The solution was allowed to warm up to room temperature and stirred for 18 h. After removal of the solvent under reduced pressure, the crude product was dissolved in ethyl acetate (15 mL) and extracted with water (2x 30 mL). The aqueous phase was extracted with dichloromethane (3x 60 mL). After removal of the solvent under reduced pressure, the title compound was obtained in quantitative yield as white solid (6.45 g, 17.8 mmol).

^{1}H-NMR (400 MHz, $CDCl_3$) δ / ppm = 7.25 (m, 2H, H-1), 7.10 (m, 2H, H-2), 6.31 (s, 1H, H-5), 3.80 (s, 3H, H-13), 3.47 (s, 3H, H-6), 2.43 (m, 6H, H-10, H-11), 2.35 (s, 6H, H-12).

^{13}C-NMR (101 MHz, $CDCl_3$) δ / ppm = 172.31 (C-7), 144.31 (C-8), 138.73 (C-3), 130.54 (C-9), 130.36 (C-4), 130.33 (C-1), 130.16 (C-2), 75.83 (C-5), 56.90 (C-6), 38.42 (C-13), 20.69 (C-12), 12.26 (C-10), 12.21 (C-11).

HRMS (EI+, 70 eV): calcd. for $C_{15}H_{19}NOS^{\cdot+}$ = 276.1417 found 276.1419.

2-(methoxy(phenyl)methylene)-3,4,5-trimethyl-2,3-dihydrothiazole 95

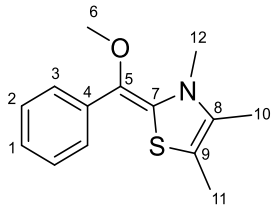

95

The tetrafluoroborate **124** (151 mg, 408 µmol, 1 equiv.) was diluted in 7.5 mL anhydrous THF. After the solution was cooled to -40 °C, it was added dropwise to NaH (27 mg, 60% (w/w), 675 µmol, 1.7 equiv.). The reaction mixture was stirred for 1 h at -40 °C. Afterward, the solution was allowed to warm up to room temperature and stirred for 18 h. After, the solution was filtered under inert conditions, the solvent was removed under reduced pressure. The title compound was obtained as yellow solid (89 mg, 360 µmol, 79%).

(*E*)-isomer (35%)

^{1}H-NMR (400 MHz, C_6D_6) δ / ppm = δ 7.79 (m, 2H, H-3), 7.29 (m, 2H, H-2), 6.99 (m, 1H, H-1), 3.34 (s, 3H, H-6), 3.00 (s, 3H, H-12), 1.59 (s, 3H, H-10), 1.32 (s, 3H, H-11).

^{13}C-NMR (101 MHz, C_6D_6) δ / ppm = 137.83 (C-4), 136.7 (C-7), 130.91 (C-8), 128.32 (C-2), 126.83 (C-5), 125.04 (C-3), 124.34 (C-1), 100.63 (C-9), 58.07 (C-6), 35.07 (C-12), 11.36 (C-10), 10.98 (C-11)

(*Z*)-isomer (65%)

^{1}H-NMR (400 MHz, C_6D_6) δ / ppm = 7.42 (m, 2H, H-3), 7.20 (m, 2H, H-2), 6.99 (m, 1H, H-1), 3.50 (s, 3H, H-6), 2.43 (s, 3H, H-12), 1.67 (s, 3H, H-10), 1.32 (s, 3H, H-11).

^{13}C-NMR (101 MHz, C_6D_6) δ / ppm = 140.84 (C-4), 135.22 (C-7), 131.87 (C-8), 127.96 (C-2), 127.14 (C-5), 126.21 (C-3), 124.61 (C-1), 105.57 (C-9), 56.13 (C-6), 37.56 (C-12), 11.52 (C-10), 11.07 (C-11)

2-(methoxy(4-methoxyphenyl)methylene)-3,4,5-trimethyl-2,3-dihydrothiazole 100

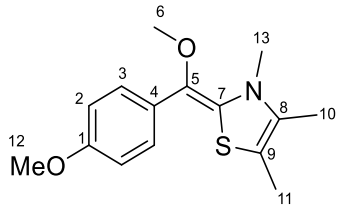

100

The tetrafluoroborate **125** (54 mg, 150 µmol, 1 equiv.) was diluted in 2.5 mL anhydrous THF. After the solution was cooled to -40 °C, it was added dropwise to NaH (17 mg, 60% (w/w), 435 µmol, 2.9 equiv.). The reaction mixture was stirred for 1 h at -40 °C. Afterward, the solution was allowed to warm up to room temperature and stirred for 18 h. After, the solution was filtered under inert conditions, the solvent was removed under reduced pressure. The title compound was obtained as yellow solid (31 mg, 111 µmol, 75%).

(*E*)-isomer (34%)

^{1}H-NMR (400 MHz, C_6D_6) δ / ppm = 7.71 (m, 2H, H-3), 6.87 (m, 2H, H-2), 3.36 (s, 3H, H-6), 3.32 (s, 3H, H-12), 3.02 (s, 3H, H-13), 1.59 (s, 3H, H-10), 1.34 (s, 3H, H-11).

^{13}C-NMR (101 MHz, C_6D_6) δ / ppm = 157.43 (C-1), [a](C-7), 130.97 (C-8), [b](C-4), [b](C-5), 127.15 (C-3), 113.93 (C-2), 100.20 (C-9), 57.93 (C-6), 54.43 (C-12), 35.01 (C-13), 11.46 (C-10), 10.99 (C-11).

(*Z*)-isomer (66%)

^{1}H-NMR (400 MHz, C_6D_6) δ / ppm = 7.39 (m, 3H, H-3), 6.81 (m, 3H, H-2), 3.51 (s, 3H, H-6), 3.33 (s, 3H, H-12), 2.46 (s, 3H, H-13), 1.68 (s, 3H, H-10), 1.34 (s, 3H, H-11).

^{13}C-NMR (101 MHz, C_6D_6) δ / ppm = 157.61 (C-1), 138.62 (C-7), 131.72 (C-8), [b](C-4), [b](C-5), [b](C3), 113.61 (C-2), 105.18 (C-9), 55.93 (C-6), 54.43 (C-12), 37.14 (C-13), 11.61 (C-10), 11.10 (C-11).

[a]Signal intensity to low.

[b]Overlap with C_6D_6 signal.

2-((4-chlorophenyl)(methoxy)methylene)-3,4,5-trimethyl-2,3-dihydrothiazole 101

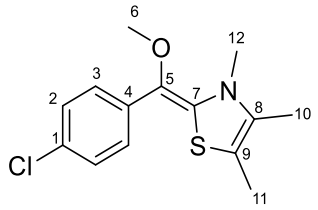

101

The tetrafluoroborate **126** (100 mg, 270 µmol, 1 equiv.) was diluted in 4.6 mL anhydrous THF. After the solution was cooled to -40 °C, it was added dropwise to NaH (17 mg, 60% (w/w), 428 µmol, 2.9 equiv.). The reaction mixture was stirred for 1 h at -40 °C. Afterward, the solution was allowed to warm up to room temperature and stirred for 18 h. After, the solution was filtered under inert conditions, the solvent was removed under reduced pressure. The title compound was obtained as yellow solid (42 mg, 168 µmol, 62%).

(*E*)-isomer (37%)

^{1}H-NMR (400 MHz, C_6D_6) δ / ppm = 7.54 (m, 2H, H-3), 7.24 (m, 2H, H-2), 3.24 (s, 3H, H-6), 2.95 (s, 3H, H-12), 1.57 (2, 3H, H-10), 1.28 (s, 3H, H-11).

^{13}C-NMR (101 MHz, C_6D_6) δ / ppm = 130.99 (C-8), 128.44 (C-2), 125.99 (C-3), 125.04 (C-5), 100.82 (C-9), 58.05 (C-6), 34.97 (C-12), 11.29 (C-10), 10.94 (C-11).

(*Z*)-isomer (63%)

^{1}H-NMR (400 MHz, C_6D_6) δ / ppm = 7.15 (m, 2H, H-2), 7.11 (m, 2H, H-2), 3.43 (s, 3H, H-6), 2.30 (s, 3H, H-12), 1.64 (s, 3H, H-10), 1.29 (s, 3H, H-11).

^{13}C-NMR (101 MHz, C_6D_6) δ / ppm = 131.87 (C-8), 128.10 (C-3), 127.07 (C-2), 125.85 (C-5), 105.89 (C-9), 56.09 (C-6), 37.57 (C-12), 11.44 (C-10), 11.03 (C-11).

2-((2,6-dimethylphenyl)(methoxy)methylene)-3,4,5-trimethyl-2,3-dihydrothiazole 115

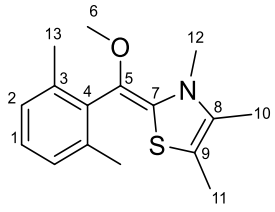

115

The tetrafluoroborate **127** (200 mg, 500 µmol, 1 equiv.) was diluted in 4.6 mL anhydrous THF. After the solution was cooled to -40 °C, it was added dropwise to NaH (30 mg, 60% (w/w), 760 µmol, 1.5 equiv.). The reaction mixture was stirred for 1 h at -40 °C. Afterward, the solution was allowed to warm up to room temperature and stirred for 18 h. After, the solution was filtered

under inert conditions, the solvent was removed under reduced pressure. The title compound was obtained as yellow solid. The yield was not determined.

(*E*)-isomer (20%)

^{1}H-NMR (400 MHz, C_6D_6) δ / ppm = 7.10–6.99 (m, 3H, H-1, H-2), 3.13 (s, 3H, H-6), 3.12 (s, 3H, H-12), 2.57 (s, 6H, H-13), 1.53 (s, 3H, H-10), 1.33 (s, 3H, H-11).

^{13}C-NMR (101 MHz, C_6D_6) δ / ppm = 139.12 (C-3), [a](C-7), 135.26 (C-4), 131.29 (C-8), 128.13 (C-2), [b](C-1), 120.61 (C-5), 100.89 (C-9), 56.06 (C-6), 34.71 (C-12), 19.17 (C-13), 11.55 (C-10), 11.06 (C-11).

(*Z*)-isomer (80%)

^{1}H-NMR (400 MHz, C_6D_6) δ / ppm = 7.10–6.99 (m, 3H, H-1, H-2), 3.26 (s, 3H, H-6), 2.41 (s, 6H, H-13), 2.09 (s, 3H, H-12), 1.68 (s, 3H, H-10), 1.27 (s, 3H, H-11).

^{13}C-NMR (101 MHz, C_6D_6) δ / ppm = 139.00 (C-3), 137.11 (C-7), 134.05 (C-4), 130.76 (C-8), 127.11 (C-2), [b](C-1), 123.67 (C-5), 103.17 (C-9), 54.97 (C-6), 34.27 (C-12), 20.50 (C-13), 11.73 (C-10), 11.12 (C-11).

[a]Signal intensity to low.

[b]Overlap with C_6D_6 signal.

E. Appendix

1. NMR-Spectra of Synthesized Compounds

^{1}H-NMR: First image

^{13}C-NMR: Second image

1.1 NMR of (4,5-dimethylthiazol-2-yl)(phenyl)methanol **116**

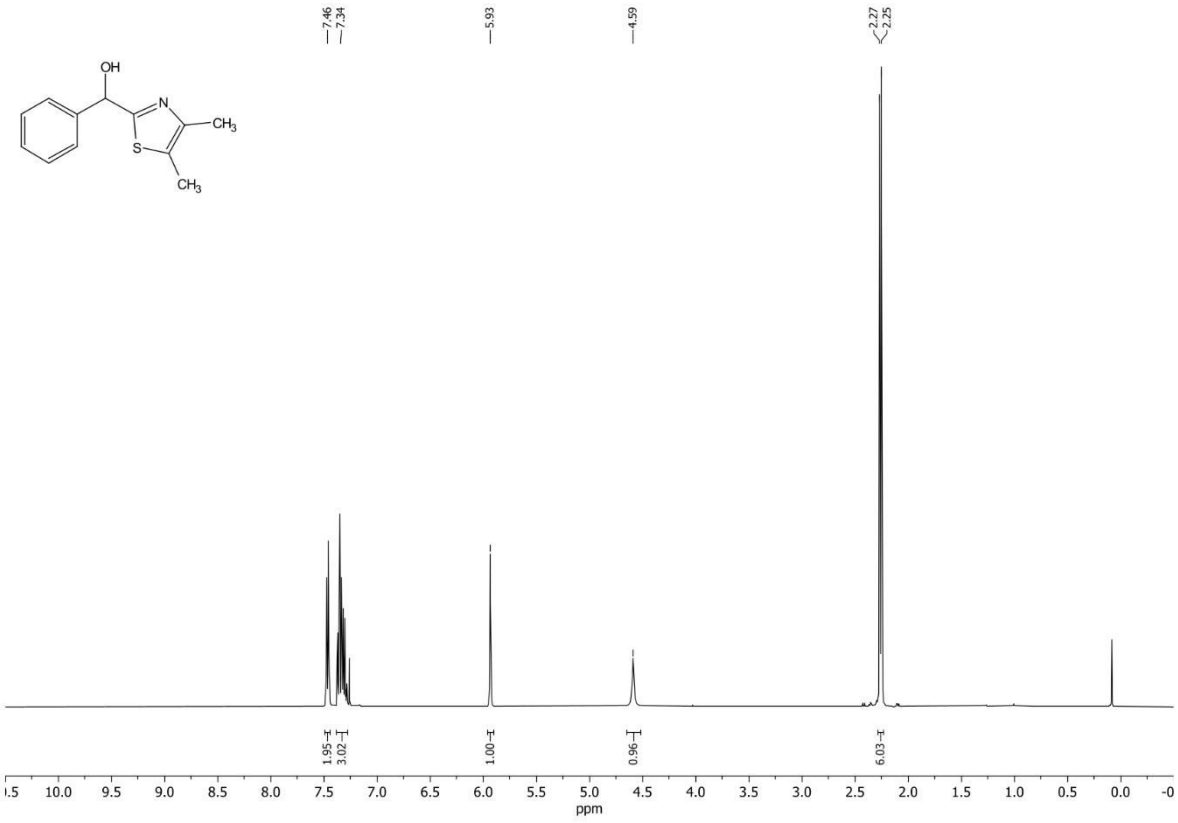

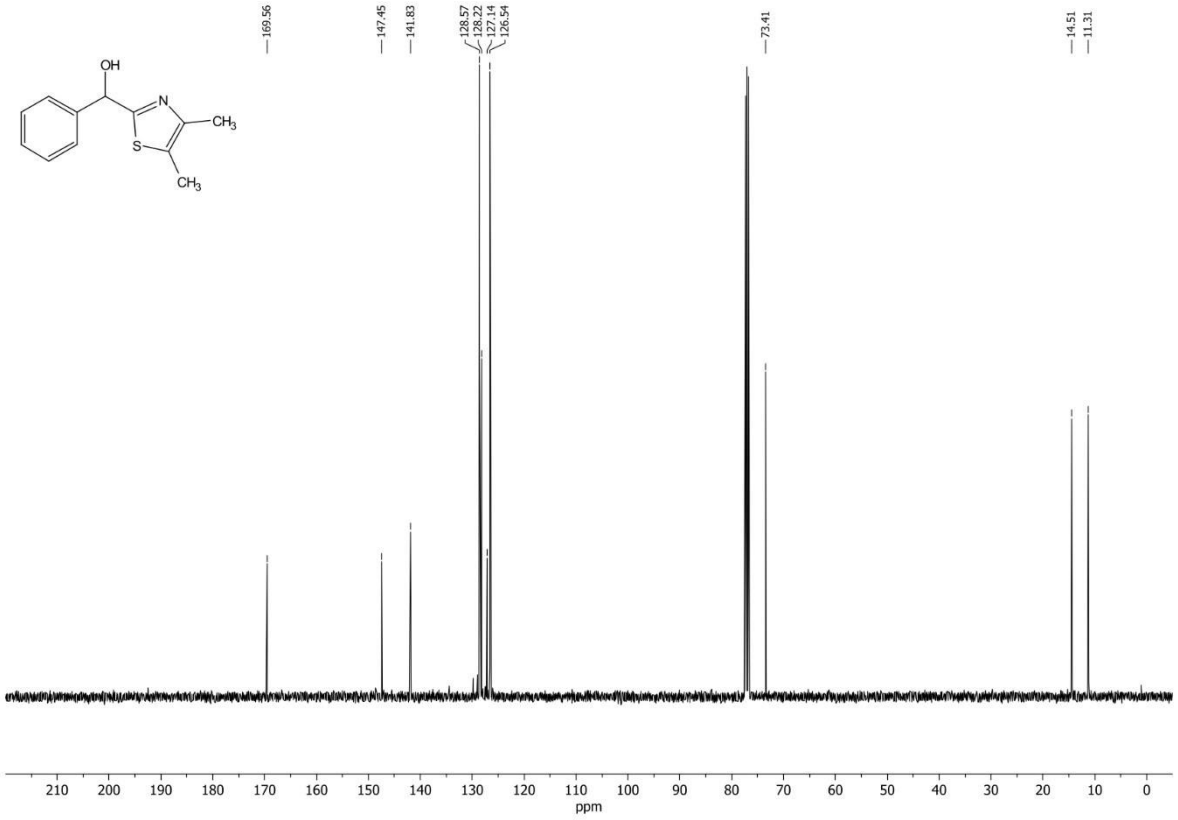

1.2 NMR of (4,5-dimethylthiazol-2-yl)(4-methoxypheny)methanol **117**

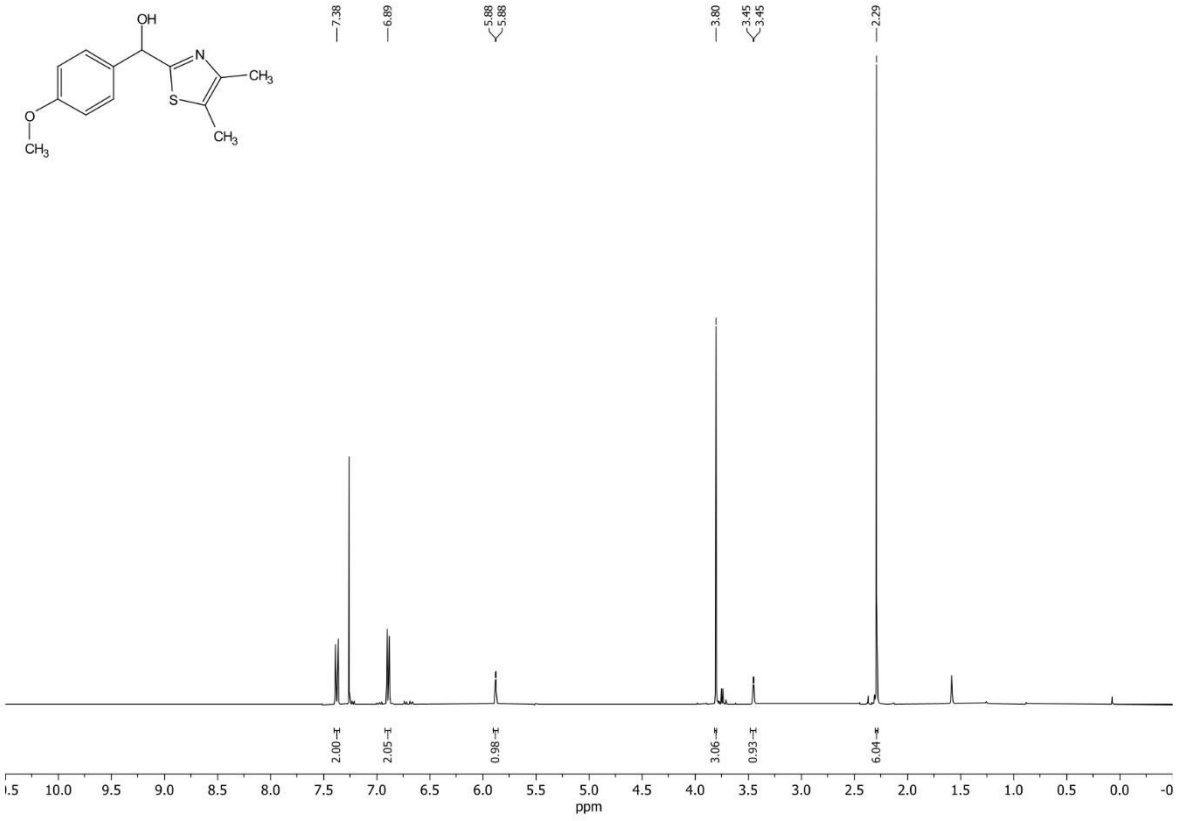

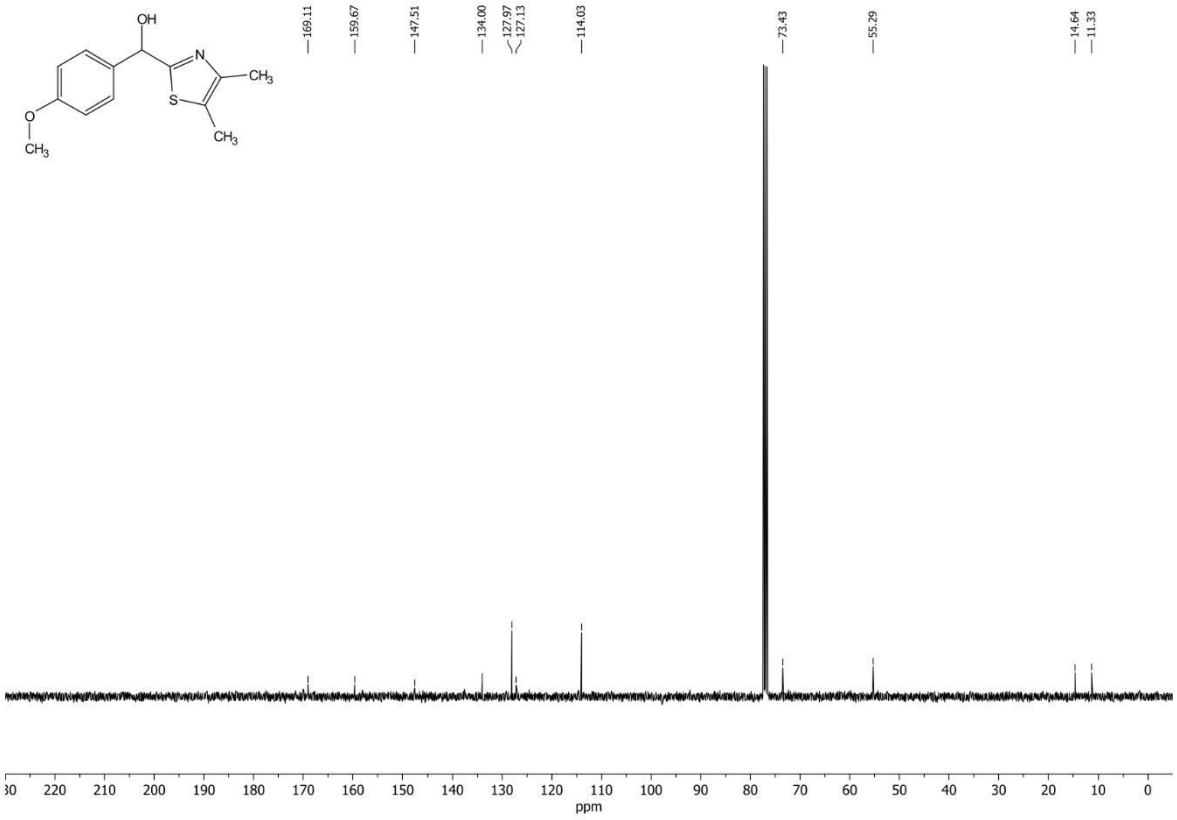

1.3 NMR of (4-chlorophenyl)(4,5-dimethylthiazol-2-yl)methanol **118**

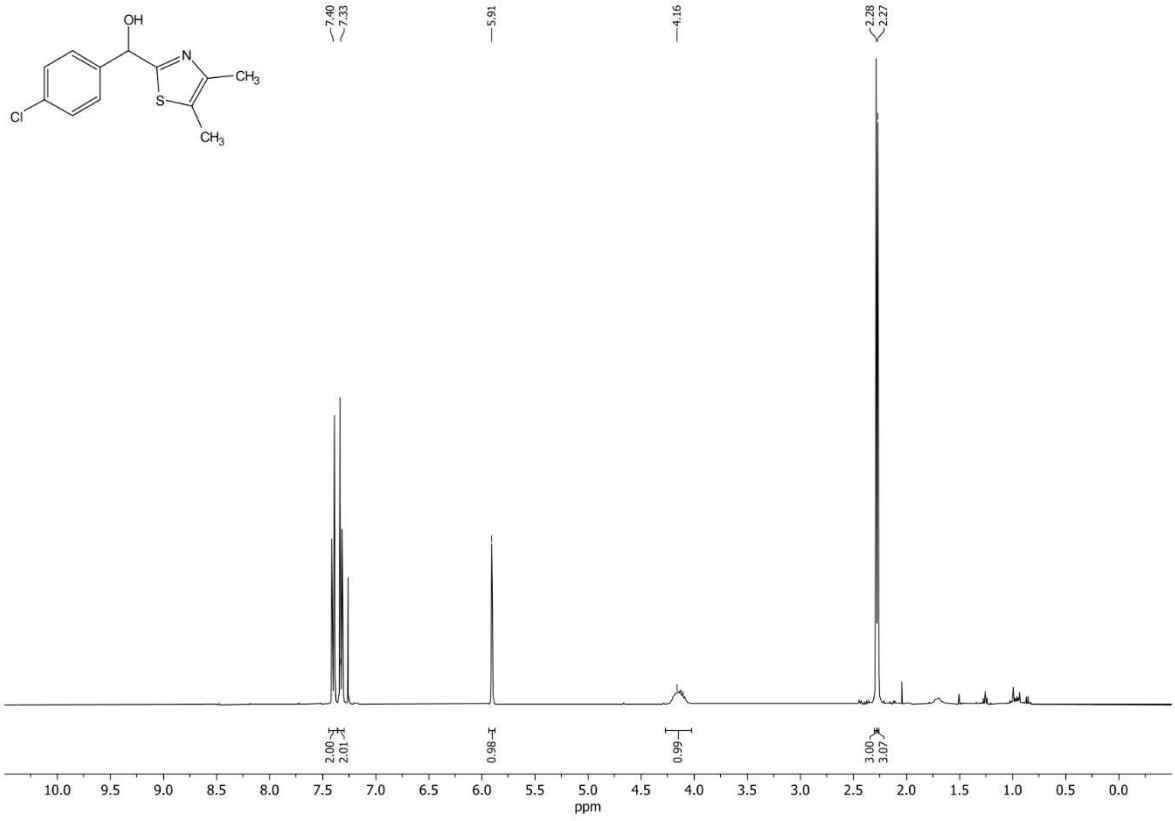

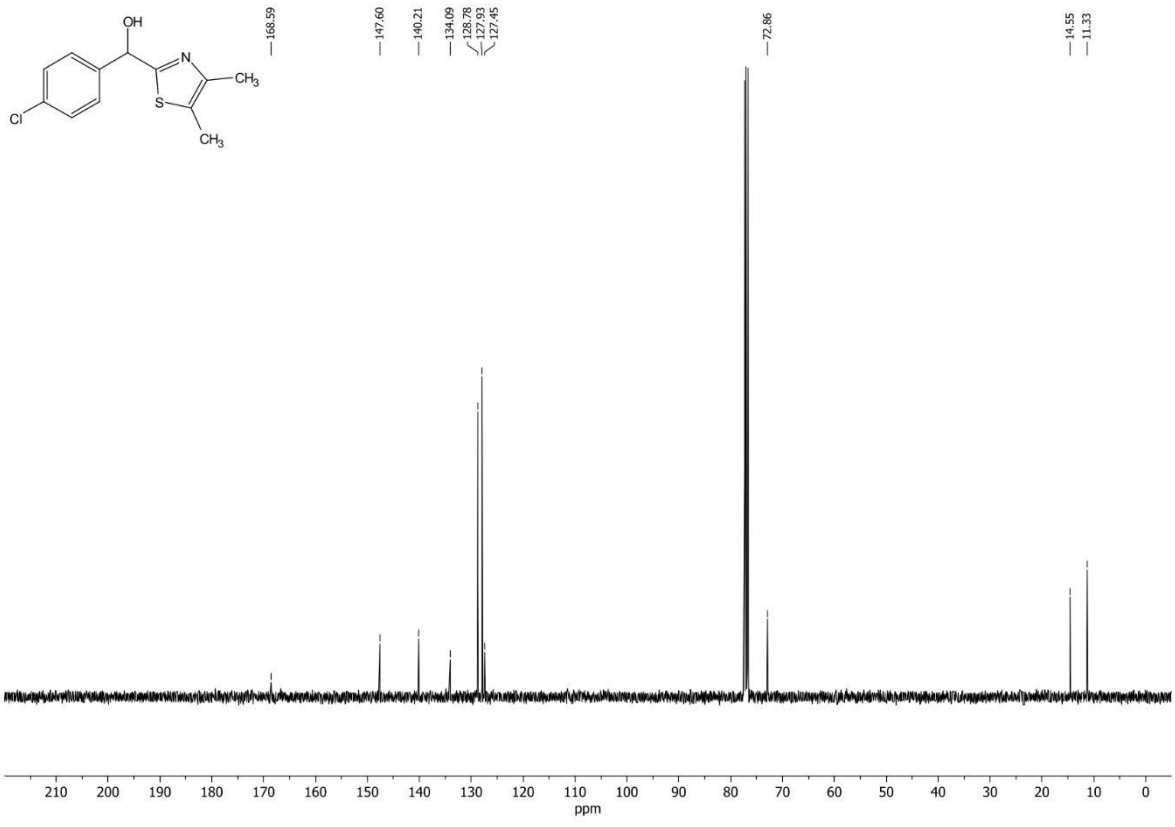

1.4 NMR of (2,6-dimethylphenyl)(4,5-dimethylthiazol-2-yl)methanol **119**

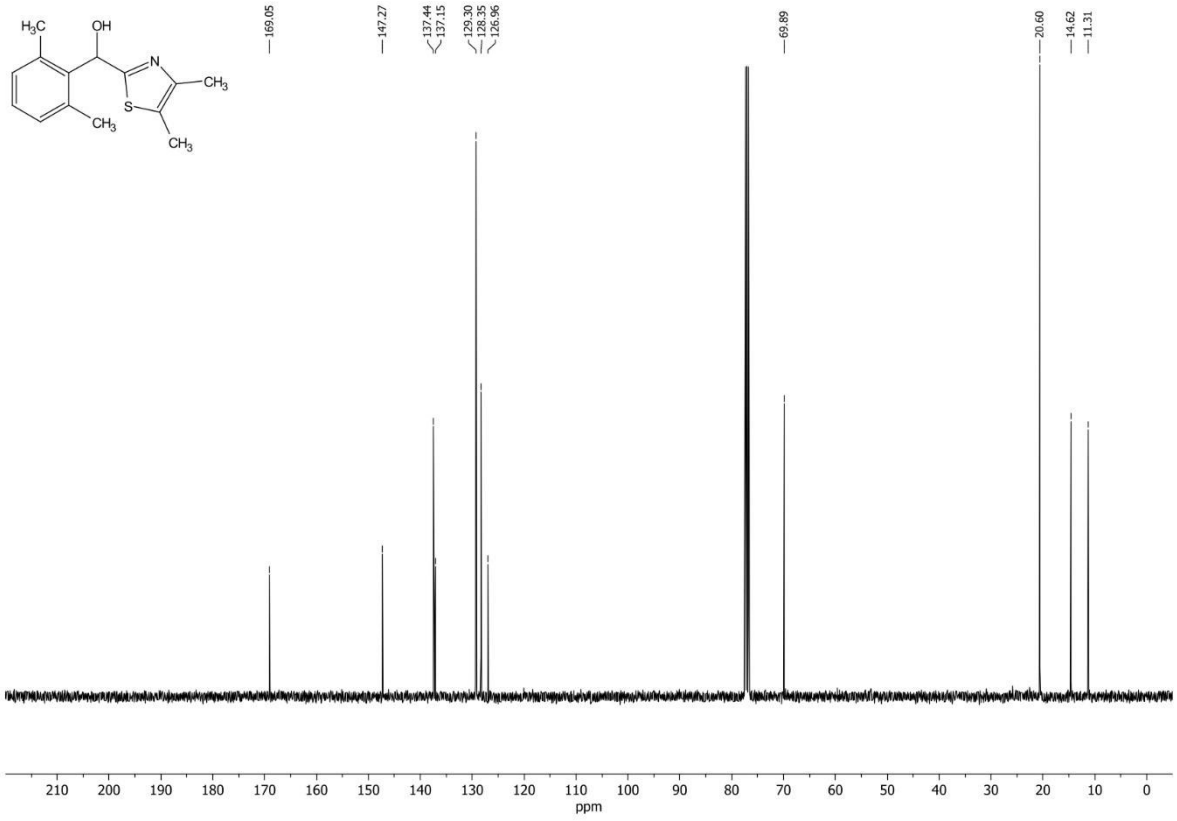

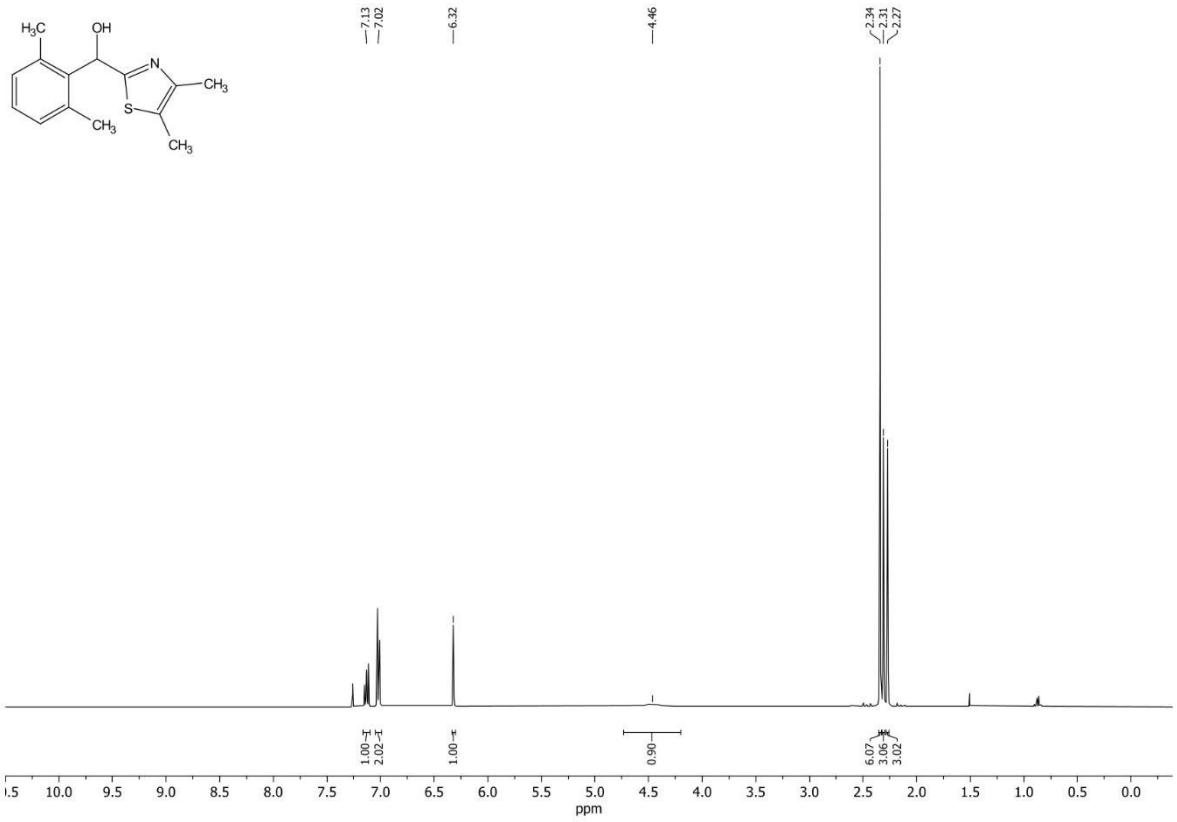

1.5 NMR of (2-(methoxy(phenyl)methyl)-4,5-dimethylthiazole **120**

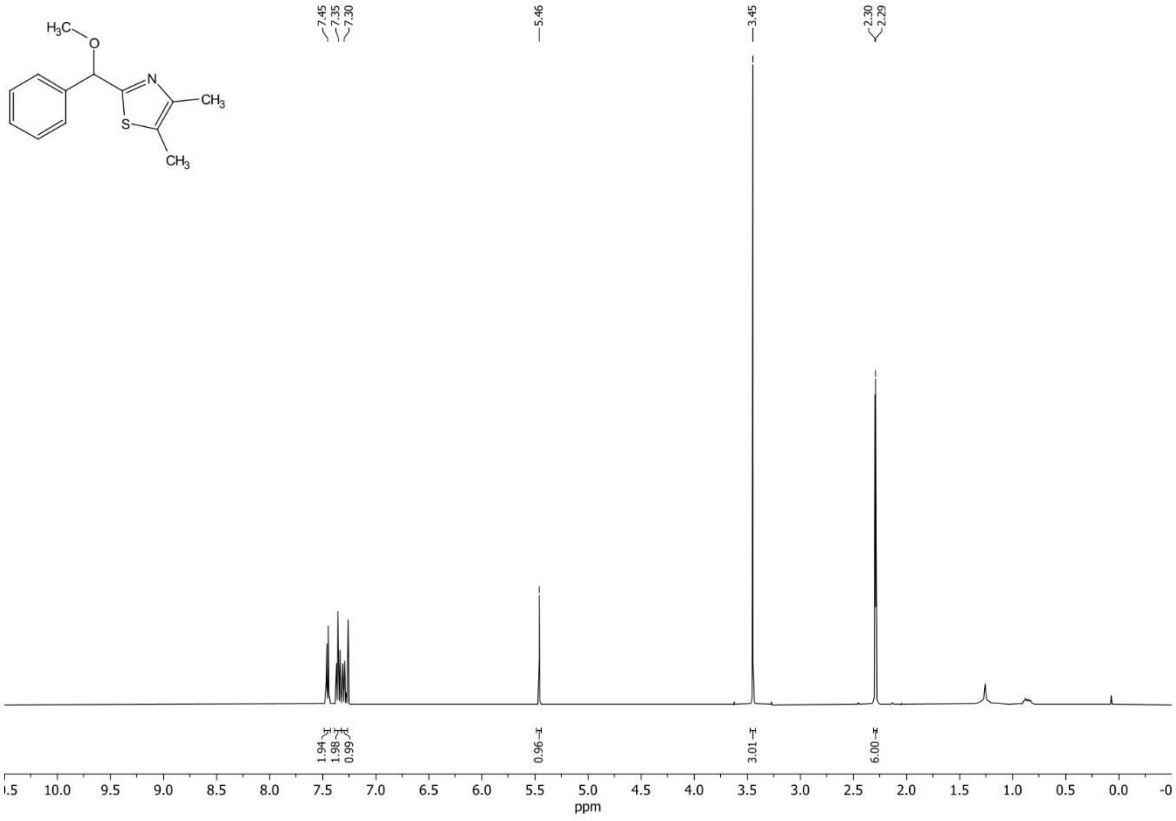

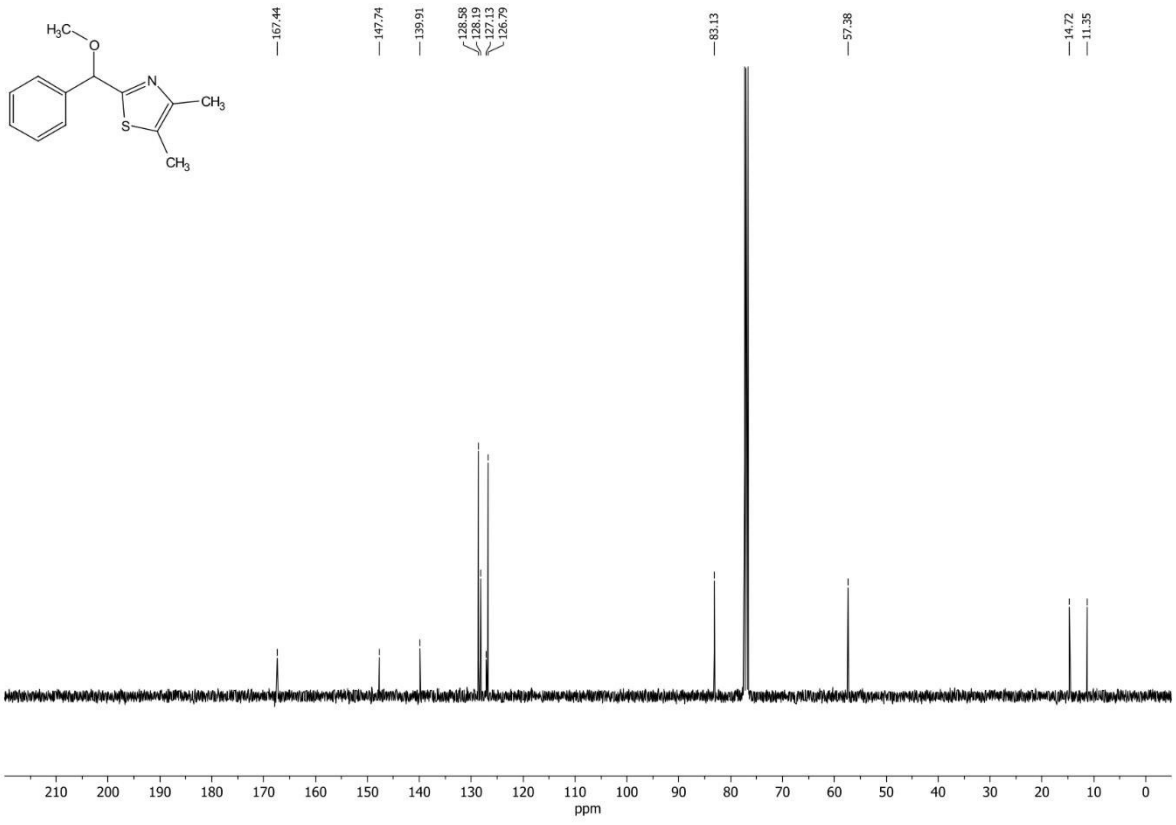

1.6 NMR of (4,5-dimethylthiazol-2-yl)(4-methoxypheny)methanol **121**

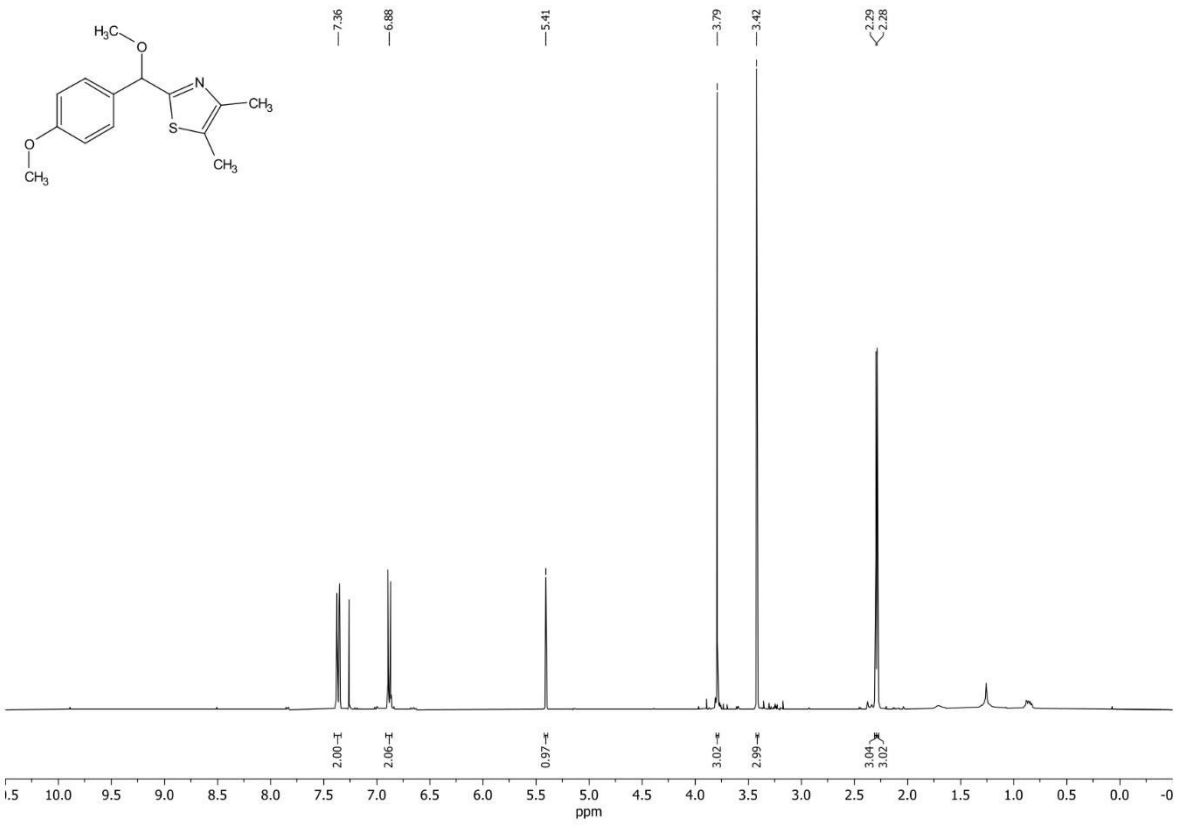

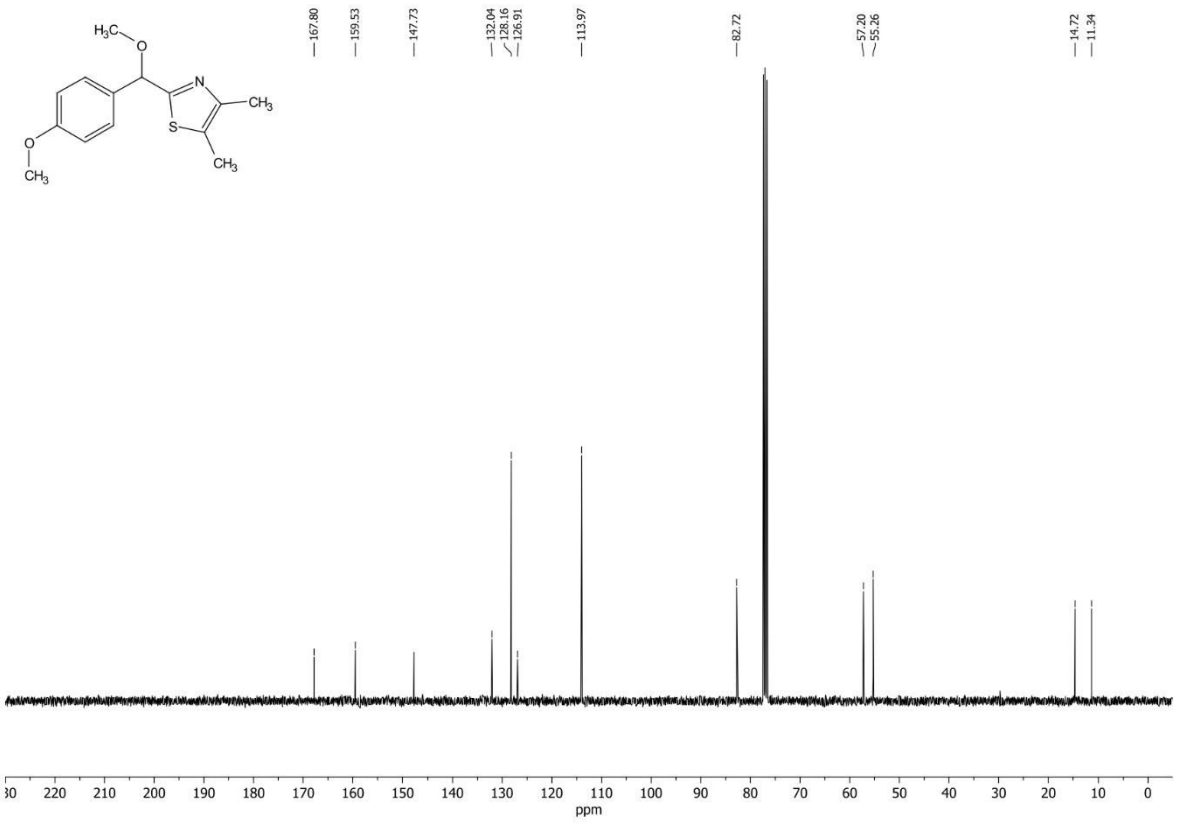

1.7 NMR of 2-((4-chlorophenyl)(methoxy)methyl)-4,5-dimethylthiazole **122**

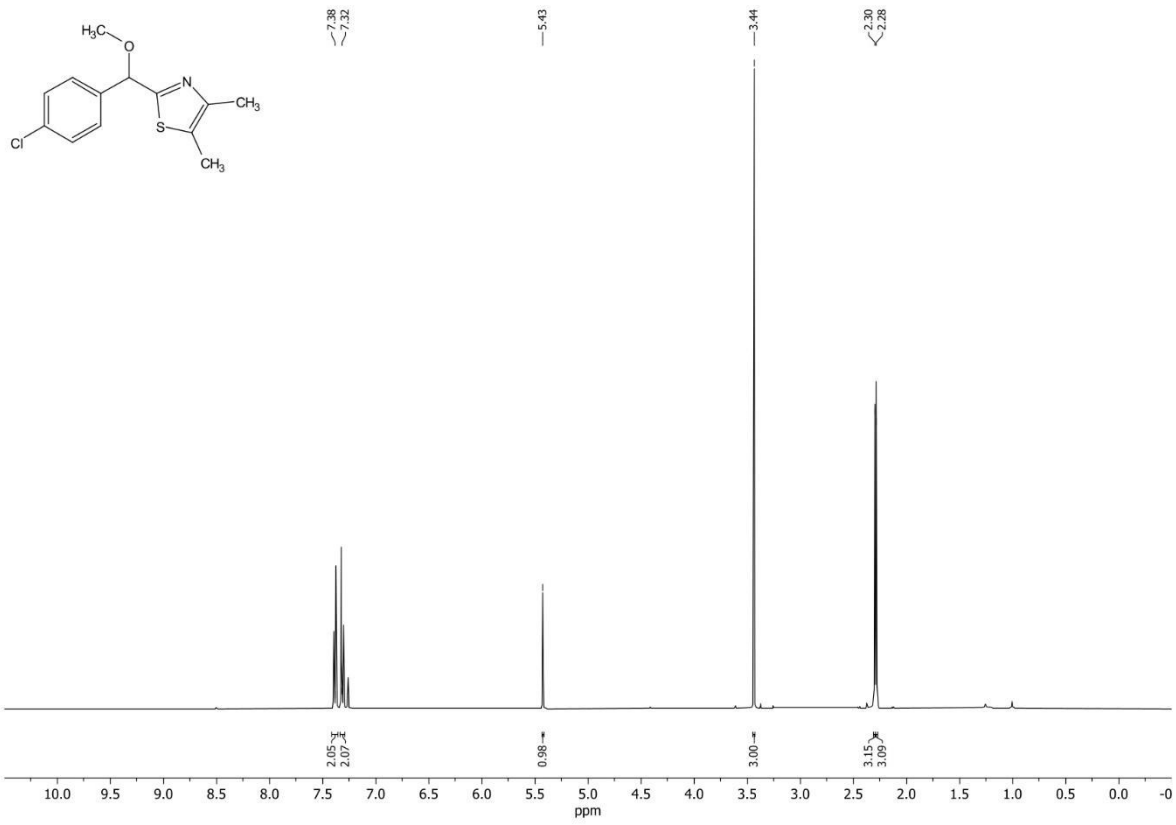

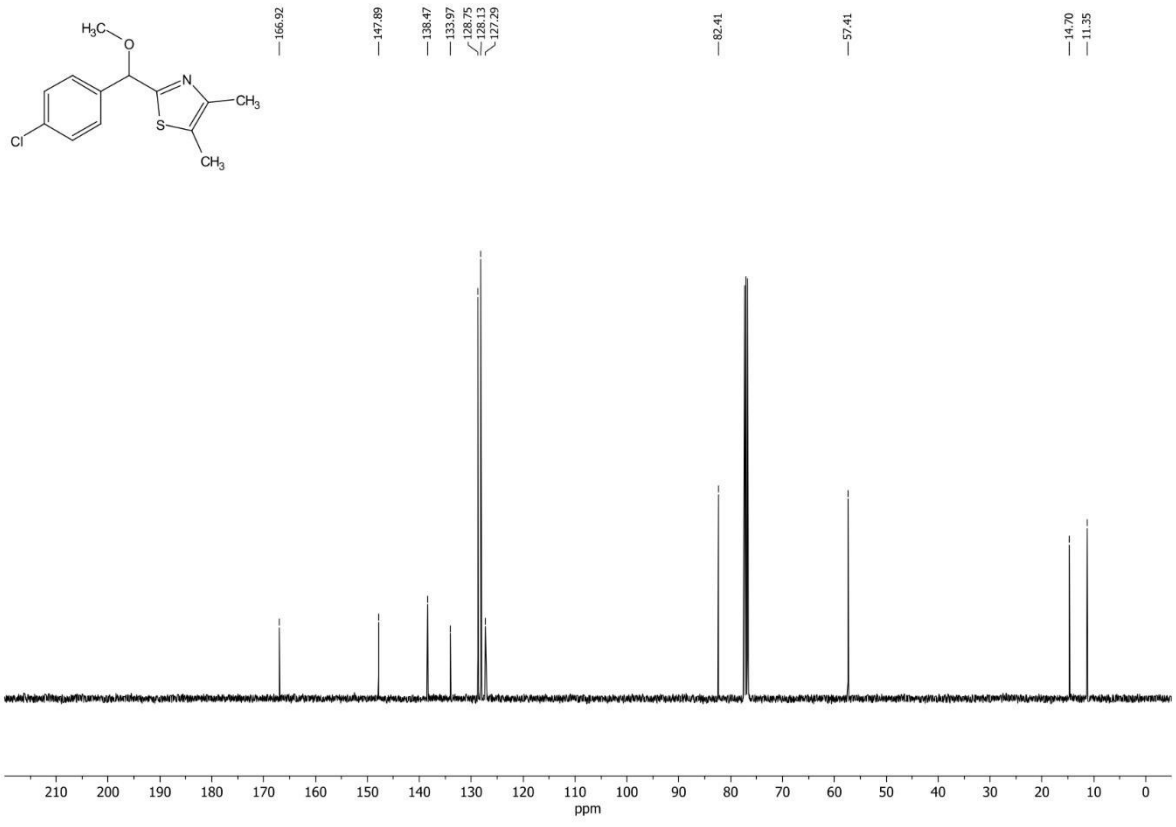

1.8 NMR of 2-((2,6-dimethylphenyl)(methoxy)methyl)-4,5-dimethylthiazole **123**

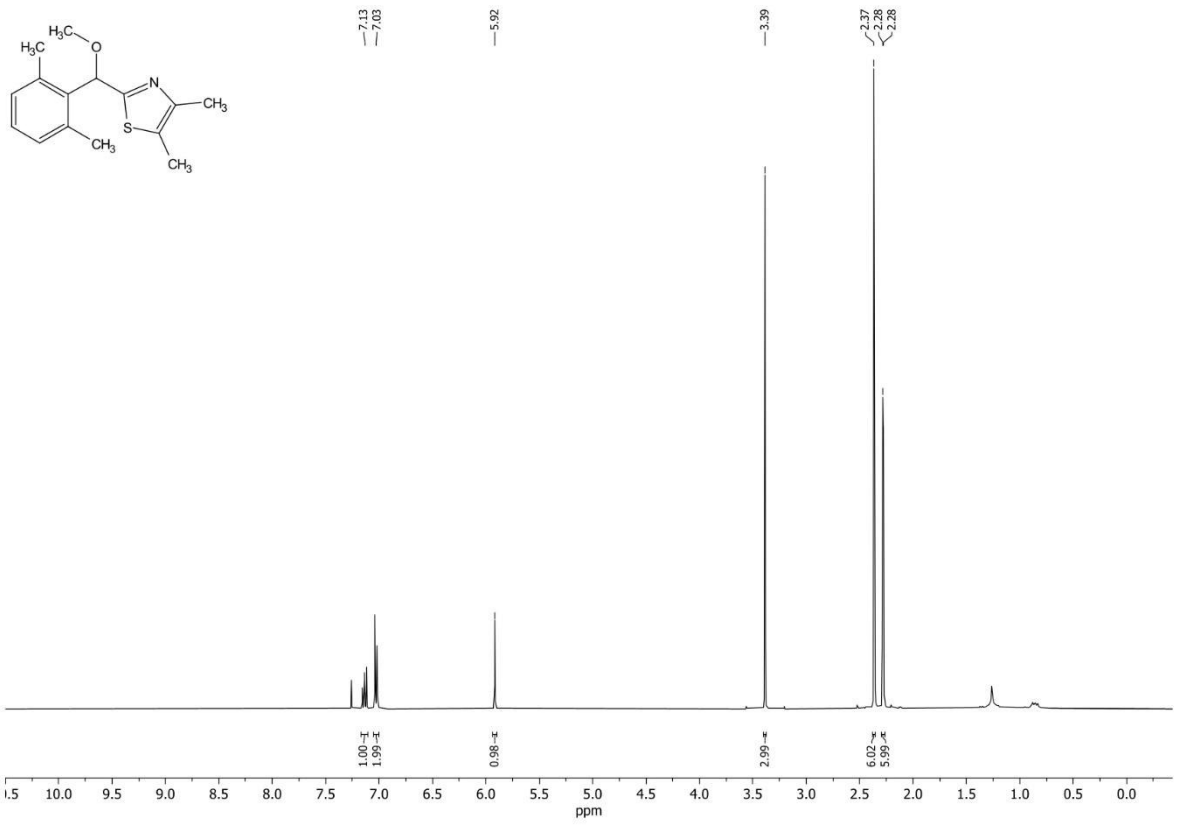

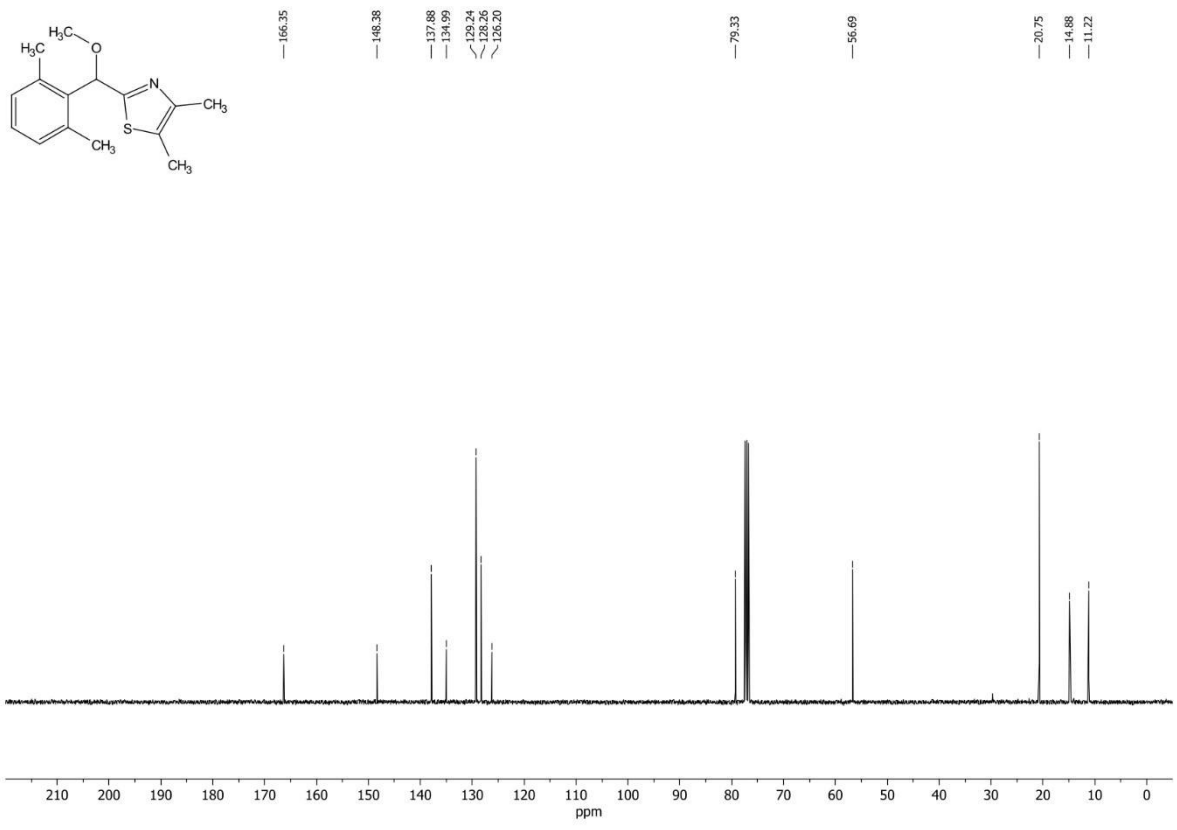

1.9 NMR of 2-((2,6-dimethylphenyl)(methoxy)methyl)-4,5-dimethylthiazole **124**

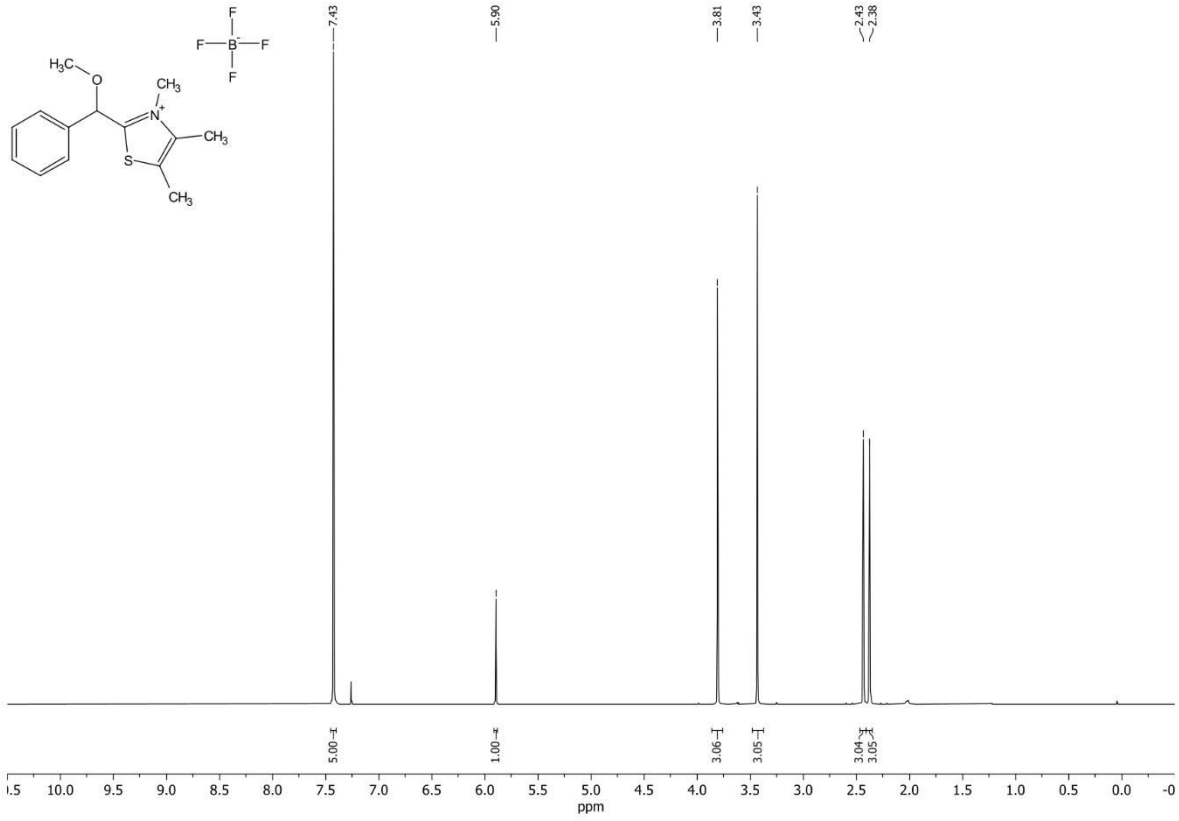

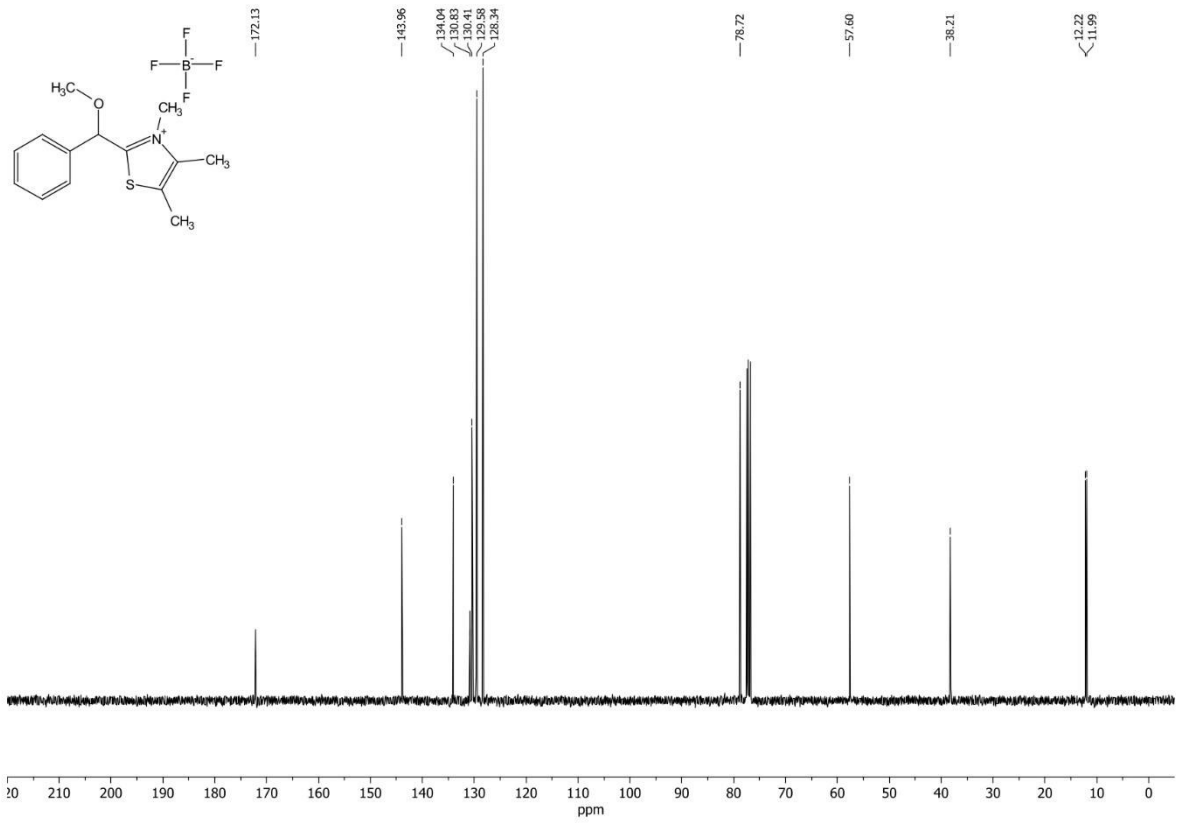

1.10 NMR of 2-(methoxy(4-methoxyphenyl)methyl)-3,4,5-trimethylthiazol-3-ium tetrafluoroborate **125**

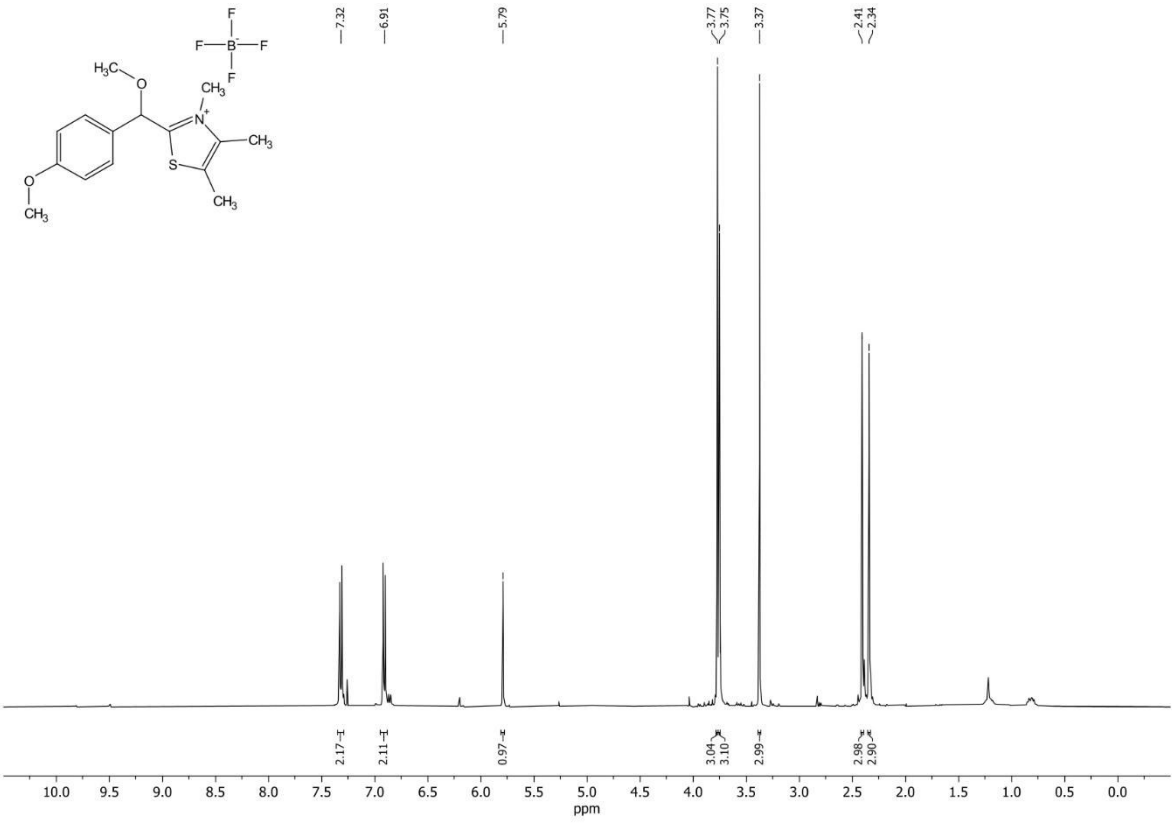

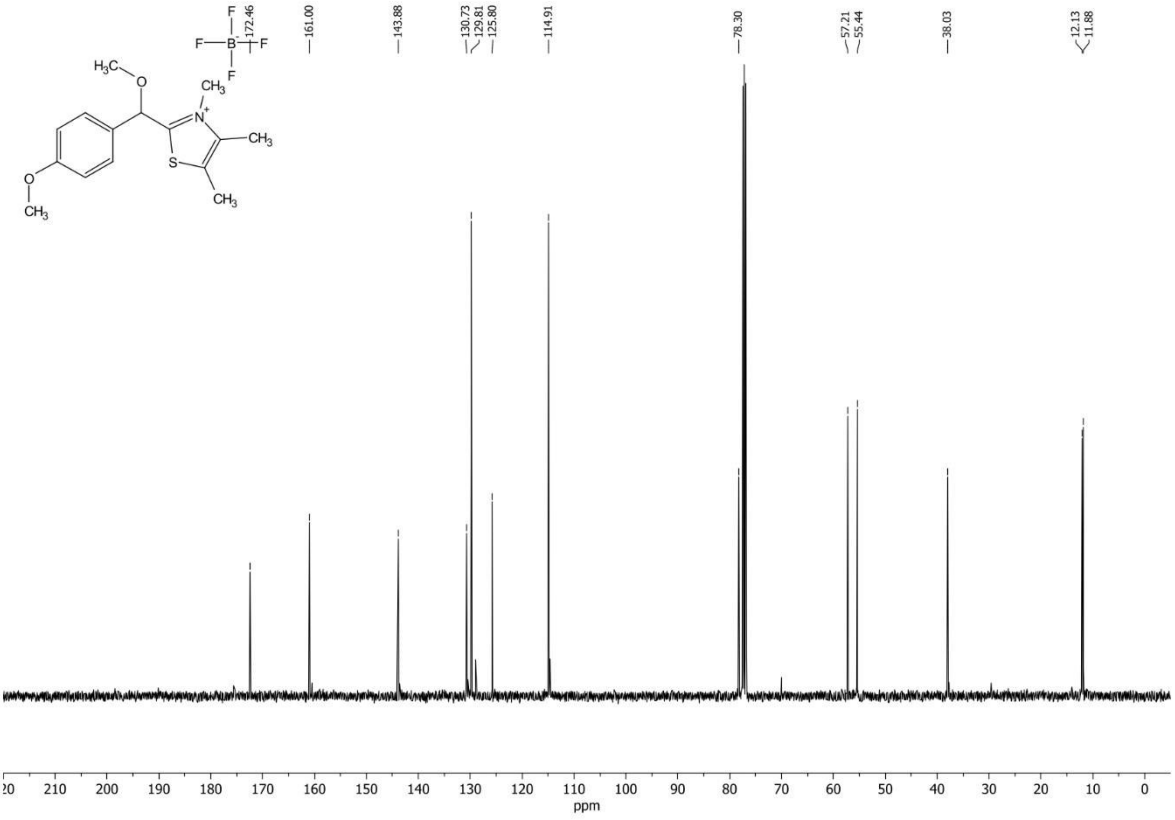

1.11 NMR of 2-((4-chlorophenyl)(methoxy)methyl)-3,4,5-trimethylthiazol-3-ium tetrafluoroborate **126**

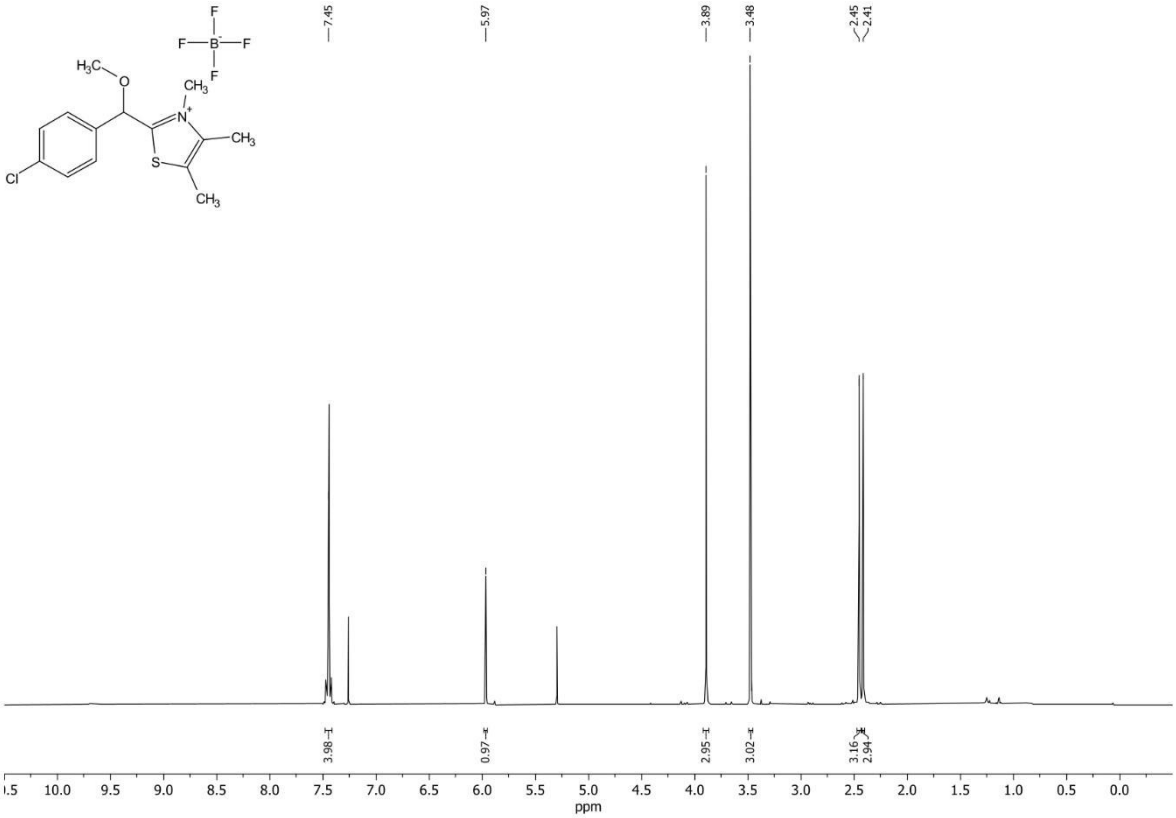

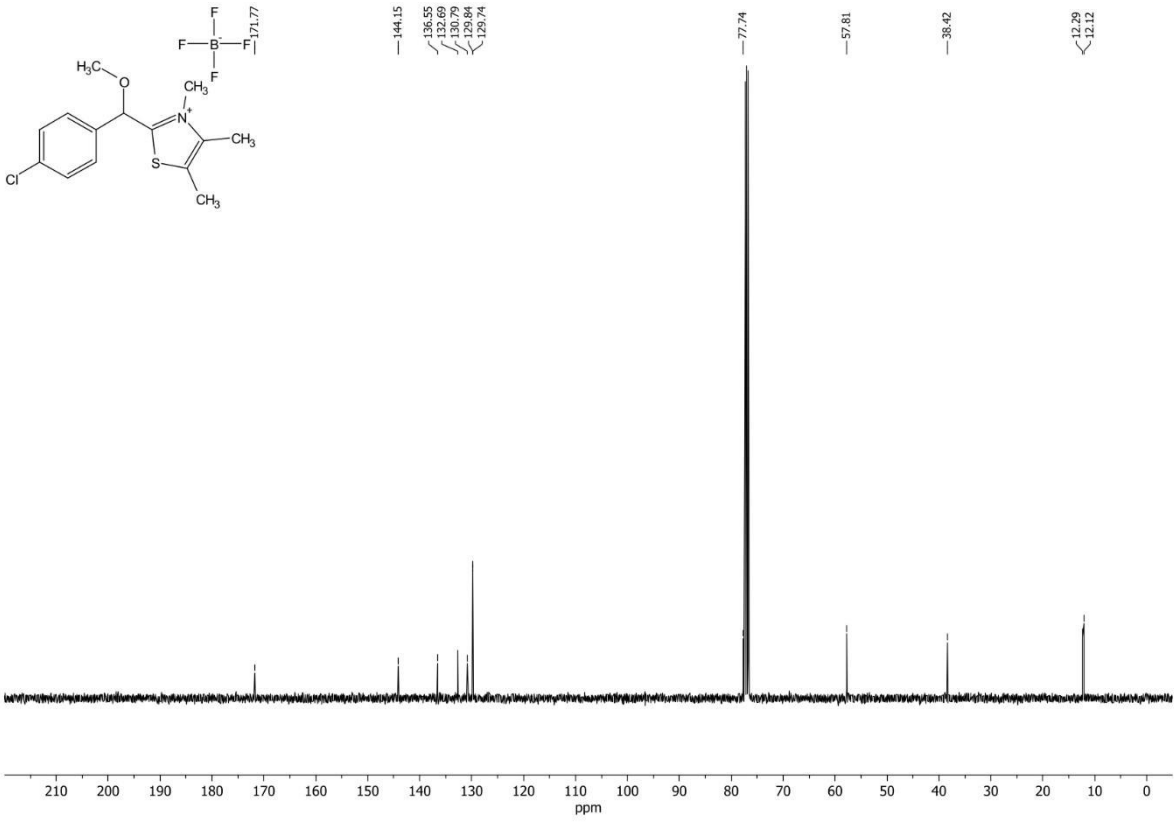

1.12 NMR of 2-((2,6-dimethylphenyl)(methoxy)methyl)-3,4,5-trimethylthiazol-3-ium tetrafluoroborate **127**

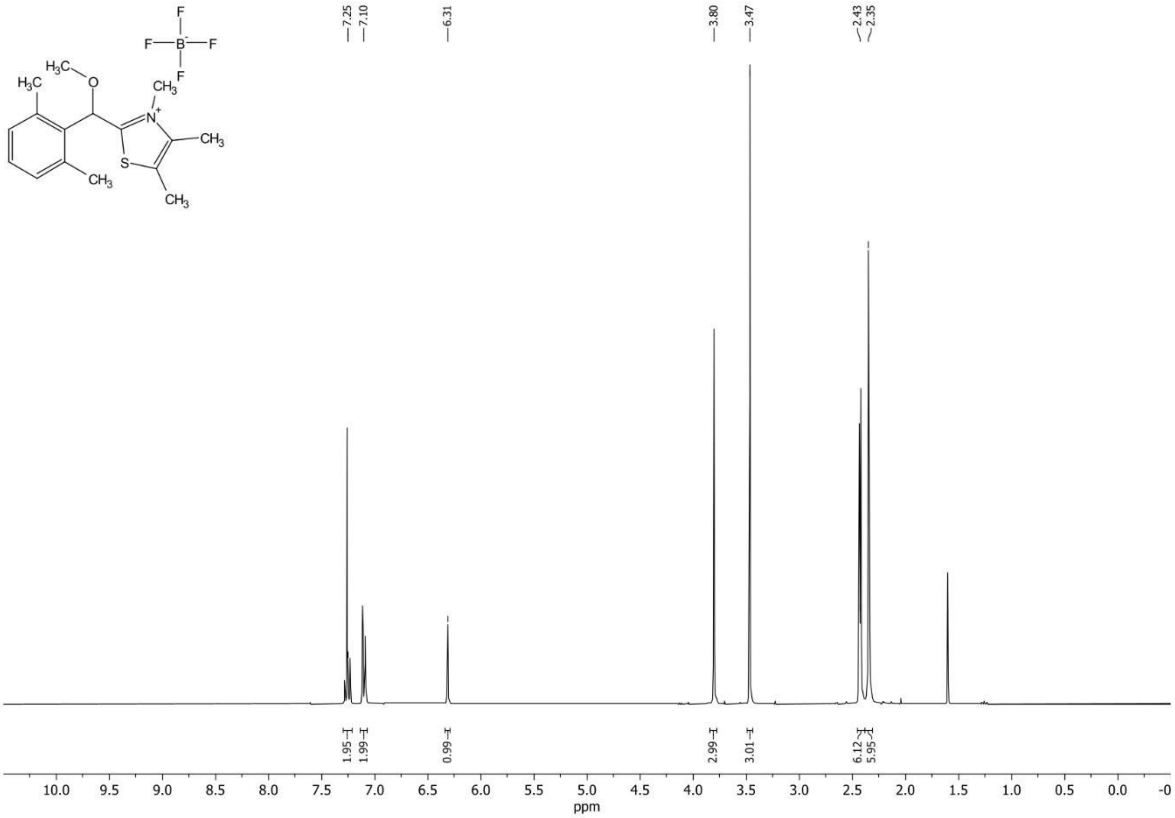

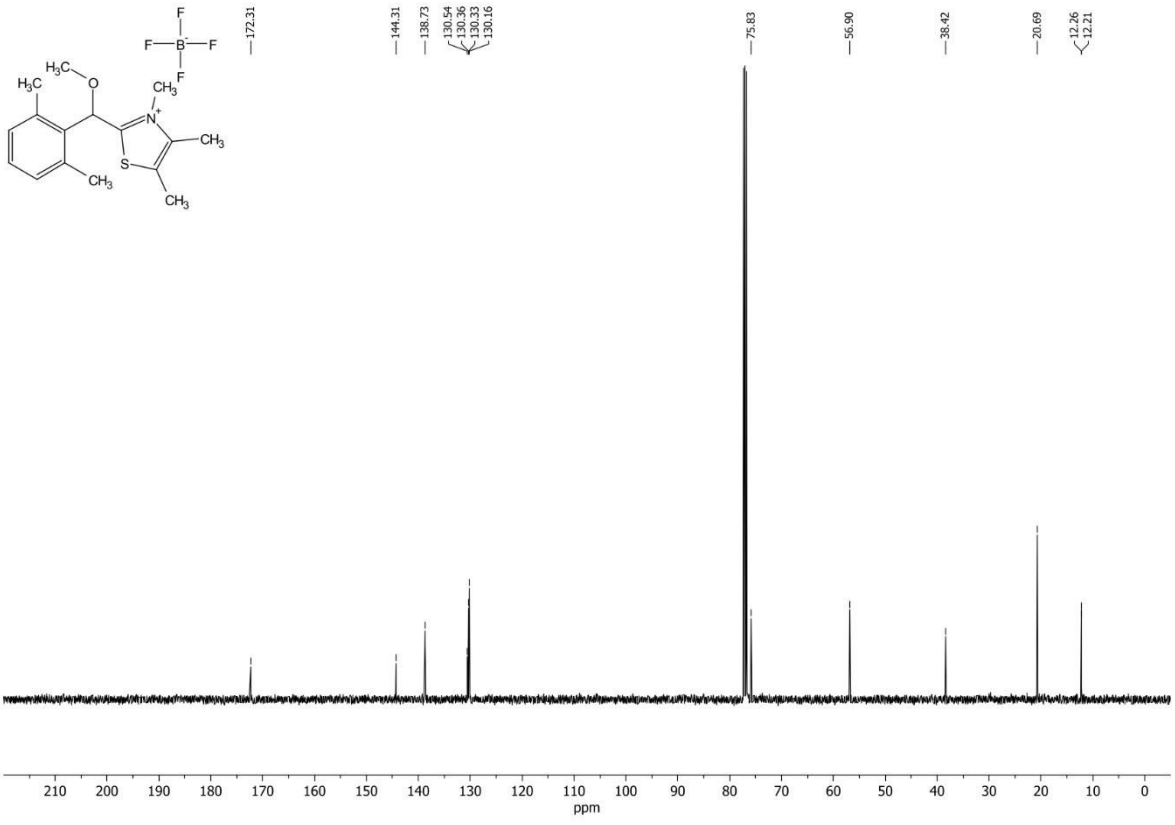

1.13 NMR of 2-(methoxy(phenyl)methylene)-3,4,5-trimethyl-2,3-dihydrothiazole **95**

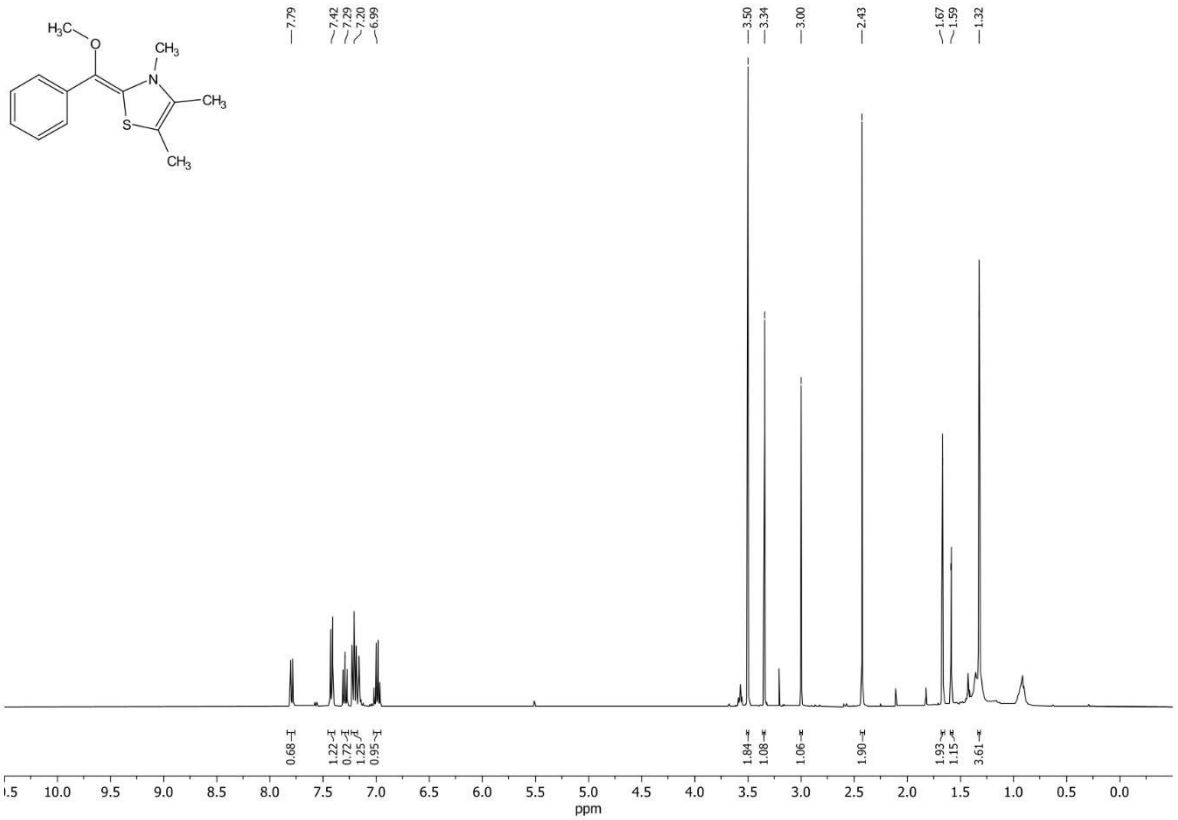

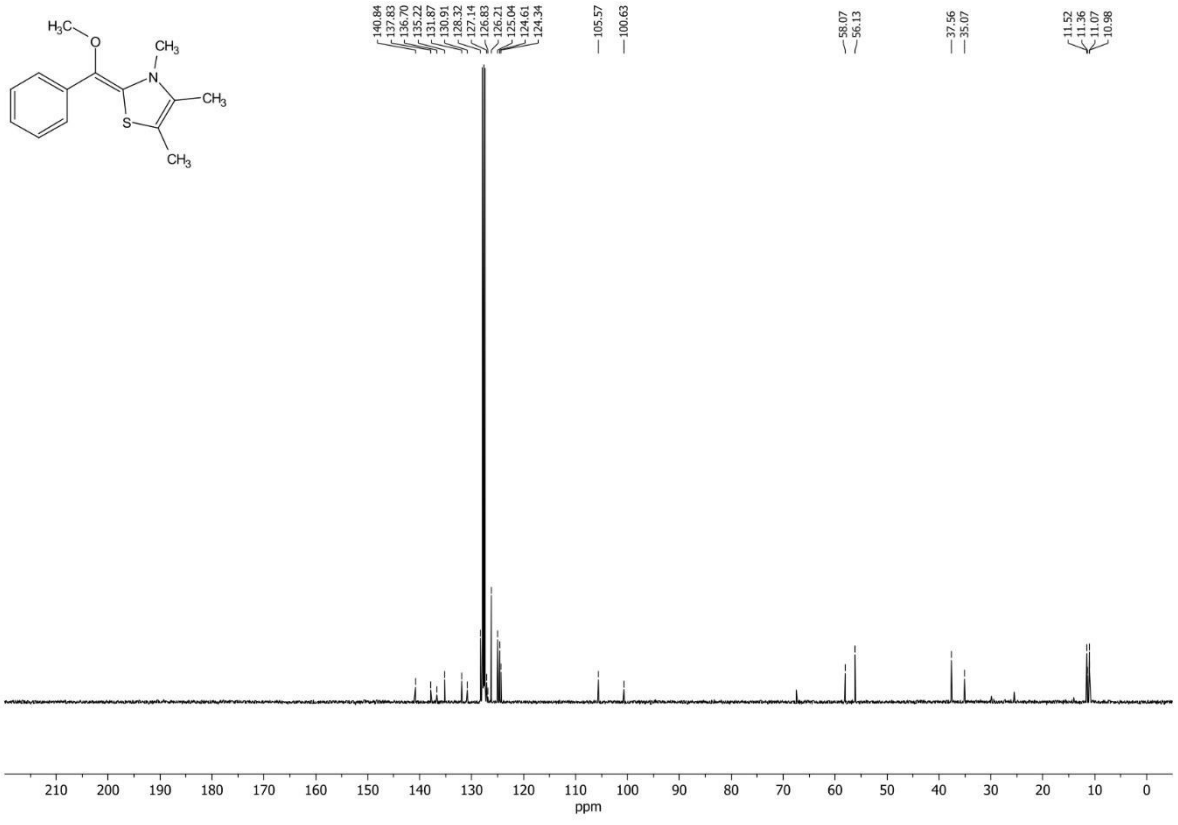

1.14 NMR of 2-(methoxy(4-methoxyphenyl)methylene)-3,4,5-trimethyl-2,3-dihydrothiazole **100**

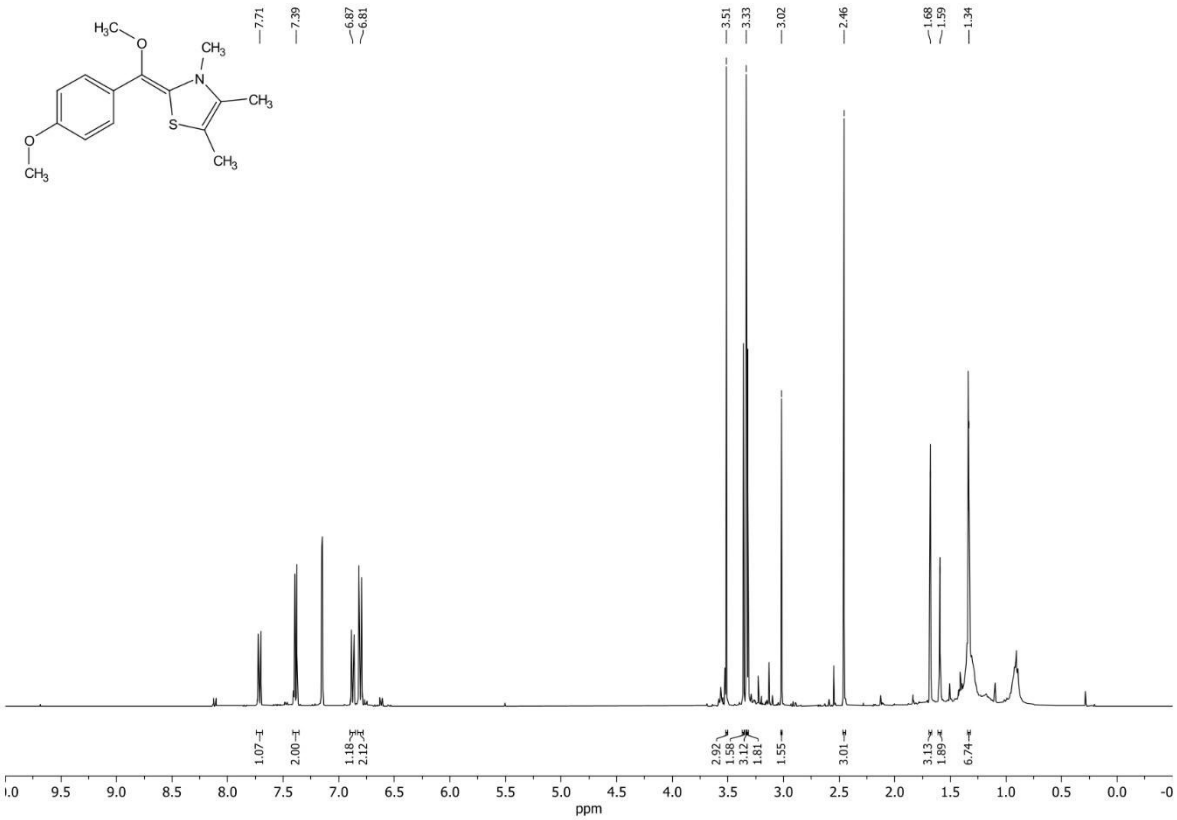

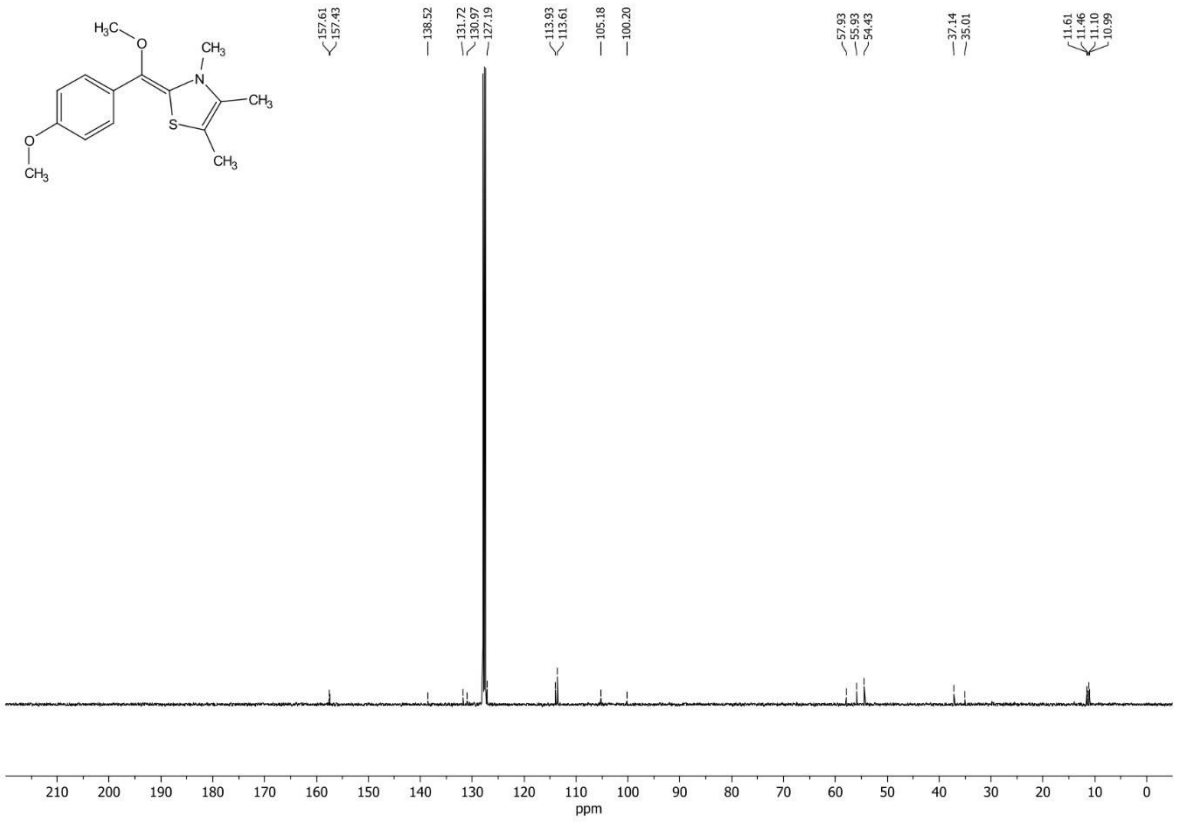

1.15 NMR of 2-((4-chlorophenyl)(methoxy)methylene)-3,4,5-trimethyl-2,3-dihydrothiazole **101**

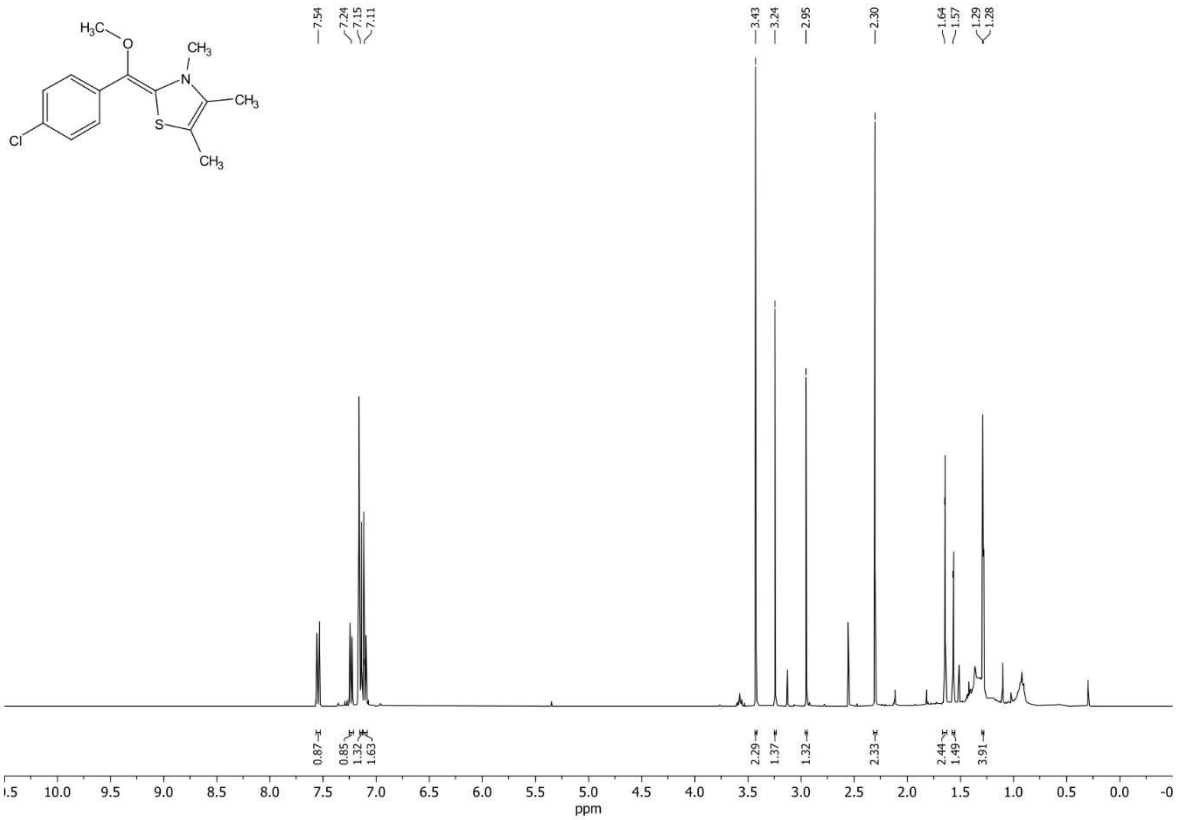

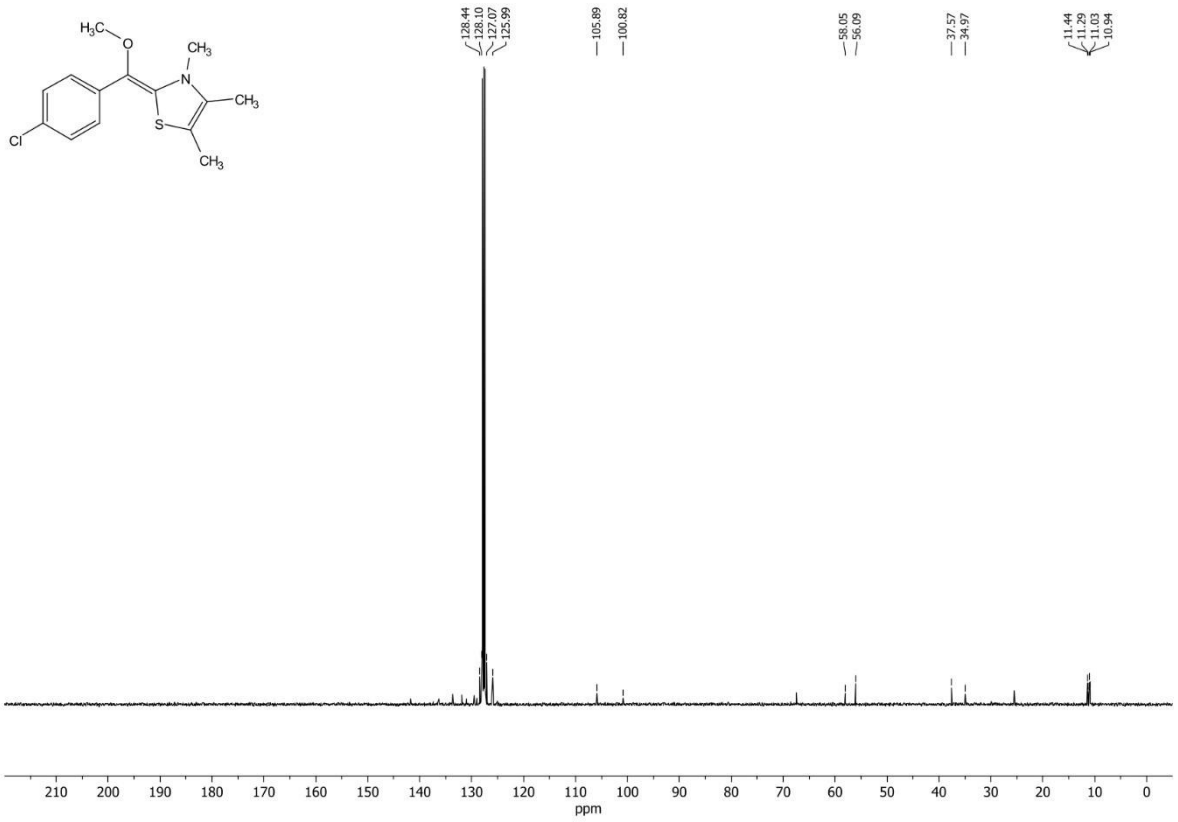

1.16 NMR of 2-((2,6-dimethylphenyl)(methoxy)methylene)-3,4,5-trimethyl-2,3-dihydrothiazole **115**

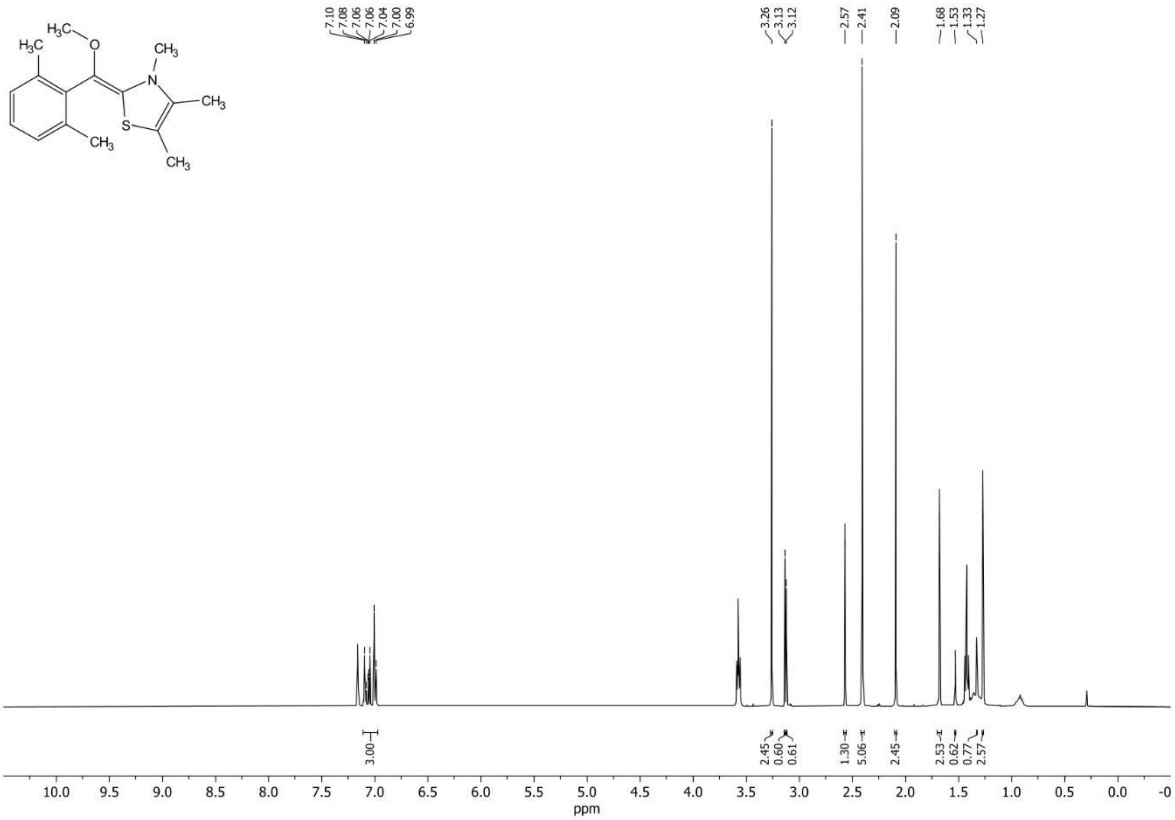

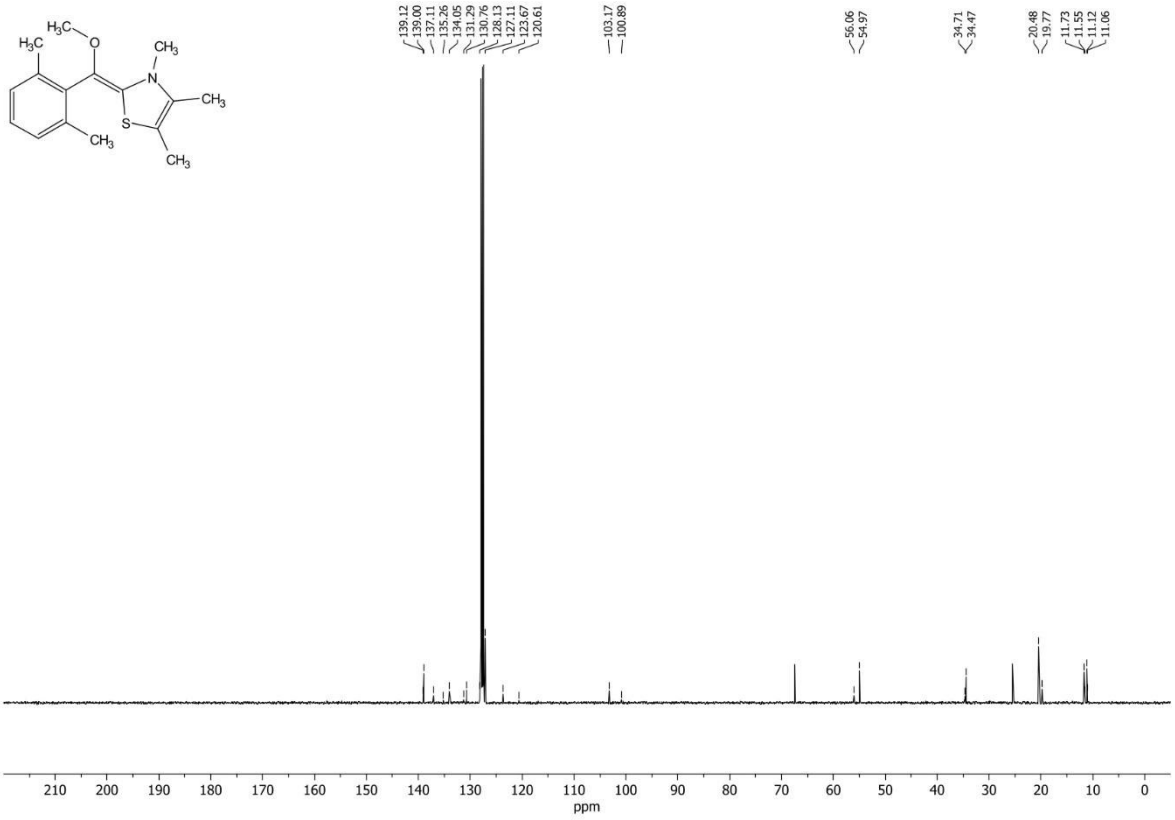

2. Isomerization Experiments of Compound **95**

2.1 Irradiation in anhydrous THF-d_8

No irradiation

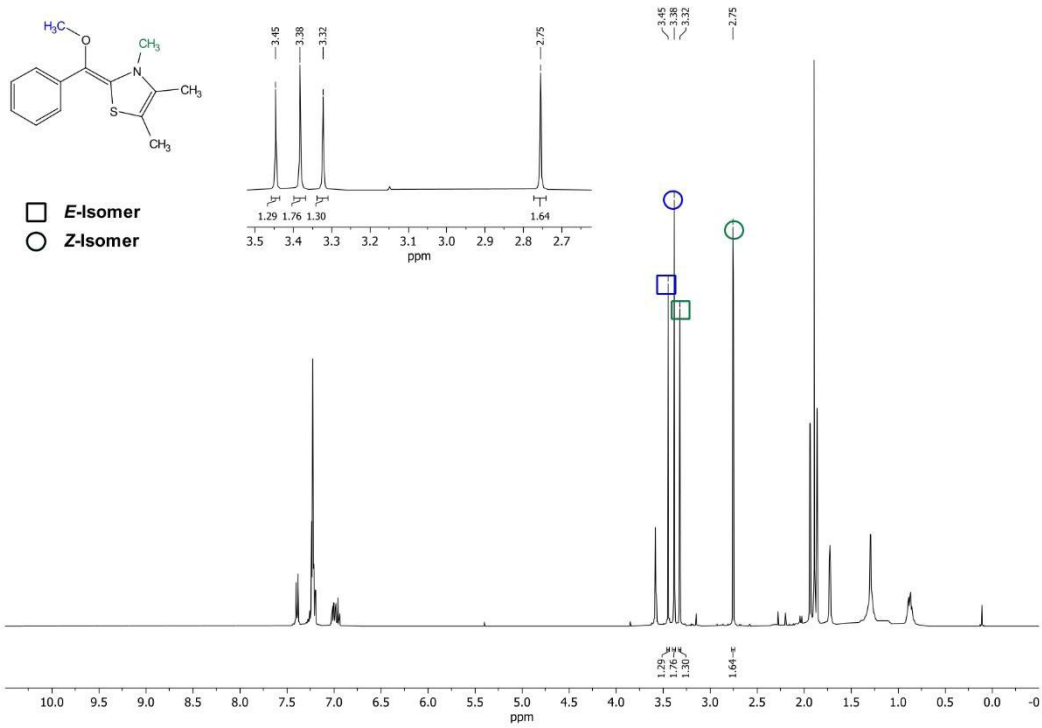

Irradiation for 30 min

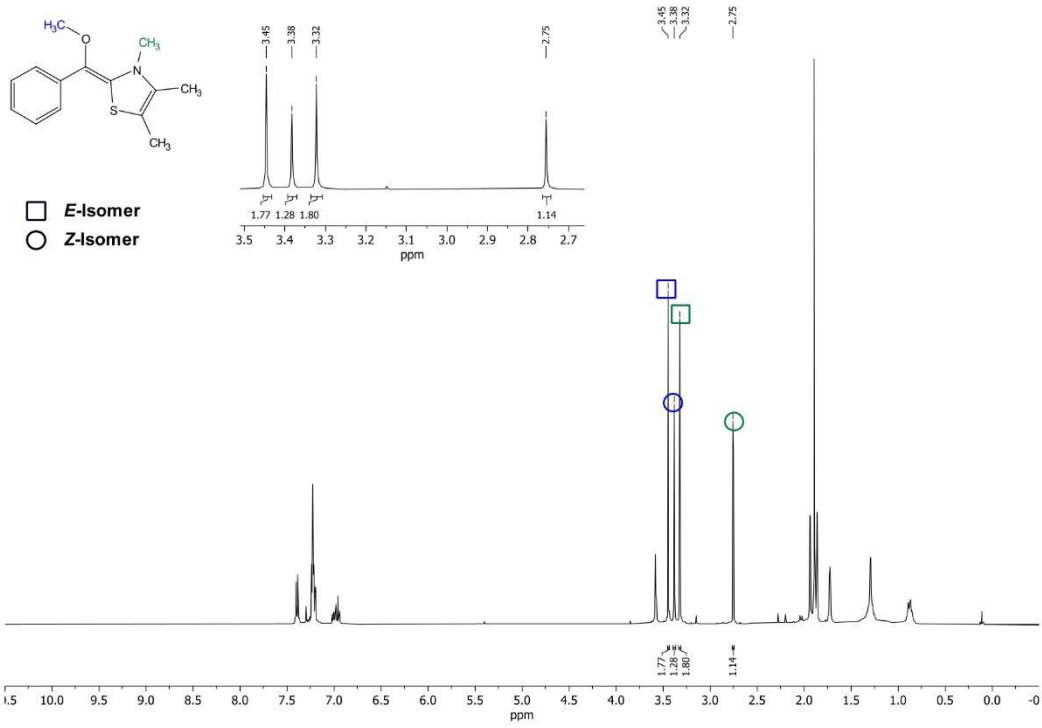

Irradiation for 60 min

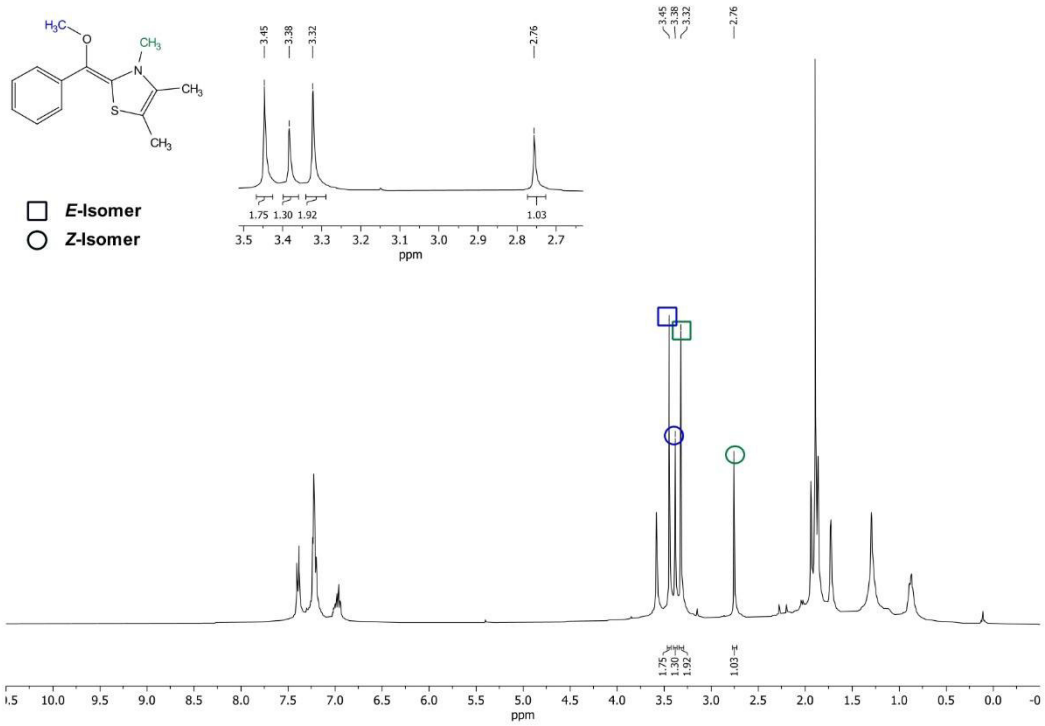

2.2 Irradiation in THF-d_8 containing 550 ppm H_2O

No irradiation

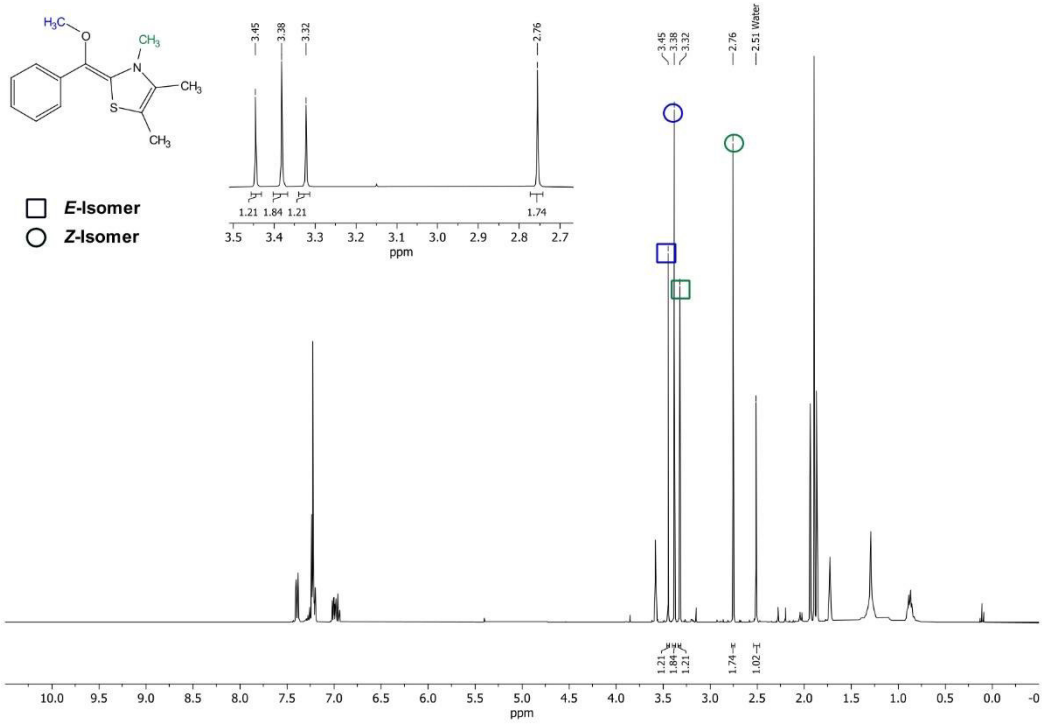

Irradiation for 60 min

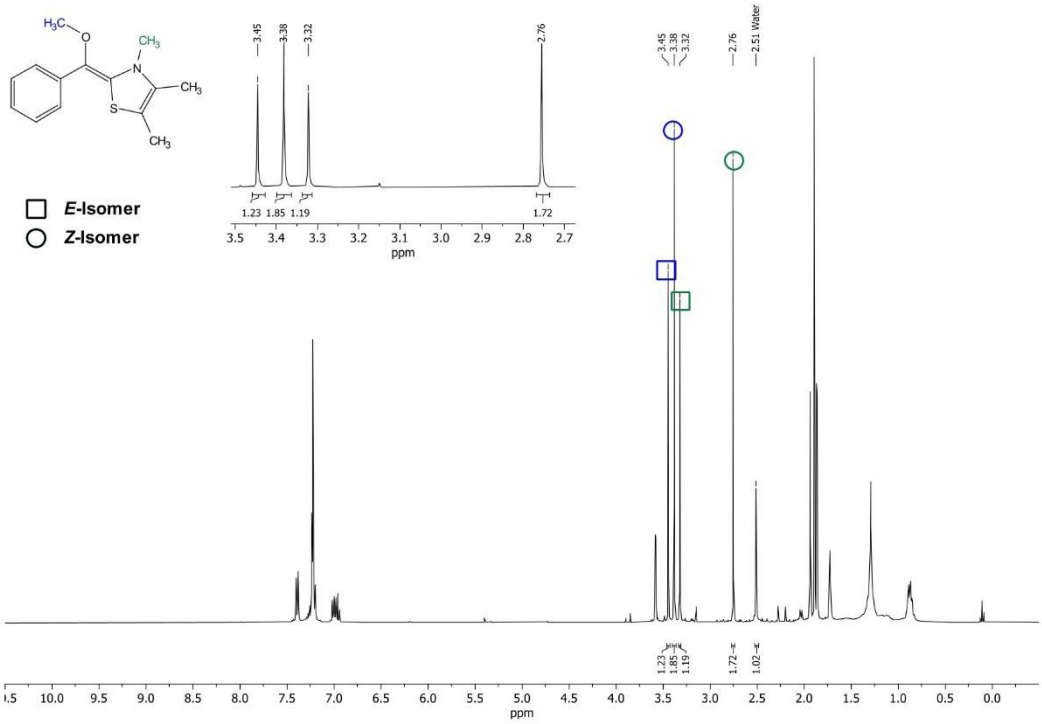

2.3 Irradiation in anhydrous MeCN-d_3

No irradiation

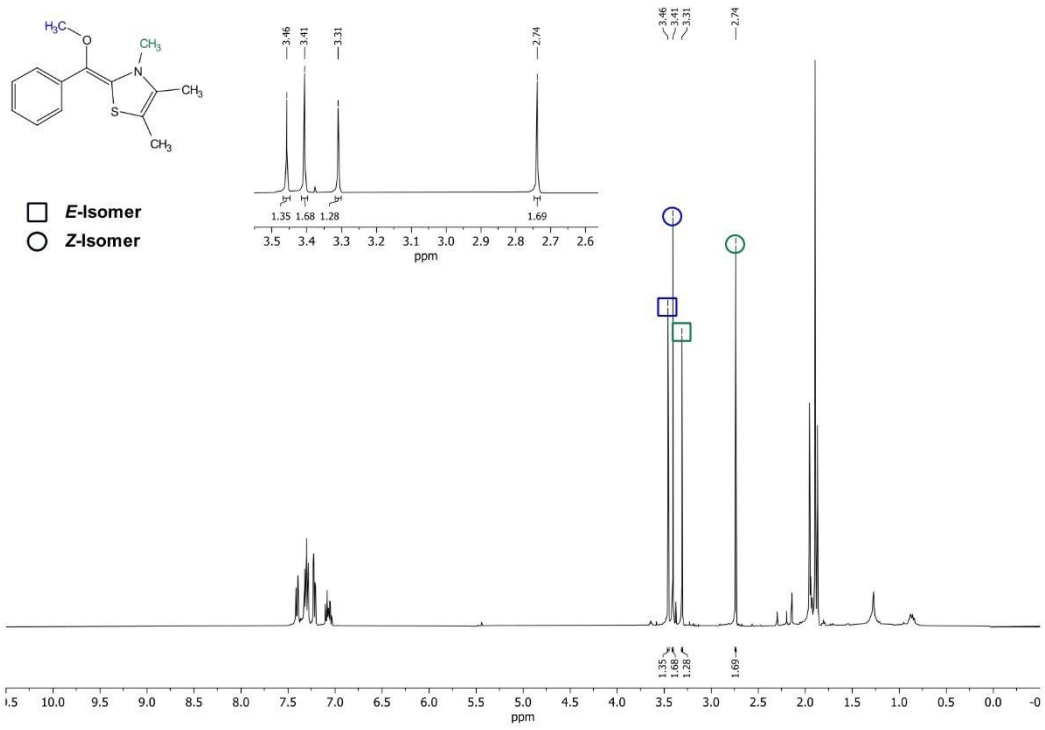

Irradiation for 60 min

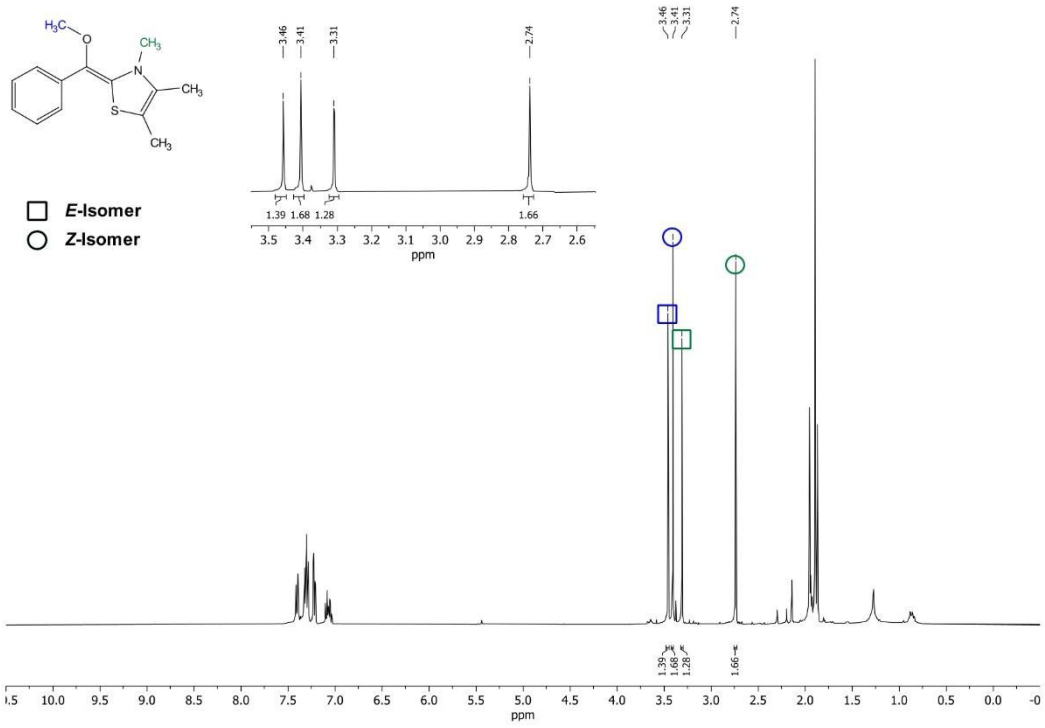

F. References

1. Huang, P.-Q., Yao, Z.-J. & Hsung, R. P. (eds.). *Efficiency in natural products total synthesis* (Wiley, Hoboken, NJ, 2018).
2. N L Batista, A., M Dos Santos, F., Batista, J. M. & Cass, Q. B. Enantiomeric Mixtures in Natural Product Chemistry: Separation and Absolute Configuration Assignment. *Molecules* **23,** 492; 10.3390/molecules23020492 (2018).
3. Scott, K. A. *et al.* Stereochemical diversity as a source of discovery in chemical biology. *Current Research in Chemical Biology* **2,** 100028; 10.1016/j.crchbi.2022.100028 (2022).
4. Elder, F. C. T., Feil, E. J., Snape, J., Gaze, W. H. & Kasprzyk-Hordern, B. The role of stereochemistry of antibiotic agents in the development of antibiotic resistance in the environment. *Environment International* **139,** 105681; 10.1016/j.envint.2020.105681 (2020).
5. Shen, Z., Lv, C. & Zeng, S. Significance and challenges of stereoselectivity assessing methods in drug metabolism. *Journal of pharmaceutical analysis* **6,** 1–10; 10.1016/j.jpha.2015.12.004 (2016).
6. Rehman, W., Arfons, L. M. & Lazarus, H. M. The rise, fall and subsequent triumph of thalidomide: lessons learned in drug development. *Therapeutic advances in hematology* **2,** 291–308; 10.1177/2040620711413165 (2011).
7. Grondal, C., Jeanty, M. & Enders, D. Organocatalytic cascade reactions as a new tool in total synthesis. *Nature Chem* **2,** 167–178; 10.1038/nchem.539 (2010).
8. Zhou, J. *Multi-catalyst system in asymmetric catalysis* (Wiley, Hoboken, New Jersey, 2015).
9. Zhao, G., Ye, Z. Q. & Wu, X. Y. Asymmetric Organocatalysis in the Total Synthesis of Complex Natural Products. In *Efficiency in natural products total synthesis,* edited by P.-Q. Huang, Z.-J. Yao & R. P. Hsung (Wiley, Hoboken, NJ, 2018), pp. 297–317.
10. Clark, J. H. Green chemistry: challenges and opportunities. *Green Chem.* **1,** 1–8; 10.1039/A807961G (1999).
11. Ivanković, A. Review of 12 Principles of Green Chemistry in Practice. *IJSGE* **6,** 39; 10.11648/j.ijrse.20170603.12 (2017).
12. Dunn, P. J. The importance of green chemistry in process research and development. *Chemical Society reviews* **41,** 1452–1461; 10.1039/c1cs15041c (2012).
13. Trost, B. M. On inventing reactions for atom economy. *Accounts of chemical research* **35,** 695–705; 10.1021/ar010068z (2002).
14. Das, J. P. & Marek, I. Enantioselective synthesis of all-carbon quaternary stereogenic centers in acyclic systems. *Chemical communications (Cambridge, England)* **47,** 4593–4623; 10.1039/c0cc05222a (2011).
15. Feng, J., Holmes, M. & Krische, M. J. Acyclic Quaternary Carbon Stereocenters via Enantioselective Transition Metal Catalysis. *Chemical reviews* **117,** 12564–12580; 10.1021/acs.chemrev.7b00385 (2017).
16. Cohen, Y., Cohen, A. & Marek, I. Creating Stereocenters within Acyclic Systems by C-C Bond Cleavage of Cyclopropanes. *Chemical reviews* **121,** 140–161; 10.1021/acs.chemrev.0c00167 (2021).
17. Schneider, T. F., Kaschel, J. & Werz, D. B. A new golden age for donor-acceptor cyclopropanes. *Angew. Chem. Int. Ed. Engl.* **53,** 5504–5523; 10.1002/anie.201309886 (2014).

18. Yedoyan, J., Wurzer, N., Klimczak, U., Ertl, T. & Reiser, O. Regio- and Stereoselective Synthesis of Functionalized Dihydropyridines, Pyridines, and 2H-Pyrans: Heck Coupling of Monocyclopropanated Heterocycles. *Angew. Chem. Int. Ed. Engl.* **58,** 3594–3598; 10.1002/anie.201813716 (2019).

19. Zellner, R. S.W. Benson: Thermochemical Kinetics, 2nd Ed. John Wiley & Sons, New York-London-Sydney-Toronto 1976. 320 Seiten, Preis: £ 16.-, $ 27.—. *Ber Bunsenges Phys Chem* **81,** 877–878; 10.1002/bbpc.19770810919 (1977).

20. Meijere, A. de. Bonding Properties of Cyclopropane and Their Chemical Consequences. *Angew. Chem. Int. Ed. Engl.* **18,** 809–826; 10.1002/anie.197908093 (1979).

21. Meazza, M., Guo, H. & Rios, R. Synthetic applications of vinyl cyclopropane opening. *Organic & biomolecular chemistry* **15,** 2479–2490; 10.1039/c6ob02647h (2017).

22. Anslyn, E. V. & Dougherty, D. A. *Modern physical organic chemistry* (University Science, Sausalito, CA, 2006).

23. Coulson, C. A. & Moffitt, W. E. Strain in Non-Tetrahedral Carbon Atoms. *The Journal of Chemical Physics* **15,** 151; 10.1063/1.1746450 (1947).

24. Zhao, C.-Y., Zhang, Y. & You, X.-Z. Theoretical Evaluation of Strain, Bent Bonds, and Bonding Behavior of Strained Organic Molecules. *J. Phys. Chem. A* **101,** 5174–5182; 10.1021/jp9634262 (1997).

25. Walsh, A. D. The structures of ethylene oxide, cyclopropane, and related molecules. *Trans. Faraday Soc.* **45,** 179; 10.1039/tf9494500179 (1949).

26. Pittman, C. U. & Olah, G. A. Stable Carbonium Ions. XVII. 1a Cyclopropyl Carbonium Ions and Protonated Cyclopropyl Ketones. *J. Am. Chem. Soc.* **87,** 5123–5132; 10.1021/ja00950a026 (1965).

27. Hanack, M. Stabilized vinyl cations. *Accounts of chemical research* **9,** 364–371; 10.1021/ar50106a004 (1976).

28. Xia, Y., Liu, X., Zheng, H., Lin, L. & Feng, X. Asymmetric synthesis of 2,3-dihydropyrroles by ring-opening/cyclization of cyclopropyl ketones using primary amines. *Angewandte Chemie (International ed. in English)* **54,** 227–230; 10.1002/anie.201407880 (2015).

29. Xia, Y. *et al.* Asymmetric Ring-Opening of Cyclopropyl Ketones with Thiol, Alcohol, and Carboxylic Acid Nucleophiles Catalyzed by a Chiral N,N'-Dioxide-Scandium(III) Complex. *Angewandte Chemie (International ed. in English)* **54,** 13748–13752; 10.1002/anie.201506909 (2015).

30. Guin, A., Rathod, T., Gaykar, R. N., Roy, T. & Biju, A. T. Lewis Acid Catalyzed Ring-Opening 1,3-Aminothiolation of Donor-Acceptor Cyclopropanes Using Sulfenamides. *Organic letters* **22,** 2276–2280; 10.1021/acs.orglett.0c00483 (2020).

31. Dange, N. S., Robert, F. & Landais, Y. Free-Radical Carbocyanation of Cyclopropenes: Stereocontrolled Access to All-Carbon Quaternary Stereocenters in Acyclic Systems. *Organic letters* **18,** 6156–6159; 10.1021/acs.orglett.6b03163 (2016).

32. Singh, S., Bruffaerts, J., Vasseur, A. & Marek, I. A unique Pd-catalysed Heck arylation as a remote trigger for cyclopropane selective ring-opening. *Nature communications* **8,** 14200; 10.1038/ncomms14200 (2017).

33. Trost, B. M. & Crawley, M. L. Asymmetric transition-metal-catalyzed allylic alkylations: applications in total synthesis. *Chemical reviews* **103,** 2921–2944; 10.1021/cr020027w (2003).

34. Shono, T., Yoshimura, T., Matsumura, Y. & Oda, R. Small ring compounds. XVIII. Formation of a .pi.-alylic palladium chloride complex from vinylcyclopropane derivatives. *J. Org. Chem.* **33,** 876–877; 10.1021/jo01266a098 (1968).

35. Nobelpreise 2010: Richard F. Heck / Ei-ichi Negishi / Akira Suzuki. *Angewandte Chemie* **122,** 8478; 10.1002/ange.201006286 (2010).

36. Heck, R. F. & Nolley, J. P. Palladium-catalyzed vinylic hydrogen substitution reactions with aryl, benzyl, and styryl halides. *J. Org. Chem.* **37,** 2320–2322; 10.1021/jo00979a024 (1972).

37. Miyaura, N. & Suzuki, A. Stereoselective synthesis of arylated (E)-alkenes by the reaction of alk-1-enylboranes with aryl halides in the presence of palladium catalyst. *J. Chem. Soc., Chem. Commun.,* 866; 10.1039/c39790000866 (1979).

38. Miyaura, N., Yamada, K. & Suzuki, A. A new stereospecific cross-coupling by the palladium-catalyzed reaction of 1-alkenylboranes with 1-alkenyl or 1-alkynyl halides. *Tetrahedron Letters* **20,** 3437–3440; 10.1016/S0040-4039(01)95429-2 (1979).

39. Beletskaya, I. P. & Cheprakov, A. V. The heck reaction as a sharpening stone of palladium catalysis. *Chem. Rev.* **100,** 3009–3066; 10.1021/cr9903048 (2000).

40. Miyaura, N. & Suzuki, A. Palladium-Catalyzed Cross-Coupling Reactions of Organoboron Compounds. *Chem. Rev.* **95,** 2457–2483; 10.1021/cr00039a007 (1995).

41. Suzuki, A. Synthetic studies via the cross-coupling reaction of organoboron derivatives with organic halides. *Pure and Applied Chemistry* **63,** 419–422; 10.1351/pac199163030419 (1991).

42. Suzuki, A. Recent advances in the cross-coupling reactions of organoboron derivatives with organic electrophiles, 1995–1998. *Journal of Organometallic Chemistry* **576,** 147–168; 10.1016/S0022-328X(98)01055-9 (1999).

43. Suzuki, M., Sawada, S., Yoshida, S., Eberhardt, A. & Saegusa, T. New ring-opening polymerization via a .pi.-allylpalladium complex. 2. Novel proton-transfer polymerization of vinylcyclopropane derivatives having two electron-withdrawing substituents. *Macromolecules* **26,** 4748–4750; 10.1021/ma00070a003 (1993).

44. Reiser, O. Catalytic Conversion of Furans and Pyrroles to Natural Products and Analogues Utilizing Donor-Acceptor Substituted Cyclopropanes as Key Intermediates. *Israel Journal of Chemistry* **56,** 531–539; 10.1002/ijch.201500103 (2016).

45. Löwdin, P.-O. Quantum Theory of Many-Particle Systems. II. Study of the Ordinary Hartree-Fock Approximation. *Phys. Rev.* **97,** 1490–1508; 10.1103/PhysRev.97.1490 (1955).

46. Weinhold, F. Natural bond orbital analysis: a critical overview of relationships to alternative bonding perspectives. *Journal of computational chemistry* **33,** 2363–2379; 10.1002/jcc.23060 (2012).

47. Glendening, E. D. & Weinhold, F. Natural resonance theory: I. General formalism. *J Comput Chem* **19,** 593–609; 10.1002/(SICI)1096-987X(19980430)19:6<593::AID-JCC3>3.3.CO;2-X (1998).

48. Glendening, E. D. & Weinhold, F. Natural resonance theory: II. Natural bond order and valency. *J Comput Chem* **19,** 610–627; 10.1002/(SICI)1096-987X(19980430)19:6<610::AID-JCC4>3.0.CO;2-U (1998).

49. Bruice, P. Y. *Organische Chemie.* 8th ed. (Pearson, München, 2022).

50. Dunnington, B. D. & Schmidt, J. R. Generalization of Natural Bond Orbital Analysis to Periodic Systems: Applications to Solids and Surfaces via Plane-Wave Density Functional Theory. *Journal of chemical theory and computation* **8,** 1902–1911; 10.1021/ct300002t (2012).

51. Glendening, E. D., Landis, C. R. & Weinhold, F. Natural bond orbital methods. *WIREs Comput Mol Sci* **2,** 1–42; 10.1002/wcms.51 (2012).

52. Foster, J. P. & Weinhold, F. Natural hybrid orbitals. *J. Am. Chem. Soc.* **102,** 7211–7218; 10.1021/ja00544a007 (1980).

53. Weinhold, F. & Landis, C. R. *Valency and bonding. A natural bond orbital donor-acceptor perspective* (Cambridge University Press, Cambridge, UK, New York, 2005).

54. Weinhold, F. & Landis, C. R. NATURAL BOND ORBITALS AND EXTENSIONS OF LOCALIZED BONDING CONCEPTS. *Chem. Educ. Res. Pract.* **2,** 91–104; 10.1039/B1RP90011K (2001).

55. Reed, A. E., Weinstock, R. B. & Weinhold, F. Natural population analysis. *The Journal of Chemical Physics* **83,** 735–746; 10.1063/1.449486 (1985).

56. Wurzer, N. *et al.* Heck-Type Coupling of Fused Bicyclic Vinylcyclopropanes: Synthesis of 1,2-Dihydropyridines, 2,3-Dihydro-1 H -azepines, 1,4-Cyclohexadienes, and 2 H -Pyrans. *ACS Catal.* **11,** 12019–12028; 10.1021/acscatal.1c02564 (2021).

57. Frisch, M. J. *et al. Gaussian 16 Rev. C.01* (Gaussian Inc., Wallingford, CT, 2016).

58. E. D. Glendening, J, K. Badenhoop, A. E. Reed, J. E. Carpenter, J. A. Bohmann, C. M. Morales, P. Karafiloglou, C. R. Landis, and F. Weinhold. *NBO 7.0* (University of Wisconsin, Madison, 2018).

59. Becke, A. D. Density-functional thermochemistry. III. The role of exact exchange. *The Journal of Chemical Physics* **98,** 5648–5652; 10.1063/1.464913 (1993).

60. Lee, C., Yang, W. & Parr, R. G. Development of the Colle-Salvetti correlation-energy formula into a functional of the electron density. *Physical review. B, Condensed matter* **37,** 785–789; 10.1103/physrevb.37.785 (1988).

61. Stephens, P. J., Devlin, F. J., Chabalowski, C. F. & Frisch, M. J. Ab Initio Calculation of Vibrational Absorption and Circular Dichroism Spectra Using Density Functional Force Fields. *J. Phys. Chem.* **98,** 11623–11627; 10.1021/j100096a001 (1994).

62. Vosko, S. H., Wilk, L. & Nusair, M. Accurate spin-dependent electron liquid correlation energies for local spin density calculations: a critical analysis. *Can. J. Phys.* **58,** 1200–1211; 10.1139/p80-159 (1980).

63. Grimme, S., Antony, J., Ehrlich, S. & Krieg, H. A consistent and accurate ab initio parametrization of density functional dispersion correction (DFT-D) for the 94 elements H-Pu. *The Journal of Chemical Physics* **132,** 154104; 10.1063/1.3382344 (2010).

64. Grimme, S., Ehrlich, S. & Goerigk, L. Effect of the damping function in dispersion corrected density functional theory. *J Comput Chem* **32,** 1456–1465; 10.1002/jcc.21759 (2011).

65. Binning, R. C. & Curtiss, L. A. Compact contracted basis sets for third-row atoms: Ga–Kr. *J Comput Chem* **11,** 1206–1216; 10.1002/jcc.540111013 (1990).

66. Blaudeau, J.-P., McGrath, M. P., Curtiss, L. A. & Radom, L. Extension of Gaussian-2 (G2) theory to molecules containing third-row atoms K and Ca. *The Journal of Chemical Physics* **107,** 5016–5021; 10.1063/1.474865 (1997).

67. Ditchfield, R., Hehre, W. J. & Pople, J. A. Self-Consistent Molecular-Orbital Methods. IX. An Extended Gaussian-Type Basis for Molecular-Orbital Studies of Organic Molecules. *The Journal of Chemical Physics* **54,** 724–728; 10.1063/1.1674902 (1971).

68. Francl, M. M. *et al.* Self-consistent molecular orbital methods. XXIII. A polarization-type basis set for second-row elements. *The Journal of Chemical Physics* **77,** 3654–3665; 10.1063/1.444267 (1982).

69. Gordon, M. S. The isomers of silacyclopropane. *Chemical Physics Letters* **76,** 163–168; 10.1016/0009-2614(80)80628-2 (1980).

70. Hariharan, P. C. & Pople, J. A. The influence of polarization functions on molecular orbital hydrogenation energies. *Theoret. Chim. Acta* **28,** 213–222; 10.1007/BF00533485 (1973).

71. Hariharan, P. C. & Pople, J. A. Accuracy of AH n equilibrium geometries by single determinant molecular orbital theory. *Molecular Physics* **27,** 209–214; 10.1080/00268977400100171 (1974).

72. Hehre, W. J., Ditchfield, R. & Pople, J. A. Self—Consistent Molecular Orbital Methods. XII. Further Extensions of Gaussian—Type Basis Sets for Use in Molecular Orbital Studies of Organic Molecules. *The Journal of Chemical Physics* **56,** 2257–2261; 10.1063/1.1677527 (1972).

73. Rassolov, V. A., Pople, J. A., Ratner, M. A. & Windus, T. L. 6-31G* basis set for atoms K through Zn. *The Journal of Chemical Physics* **109,** 1223–1229; 10.1063/1.476673 (1998).

74. Rassolov, V. A., Ratner, M. A., Pople, J. A., Redfern, P. C. & Curtiss, L. A. 6-31G* basis set for third-row atoms. *J Comput Chem* **22,** 976–984; 10.1002/jcc.1058 (2001).

75. Clark, T., Chandrasekhar, J., Spitznagel, G. W. & Schleyer, P. V. R. Efficient diffuse function-augmented basis sets for anion calculations. III. The 3-21+G basis set for first-row elements, Li–F. *J Comput Chem* **4,** 294–301; 10.1002/jcc.540040303 (1983).

76. Frisch, M. J., Pople, J. A. & Binkley, J. S. Self-consistent molecular orbital methods 25. Supplementary functions for Gaussian basis sets. *The Journal of Chemical Physics* **80,** 3265–3269; 10.1063/1.447079 (1984).

77. *Modern Theoretical Chemistry, Ed. HF Schaefer III, Vol. 3* (1977).

78. Hay, P. J. & Wadt, W. R. Ab initio effective core potentials for molecular calculations. Potentials for K to Au including the outermost core orbitals. *The Journal of Chemical Physics* **82,** 299–310; 10.1063/1.448975 (1985).

79. Hay, P. J. & Wadt, W. R. Ab initio effective core potentials for molecular calculations. Potentials for the transition metal atoms Sc to Hg. *The Journal of Chemical Physics* **82,** 270–283; 10.1063/1.448799 (1985).

80. Wadt, W. R. & Hay, P. J. Ab initio effective core potentials for molecular calculations. Potentials for main group elements Na to Bi. *The Journal of Chemical Physics* **82,** 284–298; 10.1063/1.448800 (1985).

81. Marenich, A. V., Cramer, C. J. & Truhlar, D. G. Universal solvation model based on solute electron density and on a continuum model of the solvent defined by the bulk dielectric constant and atomic surface tensions. *The journal of physical chemistry. B* **113,** 6378–6396; 10.1021/jp810292n (2009).

82. Dennington, R., Keith, T. A. & Millam, J. M. *GaussView, Version 6* (Semichem Inc., Shawnee Mission, KS, 2016).

83. Pracht, P., Bohle, F. & Grimme, S. Automated exploration of the low-energy chemical space with fast quantum chemical methods. *Physical chemistry chemical physics : PCCP* **22,** 7169–7192; 10.1039/c9cp06869d (2020).

84. Pracht, P. *et al.* CREST-A program for the exploration of low-energy molecular chemical space. *The Journal of Chemical Physics* **160**; 10.1063/5.0197592 (2024).

85. Bannwarth, C., Ehlert, S. & Grimme, S. GFN2-xTB-An Accurate and Broadly Parametrized Self-Consistent Tight-Binding Quantum Chemical Method with Multipole Electrostatics and Density-Dependent Dispersion Contributions. *Journal of chemical theory and computation* **15,** 1652–1671; 10.1021/acs.jctc.8b01176 (2019).

86. Andrew Gilbert. *IQmol* (Q-Chem Inc., 2019).

87. Claude Legault. *CYLview20* (Université de Sherbrooke, Legault, CY, 2020).

88. Angnes, R. A. *mechaSVG* (GitHub repository, 2020).

89. Griller, D. & Ingold, K. U. Free-radical clocks. *Accounts of chemical research* **13,** 317–323; 10.1021/ar50153a004 (1980).

90. Nonhebel, D. C. The chemistry of cyclopropylmethyl and related radicals. *Chem. Soc. Rev.* **22,** 347; 10.1039/cs9932200347 (1993).

91. Yuki Takekawa & Kozo Shishido. Selective cleavage of the trisubstituted cyclopropanes via cyclopropylcarbinyl radical fragmentation. *Tetrahedron Letters* **40,** 6817–6820; 10.1016/S0040-4039(99)01366-0 (1999).

92. Harrar, K. & Reiser, O. Enantioselective synthesis of (-)-paeonilide. *Chemical communications (Cambridge, England)* **48,** 3457–3459; 10.1039/C2CC18172J (2012).

93. Pilsl, L. K. A., Ertl, T. & Reiser, O. Enantioselective Three-Step Synthesis of Homo-β-proline: A Donor-Acceptor Cyclopropane as Key Intermediate. *Organic letters* **19,** 2754–2757; 10.1021/acs.orglett.7b01111 (2017).

94. Mennucci, B. *et al.* Polarizable Continuum Model (PCM) Calculations of Solvent Effects on Optical Rotations of Chiral Molecules. *J. Phys. Chem. A* **106,** 6102–6113; 10.1021/jp020124t (2002).

95. Miertuš, S. & Tomasi, J. Approximate evaluations of the electrostatic free energy and internal energy changes in solution processes. *Chemical Physics* **65,** 239–245; 10.1016/0301-0104(82)85072-6 (1982).

96. Mattay, J. *Photochemical Key Steps in Organic Synthesis. An Experimental Course Book.* 1st ed. (Wiley-VCH, Weinheim, 2008).

97. Brückner, R. *Reaktionsmechanismen. Organische Reaktionen, Stereochemie, moderne Synthesemethoden.* 3rd ed. (Spektrum Akad. Verl., Berlin, Heidelberg, 2011).

98. Clayden, J., Greeves, N. & Warren, S. *Organische Chemie.* 2nd ed. (Springer Berlin Heidelberg, Berlin, Heidelberg, 2013).

99. Nikolai Wurzer. Palladium-catalyzed ring opening of fused bicyclic vinylcyclopropanes. Dissertation. Universität Regensburg, 2021.

100. Glendening, E. D., Badenhoop, J. K. & Weinhold, F. Natural resonance theory: III. Chemical applications. *J Comput Chem* **19,** 628–646; 10.1002/(SICI)1096-987X(19980430)19:6<628::AID-JCC5>3.0.CO;2-T (1998).

101. Eckl, R. *et al.* Stereoselective Synthesis of Biologically Relevant Tetrahydropyridines and Dihydro-2H-pyrans via Ring-Expansion of Monocyclopropanated Heterocycles. *ACS organic & inorganic Au* **2,** 169–174; 10.1021/acsorginorgau.1c00042 (2022).

102. Asao, N., Nogami, T., Takahashi, K. & Yamamoto, Y. Pd(II) acts simultaneously as a Lewis acid and as a transition-metal catalyst: synthesis of cyclic alkenyl ethers from acetylenic aldehydes. *J. Am. Chem. Soc.* **124,** 764–765; 10.1021/ja017366b (2002).

103. Barciszewski, J., Jurczak, J., Porowski, S., Specht, T. & Erdmann, V. A. The role of water structure in conformational changes of nucleic acids in ambient and high-pressure conditions. *European journal of biochemistry* **260,** 293–307; 10.1046/j.1432-1327.1999.00184.x (1999).

104. Berger, I., Egli, M. & Rich, A. Inter-strand C-H…O hydrogen bonds stabilizing four-stranded intercalated molecules: stereoelectronic effects of O4' in cytosine-rich DNA. *Proceedings of the National Academy of Sciences of the United States of America* **93,** 12116–12121; 10.1073/pnas.93.22.12116 (1996).

105. Egli, M. & Gessner, R. V. Stereoelectronic effects of deoxyribose O4' on DNA conformation. *Proceedings of the National Academy of Sciences of the United States of America* **92,** 180–184; 10.1073/pnas.92.1.180 (1995).

106. Hellgren, M., Kaiser, C., Haij, S. de, Norberg, A. & Höög, J.-O. A hydrogen-bonding network in mammalian sorbitol dehydrogenase stabilizes the tetrameric state and is essential for the catalytic power. *Cellular and molecular life sciences : CMLS* **64,** 3129–3138; 10.1007/s00018-007-7318-1 (2007).

107. Jiang, L. & Lai, L. CH…O hydrogen bonds at protein-protein interfaces. *The Journal of biological chemistry* **277,** 37732–37740; 10.1074/jbc.M204514200 (2002).

108. Ornstein, R. L. & Zheng, Y. J. Ab initio quantum mechanics analysis of imidazole C-H…O water hydrogen bonding and a molecular mechanics forcefield correction. *Journal of biomolecular structure & dynamics* **14,** 657–665; 10.1080/07391102.1997.10508169 (1997).

109. Williams, M. A. & Ladbury, J. E. Hydrogen Bonds in Protein-Ligand Complexes. In *Protein-ligand interactions. From molecular recognition to drug design,* edited by H.-J. Böhm & G. Schneider. 2nd ed. (Wiley-VCH, Weinheim, 2006), pp. 137–161.

110. PAULING, L., COREY, R. B. & BRANSON, H. R. The structure of proteins; two hydrogen-bonded helical configurations of the polypeptide chain. *Proceedings of the National Academy of Sciences of the United States of America* **37,** 205–211; 10.1073/pnas.37.4.205 (1951).

111. PAULING, L. & COREY, R. B. Configurations of Polypeptide Chains With Favored Orientations Around Single Bonds: Two New Pleated Sheets. *Proceedings of the National Academy of Sciences of the United States of America* **37,** 729–740; 10.1073/pnas.37.11.729 (1951).

112. Böhm, H.-J. & Schneider, G. (eds.). *Protein-ligand interactions. From molecular recognition to drug design.* 2nd ed. (Wiley-VCH, Weinheim, 2006).

113. Guerrero-Corella, A., Fraile, A. & Alemán, J. Intramolecular Hydrogen-Bond Activation: Strategies, Benefits, and Influence in Catalysis. *ACS organic & inorganic Au* **2,** 197–204; 10.1021/acsorginorgau.1c00053 (2022).

114. Dodson, G. & Wlodawer, A. Catalytic triads and their relatives. *Trends in biochemical sciences* **23,** 347–352; 10.1016/s0968-0004(98)01254-7 (1998).

115. Buller, A. R. & Townsend, C. A. Intrinsic evolutionary constraints on protease structure, enzyme acylation, and the identity of the catalytic triad. *Proceedings of the National Academy of Sciences of the United States of America* **110,** E653-61; 10.1073/pnas.1221050110 (2013).

116. Benjamin List. Proline-catalyzed asymmetric reactions. *Tetrahedron* **58,** 5573–5590; 10.1016/S0040-4020(02)00516-1 (2002).

117. Brunel, J. M. BINOL: a versatile chiral reagent. *Chem. Rev.* **105,** 857–897; 10.1021/cr040079g (2005).

118. Curran, D. P. & Kuo, L. H. Altering the Stereochemistry of Allylation Reactions of Cyclic .alpha.-Sulfinyl Radicals with Diarylureas. *J. Org. Chem.* **59,** 3259–3261; 10.1021/jo00091a007 (1994).

119. Dam, G. K., Let, S., Jaiswal, V. & Ghosh, S. K. Urea-Tethered Porous Organic Polymer (POP) as an Efficient Heterogeneous Catalyst for Hydrogen Bond Donating Organocatalysis and Continuous Flow Reaction. *ACS Sustainable Chem. Eng.* **12,** 3000–3011; 10.1021/acssuschemeng.3c06108 (2024).

120. Doyle, A. G. & Jacobsen, E. N. Small-molecule H-bond donors in asymmetric catalysis. *Chem. Rev.* **107,** 5713–5743; 10.1021/cr068373r (2007).

121. Hine, J., Linden, S. M. & Kanagasabapathy, V. M. 1,8-biphenylenediol is a double-hydrogen-bonding catalyst for reaction of an epoxide with a nucleophile. *J. Am. Chem. Soc.* **107,** 1082–1083; 10.1021/ja00290a067 (1985).

122. Huang, Y., Unni, A. K., Thadani, A. N. & Rawal, V. H. Hydrogen bonding: single enantiomers from a chiral-alcohol catalyst. *Nature* **424,** 146; 10.1038/424146a (2003).

123. List, B. Proline-catalyzed asymmetric reactions. *Tetrahedron* **58,** 5573–5590; 10.1016/S0040-4020(02)00516-1 (2002).

124. List, B., Lerner, R. A. & Barbas, C. F. Proline-Catalyzed Direct Asymmetric Aldol Reactions. *J. Am. Chem. Soc.* **122,** 2395–2396; 10.1021/ja994280y (2000).

125. Silverman, R. B. *The organic chemistry of enzyme-catalyzed reactions* (Academic Press, An Imprint of Elsevier, San Diego, California, 2002).

126. Sohtome, Y., Tanatani, A., Hashimoto, Y. & Nagasawa, K. Development of bis-thiourea-type organocatalyst for asymmetric Baylis–Hillman reaction. *Tetrahedron Letters* **45,** 5589–5592; 10.1016/j.tetlet.2004.05.137 (2004).

127. Okino, T., Hoashi, Y. & Takemoto, Y. Enantioselective Michael reaction of malonates to nitroolefins catalyzed by bifunctional organocatalysts. *J. Am. Chem. Soc.* **125,** 12672–12673; 10.1021/ja036972z (2003).

128. Cao, C.-L., Ye, M.-C., Sun, X.-L. & Tang, Y. Pyrrolidine-thiourea as a bifunctional organocatalyst: highly enantioselective Michael addition of cyclohexanone to nitroolefins. *Organic letters* **8,** 2901–2904; 10.1021/ol060481c (2006).

129. Gaunt, M. J., Johansson, C. C. C., McNally, A. & Vo, N. T. Enantioselective organocatalysis. *Drug discovery today* **12,** 8–27; 10.1016/j.drudis.2006.11.004 (2007).

130. Palomo, C., Oiarbide, M. & García, J. M. Current progress in the asymmetric aldol addition reaction. *Chemical Society reviews* **33,** 65–75; 10.1039/b202901d (2004).

131. Sakthivel, K., Notz, W., Bui, T. & Barbas, C. F. Amino acid catalyzed direct asymmetric aldol reactions: a bioorganic approach to catalytic asymmetric carbon-carbon bond-forming reactions. *J. Am. Chem. Soc.* **123,** 5260–5267; 10.1021/ja010037z (2001).

132. Nobel Prize for Chemistry for 1950: Prof. O. Diels and Prof. K. Alder. *Nature* **166,** 889; 10.1038/166889a0 (1950).

133. Denmark, S. E. (ed.). *Organic reactions* (Wiley, Hoboken, N.J., 2006-).

134. Fringuelli, F. & Taticchi, A. *Dienes in the Diels-Alder reaction* (J. Wiley & Sons, New York, Chichester, Brisbane, 1990).

135. Holmes, H. L. The Diels-Alder Reaction Ethylenic and Acetylenic Dienophiles. In *Organic reactions,* edited by S. E. Denmark (Wiley, Hoboken, N.J., 2006-), pp. 60–173.

136. Kloetzel, M. C. The Diels-Alder reactions with maleic anhydride. *Org React* **4,** 1–59 (1948).

137. Nguyên-trong-Anh. *Die Woodward-Hoffmann-Regeln und ihre Anwendung. Enth. 2 Tab* (Verl. Chemie, Weinheim/Bergstr., 1972).

138. Brückner, R. *Reaktionsmechanismen. Organische Reaktionen, Stereochemie, Moderne Synthesemethoden.* 3rd ed. (Springer Spektrum, Berlin, Heidelberg, 2015).

139. Buddrus, J. & Schmidt, B. *Grundlagen der Organischen Chemie.* 4th ed. (De Gruyter, Berlin, Boston, 2011).

140. Lüning, U. *Organische Reaktionen. Eine Einführung in Reaktionswege und Mechanismen.* 2nd ed. (Elsevier, Spektrum, Akad. Verl., München, Heidelberg, 2007).

141. Zimmerman, H. E. & Traxler, M. D. The Stereochemistry of the Ivanov and Reformatsky Reactions. I. *J. Am. Chem. Soc.* **79,** 1920–1923; 10.1021/ja01565a041 (1957).

142. Chia, M. *et al.* Mechanistic insights into ring-opening and decarboxylation of 2-pyrones in liquid water and tetrahydrofuran. *J. Am. Chem. Soc.* **135,** 5699–5708; 10.1021/ja312075r (2013).

143. Gupta, S., Alam, M. I., Khan, T. S., Sinha, N. & Haider, M. A. On the mechanism of retro-Diels–Alder reaction of partially saturated 2-pyrones to produce biorenewable chemicals. *RSC advances* **6,** 60433–60445 (2016).

144. The Royal Swedish Academy of Sciences. An ingenious tool for building molecules. Available at https://www.nobelprize.org/prizes/chemistry/2021/press-release/ (2021).

145. Oliveira, V., Cardoso, M. & Forezi, L. Organocatalysis: A Brief Overview on Its Evolution and Applications. *Catalysts* **8,** 605; 10.3390/catal8120605 (2018).

146. Bourissou, D., Guerret, O., Gabbaï, F. P. & Bertrand, G. Stable Carbenes. *Chem. Rev.* **100,** 39–92; 10.1021/cr940472u (2000).

147. Phillips, E. M., Chan, A. & Scheidt, K. A. Discovering new reactions with N-heterocyclic carbene catalysis. *Aldrichimica Acta* **42,** 55 (2009).

148. Ukai, T., Tanaka, R. & Dokawa, T. A new catalyst for acyloin condensation. *J. Pharm. Soc. Jpn* **63,** 296–300 (1943).

149. Breslow, R. On the Mechanism of Thiamine Action. IV. 1 Evidence from Studies on Model Systems. *J. Am. Chem. Soc.* **80,** 3719–3726; 10.1021/ja01547a064 (1958).

150. Berkessel, A. *et al.* Umpolung by N-heterocyclic carbenes: generation and reactivity of the elusive 2,2-diamino enols (Breslow intermediates). *Angew. Chem. Int. Ed. Engl.* **51,** 12370–12374; 10.1002/anie.201205878 (2012).

151. Berkessel, A., Yatham, V. R., Elfert, S. & Neudörfl, J.-M. Charakterisierung der Schlüsselintermediate von carbenkatalysierten Umpolungen durch Kristallstrukturanalyse/NMR-Spektroskopie: Breslow-Intermediate, Homoenolate und Azoliumenolate. *Angewandte Chemie* **125,** 11364–11369; 10.1002/ange.201303107 (2013).

152. Rehbein, J., Ruser, S.-M. & Phan, J. NHC-catalysed benzoin condensation - is it all down to the Breslow intermediate? *Chemical science* **6,** 6013–6018; 10.1039/c5sc02186c (2015).

153. White, M. J. & Leeper, F. J. Kinetics of the thiazolium ion-catalyzed benzoin condensation. *J. Org. Chem.* **66,** 5124–5131; 10.1021/jo010244h (2001).

154. Phan, J., Ruser, S.-M., Zeitler, K. & Rehbein, J. NHC-Stabilized Radicals in the Formal Hydroacylation Reaction of Alkynes. *Eur J Org Chem* **2019,** 557–561; 10.1002/ejoc.201801185 (2019).

155. Regnier, V. *et al.* What Are the Radical Intermediates in Oxidative N-Heterocyclic Carbene Organocatalysis? *J. Am. Chem. Soc.* **141,** 1109–1117; 10.1021/jacs.8b11824 (2019).

156. Albini, A. & Fagnoni, M. 1908: Giacomo Ciamician and the concept of green chemistry. *ChemSusChem* **1,** 63–66; 10.1002/cssc.200700015 (2008).

157. Ciamician, G. THE PHOTOCHEMISTRY OF THE FUTURE. *Science (New York, N.Y.)* **36,** 385–394; 10.1126/science.36.926.385 (1912).

158. Srinivasan, R. Mechanism of the photochemical valence tautomerization of 1,3-butadienes. *J. Am. Chem. Soc.* **90,** 4498–4499; 10.1021/ja01018a080 (1968).

159. Fleming, I. *Molekülorbitale und Reaktionen organischer Verbindungen.* 1st ed. (Wiley-VCH, Weinheim, 2012).

160. Schultz, D. M. & Yoon, T. P. Solar synthesis: prospects in visible light photocatalysis. *Science (New York, N.Y.)* **343,** 1239176; 10.1126/science.1239176 (2014).

161. *Photochemie Wiley* (1998).

162. Shaw, M. H., Twilton, J. & MacMillan, D. W. C. Photoredox Catalysis in Organic Chemistry. *J. Org. Chem.* **81,** 6898–6926; 10.1021/acs.joc.6b01449 (2016).

163. Strieth-Kalthoff, F., James, M. J., Teders, M., Pitzer, L. & Glorius, F. Energy transfer catalysis mediated by visible light: principles, applications, directions. *Chemical Society reviews* **47,** 7190–7202 (2018).

164. Lakowicz, J. R. *Principles of fluorescence spectroscopy* (Springer, 2006).

165. King, C., Barbiellini, B., Moser, D. & Renugopalakrishnan, V. Exactly soluble model of resonant energy transfer between molecules. *Phys. Rev. B* **85**; 10.1103/PhysRevB.85.125106 (2012).

166. Lazarides, T., Sykes, D., Faulkner, S., Barbieri, A. & Ward, M. D. On the mechanism of d-f energy transfer in RuII/LnIII and OsII/LnIII dyads: Dexter-type energy transfer over a distance of 20 A. *Chemistry (Weinheim an der Bergstrasse, Germany)* **14,** 9389–9399; 10.1002/chem.200800600 (2008).

167. Albrecht, Ł., Jiang, H. & Jørgensen, K. A. A simple recipe for sophisticated cocktails: organocatalytic one-pot reactions--concept, nomenclature, and future perspectives. *Angew. Chem. Int. Ed. Engl.* **50,** 8492–8509; 10.1002/anie.201102522 (2011).

168. Enders, D., Grondal, C. & Hüttl, M. R. M. Asymmetric organocatalytic domino reactions. *Angewandte Chemie (International ed. in English)* **46,** 1570–1581; 10.1002/anie.200603129 (2007).

169. Walji, A. & MacMillan, D. Strategies to Bypass the Taxol Problem. Enantioselective Cascade Catalysis, a New Approach for the Efficient Construction of Molecular Complexity. *Synlett* **2007,** 1477–1489; 10.1055/s-2007-980382 (2007).

170. Wende, R. C. & Schreiner, P. R. ChemInform Abstract: Evolution of Asymmetric Organocatalysis: Multi- and Retrocatalysis. *ChemInform* **43**; 10.1002/chin.201242226 (2012).

171. Zhou, J. Recent advances in multicatalyst promoted asymmetric tandem reactions. *Chemistry, an Asian journal* **5,** 422–434; 10.1002/asia.200900458 (2010).

172. Malakar, C. C., Dell'Amico, L. & Zhang, W. Dual Catalysis in Organic Synthesis: Current Challenges and New Trends. *Eur J Org Chem* **26**; 10.1002/ejoc.202201114 (2023).

173. Skubi, K. L., Blum, T. R. & Yoon, T. P. Dual Catalysis Strategies in Photochemical Synthesis. *Chem. Rev.* **116,** 10035–10074; 10.1021/acs.chemrev.6b00018 (2016).

174. Mavroskoufis, A., Jakob, M. & Hopkinson, M. N. Light-Promoted Organocatalysis with N-Heterocyclic Carbenes. *ChemPhotoChem* **4,** 5147–5153; 10.1002/cptc.202000120 (2020).

175. DiRocco, D. A. & Rovis, T. Catalytic asymmetric α-acylation of tertiary amines mediated by a dual catalysis mode: N-heterocyclic carbene and photoredox catalysis. *J. Am. Chem. Soc.* **134,** 8094–8097 (2012).

176. Ishii, T., Kakeno, Y., Nagao, K. & Ohmiya, H. N-Heterocyclic Carbene-Catalyzed Decarboxylative Alkylation of Aldehydes. *J. Am. Chem. Soc.* **141,** 3854–3858; 10.1021/jacs.9b00880 (2019).

177. Song, R. & Chi, Y. R. N-Heterocyclic Carbene Catalyzed Radical Coupling of Aldehydes with Redox-Active Esters. *Angew. Chem. Int. Ed. Engl.* **58,** 8628–8630; 10.1002/anie.201902792 (2019).

178. Leifert, D. & Studer, A. The Persistent Radical Effect in Organic Synthesis. *Angew. Chem. Int. Ed. Engl.* **59,** 74–108; 10.1002/anie.201903726 (2020).

179. Ishii, T., Nagao, K. & Ohmiya, H. Recent advances in N-heterocyclic carbene-based radical catalysis. *Chemical science* **11,** 5630–5636; 10.1039/d0sc01538e (2020).

180. Qing-Yuan Meng, Nadine Döben & Armido Studer. Cooperative NHC and Photoredox Catalysis for the Synthesis of β-Trifluoromethylated Alkyl Aryl Ketones. *Angewandte Chemie International Edition* **59,** 19956–19960 (2020).

181. Studer, A., Liu, K. & Schwenzer, M. Radical NHC Catalysis. *ACS Catal.* **12,** 11984–11999; 10.1021/acscatal.2c03996 (2022).

182. Chergui, M. 1.19 ultrafast structural dynamics of biological systems. *Comprehensive Biophysics,* 398–424 (2012).

183. Edinburgh Instruments. An Introduction to Flash Photolysis using the LP980 Spectrometer. Available at https://www.edinst.com/wp-content/uploads/2018/03/An-Introduction-to-Flash-Photolysis-using-the-LP980-Spectrometer.pdf.

184. Edinburgh Instruments. What is Transient Absorption Spectroscopy? Available at https://www.edinst.com/blog/pump-probe-transient-absorption-spectroscopy/.

185. Berera, R., van Grondelle, R. & Kennis, J. T. M. Ultrafast transient absorption spectroscopy: principles and application to photosynthetic systems. *Photosynthesis Research* **101,** 105–118; 10.1007/s11120-009-9454-y (2009).

186. Nürnberger, P. Time-Resolved Laser Spectroscopy. a lecture on how to unveil photochemical reactions with advanced lasers. Vorlesungsskript. Universität Regensburg, 2019.

187. Barletta, G., Huskey, W. P. & Jordan, F. Observation of a 2-.alpha.-enamine from a 2-(methoxyphenylmethyl)-3,4-dimethylthiazolium salt in water: implications for catalysis by thiamin diphosphate-dependent .alpha.-keto acid decarboxylases. *J. Am. Chem. Soc.* **114,** 7607–7608; 10.1021/ja00045a069 (1992).

188. Chen, Y.-T., Barletta, G. L., Haghjoo, K., Cheng, J. T. & Jordan, F. Reactions of Benzaldehyde with Thiazolium Salts in Me2SO: Evidence for Initial Formation of 2-(.alpha.-Hydroxybenzyl)thiazolium by

Nucleophilic Addition, and for Dramatic Solvent Effects on Benzoin Formation. *J. Org. Chem.* **59,** 7714–7722; 10.1021/jo00104a030 (1994).

189. Balasubramani, S. G. *et al.* TURBOMOLE: Modular program suite for ab initio quantum-chemical and condensed-matter simulations. *The Journal of Chemical Physics* **152,** 184107; 10.1063/5.0004635 (2020).

190. University of Karlsruhe, Forschungszentrum Karlsruhe GmbH. *TURBOMOLE, Version 7.5.1* (Turbomole GmbH, 2020).

191. Schäfer, A., Horn, H. & Ahlrichs, R. Fully optimized contracted Gaussian basis sets for atoms Li to Kr. *The Journal of Chemical Physics* **97,** 2571–2577; 10.1063/1.463096 (1992).

192. Schäfer, A., Huber, C. & Ahlrichs, R. Fully optimized contracted Gaussian basis sets of triple zeta valence quality for atoms Li to Kr. *The Journal of Chemical Physics* **100,** 5829–5835; 10.1063/1.467146 (1994).

193. Weigend, F. Accurate Coulomb-fitting basis sets for H to Rn. *Physical chemistry chemical physics : PCCP* **8,** 1057–1065; 10.1039/b515623h (2006).

194. Weigend, F. & Ahlrichs, R. Balanced basis sets of split valence, triple zeta valence and quadruple zeta valence quality for H to Rn: Design and assessment of accuracy. *Physical chemistry chemical physics : PCCP* **7,** 3297–3305; 10.1039/b508541a (2005).

195. Rappoport, D. & Furche, F. Property-optimized gaussian basis sets for molecular response calculations. *The Journal of Chemical Physics* **133,** 134105; 10.1063/1.3484283 (2010).

196. Klamt, A. & Schüürmann, G. COSMO: a new approach to dielectric screening in solvents with explicit expressions for the screening energy and its gradient. *J. Chem. Soc., Perkin Trans. 2,* 799–805; 10.1039/P29930000799 (1993).

197. Marques, M. A. L. *et al. Time-Dependent Density Functional Theory* (Springer, Berlin, Heidelberg, 2006).

198. Schirmer, J. Beyond the random-phase approximation: A new approximation scheme for the polarization propagator. *Phys. Rev. A* **26,** 2395–2416; 10.1103/PhysRevA.26.2395 (1982).

199. Christiansen, O., Koch, H. & Jørgensen, P. The second-order approximate coupled cluster singles and doubles model CC2. *Chemical Physics Letters* **243,** 409–418; 10.1016/0009-2614(95)00841-q (1995).

200. Dunning, T. H. Gaussian basis sets for use in correlated molecular calculations. I. The atoms boron through neon and hydrogen. *The Journal of Chemical Physics* **90,** 1007–1023; 10.1063/1.456153 (1989).

201. Kendall, R. A., Dunning, T. H. & Harrison, R. J. Electron affinities of the first-row atoms revisited. Systematic basis sets and wave functions. *The Journal of Chemical Physics* **96,** 6796–6806; 10.1063/1.462569 (1992).

202. Woon, D. E. & Dunning, T. H. Gaussian basis sets for use in correlated molecular calculations. III. The atoms aluminum through argon. *The Journal of Chemical Physics* **98,** 1358–1371; 10.1063/1.464303 (1993).

203. Peterson, K. A., Woon, D. E. & Dunning, T. H. Benchmark calculations with correlated molecular wave functions. IV. The classical barrier height of the H+H2→H2+H reaction. *The Journal of Chemical Physics* **100,** 7410–7415; 10.1063/1.466884 (1994).

204. Martin, R. L. Natural transition orbitals. *The Journal of Chemical Physics* **118,** 4775–4777; 10.1063/1.1558471 (2003).

205. Pettersen, E. F. *et al.* UCSF Chimera--a visualization system for exploratory research and analysis. *J Comput Chem* **25,** 1605–1612; 10.1002/jcc.20084 (2004).

206. Jenny Gerstmann. Erzeugung und Charakterisierung von kurzlebigen Radikalen stabilisiert durch N-Heterocyclische Carbene. Dissertation. Universität Regensburg, 2021.

207. Turro, N. J., Ramamurthy, V. & Scaiano, J. C. *Modern molecular photochemistry of organic molecules* (University Science Books, Sausalito, op. 2010).

208. Risi, C. de *et al.* Oxidative N-Heterocyclic Carbene Catalysis. *Chemistry (Weinheim an der Bergstrasse, Germany)* **29,** e202202467; 10.1002/chem.202202467 (2023).

209. Phan, J. & Rehbein, J. *Mechanistic Investigations Towards a Successful PET with Breslow-Intermediates* (2021).

210. Frimer, A. A. (ed.). *Singlet O2* (CRC Pr, Boca Raton, Fla., 1985).

211. Bregnhøj, M., Westberg, M., Jensen, F. & Ogilby, P. R. Solvent-dependent singlet oxygen lifetimes: temperature effects implicate tunneling and charge-transfer interactions. *Physical chemistry chemical physics : PCCP* **18,** 22946–22961; 10.1039/c6cp01635a (2016).

212. Mavroskoufis, A. *et al.* N-Heterocyclic Carbene Catalyzed Photoenolization/Diels-Alder Reaction of Acid Fluorides. *Angew. Chem. Int. Ed. Engl.* **59,** 3190–3194; 10.1002/anie.201914456 (2020).

213. Armarego, W. L. F. & Chai, C. L. L. *Purification of laboratory chemicals.* 7th ed. (Butterworth-Heinemann/Elsevier, Amsterdam, Boston, 2013).

G. Declaration in Lieu of Oath

(1) I hereby declare that I have completed the dissertation presented without the impermissible help of third parties, without the use of resources other than those indicated, and that any data and concepts stemming directly or indirectly from other sources are indicated with citations to the literature.

(2) The following persons have assisted me in the selection and evaluation of the following material in the ways described in return for payment/without payment:

1. Gabriel Mayer: Performed the excited-state calculations for Part C. The respective UV-vis measurements and their evaluation were conducted jointly.

2. Aryaman Pattanaik: Assisted in interpreting mechanistic details in Parts A and B and contributed to establishing a hypothesis to rationalize the mechanisms.

3. .....

(3) No further persons were involved with the creation of the contents of the dissertation presented. In particular, I have not made use of the assistance of a doctoral consultant or other person in return for payment. No-one has received payment in kind either directly or indirectly for work which is associated with the content of the dissertation submitted.

(4) The dissertation has not been submitted in the same or similar form to another examining authority, neither in Germany nor abroad.

Vaterstetten, 20th January 2025

Dominik Kreutzer